Shedding light on the electronic structure of Mn+1AXn nanolamellar carbides

Damir Pinek

▶ **To cite this version:**

Damir Pinek. Shedding light on the electronic structure of Mn+1AXn nanolamellar carbides. Material chemistry. Université Grenoble Alpes [2020-..], 2021. English. NNT : 2021GRALI009 . tel-03218589

HAL Id: tel-03218589

https://theses.hal.science/tel-03218589v1

Submitted on 5 May 2021

HAL is a multi-disciplinary open access archive for the deposit and dissemination of scientific research documents, whether they are published or not. The documents may come from teaching and research institutions in France or abroad, or from public or private research centers.

L'archive ouverte pluridisciplinaire **HAL**, est destinée au dépôt et à la diffusion de documents scientifiques de niveau recherche, publiés ou non, émanant des établissements d'enseignement et de recherche français ou étrangers, des laboratoires publics ou privés.

Université Grenoble Alpes

THÈSE

Pour obtenir le grade de

DOCTEUR DE L'UNIVERSITE GRENOBLE ALPES

Spécialité : **PHYSIQUE DES MATERIAUX**

Arrêté ministériel : 25 mai 2016

Présentée par

Damir PINEK

Thèse dirigée par **Thierry OUISSE, Professeur, Université Grenoble Alpes**,
Et préparée au sein du **Laboratoire des matériaux et du génie physique (LMGP)**
de **l'École Doctorale IMEP2**

Exploration de la structure électronique des carbures nanolamellaires $M_{n+1}AX_n$

Thèse soutenue publiquement le **5 février 2021** ,
devant le jury composé de :

Prof, Vincent MAUCHAMP
Professeur, HDR, Université de Poitier, Rapporteur
Dr, Andres Félipe SANTANDER SYRO
Maître de conférences, HDR, Université Paris-Saclay, Rapporteur
Prof, Michel Barsoum
Professeur, Drexel university, Membre
Assoc. Prof, Takahiro Ito
Professeur associé, Nagoya university, Membre
Prof, Jean-Christophe CHARLIER
Professeur, Université Catholique de Louvain, Membre
Prof, Thierry OUISSE
Professeur, HDR, Université Grenobles Alpes, Directeur de thèse
Prof, Hubert Renevier
Professeur, HDR, Université Grenobles Alpes, Président

UNIVERSITÉ GRENOBLE ALPES

DOCTORAL THESIS

Shedding light on the electronic structure of $M_{n+1}AX_n$ nanolamellar carbides

---

Author:
Damir PINEK

Supervisor:
Pr. Thierry OUISSE

A thesis submitted in fulfillment of the requirements
for the degree of Doctor of Philosophy

Laboratoire des matériaux et de génie physique

May 4, 2021

"And so, finally, I suppose, he would be able to look upon the sun itself and see its true nature, not by reflections in water or phantasms of it in an alien setting, but in and by itself in its own place."

Plato, Republic

UNIVERSITÉ GRENOBLE ALPES

Abstract

Grenoble-INP

Laboratoire des matériaux et de génie physique

Doctor of Philosophy

Shedding light on the electronic structure of $M_{n+1}AX_n$ nanolamellar carbides

by Damir PINEK

The $M_{n+1}AX_n$, or "MAX" phases, where M is an early transition metal, A belongs to group 13-16 of the periodic table and X is C or N, are a class of nano-layered compounds that have sparked a strong interest from the material science community for their unique combinations of metal-like and ceramic-like properties. They are also precursors for MXENES, a whole family of two dimensional carbides obtained by exfoliation of 3D MAX phases and notably sought for energy storage developments. Up to 155 MAX phases have been discovered so far. Despite the attractiveness of MAX phases for a wide range of applications, the origins of several of their fundamental features are still under debate, notably regarding the relationships between their electronic structure, anisotropies and transport properties.

Herein this manuscript, we present the methodology we followed to grow MAX phase single crystals and experimentally determine the morphology of the electronic states (e.g. Band structure and Fermi surface) of Cr_2AlC, V_2AlC and Ti_3SiC_2. The output of angle resolved photoemission spectroscopy experiments carried out on single crystals are compared with density functional theory calculations. Band renormalization from electron-phonon coupling and influence of spin orbit coupling are outlined. The respective anisotropies of the Fermi surfaces are discussed with respect to the transport coefficients of each phase. The derivation of rigid band models that describe the electronic structure of M_2AC -or "211" MAX phases- is then developed. Finally, band structure and Fermi surface mappings of Ti_2SnC and of MAX phases magnetic derivatives -iMAX and 4473 phases- are briefly introduced, as well as the prospect of a potential exploration of $(M_xN_{1-x})_2AX$ solid solutions for tuning the position of the Fermi level in order to reach topological nodes within the band structure of 211 MAX phases .

Acknowledgements

La dernière page de ces quatre années de doctorat s'achève alors que je finis de peaufiner les corrections finales de mon manuscrit de thèse. C'est justement en ces derniers instants qu'il me paraît important de rendre hommage aux personnes qui m'ont soutenu au cours de cette aventure et sans qui tout ceci n'aurait pas été possible.

Tout d'abord, je tiens à remercier Dr. Andres Santander Syro, Prof. Vincent Mauchamp, Prof. Michel Barsoum, Ass. Prof. Takahiro Ito, Prof. Jean Christophe Charlier et Prof. Hubert Renevier pour avoir accepté de participer à ma soutenance de thèse. Je remercie tout particulièrement Andres et Vincent, les deux rapporteurs qui ont évalué mon travail de thèse.

Il y a bien sur quelqu'un que je ne peux pas ne pas mentionner ici : Mon directeur de thèse Thierry Ouisse, ou bien comme on le surnommait pendant mon master : Ouisse Titi ! Et par où commencer… Thierry est un scientifique extraordinaire, un physicien hors-pair qui m'a impressionné par ses raisonnements fins et juste et sa capacité à appréhender et maitriser un nouveau domaine ou une nouvelle technique en un temps record. Mais il a été surtout pour moi un mentor, toujours présent et à l'écoute ; un pilier scientifique et un grand support moral au cours de ces quatre années. Je suis fier d'avoir été son doctorant.

Une autre personne que je me dois de remercier est le professeur associé Takahiro Ito, Takahiro san ou encore appelé « Captain Ito », qui a été mon hôte pendant mes séjours à l'université de Nagoya pour une durée totale d'environ 7 mois. Je n'aurais certainement pas pu obtenir la plupart des résultats de ma thèse s'il ne m'avait pas ouvert les portes des synchrotrons UVSOR et AichiSR. Takahiro san, c'est un véritable artiste de la photoémission qui sait parfaitement comment orienter une expérience vers le succès.

Je tiens également à remercier tous les collègues avec qui j'ai eu la joie de travailler directement, en France comme au Japon, à commencer par Maxime, l'autre grand acolyte de Thierry qui nous a rejoints lorsque j'étais déjà en troisième année. Avant Maxime est venu Naud, un stagiaire avec qui j'ai passé moult journées à préparer des croissances, Kanji san qui a travaillé sur les manips ARPES au Japon et à SOLEIL à Paris, et Masashi san qui travaillait sur V2AlC. Un grand merci aux autres membres des équipes phases MAX à Grenoble et aux membres synchrotron radiation research center à Nagoya : Youngsoo, Thanasis, Isabelle, les deux Naoki, Shinnosuke san, Kontani san et j'en passe..

Je me souviendrais toujours de mes autres compères doctorants du LMGP et d'ailleurs, Guillaume et Monica et nos pauses cafés endiablés, Neha qui est passée pour des manips un été et qui m'a accueilli à Philadelphie, Fanny et Jordy et leur sens de la fête, Pierre, Raquel, Larry, Ragnar, Julius, Charlotte et bien

d'autres... Merci aussi à l'ensemble du personnel permanent du LMGP pour ces 4 années, merci à la direction, aux chercheurs des autres équipes et à l'ensemble du personnel technique et administratif. Je suis également reconnaissant à Laurence et Hubert d'avoir fait partie de mon comité de suivi de thèse pendant 4 années.

Jérôme, Guillaume, Pierre-Michel, Thomas, Louis, Naoufel, Claude, Manu, tous les Black Snails, Folikan, les membres du BMF et les autres jazzeux, merci à vous pour avoir rempli ces quatre années de groove et de belles énergies. Merci aux vieux fossiles qui sont toujours là, à mes vieux amis que je connais depuis bien longtemps, Williaume, Rafa, Loic, Sei, Eve; Denis, Adrian, Lisa, Thibaud et tout le monde !

Enfin, quelques mots pour ma famille et en particulier mes deux sœurs, Liliana et Lucile, et mes parents pour leur soutien indéfectible et qui ont toujours cru en moi, même quand personne ne me voyait réussir en quoi que ce soit.

A ma grand-mère qui nous a quittés il y a deux ans.

Contents

List of Figures

List of Abbreviations

MAX	$M_{n+1}AX_n$ nanolamellar carbides
MXENE	$M_{n+1}X_n$ bidimensional carbides
iMAX	In-plane ordered MAX phase
4473	$Mo_4Ce_4Al_7C_3$ phase
oMAX	Out-of-plane ordered MAX phase
BS	Band Structure
DOS	Density Of States
pDOS	Partial Density Of States
BZ	Brillouin Zone
IBZ	Irreducible Brillouin Zone
FS	Fermi Surface
XPS	X-ray Photoelectron Spectroscopy
ARPES	Angle Resolved Photoelectron Spectroscopy
UHV	Ultra High Vacuum
HF	Hartree-Fock
DFT	Density Functional Theory
LDA	Local Density Approximation
GGA	General Gradient Approximation
PBE	Perdew, Burke and Ernzerhof
SCF	Self Consistent Field
APW	Augmented Plane Wave
lo	local orbital
SOC	Spin Orbit Coupling
S-pol	Linear horizontal light polarization and Vertical analyzer slit configuration
P-pol	Linear vertical light polarization and vertical analyzer slit configuration
AFM	Antiferromagnetism / Antiferromagnetic
RBM	Rigid Band Model
SHE	Spin Hall Effect

List of Symbols

$\hbar$	Planck constant	$1.0545718 \times 10^{\neg 34} m^2.kg.s^{\neg 1}$
m_0	Free electron resting mass	$9.1 \times 10^{\neg 31} kg$
c	Speed of light	$2.99792458 \times m.s^{\neg 1}$
v_F	Fermi velocity	$m.s^{\neg 1}$
m_*	Effective mass	m_0
ρ_{ab}	In-plane resistivity	$\Omega.m$
ρ_c	Out-of-plane resistivity	$\Omega.m$
R_H	Hall constant	$m^3.C^{\neg 1}$
ρ	Electron density	$cm^{\neg 3}$
$h\nu$	Photon energy	eV
V_0	Inner potential	eV
ϕ	Work function	eV
E_{kin}	Kinetic energy	eV
θ_k or (θ_x, θ_y)	Angular coordinates	
$k_{\|\|}$ or (k_x, k_y)	In-plane wavevector component	$A^{\neg 1}$
$k_\perp$ or k_z	Out of plane wavevector component	$A^{\neg 1}$
Γ, M, K, A, L, H	Hexagonal BZ symmetry points	*Nounits*

Dedicated to all the people who helped me to overcome adversity throughout my life . . .

Explorer la structure électronique des carbures nanolamellaires $M_{n+1}AX_n$, résumé en Français

Les phases $M_{n+1}AX_n$ ou phases “MAX” -avec M un métal de transition, A un élément des groupes 13 à 16 du tableau périodique et X soit C ou N- forment une classe de composés nanolamellaires qui a suscité un fort intérêt scientifique pour leur unique combinaison de propriétés métalliques et de propriétés issues des céramiques. Il s’agit également des précurseurs des MXENES, une famille de matériaux bidimensionnels obtenus par exfoliation des phases MAX tridimensionnelles qui génèrent un fort engouement pour des applications potentielles dans le domaine du stockage d’énergie. Environ 150 phases MAX ont été découvertes à ce jour, mais malgré le potentiel applicatif de ces composés, l’origine d’un certain nombre de leurs propriétés fondamentales reste une question ouverte. On ne trouve qu’un nombre relativement faible d'études où l’origine des propriétés électroniques et thermoélectriques des phases MAX est discutée vis-à-vis de mesures directes de leur structure électronique. Nous donnons ci-dessous une liste non exhaustive de quelques questions qui se posaient avant le début de ce travail de thèse:

- Dans quelle mesure les structures de bandes expérimentales et les surfaces de Fermi des phases MAX différeraient elles des spectres théoriques?

- Quelle serait l'influence des corrélations électroniques, des interactions magnétiques, du couplage spin orbite ou encore du couplage électron-phonon sur structure électronique de phase MAX?

- A quel point l’anisotropie structurelle de ces composés nanolamellaires influe-t-elle sur leur structure électronique ? Comment peut-on la mettre en évidence avec des spectres de photoémission expérimentaux?

- Connaissant la morphologie de leurs états électroniques proches du niveau de Fermi, peut-on facilement construire un modèle qui décrirait le transport électronique dans les phases MAX plus rigoureusement que des modèles de Drude à deux bandes qui ont été utilisés auparavant?

- Est-il possible de trouver un point commun fondamental entre les structures électroniques des différentes phases MAX?

Pour tenter d'apporter des réponses à ces questions, la méthodologie suivante a été appliquée:

- (i) Des monocristaux de dimensions macroscopiques (1 mm^2-1 à 2 cm^2) ont été synthétisés au LMGP à Grenoble pour plusieurs phases, par procédé de croissance en solution liquide à haute température.
- (ii) Ces échantillons monocristallins ont été amenés à divers lignes synchrotron afin d'effectuer des mesures de spectroscopie de photoémission résolue en angle (ARPES), à AichiSR, UVSOR BL5U et BL7U au Japon ainsi que sur la ligne Soleil Cassiopée en France.

- (iii) Des calculs de théorie de la fonctionnelle de densité (DFT) ont été réalisés à Grenoble et ont été comparés aux résultats des expériences ARPES.

Avant ce travail, l'absence de larges monocristaux de phases MAX a été un frein significatif à la détermination expérimentale de leur structure de bande et surface de Fermi. En effet, les méthodes permettant de mesurer expérimentalement ces dernières, comme par exemple l'ARPES, nécessitent des monocristaux purs et de très haute qualité.
Ainsi, un des succès majeur de notre approche, combinant calculs DFT et spectroscopie ARPES sur monocristaux, a été la première observation expérimentale de la Surface de Fermi et structure de bande d'une phase MAX: Cr_2AlC. V_2AlC et Ti_3SiC_2 ont suivi, et l'excellent accord trouvé entre les expériences et la théorie a permis de fournir une description détaillée et sans équivoque des états électroniques des phases MAX et de leur morphologie. Dans une certaine mesure, on pourrait affirmer que cette approche a permis d'au moins partiellement répondre aux questions mentionnées ci-dessus.
Avant de détailler le contenu des différents chapitres de cette thèse, les résultats principaux obtenus pour chaque phase sont brièvement présenté :
- La surface de Fermi de Cr_2AlC s'avère être composée d'une combinaison complexe de tubes d'électrons et de trous tous quasi-bidimensionnels. L'anisotropie obtenue pour la surface totale est cohérente avec le résultat de mesures de magnéto-transport sur monocristaux. Une renormalisation d'une des bandes au voisinage de K survient au niveau de Fermi et semble suivre les prédictions que l'on attendrait pour un système ou le couplage électron-phonon aurait une influence.

Malgré les précédentes études affirmant que l'état fondamental de Cr_2AlC serait Antiferromagnétique, des calculs DFT non magnétiques ont permis de retrouver la plupart des caractéristiques des bandes expérimentales et aucune signature claire d'un ordre ou d'une transition antiferromagnétique n'a été mise en évidence par les mesures de diffraction neutron sur poudre que nous avons effectué. Les lignes de Fermi issues du calcul DFT ont été utilisées pour calculer différents coefficients d'Onsager dans le plan via l'équation de Boltzmann et en choisissant une approximation pertinente des mécanismes de relaxation et du comportement du temps de relaxation en température.
La dépendance expérimentale en température des composantes dans le plan de la résistivité de la constante de Hall a ensuite pu être déterminée pour ce système à

plusieurs bandes, ainsi que la densité électronique associée. Ces résultats ont permis de démontrer l'insuffisance du modèle de Drude à deux bandes pour décrire le transport électronique dans les phases MAX.

- Nos analyses ARPES et DFT ont révélé que la structure électronique de V_2AlC proche du niveau de Fermi était sensiblement plus tridimensionnelle que celle de Cr_2AlC. L'influence du dit k_z-broadening a été déterminée avec succès et est venue en appui à l'évaluation du caractère tridimensionnel de la structure électronique de ce matériau. Une analyse approximative des anisotropies de la surface de Fermi et des vitesses de Fermi a indiqué que nos résultats n'allaient pas dans le sens d'autres mesures d'anisotropie réalisées sur des monocristaux de V_2AlC, et pour lesquels l'anisotropie de transport s'est avéré être un ordre de grandeur plus élevé que pour Cr_2AlC.

Des états de surface volatiles ont été observés pour la première fois sur une phase MAX, centrés sur les points M de la zone de Brillouin de V_2AlC. Une ligne nodale « Gappée » a également été mise en évidence dans la structure de la bande V_2AlC, autour de 0,27-0,29 eV sous le niveau de Fermi.

-Des calculs DFT pour Ti_3SiC_2 ont reproduit avec succès les mapping de surface de Fermi et structure de bande obtenus avec l'ARPES. Après avoir corrigé la position du niveau de Fermi de quelques meV, la surface de Fermi obtenue semblé être légèrement différente des études antérieures.
On obtient toujours un mélange de bandes de trous et d'électrons au niveau de Fermi, avec la surface de Fermi de la bande 50 qui apparaît clairement responsable de la délocalisation des états électroniques selon l'axe c. Le niveau d'accord entre l'ARPES et la DFT nous a permis d'étudier plus en détail la structure électronique de ce composé, notamment les effets du couplage spin orbite. Des inversions de bande et des croisements de bandes présentant des dispersions linéaires ont été repérés au niveau de Fermi. Nos calculs DFT ont montré que des « Gap » s'ouvrent au niveau de ces croisements lorsque le couplage spin-orbite est pris en compte. Ainsi, Ti_3SiC_2 pourrait être un hôte potentiel de certains phénomènes de transports exotiques tels que la conversion courant de charge en courant de pur spin via les mécanismes de l'effet Hall de spin intrinsèque.

En suivant les résultats énumérés ci-dessus, il serait aisé d'avancer que les phases MAX montrent un panel de diverses structures électroniques et surfaces de Fermi différentes. Est-ce-à dire que celles-ci seraient totalement disjointes ?
Malgré les différences observées entre les surfaces de Fermi de Cr_2AlC, V_2AlC, Ti_3SiC_2 et d'autres phases MAX, nous avons également mis en évidence quelques caractéristiques remarquables partagées par tous ces composés:

- Tout comme cela a été indiqué dans de nombreuses études antérieures, nous avons vérifié que les orbitales d des atomes M dominaient la structure électronique de Cr_2AlC, V_2AlC et Ti_3SiC_2 près de leurs niveaux de Fermi respectifs.

- Il suffit de 5 modèles de bandes rigides différents pour décrire la structure électronique de la plupart des phases MAX 211 (ou M_2AX), ce qui permet de construire une classification de ces phases qui comprendrait cinq sous-familles. Changer la nature de l'élément M permet de modifier la position de E_F et ainsi de naviguer à travers une seule "structure de bande rigide".

- L'applicabilité des modèles de bandes rigides ainsi que le succès du calcul DFT "standard" pour la description des états électroniques des phases MAX suggèrent que, pour ces composés, les corrélations électroniques ne jouent pas un rôle majeur.

De ces considérations, il apparaît que malgré leur apparente diversité, les structures électroniques de diverses phases MAX partagent certains traits fondamentaux. Dans le cas des phases MAX 211, on pourrait même affirmer que l'applicabilité des modèles de bandes rigides implique une certaine unicité au sein des sous-familles de phases MAX.

Un bref résumé des définitions et propriétés des phases MAX et de leurs dérivés est donné au chapitre deux, suivi d'un rappel de quelques fondamentaux de physique du solide. Les principes de base des techniques de croissance cristalline, de la spectroscopie de photoémission résolue en angle (ARPES) et la théorie fonctionnelle de la densité (DFT) sont résumés dans le troisième chapitre de ce manuscrit. Ensuite, les résultats de la plupart des travaux de recherche effectués au cours de cette thèse de doctorat sont présentés dans les autres chapitres de cette thèse.

Cr_2AlC est au centre du chapitre 4, et beaucoup d'attention à la comparaison entre les expériences et calculs y est accordée. L'influence potentielle du couplage électron-phonon et du magnétisme est examinée, et les coefficients de magnétotransport Cr_2AlC sont dérivés à partir de la morphologie de sa surface de Fermi.

Au chapitre 5, on constate que la structure des bandes expérimentales et les cartes de surface de Fermi de V2AlC correspondent remarquablement bien aux calculs. L'anisotropie de la surface de Fermi de V_2AlC est discutée et est comparée au cas de Cr_2AlC. Des états de surface sont mis en évidence dans les spectres expérimentaux.

Le chapitre 6 est consacré à une description de la structure électronique de toutes les phases 211, basée sur ledit modèle de bande rigide. Une tentative de construire une classification des phases MAX y est exposée. De nombreuses phases semblent

posséder une «structure de bande rigide» similaire et, de manière surprenante, des « nœuds topologiques », par ex. les croisements de bandes linéaires et une ligne nodale de Dirac, sont mis en évidence au sein de ces structures de bandes rigides.

Enfin, le chapitre 7 traite de l'étude des spectres électroniques de Ti_3SiC_2. Une cartographie ARPES haute résolution a permis de sonder les caractéristiques fines de la structure de bande Ti_3SiC_2 et de sa surface de Fermi. Une nouvelle interprétation de la valeur quasi nulle du coefficient Seebeck de Ti_3SiC_2 est donnée et l'impact du couplage spin orbite sur certaines bandes est considéré.

Finalement, après une courte conclusion sur les résultats expérimentaux et théoriques obtenus pendant la durée de cette thèse, d'autres composés nano-lamellaires dérivés des phases MAX – les phases iMAX et 4473- sont rapidement présentées. Les propriétés magnétiques ainsi que le comportement Kondo de $Mo_4Ce_4Al_7C_3$ sont abordés. La perspective de l'exploration des solutions solides $(M_xN_{1-x})_2AX$ pour pouvoir contrôler la position du niveau de Fermi des phases MAX 211 - afin d'atteindre de potentiel nœuds topologiques- est également discutée.

Chapter 1

Introduction

Materials, solids, crystals, metals, insulators! These are concepts referring to physical objects which are parts of our everyday environment as beings inhabiting planet earth. As trivial as this may sound, it is undeniable that the human's capacity to understand and control the properties of such objects or systems has become quite advanced. An incredible number of materials have been engineered by man over the centuries, going from alloys of elemental metals as ancient as bronze or steel to organic polymers synthesized from petroleum byproducts, and recently to bidimensional systems such as graphene. Going to a more fundamental level, superconducting materials -through which electric current is transported without any resistive losses- have been discovered at the beginning of the past century. Another impressive development is how the electronic conductivity of semiconductors such as silicon -which is used as a building block for nearly all daily electronic devices- can be tailored up to a far-fetched precision.

Beyond the impressive level of mastery over material synthesis that has been achieved over history, understanding what makes the nature of a solid material as a system has been a fundamental problem which was decisively answered relatively late in the history of science. This question would deserve to be discussed much more systematically than it is within the scope of this manuscript. One can argue that the first significant attempt of an answer was formulated more than 2000 years ago by the greek philosopher *Democritos*. He is thought to be the first to claim that all physical bodies are constituted of indivisible 'bricks' of matter, the *Atomoi* or atoms. A journey 2000 years ahead proves how formidable his intuition was. The great scientific revolution of the early 20th century provided evidence for the existence of atoms and their constituents: the nucleus and the electrons. It also brought about the birth of quantum mechanics, possibly the most important theory in Physics, which describes most systems at the microscopic scale. Particles such as electron are no longer localized but rather described by wavefunctions. The work of the pioneers of quantum physics such as Bohr, Sommerfeld, Heisenberg, Dirac, Bloch, Brillouin and many more led to the development of a quantum theory of solids which later became known as Solid State physics. Up to the present day, it probably gives the most accurate answers to the question of the physical nature of solid materials.

Keeping aside the case of amorphous materials which are inherently disordered, a crystalline solid can be seen as an almost infinite collection of atoms where the nuclei remain (quasi) static and arranged in space

in a somehow ordered and periodic manner, while the electrons wavefunctions are more or less delocalized depending on the material considered and on the electron native atomic shell. A given ordering of atoms will be stable under specific thermodynamic conditions. Electrons that are shared between atoms –notably forming various kind of bonds- will play a most important role in setting the energy of the system and dictating its stability and overall properties.

All the information regarding the state of the electrons in a solid and their various interactions is encompassed within the electronic structure, a mathematical object that underline many of the electronic properties of the solid.

The following thesis is an attempt to shed some light on the electronic structure of a specific class of materials: the $M_{n+1}AX_n$ nanolamellar carbides, or MAX phases. Discovered in the 1960s and extensively studied since the late 1990s, MAX phases form a large family of more than 155 compounds which share the same crystal structure and a common set of properties. Their nanolamellar structure leads to a peculiar blend of metallic and ceramic properties. We seeked to explore the morphology of the electronic states of these compounds through the means of photoelectron spectroscopy performed on single crystals and *ab initio* calculations.

This manuscript consists of 8 separate chapters. Chapter 2 is a short bibliographic review of MAX phases and their derivatives, ranging from their basic properties to their applications. Chapter 3 details the synthesis, spectroscopic and computational methods we used. Chapter 4 to 7 focus either on the electronic structure of a specific compound (chapters 4, 5 and 7) or on whole subclasses of MAX phases (chapter 6). Finally, the conclusions of the thesis and perspectives are given in chapter 8

Chapter 2

MAX phases: A class of peculiar transition metal carbides

2.1 A brief overview of MAX phases

The acronym M. A .X. refers to a class of nanolamellar carbides (nitrides) that all share the same chemical formula: $M_{n+1}AX_n$, where M is a transition metal, A belong to the group 13 to 16 (mostly 13 and 14) and X can be either C or N [1, 2]. The M_2AX's are labelled as (211) phases, the M_3AX_2's (312), the M_4AX_3's (413) and so forth. Their respective crystal structure is given in figure 2.1.

MAX phases exhibit a unique blend of metallic and ceramic like properties that makes them particularly attractive for applications in extreme conditions [1, 2]. The origin of many of these properties can be understood from their electronic structure, e.g. the morphology of their electronic states in quasi-momentum space [3]. One of their most ubiquitous feature is how large this family of compound becomes when varying the M or A elements while keeping the structure the same [4].

There are more than 80 different MAX compounds that have been discovered by today, and even more when considering the MAX derived materials such as MAX solid solution, iMAXs, oMAX or even the MAB phases [7] (see figure 2.2) . One should also note that it is possible to exploit the MAX nanolamellar structure to synthetize bidimensional compounds called MXENES [8]. But before we delve deeper into the basic properties of MAX phases and their derivatives, we believe it is necessary to give some insight on how these compounds were discovered and how they became a major topic of research within materials science.

2.1.1 Chronology

The story of MAX phases begins in the 1960s, in Vienna, when the compounds that were later to be named MAX were discovered for the first time [9]. Nowotny and his coworkers synthetized many new carbides and nitrides [10], and some among them happened to share a common chemical formula, M_2AX. At first, they were labelled as H phases. Then, apart from the first synthesis's of the future 312 phases Ti_3SiC_2 and

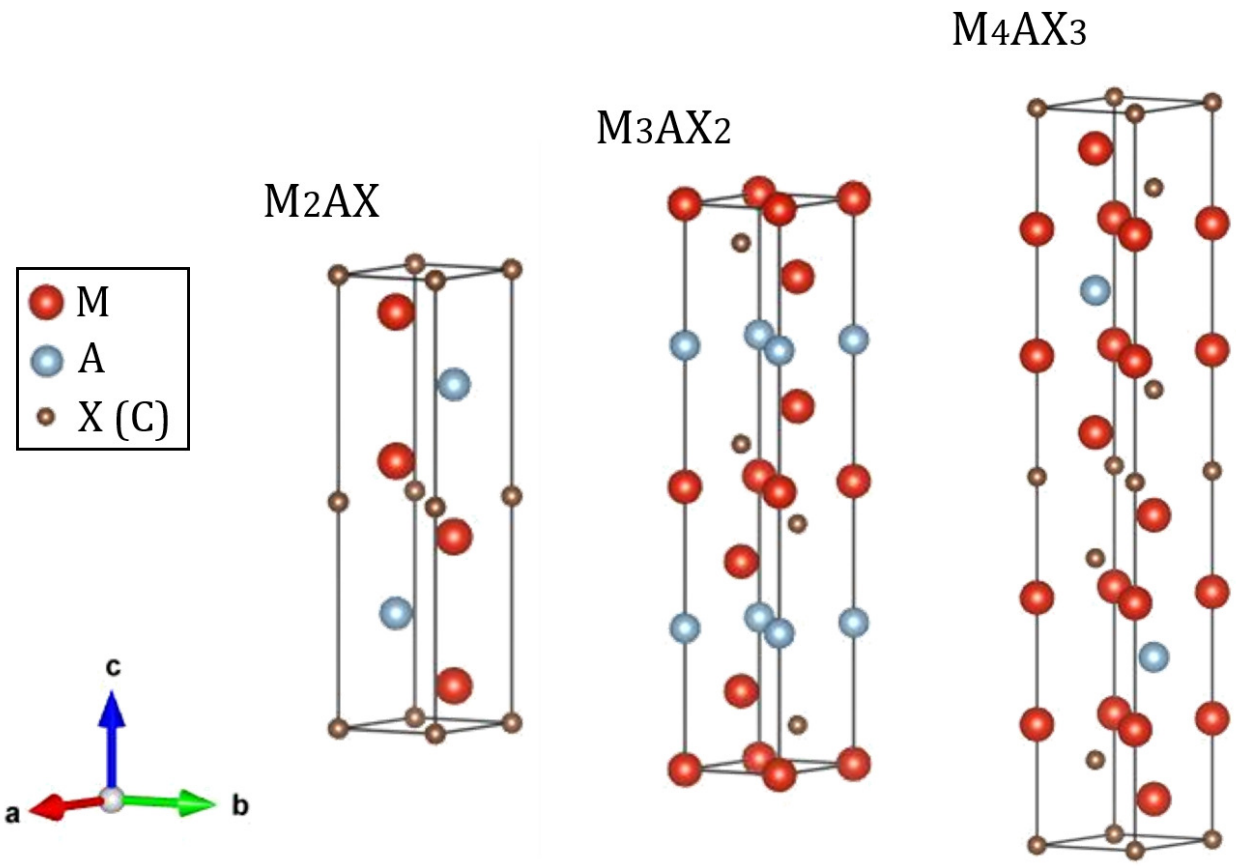

FIGURE 2.1: Unit cells of $M_{n+1}AX_n$ phases, for n=1,2,3, respectively from V_2AlC [5], Ti_3SiC_2 [2] and Nb_4SiC_3 [6]. One should notice that the $M_{n+1}X_n$ layers get larger as n increases, but they keep being separated by monoatomic A atoms planes. Polymorphisms of (312) and (413) are ignored in these schematics

Ti_3GeC_2 to be carried out in 1967, the H phases were mostly forgotten and their properties mainly ignored. In the case of Ti_3SiC_2, it can be attributed to the lack of pure, high quality bulk samples [1], thus not allowing for an accurate determination of many of its physical properties.

The interest for these materials arose from slumber about 30 years after their initial discovery, in a dynamic initiated by the group of Michel Barsoum in 1996 [11]. Using reactive hot pressing sintering at high temperature (1600°C) from Ti, SiC and graphite powders, they managed to synthetize dense, single phase polycrystalline samples of Ti_3SiC_2[12]. From there, they could assess the basic properties of this material: a room temperature electrical conductivity about twice as high as pure Ti, a thermal conductivity and heat capacity of respectively 43 W/m K and 110 J/mol K, apparent resilience to thermal shock , machinability close to graphite and the list goes on [2, 11, 13, 14]. What drove impetus towards Ti_3SiC_2 was not one single characteristic, but rather its whole combination of properties and how they were related to its nanolamellar structure [13]. From there, and as Ti_3SiC_2 structural kinship to the 211 or H phases came to be recognized,

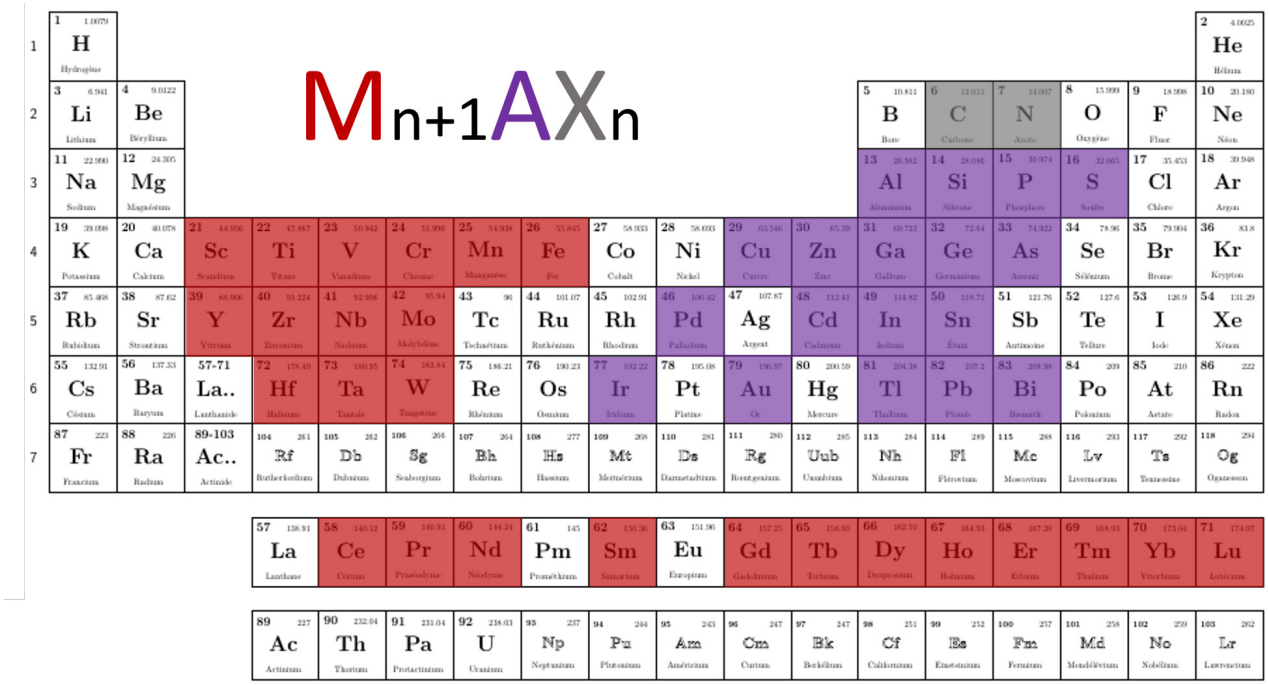

FIGURE 2.2: A periodic table of MAX phases, where M and A refers to the building blocks to pristine MAX phases, solid solutions and other derivatives

synthesis and characterization of the latter was the next natural step to perform. By the end of the decade, phases such as Ti_2AlC, Ti_2AlN, Ti_3GeC_2, Hf_2SnC and V_2AlC were synthetized by hot press sintering [2, 15]. As they exhibited the same structure and a similar blend of properties as Ti_3SiC_2, it was held as a consensus that the '(312)' and '(211)' belong to a same group of compounds, different to most other ceramics or metals.

But these materials really acquired the denomination 'MAX' when the firsts 413 were discovered, between 1999 (Ti_4AlN_3) and 2009 (Ti_4GaC_3) [16, 17, 18, 19]. Higher order phases have been hinted at [20, 21], as well as other MAX derivatives such as 513 or 725 [1, 22]. The general formula $M_{n+1}AX_n$ was acknowledged before the acronym MAX started to be used widely.

Regarding MAX phases synthesis, the most widely used technics has been reactive hot pressing sintering to process bulk samples from elemental powders [12, 11, 13, 15, 23]. Alternative synthesis methods exist, such as self-propagating high-temperature synthesis [24, 25], plasma spark sintering [26, 27] or solid liquid reaction synthesis [28, 29]. Growth technics such as PVD are also extensively used to grow MAX thin films [4, 22, 30, 31, 32, 33, 34]. Nearly single crystalline quality can be reached through PVD, while the samples obtained by most bulk synthesis technics are found to be highly polycristalline. In 2011, Mercier *et.al* synthetized the first Ti_3SiC_2 bulk single crystals by high temperature solution growth [35]. This process will be detailed in the third chapter of this manuscript.

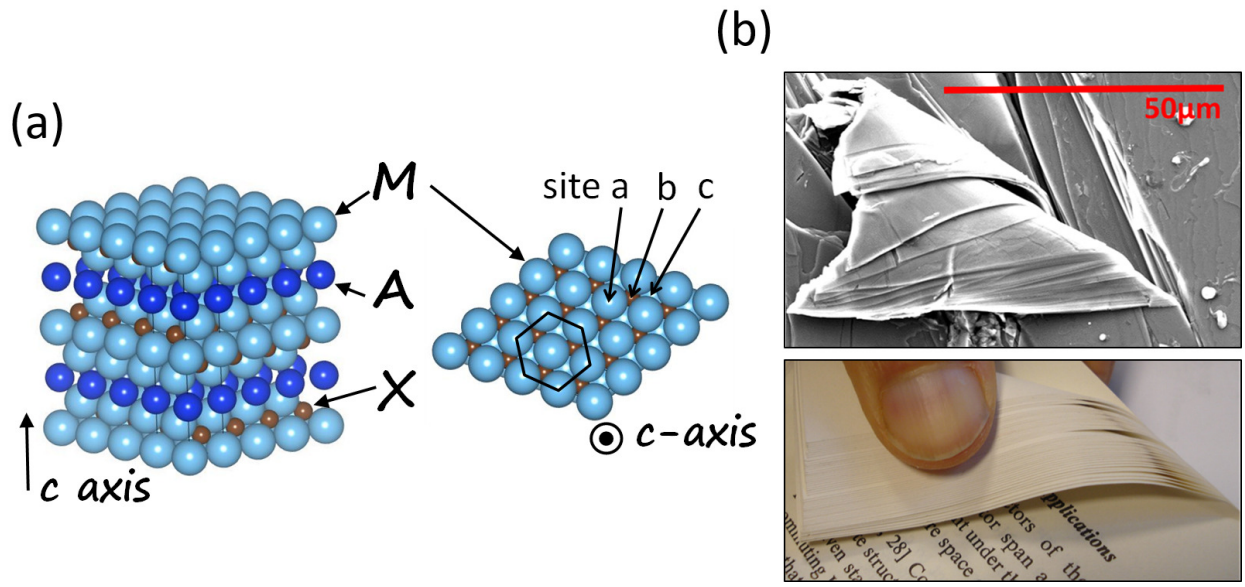

FIGURE 2.3: (a)Nanolayered structure of MAX phases, with M, A and X monoatomic planes. (b)top surface of Cr_2AlC crystals mechanically scratched using a scalpel blade and the thumb of my supervisor on top of a physics book.

2.1.2 A remarkable combination of properties

Ternary $M_{n+1}AX_n$ carbides and nitrides all crystallize in the $P6_3/mmc$ space group, with two formulas per unit cell. X atoms are located at the center of octahedral sites with M atoms on the edges of these octahedrons, while A atoms are located within somewhat larger prisms [1]. There exist different MAX polymorphs: one single polymorphs for the 211's, two and 3 polymorphs for the 413's. In all cases, the M-X blocks show a characteristic zig zag pattern along the $[11\bar{2}0]$ planes whereas the A atoms always remain in the mirror planes (see figure 2.1). In most phases, M-X bonds are stronger than the M-A bonds. While some of MAX phases properties can be related to their MX counterparts, others are inherent to their nanolamellar structure [2] (see figure 2.3). For both family of materials, bondings are a mixture of metallic, covalent and ionic [3]. As for their MX counterpart [36, 37], MAXs are metals and density of states at the Fermi level is far from negligible and is dominated by the d orbitals of the M atoms. It is the reason why these two families of compounds are good conductors of electricity and heat. To be more specific, MAX phases are actually superior to MXs in term of electrical conductivity [1]. For example, the conductivity of pure V_2AlC is about a few fractions of ten the conductivity of copper [38].

Yet, MAXs show a significantly higher degree of anisotropy than MXs. Their c/a ratios range from about 4.45 for typical 211s to 5.75 for 312s and 7.2 for 413s [5, 2, 6], while c/a values for MX compounds are generally of the order of one, with most of the MX exhibiting fairly isotropic Rock salt (sodium chloride) structures [36, 37, 39]. MAXs strong anisotropy is to be linked to their layered nature and, as we will see throughout this manuscript, the relationships between the anisotropies of observables such as electrical resistivity or thermopower and structural anisotropies are not always simple [40]. Electrical transport and anisotropies as

well as their relation to the electronic structure of MAX phases will be discussed further in 2.3 and throughout chapter 4, 5 and chapter 7. MAX phases good electric conductivity is mainly responsible for their thermal conductivity. In general, the thermal conductivity of most material can be separated in two contribution [40]:

$$K = Kel + Kphon \tag{2.1}$$

The phonon contribution to most MAX phase thermal conductivity was found to be negligible compared to the electronic one [38]. This has been attributed to the rattler effect e.g. in our case the strong vibrations of the A atom of most MAX phases which act like scattering centers for phonons [41, 42] (with the notable exception of MAX phases containing lighter A element, which are weaker scattering centers). Regarding thermal stability, MAX phases are found to be kinetically stable up to temperature of the order of 1500 to 1800°C [1]. They do not melt congruently but peritectically decompose as follows:

$$M_{n+1}AX_n \longrightarrow M_{n+1}X_n + A \tag{2.2}$$

The formation of the MX transition metal counterpart of MAX phases can be correlated to the relative strengths of the covalent bounds between M and X atoms compared to the one between A and M atoms. When it comes to the actual thermodynamic stability of MAX phases, they would occupy a very narrow window within the compositional parameter space of (A,M,X) ternary diagram at a given temperature [1, 43]. This point is of crucial importance for the growth of single crystals, as we will see in section 3.1.2. When it comes to chemical stability, MAX phases reacts very little with their surrounding and if a reaction is to occur, it will preferably involve the A element [44, 45, 46]. Very stringent solutions would be needed to dissolve a MAX phase. For example, nearly pure HCl would merely clean the surface of a Cr_2AlC single crystal. Yet, a chemical route to selectively get rid of the A atomic plane and transform MAX phases into bidimensionnal MXENES does exist [47] and will be discussed in section 2.2.1.

MAX phases possess excellent high temperature mechanical properties and a high degree of damage tolerance while they possess many ceramic like properties [1, 48, 49, 50, 51]. It can be related to their nanolayered structure, with alternate atomic planes with weaker M-A and very strong M-X covalent bonds. However, for these properties to be useful at high temperature, an oxide layer needs to be formed at the surface of the material. Al based MAX phases are very interesting in that regard, as they form a protective layer of Al_2O_3 above 800°C which is then stable up to 3000°C in the case of Ti_2AlC [52, 53, 54]. Overall, MAX phases exhibit a blend of chemical and physical properties that place them at the interface between metal and ceramics. These are summarized in figure 2.4.

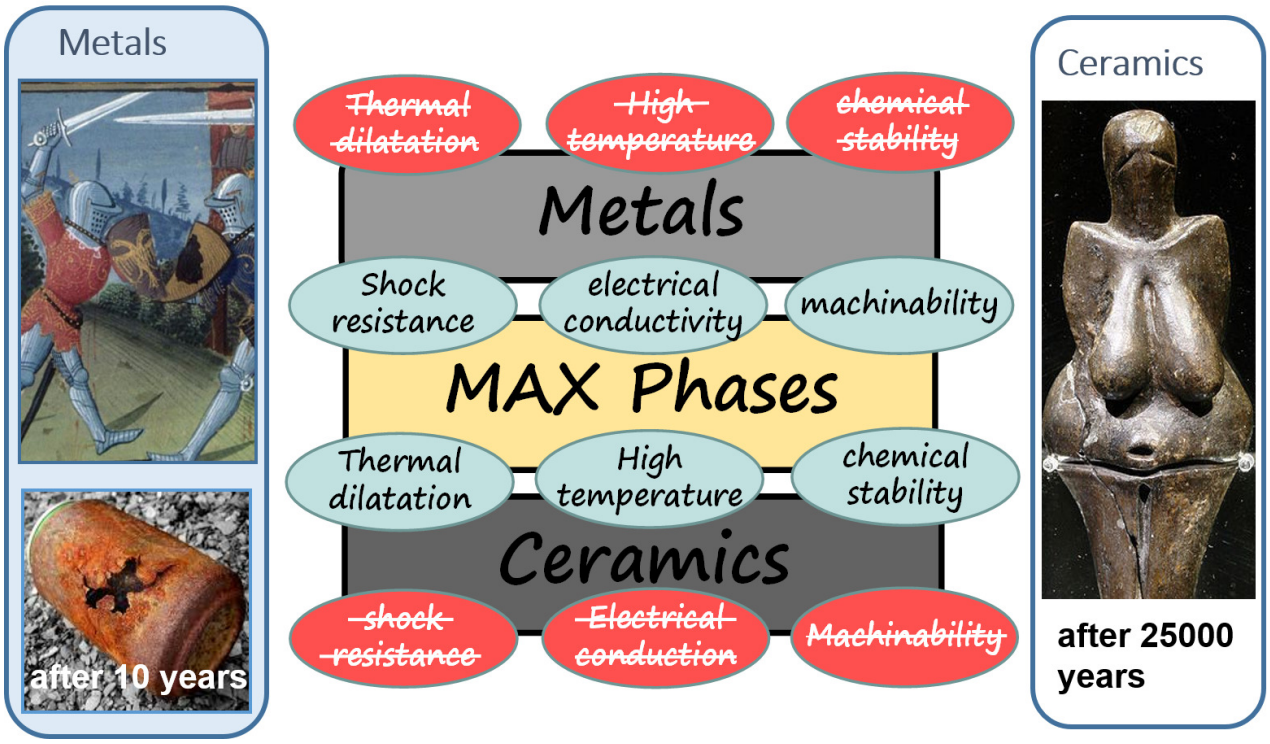

FIGURE 2.4: MAX phases basic properties, at the interface between metal and ceramics

2.1.3 Applications

As aforementioned, MAX phases all have a high degree of damage tolerance, a high degree of chemical resilience, a relatively low thermal expansion coefficient (as expected of ceramics) while their thermal and electrical conductivities are typical of good metals. They are mechanically stiff and can withstand extreme thermal shock while being relatively soft and readily machinable. Due to this remarkable combination of metal and ceramics properties, they are sought for a number of applications . These mainly concern extreme conditions, at high temperature or high pressure. Most of them can be found in the reference book of Michel Barsoum [1] as well as from other sources with only a few selected here [55, 56, 57]. Ti_2AlC, Ti_3SiC_2 and Cr_2AlC are the most promising candidates for applications. Ti2AlC in particular, can withstanding up to 10000 thermal cycles at 1350°C due to the insulating Al2O3 oxide layer that forms at its surface. They could potentially replace graphite for many of its high temperature applicationa, such as heating elements or thermal shields. Their machinability as well as their thermal properties are definitely an advantages, but they cannot be used at temperature in the 2000°C range or higher, where graphite is one of the only affordable material to be used. MAX phases good metallic properties combined with the high temperature, mechanical and chemical stresses they can withstand make them a potential material to replace noble metals within system that would have to overcome rather harsh conditions. The Swedish start up Impact Coatings, for example, seeks to replace gold electrical contact by MAX phases. They also produce MAX phases based bipolar plates for Fuel cells [58]. The remarkable damage tolerance and tribological properties of Ti_3SiC_2 and Ti_2AlC have lead them to be used to build the pantographs prototypes of Chinese high speed trains [7]. Cr_2AlC is

also considered for aeronautic applications. MAX phases oxidation resistance are also considered to be put to use in another field: Nuclear cladding. Ti_3AlC_2, Ti_2AlC or other MAX phases can be sprayed onto the Zircaloy crust protecting the nuclear fuel [59]. The additional Al_2O_3 layer at the surface of the MAX phase would then keep the Zircaloy protected from oxidation by steamed water within the primary circuit of the nuclear reactor. If the Zircaloy were to be oxidized, significant quantity of H2 would be released, potentially provoking an explosion similar to the one that destroyed the reactors 1, 2 and 3 of the Fukushima Daishi power plan in 2011.

MAX phases overall show great promises for future applications, even if the projects listed above are currently at the development stage. One important point to consider for a potential industrial willing to invest in MAX phase based products would of course be the price of such compounds. As for now, MAX phases are available commercially and distributed by many suppliers of materials for research or industrial applications (See Alibaba.com, for example). For most cases, MAX phases are synthetized by hot press sintering from powder of elemental compounds and binaries. Taking into account the market demands, prices of commercialized MAX powder is presently in the order of 500 euros per kg, which is way more expensive than other high temperature ceramics such as SiC or Si_3N_4. From now, we will shift our focus from the potential applicability of MAX phases research to the understanding of the fundamental features of these materials, which is the main scope of this manuscript.

2.2 MAX phases derivatives

We will now present a taxonomy of the derivatives of the Mn+1AXn layered transition metal carbides. MAB phases as well as out of plane ordered oMAX will not be considered within this section. Despite the growing scientific interest on these compounds, we decided to restrain ourselves to compounds that are closely related to the topic of this manuscript or that are of the uttermost importance for the specific field of MAX phases.

2.2.1 From MAX to MXENES

Dimensionality is certainly one among the key parameters that have been tuned by physicists to explore new states of matter in the late 20th and early 21th century, notably with the development of quantum dots (0D) [60, 61], nanowires and nanotubes (1D) [62, 63, 64]. A central concept for the development of such systems is quantum confinement, e.g. potential barrier or constriction over one or several direction leading to an uplift of the degeneracies of the energy levels up to a point when only a single level is occupied. It has in particular led to the development of bidimensional electron gases within the quantum well found at the interface of As/GaAs heterojunctions, for example (2D)[65].

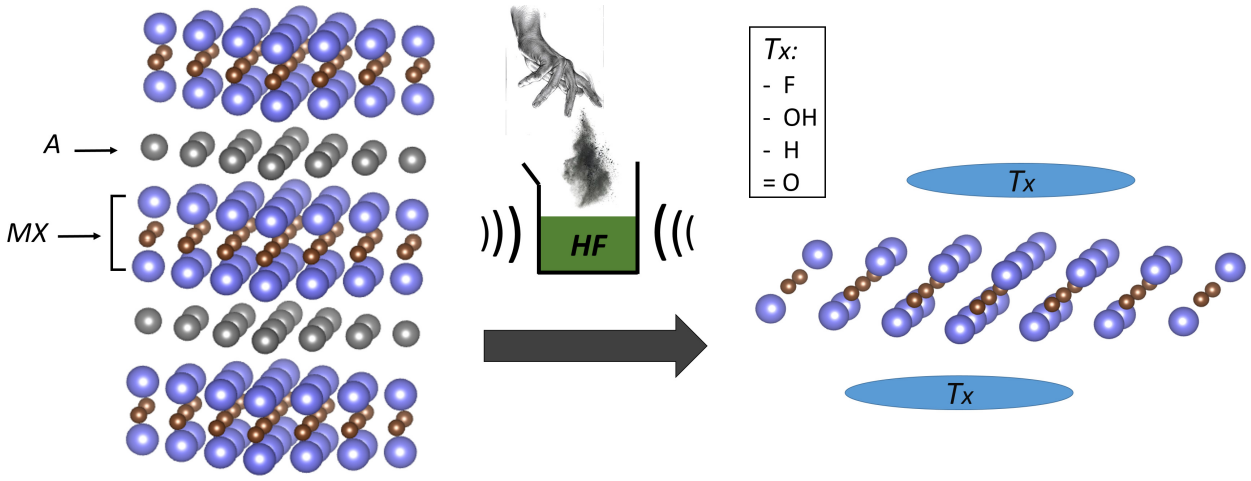

FIGURE 2.5: MXENES synthesis scheme in solution. MAX phase powder is used as a precursor. After being introduced into a 50 percent HF solution and sonicated/ centrifugated for 2 to 72 hours, one obtains stagnant MXENES flakes in solution. MXENES main terminations types Tx's are indicated.

But the perhaps most iconic system in that regard is Graphene, discovered in 2004 by mechanical exfoliation of graphite [66, 67]. Truly two dimensional and, to list a few of its properties, with electrons confined in one dimension while being a poor metal in the other two [68], with an exceptionally large mean free path and linear dispersions crossing at the Fermi level [69, 70], e.g. dirac points, Graphene has become one of the flagships of nanoscience and condensed matter physics. The discovery of many 'single layer' bidimensional systems followed and about ten classes of 2D crystals have been synthetized up to date [71, 72, 73, 74, 75] : Transition metal dichalcogenides (MoS_2, $MoSe_2$, WS_2, VSe_2, TiS_2,...) and trichalcogenides ($TiTe_3$, $MnPS_3$,...), Hexagonal boron-nitrides, 2D oxides (TiO_2, Ti_3O_7, Nb_3O_8, MnO_2, V_2O_5,...), phosphorenes,.... Most of these have a bulk parent compound than can be processed to synthetize the targeted 2D system, by either mechanical exfoliation (Similarly to the Graphene case, using scotch tape to remove layers from the bulk material until one gets a single layer) or chemical exfoliation in solution [76].

In 2011, processing Ti3AlC2 in hydrofluoric acid (HF) , Naguib *et.al* managed to exfoliate their polycrystalline powder [47] and to extract the Al atoms from the MAX compound, thus isolating the MX planes from a MAX phase and obtaining a new 2D material: Ti_3Si_2

Quickly later, other MAX phases were exfoliated and the byproduct of these exfoliations were to be called MXENES, emphasizing their kinship to MAX phases and the bidimensional nature they share with graphene. About 30 different MXENES have been synthetized up to now [77, 78, 4, 79]. Their chemical formula is $M_{n+1}X_n$ and their structure is the same as MAX phases M-X layer (see figure 2.5). Depending on the concentration of HF used, on the time duration the powder is left in solution, on the centrifugation or sonication technique after or during the HF treatment or on the intercalation method used, one may obtain single layers or most often stacks of several MXENES layers. The MXENES flakes obtained in solutions are generally relatively small, polycrystalline and accordion like shaped [78, 4, 79].

The reactions accounting for the transformations of MAX phases to MXenes within HF solutions are the following:

$$M_{n+1}AX_n + 3HF \longrightarrow M_{n+1}X_n + AF_3 + (3/2)H_2 \tag{2.3}$$

$$M_{n+1}X_n + 2H_2O \longrightarrow M_{n+1}X_n(OH)_2 + H_2 \tag{2.4}$$

$$M_{n+1}X_n + 2HF \longrightarrow M_{n+1}X_n(F)_2 + H_2 \tag{2.5}$$

As laid out from reactions 2 and 3, MXENES will systematically be functionalized so that the actual system one obtains would be $M_{n+1}X_nT_x$, where T_x refers to a specific termination [78, 79]. T_x can be either $(OH)_2$ and $(F)_2$ as above, but also $(H)_2$ or $(=O)_2$ (-Cl is also reported) (see figure 2.5). The predicted electronic properties of MXENES will drastically change depending on the nature of the termination [80, 81]. $M_{n+1}X_n$ MXENES without termination are predicted to be metallic with a density of states at the Fermi level $N(E_F)$ greater than MAX phase , with the d orbitals still dominating conduction states [79, 80]. Based on DFT calculations only, OH and F terminated Ti_3C_2 MXENES are predicted to see small gaps of respectively 0.05 and 0.1 eV to open at E_F, but the value of these gaps is predicted to depend upon the orientation of the termination [78]. If it were not enough to emphasize on the influence of termination on the electronic structure of MXENES, (O) terminated MXENES shall possess gaps going from 0.24 eV for Ti_2CO_2 to 1.8 eV for Sc_2CO_2. So MXENES can either be metallic or semiconducting depending on the termination group attached to them.

One important point to mention is that experimentally produced MXENES are shown to exhibit a combination of multiple types of terminations at the same time [78, 82], while, due to computational complexity, only one termination type is generally taken into account by DFT calculations. Also, most of DFT calculations have been performed on unterminated multilayers of MXENES with a very high distance set between each layers so as to reproduce the properties of a single flake while the majority of experimentally produced MXENES are stacked multilayered systems with a lesser distance between layers, with each of them sometimes featuring different termination types. It thus questions the current compatibility of DFT based studies on MXENES with experimental results currently available. Also, the bandgap values are not necessarily correct. Indeed, one of the famous shortcomings of Density Functional Theory is precisely its failure to assess the bandgaps of semiconductors [83].

So far, and despite the impressive number of publications related to MXENES that are being published each year, transport or electronic structure measurements on a monolayer, single crystalline MXENE flake are still hard to find within the litterature [84]. Producing such sample is a highly difficult task, due to the fact that the M-A bonds, though weaker than the M-X bonds, are way stronger than in most compounds

that are parents to a class of bidimensional materials [79]. Also, chemical exfoliation generally leads to many defects within MXENES samples, as well as a poor crystalline quality [78]. Yet, a new mechanical exfoliation route for MAX phase has recently been developed [85]. Relatively large high quality flakes were obtained, with some thick to less than half the unit cell of the starting MAX phases. The obtained layered system yet conserves the A element and cannot be called MXENE but MAXENE [85].

Overall, within less than 10 years after their discovery, MXENES have become a very prolific topic of research. They show great promises for energy storage [86], biomedical applications [87, 88], transparent electrodes [89] and electromagnetic shielding [90]. One can mention that some MXENES are potential hosts for exotic states of matter. Topological features have been recently hinted on MoHf2C2O2 from calculations [91], and the quest for potentially magnetic MXENES is also ongoing [92]. But, and though we briefly discussed a few the MXENES properties, the center of this manuscript is the understanding of the bulk electronic properties of MAX phases, not of their bidimensional counterparts. Therefore, MXENES will not be extensively mentioned hereafter.

2.2.2 Solid solutions

Going back to the $M_{n+1}AX_n$ carbides, it is worth mentioning the possibility to tune the ratio between different M, A or X element in order to tailor the properties of a given phase. The most straightforward approach is to have a given proportion x (0<x<1) of one of the site, that shall be set as M atom site for the sake of clarity, to be occupied by an atom of another type N. We will then have a solid of chemical formula $(M_{1-x}N_x)_{n+1}AX_n$ with the N atoms randomly distributed over a fraction x of the M sites. Such a system is hence a solid solution of MAX phase. A site or X site solid solutions also exist.

It is noteworthy to mention that, for most MAX phases solid solutions, randomly changing the occupation of a site to another atom shall not alter the symmetry e.g the $P6_3/mmc$ space group of the system [4].

Similarly to 'standard' MAX phases, solid solutions have been widely produced by isostatic hot press sintering and other conventional powder metallurgy techniques, but involving the 4 (or more) targeted elements of the solid solution [23, 93, 94, 95]. Some phases can also be produced as thin films or thin films derivatives grown by methods such as PVD or CVD [96, 97].

211 MAX phases make for the largest number of solid solutions, with a very large number of $(M_{1-x}N_x)_2AlC$ compounds (M=V, Cr, Nb, Ti and N=V, Ti, Mn, Zr, Fe and Sc) [1, 7, 98, 99]. M atoms solid solutions with In, Ge and Ga as fixed A atoms also exist [100, 101]. Insertion of magnetic elements such as Mn or Fe have allowed some 211 MAX to develop magnetic properties. For example, clear ferromagnetic features were found to thin film of $(Mo,Mn)_2GaC$ and $(Cr, Mn)_2GaC$ at relatively high temperature [102, 103], while Cr_2GaC and Mo_2GaC do not seem to exhibit such clear behavior. $(Cr,Fe)_2AlC$ as well as $(V,Mn)_2AlC$ are also magnetic solid solutions that were discovered recently [104, 105].

Numerous A element solid solutions are reported as well [1, 7, 106]. For example, heavy atoms have been incorporated with phases such as $Zr_2(Al_{1-x}A_x)C$, A=Bi, Sb and Pb [107, 108]. Regarding the X site, syntheses of $Ti3Al(C_{0.5}N_{0.5})_2$ and $Ti_2Al(C,N)$ have been reported, performed by milling, cold compaction and annealing of Ti, TiC , Al and AlN powders [109, 110, 111]. It is important to note that for all solid solutions as well as 'Pure' 211, 312 and 413 MAX phases can show significant substochiometry. It is especially true for $Ti_2Al(C_{1-x}N_x)$ which shows 20 percent of vacancies on the X site. It is not surprising when looking at the MX monocarbides and mononitrides vacancies range, with TiC actually going from $TiC_{0.5}$ to $TiC_{0.98}$ [34].

About 45 solid solutions of 211, 312 and 413 MAX phases have been reported. One interesting recent discovery is $Ti_3(Al_{1-x}Cu_x)C_2$, were Cu incorporation leads to the loss of MAX hexagonal symmetry [112]. The space group of this solid solution turn out to be C2/c monoclinic rather than $P6_3/mmc$. Interestingly, C2/c turns out to be the same space group as in plane ordered MAX phases (iMAX) that were recently discovered.

2.2.3 In plane and Out of plane ordered MAX phases

So far, we only described MAX phase based solid solutions where the the fourth (or fifth) extra atoms to be added are randomly distributed across either M, A or X sites. Quaternary ordered MAX phases based compounds yet do exist, and they can be separated into two different subclasses: out of plane ordered MAX phases (oMAX) and in plane ordered MAX phases (iMAX).

oMAX crystal structure is very similar to pristine MAX phase, and both share the same P63/mmc hexagonal space group. In the case of 312 oMAX, one of the M site is occupied by another metallic element following the formula: $(M'_{2/3}M''_{1/3})_3AX_2$. A comparison of Ti_3AlC_2 and Ti_2MoAlC_2 oMAX unit cells is given in figure 2.6a. The first oMAX to be discovered was Cr_2TiAlC_2 in 2014 [113] and so far they have been only synthetized by standard ceramic synthesis processes (typically through powder mixing and heating). It must be noted that the ordering within oMAX is not perfect, as some atoms M'' can occupy M' sites and vice et versa [95]. High concentration of C vacancies have also been found, similarly to solid solutions and higher order compounds [34, 114]. Up to now, only a few oMAX's have been synthetized [113, 95, 115], but way more are predicted to be stable at ambient temperature[116].

oMAX are also the precursor of a new kind of MXENES: $(M'_{2/3}M''_{1/3})X_2$, which are, unsurprisingly, obtained by chemical exfoliation of oMAX powders [117]. These MXene have attracted the attention of theoreticians, and some of them are predicted to be potential hosts for spin quantum hall effect [91]. Yet, coumpounds such as $(Mo_{2/3}N_{1/3})_3C_20_2$ (N=Ti, Zr or Hf)have never been synthetized and their actual stability has yet to be demonstrated.

In 2017, a 3D laminate sharing a structure closely related to 211 MAX phase was discovered for the first time [118] in Linkoping: $(Mo_{2/3}Sc_{1/3})_2AlC$. It was the first of a serie of $(M'_{2/3}M''_{1/3})_2AlC$ iMAX family of compounds to be synthetized. Here, M', M'' and C atoms constitute a plane similar to the MX plane of MAX

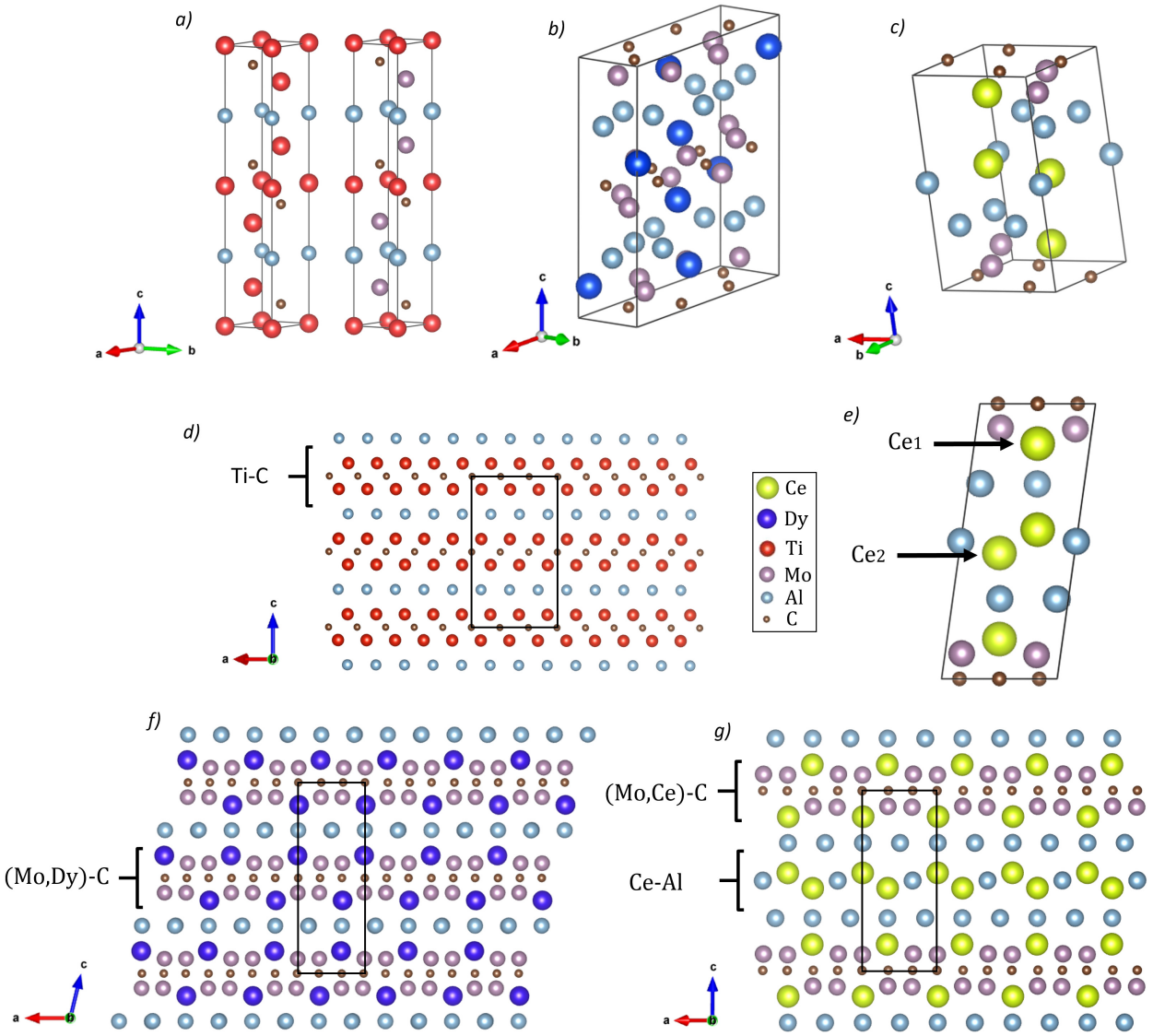

FIGURE 2.6: (a) MAX and oMAX crystal structure of Ti_3AlC_2 (left) and Ti_2MoAlC_2 (right). Unit cell of (b) monoclinic $(Mo_{2/3}Dy_{1/3})_2AlC$ and (c) triclinic $Mo_4Ce_4Al_7C_3$. (d) the Ce1 and Ce2 sites within $Mo_4Ce_4Al_7C_3$ and their environments are highlighted. (e-g) MAX, iMAX and 4473 nanolamellar structure are compared over an equivalent supercell. The relationship between MAX M-X layers and the layers constituting other phases is made explicit.

phases. The M' are arranged in a honeycomb lattice while the M" are located at the center of each hexagon (Thus resulting in a 2:1 ratio). Al atoms are arranged within one plane, as for standard MAX phases. But where MAX phases Al atoms would follow an hexagonal pattern, iMAX's Al atoms form here a kagome like lattice.

Contrary to oMAX's, iMAX phase do not share MAX phases hexagonal structure. They crystallize into 3 different polymorphs whose spacegroups are monoclinics C2/c, C2/m, and Cmcm [119]. A C2/c iMAX unit cell is shown in figure 2.6b. Typical lattice parameters values are 5.5 Angstrom for a=b and 14 Angstrom for c. The c/a ratio is thus almost two times smaller than for corresponding 211 MAX phase. Going back to $(Mo_{2/3}Sc_{1/3})_2AlC$, selective chemical etching in HF solution of both Sc and Al allowed to synthetized $Mo_{1.33}C$ MXene [118], a 2D material with ordered vacancies located at the sites where the Sc atoms

were located within MoScAlC. Prediction and synthesis of other iMAX phases such as $(Cr_{2/3}Y_{1/3})_2AlC$, $(Cr_{2/3}Ti_{1/3})_2AlC$ or $(Cr_{2/3}Zr_{1/3})_2AlC$ quickly followed [119, 120, 121].

Not only additional transition metals can be incorporated within MAX phase formula to form an iMAX, but also rare earth element. $(Mo_{2/3}RE_{1/3})_2AlC$ compounds also exist (RE= Ce, Pr, Nd, Sm, Gd, Tb, Dy, Ho, Er, Tm and Lu). These have been firsthand synthetized by the MAX phase group of Linkoping, in powder form and through pressureless sintering [122]. Bulk single crystals of $(Mo_{2/3}RE_{1/3})_2AlC$ (RE = Nd, Gd, Dy, Ho, Er) have also been grown through liquid solution growth [123]. The growth of these iMAX single crystals was performed at LMGP in parallel to the other scientific results that make for the content of this manuscript and as a part of a larger scientific collaboration involving several academic actors . More details on MAX phases single crystal growth and its particular challenges will be given in section 3.1.

The presence of localized 4f orbitals in the M-X plane leads to strong electronic correlations , way stronger than what is expected from the sole d orbitals of MAX phases transition metals. It is also the case of a large number of Lanthanides (or Actinides) based lamellar or non-lamellar compounds [124, 125, 126, 127, 128, 129]. Many of them are labelled as heavy fermion [130], with the notable examples of $CeAl_3$ and $CeCu_6$. In these compounds, the presence of unfilled 4f shells leads to an extremely high value of the electronic density of states at the Fermi level, which can be related to a renormalized effective mass up to three order of magnitude higher than the electron rest mass [130, 131]. Unconventionnal superconducting phase [132, 133], Kondo insulator phase [134], or quantum critical point [135, 136] can be found within the phase diagrams of specific Heavy Fermion compounds. Complex magnetic orders are also common for such compounds, where the interactions are in most cases antiferromagnetic [130, 136]. As a matter a fact, Bulk magnetization measurements at low temperature on single crystals allowed us to evidence various magnetic phase transition for iMAX compounds that we grew [137]. A Curie temperature of 14.9 K was found for $(Mo_{2/3}Dy_{1/3})_2AlC$, with an antiferromagnetic phase below the transition. $(Mo_{2/3}Gd_{1/3})_2AlC$ seemingly becomes antiferromagnetic below Tc=26K. In contrast, $(Mo_{2/3}Ho_{1/3})_2AlC$ shows ferrimagnetic order below T=8.2K. The exact magnetic structure of these three compounds has yet to be determined by neutron diffraction.

When attempting to grow single crystals of Cerium based iMAX (discovered in Linkoping in powder form), we instead obtained single crystals of another rare earth based nanolamellar compound: $Mo_4Ce_4Al_7C_3$, also called 4473 phase [138]. Its structure is very similar to iMAXs, expect that if one compares a supercell of 211 MAX phase and iMAX (see figure 2.6d-f), one of the M-X plane would be replaced by a Ce-Al plane. The structure ends up being less symmetrical than iMAXs as $Mo_4Ce_4Al_7C_3$ space group is triclinic P-1 (figure 2.6c). The Cerium atoms occupy two different sites Ce_1 and Ce_2 with very different surroundings (See figure 2.6). While the Ce_1 in the MX conductive plane has the same surroundings as rare earth atoms in iMAX's, the Ce_2 site closest neighbors are Aluminium atoms from the kagomé-like layer above the Ce-Al layer as well as other Cerium atoms from the same Ce-Al plane. This is of the utmost importance for understanding the differences between iMAX and 4473 properties. In contrast with iMAX phases, $Mo_4Ce_4Al_7C_3$ is found

to exhibit ferromagnetism below 10.5 K, as well as mixed-valence states [138]. Cerium is well known for its two possible oxidation states, Ce_{3+} ($4f_1$) and Ce_{4+} ($4f_0$). In a Ce mixed valence system, in at least one Ce site, the electronic configuration shall oscillate between Ce_{3+} and Ce_{4+} while the average ratio between these two would be fixed [139]. For a given compound, the oxidation or valence states would be imposed by cerium atoms environment and the local crystal fields.

In the case of $Mo_4Ce_4Al_7C_3$, XMCD and XANES absorption spectroscopies allowed to demonstrate that the Ce_1 atoms belonging to the metallic plane exhibit mixed valence state while the Ce_2 are seemingly the ones carrying a non-zero magnetic moment and would be responsible for the ferromagnetic nature of this compound. We also very recently evidenced Kondo lattice behaviour in this material that would coexist with a ferromagnetic order at low temperature [140], but this stands beyond the scope of this manuscript (More informations on magnetism, Kondo effect and mixed valence states in $Mo_4Ce_4Al_7C_3$ are provided in [140]). Overall, in plane and out of plane ordered MAX phases show great promises for the search of new magnetic and high electronic correlation within the MAX phase family. iMAX might also be the first stone for the discovery of a new class of rare earth based highly correlated iMXenes, if such a system is indeed stable.

2.3 The electronic structure of MAX phases

Bringing new insights to the understanding of MAX phases electronic structure has truly been the main scientific output of this doctoral thesis. Yet, before we come to literally state the questions we have attemtped to answer during the past four years, we believe that it is necessary to review some very basic concepts of solid state physics that are central to this work. We will later come to a short review of the preexisting literature on MAX phases electronic structure, and how to relate the near Fermi level electronic structure of MAX phases to their macroscopic properties.

2.3.1 A short summary of electronic structure and band theory

The knowledge of the quantum states of electrons is key to the understanding of a large number of properties of systems made of atoms, whether it might be a single atom, a molecule, a periodic arrangement of atoms forming a crystalline solid, a gas made of scarce and randomly distributed atoms (or molecules) or a disordered liquid. We define here the ensemble of electronic quantum states of a system as well as their morphology in phase space (a four dimensional space hereby defined by energy and the three components of a momentum variable) as the electronic structure of this system, also referred to as its electronic spectra. From now, we will be giving shortened and oversimplified narrative inspired by the fundamentals of Solid states physics and quantum mechanics. The reader can refer to foundational text books as the ones from Ashcroft and Mermin or Kittel [40, 141, 142]. To exemplify the concept of electronic structure, we will consider a very

simple system: the Hydrogen atom. Neglecting any fine and hyperfine structure terms, the hydrogen atom Hamiltonian $\mathcal{H}$ stands within the Hydrogen atom Schrodinger equation as:

$$\mathcal{H}\phi = (E_{kin}\phi + V\phi) = (\frac{-\hbar^2\nabla^2}{2m_e} + \frac{-e^2}{r})\phi = E\phi \tag{2.6}$$

Here, ϕ is the electron wavefunction, $E_{kin} = \frac{-\hbar^2\nabla^2}{2m_e}$ the kinetic energy operator, $V = \frac{-e^2}{r}$ the central coulombian potential and m_e the electron rest mass. After separating the angular and radial part of the Hamiltonian and diagonalizing both, one obtains a set degenerate energy eigenvalues associated with the radial component of the electron wavefunction:

$$E_n = -\frac{E_i}{n^2} \tag{2.7}$$

Where E_i= -13.6 eV is the ionization energy of the Hydrogen atom and n is an integer called the principal quantum number. This infinite set of energy level stands for the electronic structure of the sole hydrogen atom. Considering additional terms of the Hamiltonian into the potential V will lift the orbital degeneracies and lead to a slightly different electronic structure. Through perturbation theory, one can eventually take into account effects such as spin orbit coupling and other relativistic effects as well as the hyperfine coupling between electrons and nucleus spins.

Now, getting closer to the case of an actual material, if one consider an infinite set of atoms forming a periodically arranged solid, the electronic structure of this system will naturally show a higher degree of complexity than the energy levels of a single atom. The Hamiltonian of a given solid consituted of N electrons in a Bravais lattice would be:

$$\mathcal{H}\phi = \sum_{i=1}^{N}(\frac{-\hbar^2\nabla_i^2}{2m_e}\phi - e^2\sum_{\mathbf{R}}\frac{Z}{||\ \mathbf{r_i} - \mathbf{R}\ ||}\phi) + \frac{1}{2}\sum_{i\neq j}\frac{e^2}{||\ \mathbf{r_i} - \mathbf{r_j}\ ||}\phi \tag{2.8}$$

Where $\vec{R}$ is a real space vector which follows the lattice periodicity and $\vec{r_i}$ are the vectors associated to the position of the electrons. There is naturally no hope in trying to solve this problem analytically. But regardless of the complexity of the Hamiltonian, we can still write it as :

$$\mathcal{H}\phi = (E_{kin}\phi + V_{cry}\phi) \tag{2.9}$$

E_{kin} is the kinetic energy associated to the many body electronic wavefunction and V_{cry} encompasses all the atomic potentials as well as all electron-electron interactions and other terms. There is one common characteristic to the potential distribution of any crystalline system: it follows the periodicity of the lattice (ignoring magnetic superstructure or incommensurate magnetic order!):

$$V_{cry}(\mathbf{x} + \mathbf{R}) = V_{cry}(\mathbf{x}) \tag{2.10}$$

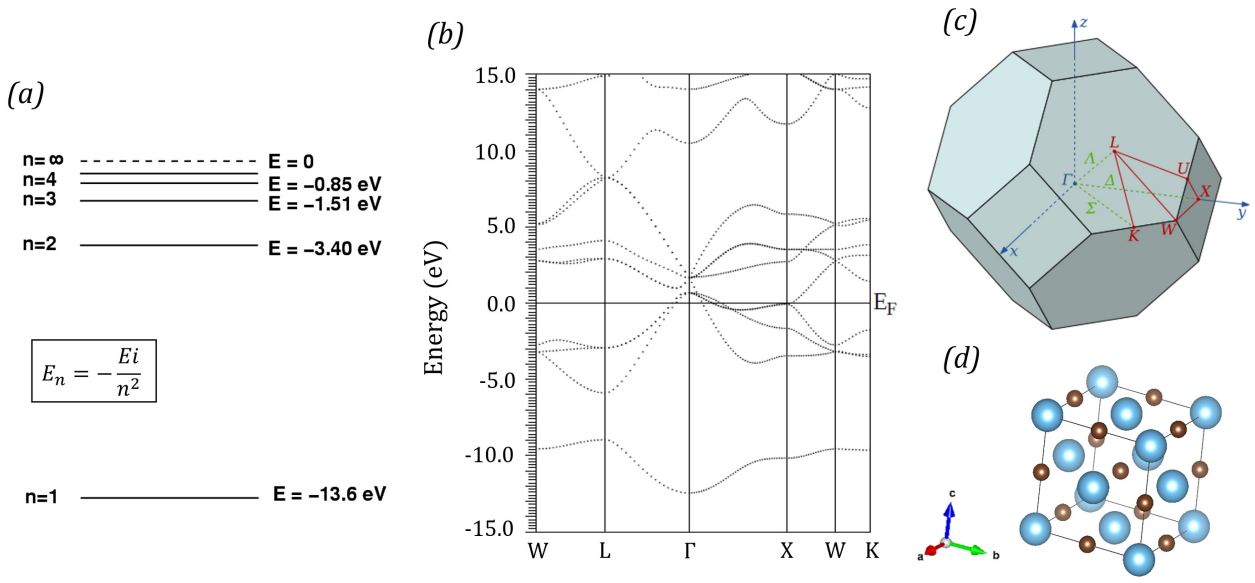

FIGURE 2.7: (a) Schematic of the energy levels of Hydrogen atom. (b) TiC BS computed as computed by GGA DFT calculations. (c) First BZ of cc TiC (d).

This later imposes the eigenstates of the Hamiltonian ψ to follow Bloch theorem:

$$\psi(\vec{x} + \vec{R}) = e^{i\mathbf{k}.\mathbf{R}}\psi(\mathbf{x}) \tag{2.11}$$

Here $\vec{k}$ stands for the wavevector as a parameter associated to this eigenstate. Cantoning to real space is not fitting for studying the properties of these Bloch eigenstates, nor the electronic structure of a solid. One needs to look at the dual to the real space lattice: The reciprocal space or also refered to as k space or 'wavevector' space . It is defined by its unit vectors $\vec{a^*}$, $\vec{b^*}$, $\vec{c^*}$ that are themselves derived from the real space unit vector $\vec{a}$, $\vec{b}$, $\vec{c}$ for a crystalline solid with fixed lattice parameters and a specific space group:

$$\vec{a^*} = 2\pi\frac{\vec{b} \times \vec{c}}{\vec{a} \cdot (\vec{b} \times \vec{c})} \tag{2.12}$$

$$\vec{b^*} = 2\pi\frac{\vec{c} \times \vec{a}}{\vec{a} \cdot (\vec{b} \times \vec{c})} \tag{2.13}$$

$$\vec{c^*} = 2\pi\frac{\vec{a} \times \vec{b}}{\vec{a} \cdot (\vec{b} \times \vec{c})} \tag{2.14}$$

The energy level of the periodic solid will show a dependency on the electron wavevector $E_n(k)$, with a periodicity in k space imposed by the periodicity of the solid.

We will thus obtain n k dependent eigenvalues graphs $E_n(k)$ which are labelled as **Bands**. Here, n is called the band index and plays a similar role as the principal quantum number for atomic physics. It allows to classify bands by the minimum energy value they exhibit. The ensemble of all the bands of the energy spectra

is called the **Band Structure** (BS) of the solid. Studying a band structure along the whole infinite reciprocal space proves to be useless. There exists one specific Wigner Seitz unit cell of reciprocal space called the first **Brillouin zone** (BZ). It can be showed that the periodicity of the band structure in three dimensional k space is the same as the BZ so that one can only trace the bands within this restricted volume (a detailed example of a band structure is given in figure 2.7b, for the case of TiC). By convention, the band structure is generally plotted over specific symmetry axes of the BZ that will depend on the space group of the system. Indeed, the symmetry of the Brillouin zone is naturally dual to the one of the Wigner Seitz cell of the real space lattice. An example of a BZ main symmetry axis nomenclature is given in figure 2.7c for cubic centered (cc) TiC.

As in the case of the energy level of an atom associated to certain orbitals, at each k point of a band a given combination from each initial atomic orbitals will form a k dependent eigenvector $\psi_n(\mathbf{k})$:

$$\psi_n(\mathbf{k}) = \sum_{i=1}^{Norb} c_{n,i}(\mathbf{k}) O_i \tag{2.15}$$

The ratio $c_{n,i}$ between the different orbitals will change as one follows the coordinates of the band through the BZ. It will be referred to as the orbital character of a band. It means that one can distinguish the orbital contribution to each band within the solid by projecting the eigenstate ψ_n at an (E,k) coordinate unto the considered orbital O_i:

$$c_{n,i} = \langle \psi_n(\mathbf{k}), O_i \rangle \tag{2.16}$$

Looking at specific directions or k point does not allow one to have access to 'global' properties of a material. For this one needs to integrate quantities over the quantum state of the electron, in energy and over the first BZ in k space. One very important tool for handling such operations is the **Density of States** (DOS) which is defined as the number of electronic states per volume unit and energy unit. It can be related to other mathematical objects: **the Isoenergy Surfaces**. For a three dimensional system, an isoenergy surface of energy $E=E_{is}$ can be defined as the ensemble of all k points of all bands $E_n(k)$ crossing the constant energy segment $E=E_{is}$ within the first BZ (See figure 2.8). It thus not only defines the morphology of all the electronic states at $E=E_{is}$, but integrating this isoenergy surface will give access to the number of states available at $E=E_{is}$, thus to the density of states at $E=E_{is}$. While the band structure of a solid appears as a collection of discrete k dependant quantum states, the energy dependence of the density of state makes them appear as continuous (see figure 2.8). Not all the levels are of course occupied. As electrons are fermions, they obey the Fermi Dirac distribution

$$f(E) = \frac{1}{1 - e^{\frac{(E-E_F)}{k_B T}}} \tag{2.17}$$

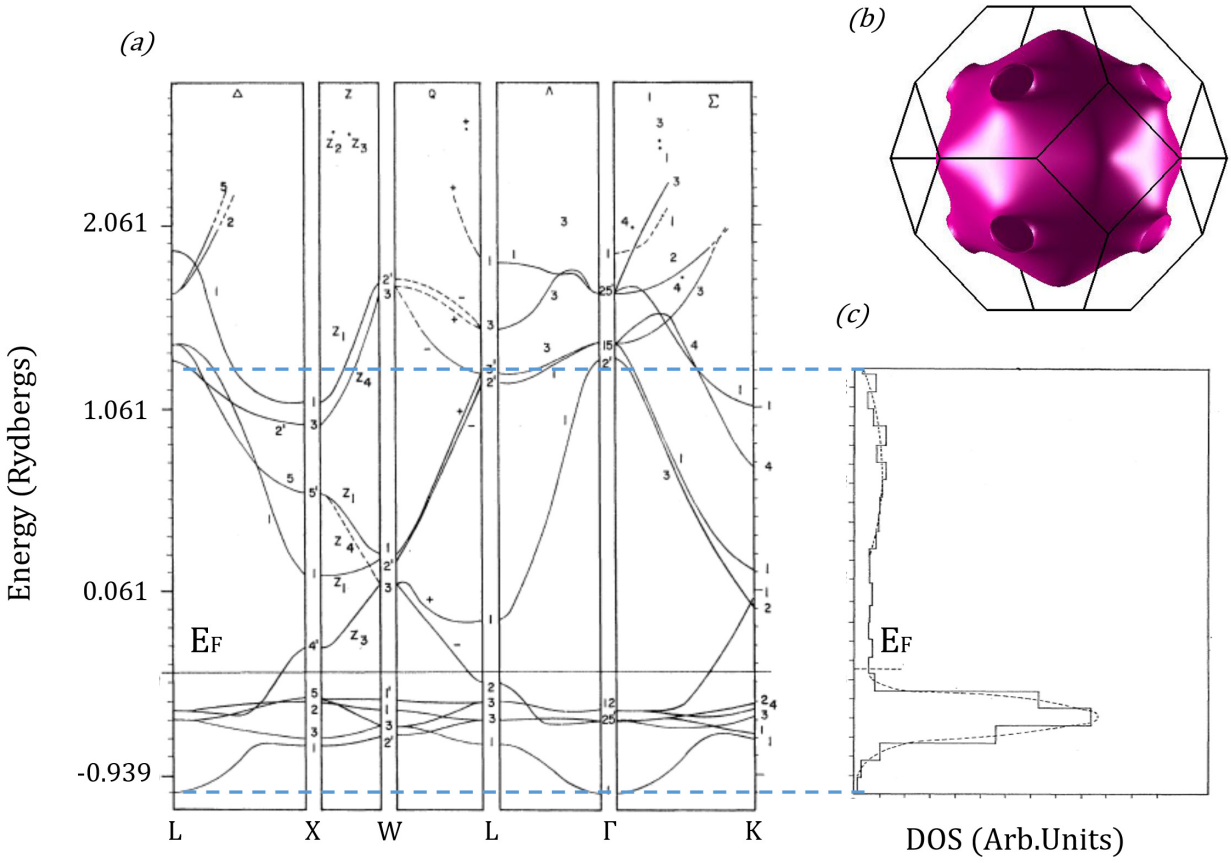

FIGURE 2.8: (a) BS of Cu from Phys.Review 129, 1 (1963) [143]. Copper electronic structure was calculated through diagonalizing the Hamiltonian with the slater APW method and by taking the Chodorow potential for Cu (b) Cu Fermi surface as computed by GGA DFT calculations (c) DOS of Cu from Phys.Review 129, 1 (1963) plotted in the same energy range as (a) and highlighting the relation between Cu DOS and BS.

The total density of electron in the solid is then given by:

$$N = \int_0^{+\infty} f(E)g(E)dE \tag{2.18}$$

Where E_F is the socalled **Fermi level** or Fermi Energy separating occupied and unoccupied energy bands and g is the density of states of the system. At 0K, the Fermi-Dirac distribution becomes identical to a heavyside function and all the energy bands above E_F are unoccupied. At 300K, f only differs slightly from a heavyside function so that the bands above E_F are nearly unoccupied. The isoenergy surface at the Fermi level is called the **Fermi Surface** and it is a central concept for understanding the many properties of a metal from a solid state physics perspective.

As an important reminder, we will give a very simplified picture of how the position of the Fermi level within the electronic structure of a material determines whether one gets a metal or a semiconductor. If the Fermi level of a given material happens to cross one or several existing bands, then this material would be a metal with a potent conductivity. Indeed, unoccupied states would be available at an infinitesimal distance

from the lastly occupied level for electrons to be excited in or for holes to be inserted within the Fermi sea e.g. the continuum of states below E_F. Electronic transport can then be met through mobile electrons and holes. If E_F does not cross any band, then the material would be a semiconductor or an electronic insulator. It would require a significant temperature or a significant external perturbation for electrons to cross the energy gap between the last occupied bands and the first unoccupied bands above. A rigorous demonstration based on the semi-classical analog of the Liouville theorem [40] would prove that a band completely filled or empty would stay inert even in presence of a magnetic field or an electric field varying over space or time. Electric conduction would then arise due to electrons (or holes) in partially filled (or partially empty) bands.

As it will be illustrated with the specific case of MAX throughout this manuscript, the electronic structure at or near the Fermi level are determinant to most of the properties of materials, metals in particular. One shall still remember that the description of the electronic structure we gave above is solely based on Band Theory which, and though it remains valid for most of the existing metals, insulators and semiconductors alike, fails to describe some classes of highly correlated systems (iMAX and 4473 phases typically fall in that category). But as MAX phases are relatively standard metals, the portrait of Bands Theory we gave above is sufficient to decipher their electronic structure.

2.3.2 Trends within the electronic structure of MAX phases

Until 2017, MAX phases electronic structure has been mainly studied by the means of DFT calculations and experimental probes such as X ray absorption spectroscopy (XAS) [144], X ray emission spectroscopy [145, 146, 147], electron energy loss spectroscopy (EELS) [144] and X ray photoemission spectroscopy (XPS) [148, 149]. DFT calculations have brought knowledge on the density of states of most of MAX compounds, and the spectroscopic studies mentioned above were mainly aimed at understanding their bonding mechanisms through the study of their electronic structure. Comparative analysis of experimental and theoretical results have allowed to establish clear trends within the electronic structure of MAX phases:

-Nearly all MAX phase densities of states are dominated by the transition metal d orbitals near the Fermi level. Similarly to the 'global' density of states, one can compute Partial densities of states (pDOS) by projecting the quantum states obtained by calculations unto the set of all orbitals of a specific atom (Atomic partial DOS) or unto one orbital (orbital partial DOS). DOS and partial density of states (pDOS)of Ti_3SiC_2 from [150] are given in figure 2.9, as well as Cr_2AlC and Ti_2AlC pDOSs from [151]. The shape of the near E_F spectra of the DOS is identical to the M atom pDOS (in the area where Ti d orbitals ought to stand) for Ti_3SiC_2, Cr_2AlC or Ti_2AlC or Ti2 cases. Most of other phases exhibit similar near E_F profiles, therefore demonstrating the prominent role of the M atoms influence in the near Fermi level electronic structure. The prominence of d orbitals on the near E_F electronic spectra is also a characteristic of the MX binary counterparts to MAX phases. It must be noted that a reasonable yet imperfect agreement between experimental spectra and calculation can be obtained when it comes to comparing the DOSs and XPS results [149, 152].

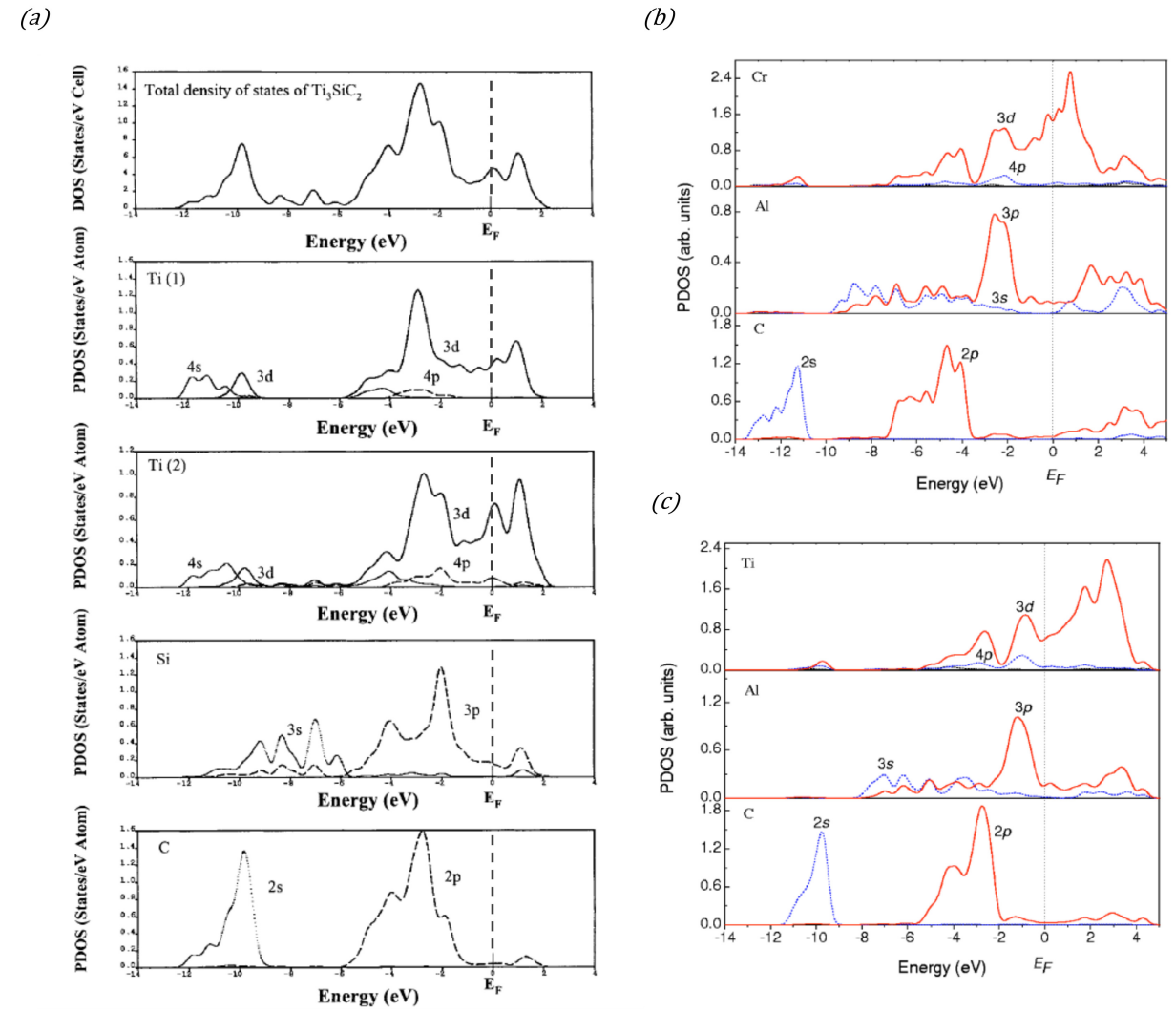

FIGURE 2.9: (a)Ti_3SiC_2 DOS and atomic pDOSs by DFT calculations, from Zhou et.Al [150]. The domains where given orbital contribution dominate are highlighted. M atom, Al and C pDOSs of (b) Cr_2AlC and (c) Ti_2AlC from [151]

-The strength and relative energy of various bonds within MAX phases has been be elucidated both experimentally and computationally . If one looks back at the different pDOS of Ti_3SiC_2 (Figure 2.9a), one can decompose them into four domains : the 0-1 eV below E_F domain, where the Ti d orbitals dominate. In the 1-5 eV range, Ti 3d, Si 3p and C 2p orbitals are the main contributors to the bands. In 5-9 eV range, the main contribution comes from Si 3s orbital and C 2s in the 9-12eV range. This is to be correlated to X ray emission spectra of Ti_2AlC [146]. M 3d to A 3p bonds would be relatively weak with an associated peak around 1 eV below Ef while M 3d – C 2p and M 3d - C 2s are found to be stronger and at way lower energies, respectively 2.6 and 10 eV below E_F.

Though BS calculations of MAX phases are to be found in the literature, only theoretical DOSs have been compared to experimental results, which means that the actual morphology of their electronic states has not been confirmed experimentally before. Yet, the morphology of electronic states near the Fermi level, and more specifically the shape of the Fermi surface, is at the very root of electronic transport in most metals [40]

and MAX phases do not escape that rule.

As a quick reminder, let us recall that one can derive the Fermi velocity, or the group velocity of electrons from a given band and at the Fermi level, directly from the band structure as :

$$\mathbf{v_F} = \frac{1}{\hbar}(\frac{\partial E}{\partial \mathbf{k}})_{\mathbf{k}=\mathbf{k_F}} \tag{2.19}$$

Were k_F is the value of the wavevector at E_F . Another parameter that can be extracted from the band structure is the effective mass of the electron m^*. It is a renormalized mass that would act as the mass that an electron in a band at a given (E,k) coordinate would bear if portrayed as a free electron, but with all the effect of the potential condensed in m^* . Depending on the shape of each bands, local effective masses can be higher or smaller than the rest mass of the electron m0=9.0110-31 kg. Effective masses can be deduced directly from the local curvature of the bands:

$$\frac{1}{m_*} = \frac{1}{\hbar^2}\frac{\partial^2 E}{\partial^2 k} \tag{2.20}$$

Considering the first order out equilibrium term of the distribution function when applying an external electric field, one obtains the following formula for the electronic conductivity [40] :

$$\sigma = e^2 \sum_n (\int \frac{\mathbf{dk}}{4\pi^2}\tau_n(\epsilon_n = \epsilon(\mathbf{k}))v_n^2(\mathbf{k})(\frac{-\partial f}{\partial \epsilon})_{\epsilon_n=\epsilon(\mathbf{k})})_{E=E_F} \tag{2.21}$$

Where the term $(\frac{\partial f}{\partial \epsilon})$ can be taken as a Dirac distribution centered at the Fermi energy so that we obtain integrals over the Fermi surface. This is but among the many relations that express the fundamental link between transport and the electronic quantum states of metals. Other Onsager coefficients such as the Hall coefficient or the thermal conductivity can be directly related to integrals over the Fermi surface and Fermi velocity maps within the first BZ.

Now how does this apply to the MAX phases? The vast majority of the MAX phases are characterized by extremely small Hall coefficients R_H, which sometimes change sign with increasing T, small magnetoresistances, and for some phases vanishingly small Seebeck coefficients over extended T ranges [1]. The nearly zero values of R_H has been interpreted as a proof that MAX phases are compensated conductors. Electronic transport within Max phases have indeed mainly been described in the frame of an isotropic two bands Drude model, with [1]:

$$\sigma = e(n\nu_n + p\nu_p) \tag{2.22}$$

$$R_H = \frac{p\nu_p^2 - n\nu_n^2}{e(n\nu_n + p\nu_p)^2} \tag{2.23}$$

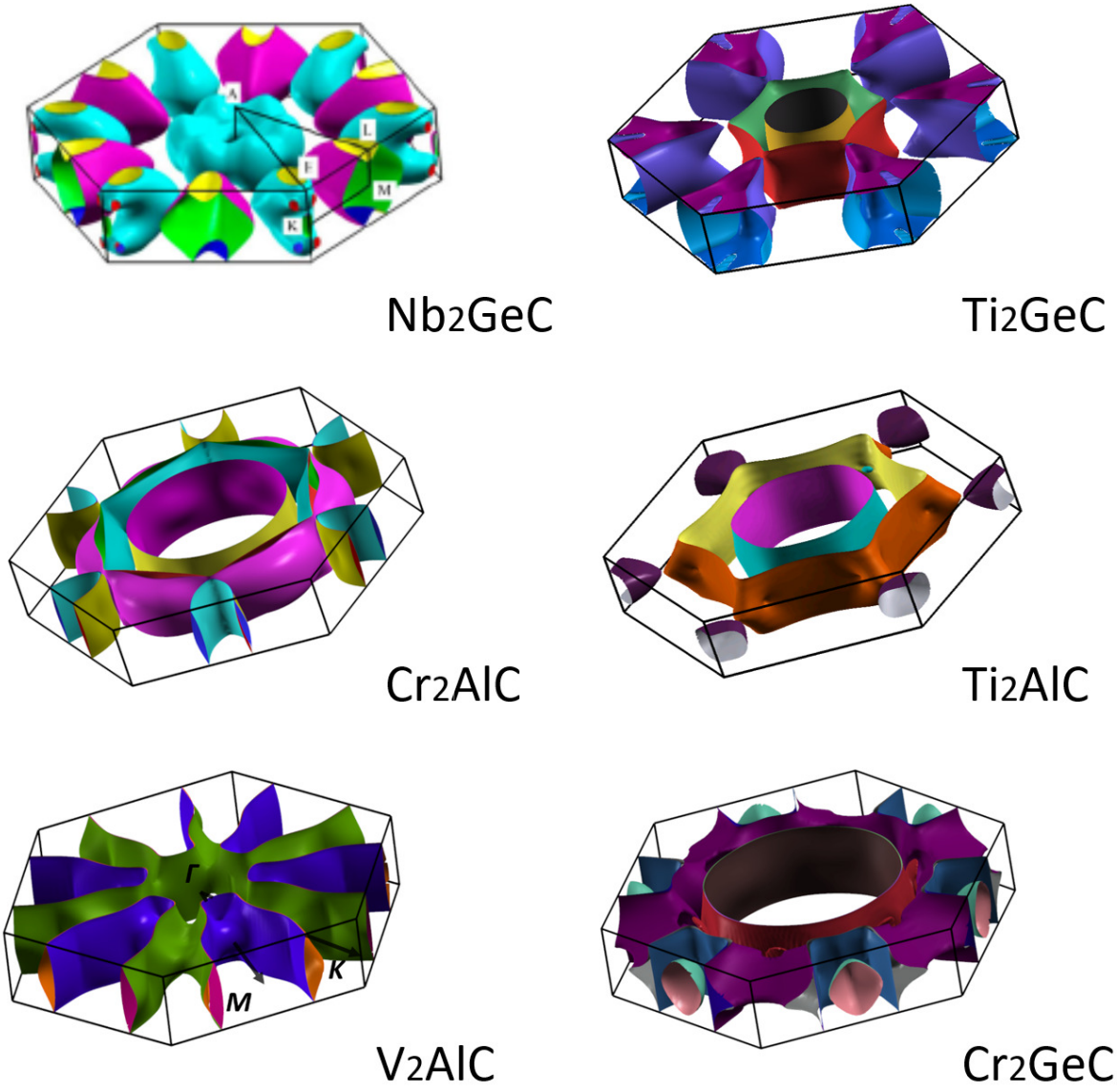

FIGURE 2.10: Fermi surface of Nb_2GeC (from Shein I et.Al, Physica B. 2013 [153]), Ti_2GeC, Cr_2AlC, Ti_2AlC, V_2AlC and Cr_2GeC all computed by DFT calculations. Apart from Nb2GeC. All of them were computed with the PBE functional embedded within wien2K

$$\frac{\nabla\rho_B}{\rho_B} = \frac{npv_nv_p(v_n+v_p)^2}{(nv_n+pv_p)^2}B^2 \tag{2.24}$$

From the small value of R_H, it was assumed in the frame of this two band model that n=p and $v_n = v_p$, thus implying that MAX phases would be compensated metals.

A simple two band based Drude model might decently well render the main features of a semi-conductor where the only parts of the bands that contribute to transport are the bottom of the conduction band for electron and the top of the valence band for holes, and where both will exhibit nearly isotropic parabolic dispersion near their respective minimum and maximum. In contrast, such a model does not bode well with metals where the Fermi level is located deep within the bands and often comes to cross more than two

electron or hole bands alike [154]. Also considering the intricate and highly anisotropic shapes of the MAX phase Fermi surfaces that have been computed thus far, it is highly unlikely for the electronic states to be isotropic or free electron like. A strong anisotropy makes sense here because of MAX phase layered structure

.

For Ti_2GeC, 6 bands are present at the Fermi level [154] , with four hole tube like FSs and two electron pockets centered in K (shown on figure 2.10) A pocket referring to a Fermi surface encompassing a close volume, in opposition to open volumes like tubes. With the lack of applicability of this model, one can question whether MAX phases can be considered as isotropic compensated metals.

One can as well wonder if the available data measured on highly polycrystalline samples can be straightforwardly related to the intrinsic electronic structure of MAX phases. It is a question of even greater importance when it comes to anisotropy. Determination of anisotropy ratios $\rho_c/\rho_{a,b}$ of a layered system seems like an impossible task when working with a disordered, imperfect polycrystalline sample issued from ceramic sintering processes. Values of resistivity anisotropies of Ti_2GeC measured on thin film of high quality are yet found in the literature [155] and the ratio between out of plane and in plane resistivity would be about 2, but the very short dimensions over the c axis of the obtained thin films makes this value questionable. It also conflicts with the published band structure of Ti_2GeC [156], from which this material is described to be nearly two dimensional and thus highly anisotropic . A more accurate picture of transport could be established if high quality macroscopically sized Bulk single crystals were at disposal. Measurements on such systems would hold closer to the intrinsic resistivity, hall constant or magnetoresistance of the material. Bulk single crystals of MAX phases such as Ti_3SiC_2, Cr_2AlC or V_2AlC have been synthetized from 2011 in Grenoble [35, 157, 158]. Hall bar measurements on V_2AlC and Cr_2AlC single crystals revealed resistivity values about 10 times smaller than polycrystalline samples and the newfound anisotropy ratios are about a few hundreds for Cr_2AlC and one order of magnitude higher for V_2AlC [159].

2.3.3 Leitmotiv of this doctoral thesis

The review above summarizes the scientific context in which this PhD was set. Despite the large corpus of scientific work on MAX phase, there is a relatively scarce number of studies where the actual origins of their electric and thermoelectric properties are discussed and interpreted in the light of a very direct measurement of their electronic structure. Before this work started, a handful number of questions remained untamed, of which we will be giving a non-exhaustive list below:

- How different would be experimental MAX phases band structures and Fermi surfaces from calculated spectra?
- What would be the influence of electronic correlations, magnetism, spin orbit coupling or even electron phonon coupling on MAX phase electronic structure?

- How anisotropic the experimental spectra would be respectively to the layered structure of MAX phases?
- From the knowledge of the morphology of their electronic states near the Fermi level, can we easily build a model that describes MAX phases transport in a more meaningful manner than a two band Drude model?
- Is it possible to find a fundamental unicity within all MAX phases electronic structures?

As an attempt to bring answers to these questions, the subsequent methodology was applied:
-(i) Macroscopically large single crystals (1mm^2- 1 to 2 cm^2) were grown at LMGP Grenoble by Liquid Solution Growth.
-(ii) Single crystalline sample were brought to various synchrotron lines in order to perform Angle resolved photoemission spectroscopy (ARPES) experiments (=AichiSR , UVSOR BL5U and BL7U lines in Japan as well as Soleil Cassiopée line in France).
-(iii) DFT calculations were carried out in Grenoble, and results were compared to the output of ARPES experiments.

The lack of availability of large single crystals prevented the actual experimental determination of MAX band structure and Fermi surface before this work. Existing methods allowing for their experimental determinations such as Angle resolved photoemission spectroscopy and De Haas van Haafen oscillations indeed require pure, high quality bulk single crystals.

The basic principles of our Crystal Growth techniques, of Angle resolved photoemission spectroscopy (ARPES) and Density Functional Theory (DFT) calculations are summarized in the third chapter of this manuscript. Then, the outcome of most of the research work performed during this PhD thesis is given in the other chapters and we will see how one could at least partially answer to the questions listed above. Cr_2AlC is the focus of chapter 4, with a lot of attention given to the level of resemblance between experiments and calculations. The potential influence of electron-phonon coupling and magnetism is looked upon, and Cr_2AlC magnetotransport coefficients are derived from the shape of its Fermi surface. In Chapter 5, V_2AlC experimental band structure and Fermi surface maps are found to match calculations to a remarkable level. The anisotropy of this Fermi surface is discussed and the situation is compared to the case of Cr_2AlC. Volatile surface states are evidenced within the experimental spectra. Chapter 6 is devoted to a description of all 211 phases electronic structures based on the socalled Rigid Band Model as an attempt to build up a consistent classification of MAX phases. Many phases are shown to exhibit similar 'rigid band structure' and, surprisingly, topological features, e.g. linear band crossings, such as a Dirac nodal line, are evidenced. Finally, chapter 7 deals with the experimental and theoretical electronic spectra of Ti_3SiC_2. High resolution ARPES mapping have allowed us to probe fine features of the Ti_3SiC_2 band structure and Fermi surface. A new interpretation for the nearly 0 Seebeck coefficient of Ti_3SiC_2 is given and the role of spin orbit coupling on the bands is considered.

Chapter 3

Materials and Methods

3.1 MAX phase single crystals

3.1.1 Crystal growth techniques

Many bulk crystal growth techniques rely on reaching thermodynamic conditions where the species one wants to grow is close to equilibrium with another phase (For example a liquid a or gaseous phase. To be more precise, one needs to reach a metastable supersaturation state). One would typically target a composition within a binary or ternary diagram at a given T. Then, one has to vary the kinetic, slowly departing out of equilibrium so that crystallization conditions are met and nucleation centers start to form and eventually aggregate before the growth continues. As a heuristic tool to predict which compound would form or not as a result of the growth process, one makes use of binary or ternary diagrams.

There are four main classes of crystal growth techniques for synthesizing bulk inorganic single crystals. They are summarized schematically in figure 3.1 but also briefly outlined below:

-Growth from congruent liquid phase -often referred to as melt growth- which comprises the most commonly used methods to grow single crystals. Not all materials can be grown using these methods, since congruent melting is one of their key requirements and only a few materials exhibit such a congruent melting point (when going through congruent melting, the composition of the liquid remains the same as the native compound, as illustrated in figure 3.2). Among melt growth techniques, the Czochralski method is probably the most widespread as it allows to grow 300-mm diameter, nearly defect-free, bulk single crystalline of silicon that are later cut and used as the building blocks of modern micro-electronic technologies [160, 161]. Essentially, the driving force for crystallization is the controlled pulling of a single crystalline seed inserted within the melt [162] . Other elementary compounds such as germanium [163] can be grown through this process, as well as more complex or exotic compounds as $YbNi_4P_2$ [164] which exhibits non Fermi liquid behavior at very low temperature [164, 165].

- Vapor phase growth allows the production of single crystals at temperatures lower than the other available techniques, although higher temperatures are needed for specific compounds like SiC . It can also deal

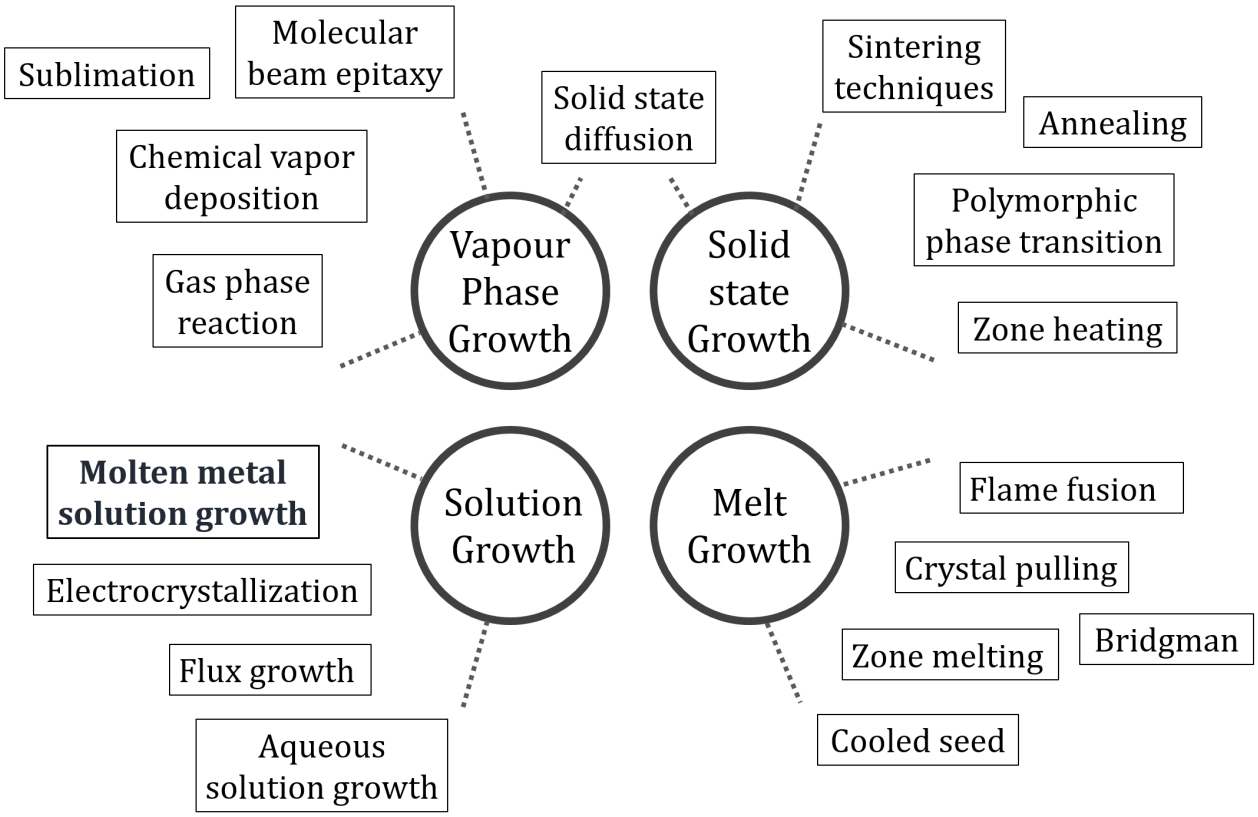

FIGURE 3.1: Summary of the four main classes of crystal growth methods and a non exhaustive list of the technics that can be derived from them. Molten solution growth, also called high temperature solution growth, is highlighted as the technic used to grow incongruent MAX phase bulk single crystals.

with compounds which do not feature a congruent melting point. High crystal quality can hardly be reached through methods such as sublimation, e.g. physical or chemical vapor transport growth [166, 167, 168] . A source material is sublimated at a temperature T1 and is transported in gaseous form to a single crystalline seed at temperature T2 onto which the gas particles crystallize. Sublimation is notably used at an industrial scale to grow high quality silicon carbide single crystals [169]. However, the low growth rates of these techniques compromise their ability to grow bulk sized crystals for most materials. In contrast, vapor phase growth methods -such as chemical vapor deposition and molecular beam epitaxy- are widely used to grow single crystalline thin films of various materials with an impressive degree of cristallinity [170].

-Solid state growth is less of a common technique than the three others despite the considerable reduction of fabrication costs it allows and the less stringent synthesis condition it permits . Through these methods, one can convert a polycrystalline sample into a single crystal by sintering a single crystalline seed of the desired material together with a larger polycrystalline sample of that same material. The temperature is set below the melting point of the material. The underlying processes of the polycrystal to single crystal conversion are still under debate [171]. Only a relatively small number of materials can be synthetized in single crystal form by these methods and the tyical size of the crystals grown in laboratory conditions is limited to a few centimeters [172].

- Solution growth is the standard crystal growth technique when the material one aims to synthetize in single crystalline form does not melt congruently (as illustrated by the binary diagrams in figure 3.2). The single crystalline phase would solidify directly from a liquid phase it stands in equilibrium with. To achieve the growth, one then needs to reach supersaturation of the targeted solid phase in solution [168, 173]. This can be achieved by different methods: the solution can be slowly cooled down if the solubility of the compound decreases with decreasing temperature. Alternatively, it is possible to directly purge or remove the solution once the crystals are formed, for example by evaporation at constant temperature. Another route is to apply a temperature gradient to the solution. In that case, the growth may arise in the region of lower temperature while the crystals as well as all the input materials will be dissolved in the melt within the higher temperature region. Depending on the material to be grown, solution growth can take place at low or high temperature, at high pressure, and in aqueous environments for the case of hydrothermal growth (Notably exploited for the growth of synthetic quartz single crystals [173]). High temperature solution growth is often performed with an additional solvent, also called a flux, added to the solution so as to increase the solubility of targeted elements into the solution. For the case of metallic compounds, we often refer to this high temperature solution growth as molten metal solution growth.

We will now extensively describe how this technique is applied to the growth of single crystals of various $M_{n+1}AX_n$ nanolamellar carbides, that are indeed non-congruent ternary compounds.

3.1.2 High temperature liquid solution growth

A full description of the growth of MAX phase single crystal protocols will now be given through the examples of Cr_2AlC, V_2AlC, Ti_3SiC_2 and Ti_2SnC:

1. We firstly choose a point in compositional space within an area of the M,A,C ternary diagram where we have an equilibrium between the ternary MAX phase and the liquid melt (see figure 3.2). We also need to make sure that other ternary or binary compounds will not predominantly form, thus restricting the workable composition ranges to very narrow windows. One dispenses a given quantity of processed M and A elements, either from powder or pre-formed pellets, with a ratio between the two elements that follows the chosen coordinates within the phase diagram. If the ternary diagram is not known ,as for example for the Ti, Sn, C system, one can only rely on the binary diagrams and guess a starting composition for growth where one will not see too much competition with other phases. The Ti to Sn ratio would later be optimized to obtain large single crystals, after many trial experiments.

Once properly weighted, all the precursors are put within either a graphite or an alumina crucible (see figure 3.3). Which crucible to choose will be of crucial importance once high temperatures are reached. The targeted carbon content, not mentioned thus far, will not be set by putting a given amount of graphite powder or blocks inside the crucible, as for M and A. It will instead be incorporated within the molten metallic

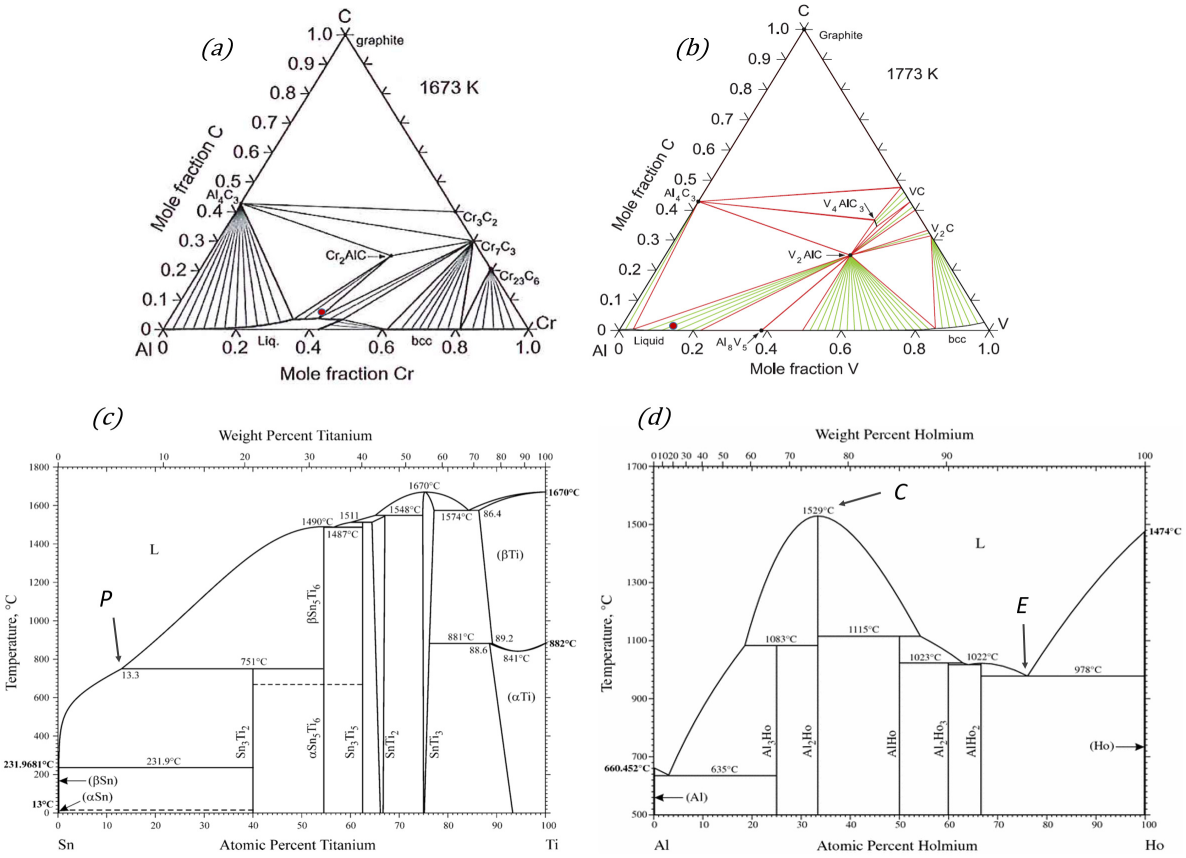

FIGURE 3.2: Ternary diagrams of Cr-Al-C at 1673K (a) and V-Al-C at 1773K (b). the compositions respectively associated to Cr_2AlC and V_2AlC are given. The compositions points to choose for crystal growth have to be located within the triangle areas where one has an equilibirum between the ternary MAX phase and a liquid phase. They are annoted as red dots for Cr_2AlC and V_2AlC. Binary diagrams of Sn-Ti (c) and Al-Ho (d), used to plan the growth of Ti_2SnC and $(Ho_{1/3}Mo_{2/3})_2AlC$. A Peritectic , an Eutectic and a congruent points are indicated by the letters P, E and C.

solution at high temperature, as we will see in the second step of the growth process (either by dipping a graphite rod within the melted metallic solution or by partial dissolution of the inner borders of a graphite crucible).

2. Before being introduced into the growth reactor, the alumina or graphite crucible is placed within a set of thermal shields as illustrated in figure 3.4. Pieces of zirconia pellets are introduced within the thermal shield in order to absorb oxygen that may be expelled once elemental pellets of M and A elements begin to melt. The block containing the crucible is placed at the center of an induction coil inside a reactor (figure 3.5).

The growth reactor is the corner stone of the whole synthesis process. Two reactors with similar designs and working conditions were used to grow crystals for this work, one of which is illustrated in figure 3.5a. When a growth experiment is running, a very high current is applied to the coil inside the reactor, thus generating a relatively high magnetic field. This will in turn generate induction currents within the outer graphite shell inserted within the coil and thus heat up the crucible and its environment through the Joule

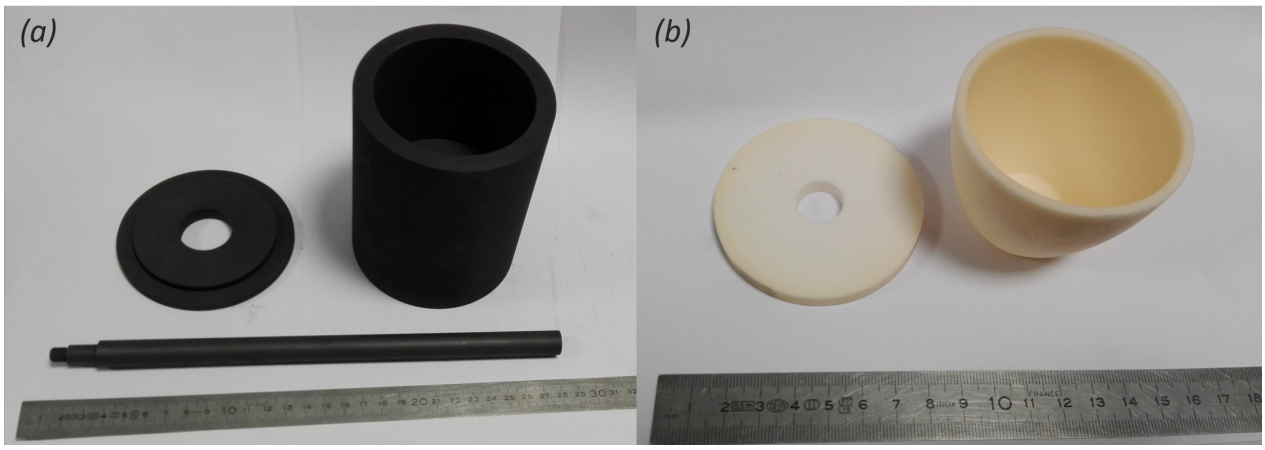

FIGURE 3.3: Shape and dimensions of typical Graphite (a) and Alumina (b) crucibles used for the growth.

effect. The input electrical power is controlled by a high-throughput power source. In order to generate very high currents, one applies an alternative current to an RLC system where the inductance corresponds to the coil inside the reactor. By fixing the frequency to the circuit resonance frequency, one achieves significantly higher-amplitude alternative current in the coil, and thus a more rapid heating effect. One does not have to provide the full instantaneous power from the generator, which would be impossible, but just the part which is dissipated to produce heat, whereas most of the instantaneous power is provided by the charging-discharging of the capacitor into the coil. To prevent damage to the inner growth chamber when heating, the coil as well as the whole enclosure of the reactor are cooled by a water circuit.

All growth experiments are performed under argon atmosphere with a pressure of 1 bar within the chamber. A typical crystal growth run starts after introducing the graphite blocks containing the crucible within the reactor chamber (see figure 3.6). After pumping and introducing argon gas, we apply 3.4 kW to the coil through a high power generator. Such conditions enable a temperature as high as 1000 °C in the interior of the crucible. The temperature is measured by an infrared pyrometer set to measure graphite surfaces (see figure 3.4). Once a temperature of 1000 °C is reached, a closed loop feedback control is set and the applied power would be regulated by the temperature measured by the pyrometer so that the temperature would slowly increase to reach the targeted plateau where the next step of the growth process will be set (both the pyrometer and the generator are controlled by a microcontroller which is itself connected to a computer terminal where the growth commands are set by the user). Temperature must increase slowly, over 2-5 hours, in order to prevent possible damages to the crucible or even to the chamber. It can take some time for the whole crucible and thermal shield blocks to thermalize.

Once the temperature plateau is attained and a stable metallic liquid is obtained (see figure 3.6), the input power is generally held constant for a few hours so that the carbon source can be dissolved into the solution (see below) . The magnetic field generated by the coil (as well as a temperature gradient within the crucible) causes the molten metal to experience magneto-convection , thus ensuring a certain degree of homogeneity

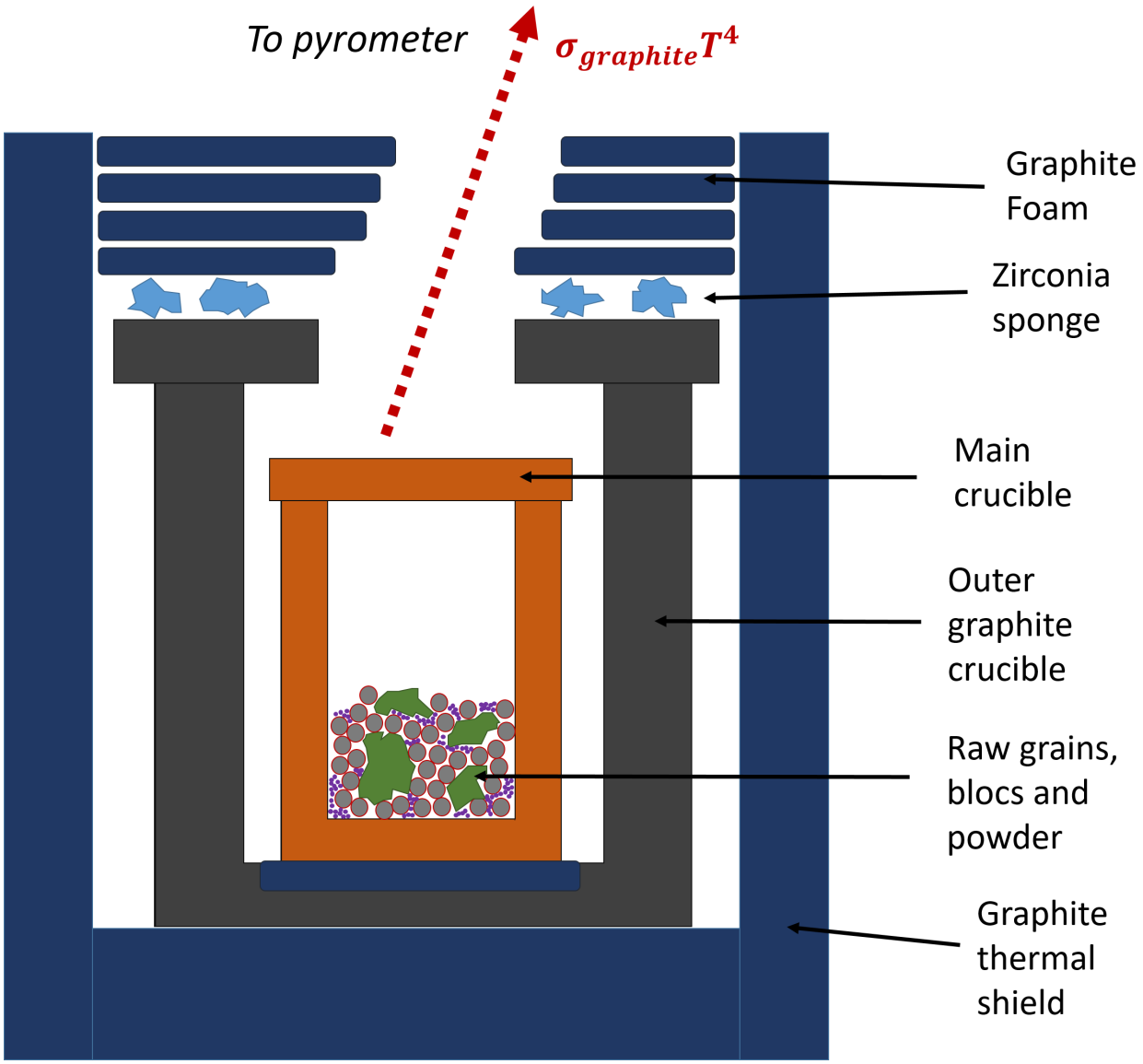

FIGURE 3.4: A typical crucible kit to be introduced within the growth reactor chamber. During the growth, a pyrometer will point towards the inner graphite crucible for temperature measurement. When using alimina as a main crucible, the outer graphite crucible will serve as a target for the pyrometer.

within the melted solution. The choice of the crucible is a sensitive parameter depending on the phase one wants to grow. The most straightforward choice would be a graphite crucible. Graphite itself is in some sense one of the most refractory materials in existence, with T_{sublim} higher than 3600°C at ambient pressure [174]. It is thus one of the only materials that can be considered be considered for working at the highest temperatures. Also, one can take advantage of carbon solubility to use the graphite crucible as an in situ source of carbon at high temperature. We proceed with this technique for the growth of either Ti_3SiC_2 or Ti_2SnC. But problems arise when dealing with aluminum based MAX phase. Somewhere between 1200°C and 1400 °C, liquid aluminum that would have already melted at 660°C reacts with the graphite crucible, leading to the formation of Al_4C_3, the destruction of the crucible, and eventually a leak of liquid metal within

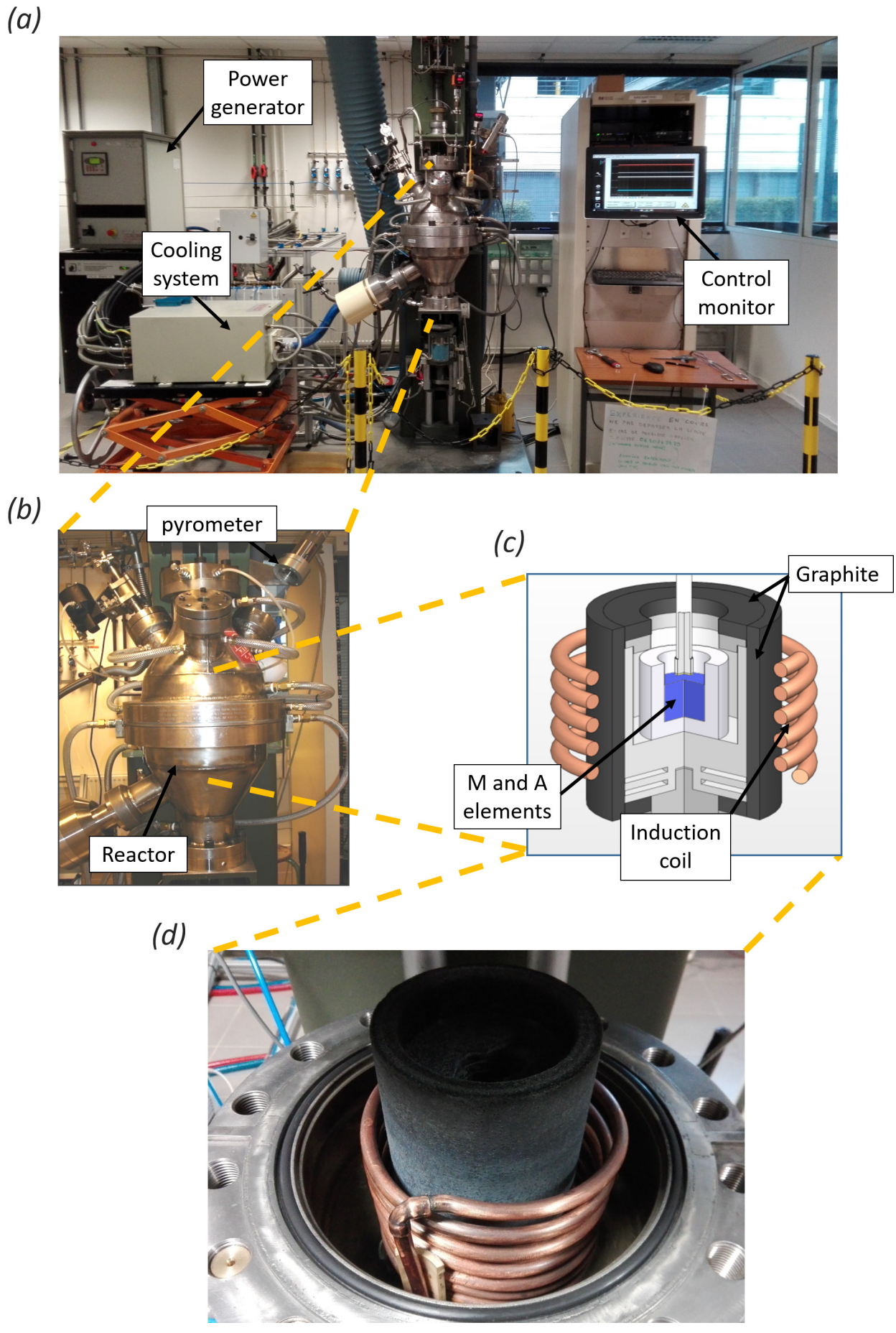

FIGURE 3.5: 'Memere' reactor setup, going from outer elements (a) to the whole reactor (b) and the inner chamber where the crucible kit is inserted (c,d).

the reactor chamber.

Fortunately, rather than graphite, it is also possible to use other types of crucibles such as those composed of alumina. Alumina cannot survive temperature higher than about 1700°C as $T^{melt}_{Al_2O_3} = 1800C$. But one can use it to grow most Al based 211 MAX phases. The source of carbon would then come from a graphite rod dipped inside the molten metal solution when reaching the temperature plateau (see figure 3.6). Another challenge that arises when dealing with Al-based MAX phase is liquid aluminium and vapor pressure that tends to become highly non-negligible at high temperature. It may lead to a strong Al evaporation that might darken the glass window through which the pyrometer is targeting the graphite surface, thus deteriorating the reliability of the temperature measurement .

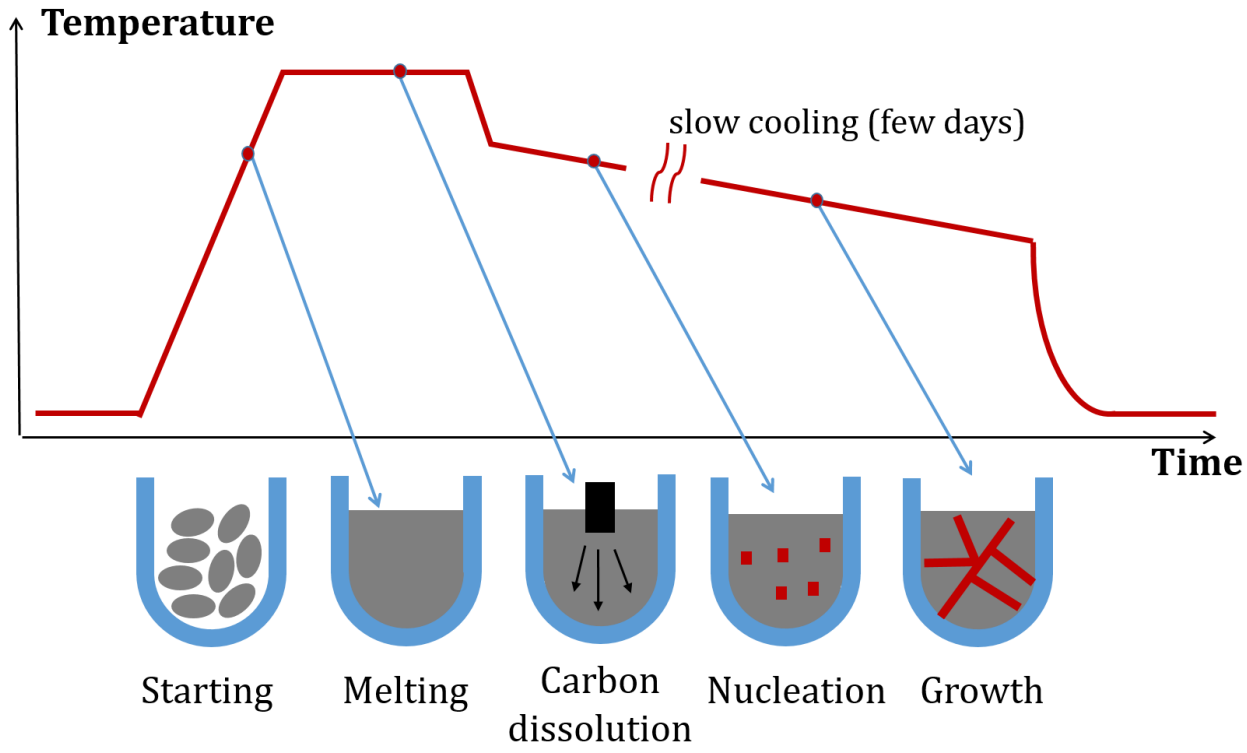

FIGURE 3.6: Main steps of high temperature solution growth performed at LMGP. The temperature increase generally lasts 2-5 hours before reaching a plateau which is maintained about 30 minutes to 2 hours. The cool down lasts from 2 to 6 days depending on the experiment.

3. Finally, the applied power is slowly decreased from about 10-15 kW at very high temperature to a power corresponding to a targeted temperature for ending the growth. After that, the generator is turned off, the crucible can be recovered and any crystal that have formed can be extracted from the flux. All steps of this process are outlined schematically in figure 3.6. Cooling usually lasts from 2 to 6 days, depending on the phase grown and the crystal size one wants to obtain. It is probably the most important step of the process since the actual growth of the single crystals arise during the cooling step of the process, if of course the basic thermodynamic parameters, e.g. the upper temperature plateau and the composition in M, A and C, are properly fixed. The choice of temperature at which the growth is stopped can be crucial if the MAX

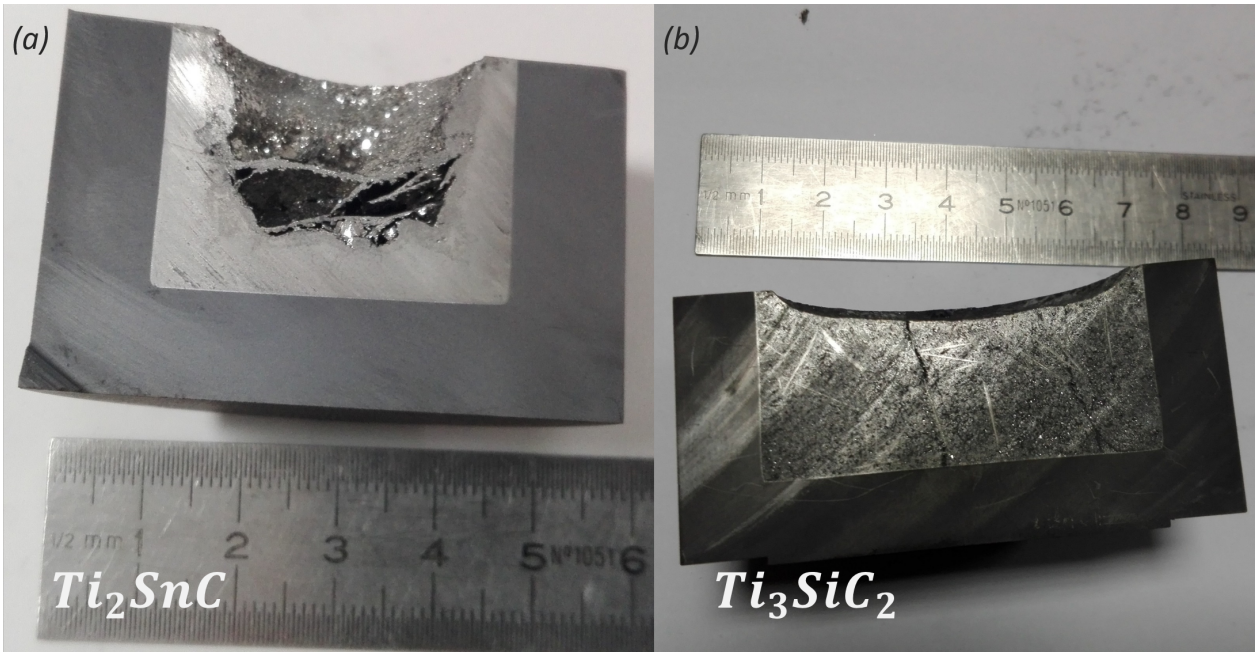

FIGURE 3.7: Two cuts of graphite crucibles after high temperature solution growth experiments. In (a), Ti_2SnC single crystals flakes are visible at the top of the solidified melt. In (b), Ti_3SiC_2 single crystals are found within the solidified melt, thus indicating they would not specifically form at the liquid surface.

phase one aims to synthetize undergo a peritectic transformation at intermediate temperature. For example, V_2AlC would peritectically decompose within the 1100-1200°C range. Stopping slightly above the peritectic temperature avoids the decomposition and single crystals will stay intact within the remaining flux.

If, after several trial experiments, the kinetic parameters of the growth happen to be well optimized, nucleation will occur during the cooling and the single crystalline nucleation centers will grow to macroscopic size. Since no single crystalline seeds are introduced in the melt, we can assume that primary nucleation spontaneously occurs during cooling down. Crystals of Ti_2SnC and Ti_3SiC_2 embedded within their flux are shown in figure 3.7. From the geometry of the crystals, the growth is found to be highly anisotropic and highly favored in the a,b directions. Due to the the layered structure of MAX phases [35, 157, 158, 175], the shape of the seeds will not be spherical but planar. It will subsequently favor the formation of thin flake-shaped single crystals with nearly "layer by layer" terrace growth over c axis [175].

Pictures of representatives examples of crystals grown with this procedure are shown in figure 3.8 , with the c axis being perpendicular to the crystal plane. They are about 100 μm to 1 mm thick with a surface of about $5mm \times 5mm$ for V_2AlC and Ti_2SnC and as large as a few square-centimeters for Cr_2AlC.

3.1.3 MAX phase single crystals, derivatives, and characterization techniques

From the flux or the 'growth' cake that contains MAX phase single crystals as well as many other byproducts formed during the solidification of the melt it is possible to extract the single crystals either by waiting for most of the unstable compounds to disaggregate, or by dipping the flux into 50 percent pure HCl wherein

all unwanted compounds that otherwise would have formed competitively to the MAX phase would be dissolved . Only the chemically resilient MAX single crystals would remain, as seen in figure 3.9.

MAX phases, iMAXs and derivatives grown during the course of this PhD are listed below:

- Cr_2AlC is grown with a molar fraction of chromium going from 0.3 to 0.35, a fraction of alminium of 0.55 to 0.6 and a fraction of carbon of about 0.07 (though the exact amount of incorporated carbon added to solution is hard to determine). An alumina crucible is used and the carbon source is a rod that is dipped into the solution after reaching a temperature plateau of 1670°C. The depth that the rod is dipped into the solution is mechanically controlled and connected to a microcontroller so that one can approximately monitor how much will be dissolved into the solution, knowing graphite density and the dimensions of the rod. The duration of the temperature plateau is typically about an hour before starting the cool down.

-V_2AlC is grown with an Al ratio of 0.75 to V. Similarly to the case of Cr_2AlC, we use an alumina crucible to prevent the destructive reaction of melted alumina with the graphite crucible, and carbon is incorporated by dipping a mechanically controlled rod into the melted solution at the temperature plateau of roughly 1700°C.

- Ti_2SnC is grown with a Ti to Si ratio of 0.5. A initial temperature plateau of 1800°C is maintained during 30 min in order to increase the carbon solubility in the melt. Then, we ramp up to another plateau at 1600°C for 30-60 min before starting the actual cool down. Due to the absence of aluminium within the melt, a graphite crucible is used. Here, the crucible is the sole source of carbon.

-Ti_3SiC_2 is grown with a ratio of 0.34 Ti to 0.66 Si. The temperature plateau is set to about 1650°C. Due to the absence of alumina in the melt, one can also use the graphite crucible as a source of carbon. Residual $TiSi_2$ droplets appear to solidify on the top of Ti_3SiC_2 crystals during the growth. These can be removed when cleaving.

- The case of iMAXs, exemplified by $(Ho_{1/3}Mo_{2/3})_2AlC$, is far more complex than their ternary counterparts. Working within an unknown fourth dimensional quaternary phase diagram makes it very difficult to choose a starting composition for the growth. Our approach is to have enough aluminium content to allow for the dissolution of Molybdenum in solution while avoiding the area of Ho-Al phase diagram where a congruent point is located. The following composition allowed us to grow single crystals up to a scale of roughly 1mm: $X_{Ho} = 0.7$, $X_{Mo} = 0.1$ and $X_{Al} = 0.2$. Not only aluminium but also holmium melts before reaching the critical 1200°C range, and we witnessed that in the case of an Al-Ho melt, no reaction leading to the destruction of carbon crucibles would occur, so it could be used for the growth of this phase as well as other rare earth based iMAXs. We reach a temperature plateau of 1800°C that lasts about 2 hours before starting the cool down. The output of the growth is a 'colored cake' that contains a few iMAX single crystals and many other binaries/ternaries. After a few days in hydrated atmosphere, the resulting flux decomposes and we can then retrieve the $(Ho_{1/3}Mo_{2/3})_2AlC$ crystals among the remaining poweder. The other compounds identified within the cake are the following: $HoAl_2$, Ho_2O_3 and HoC_2.

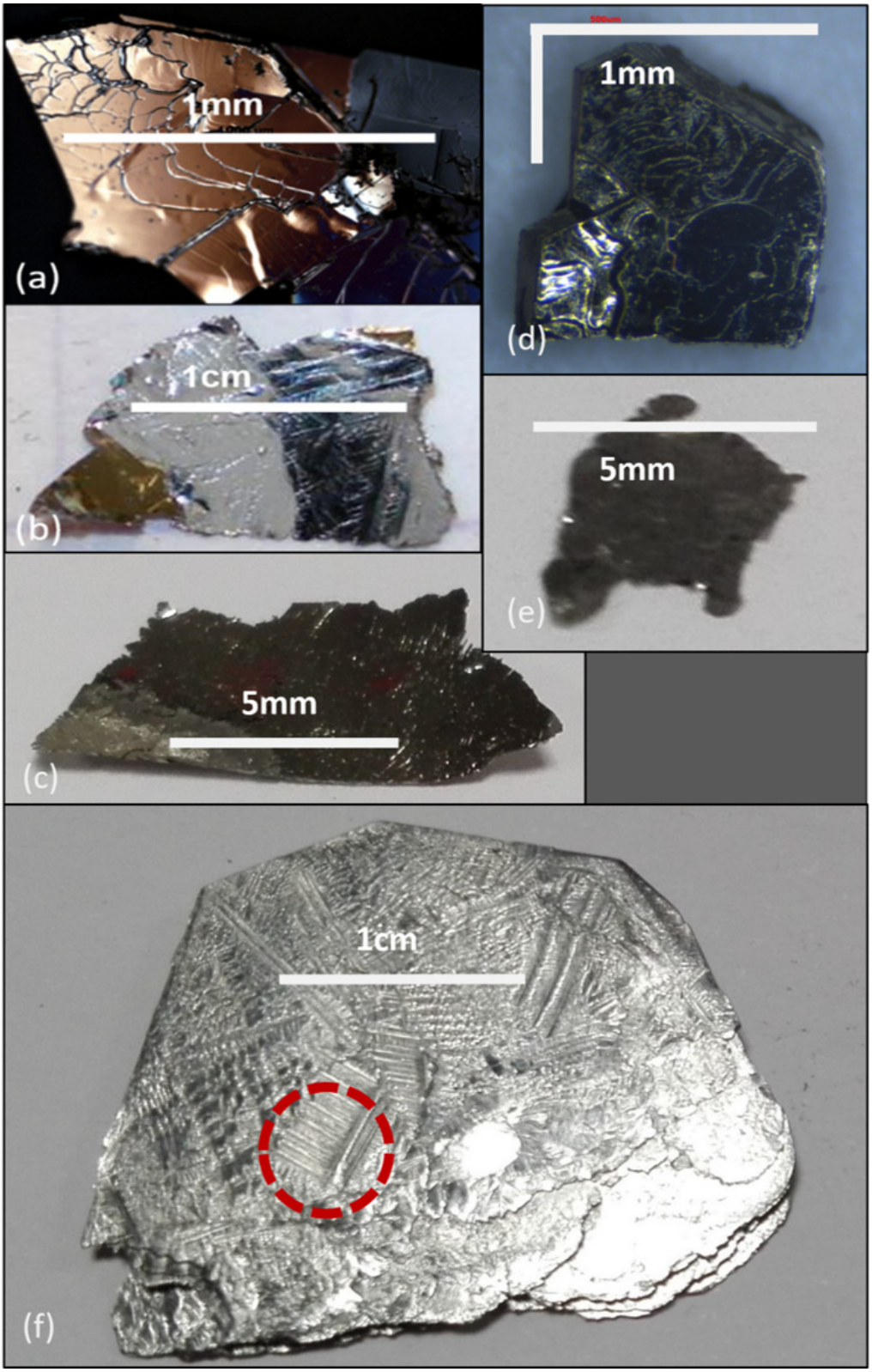

FIGURE 3.8: $Mo_4Ce_4Al_7C_3$(a), Ti_3SiC_2(b), Ti_2SnC (c), $(Ho_{1/3}Mo_{2/3})_2$ (d), V_2AlC (e) and Cr_2AlC (f) single crystals. The area of Cr_2AlC single crystal highlighted in (f) match to figure 20.a. It corresponds to one of the many dendrites at the surface of these crystals

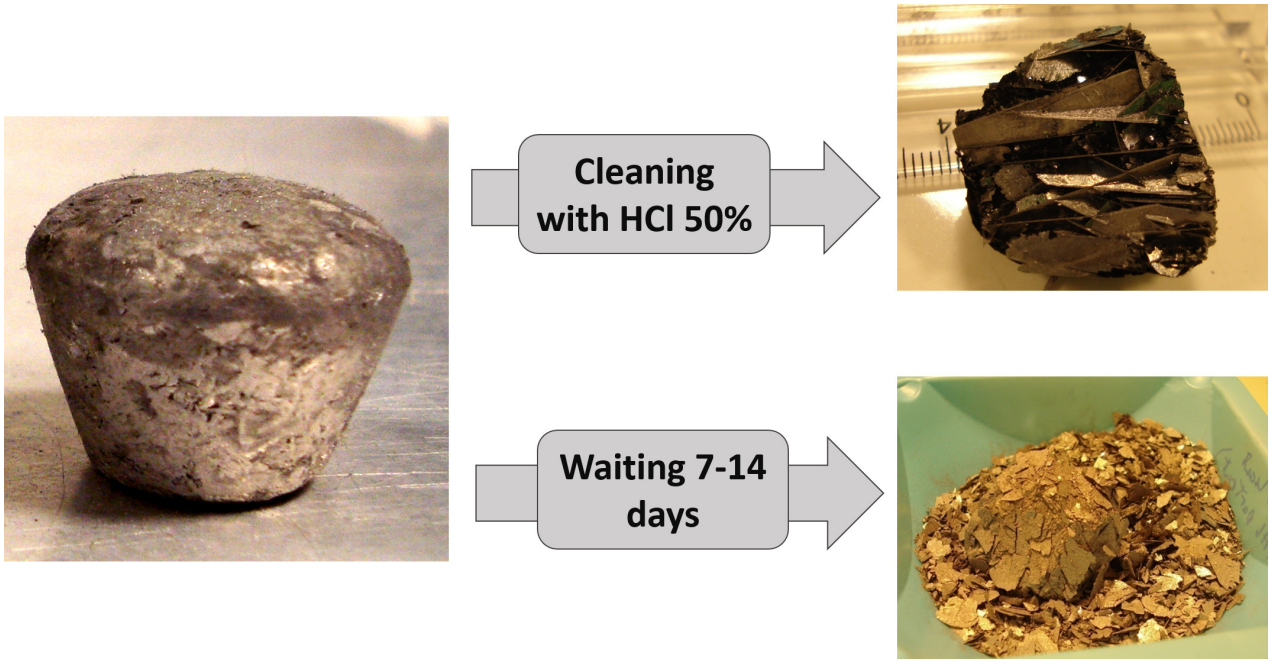

FIGURE 3.9: Two possible pathways for extracting the single crystals from the solidified melt: After one to two weeks, most of the unwanted compound would decompose into powder but the more stable MAX phase single crystals. If the 'growth cake' is directly put in highly concentrated HCl solution, one can take advantage of the high chemical resilience of MAX phase single crystals to recover them faster as the rest of the solidified melt will be quickly dissolved.

-$Mo_4Ce_4Al_7C_3$ is grown with a Ce fraction of 0.44, an Al fraction of 0.44 and 0.12 for Mo. A procedure similar to that for iMAX phases is followed. One must notice that, in contrast to other rare earth materials, blocks of elemental cerium are relatively affordable. It makes it possible to perform a significant number of growth experiments for this compound while the growth of Ho, Dy or Gd-based iMAX has to be considered with greater care considering the raw material price (about 1000 euros for 100g of elemental Ho). As for $(Ho_{1/3}Mo_{2/3})_2AlC$, it must be emphasized that growing single crystals of a complex quaternary compound, for which not even ternary diagrams are known, is generally far more challenging than the growth of ternary compounds even when ternary diagrams are not known. Contrary to the case of MAX and iMAX phase, HCl cannot be used to dissolve the flux without damaging the crystal. We just wait a few days before the resulting flux decomposes within a highly hydrated atmosphere. Additional phases found within the powder are: Cerium oxides, Cerium carbide, Ce_2C, $CeAl_2$, Al_4C_3, Al_8Mo_3 and MoC.

Once again, single crystals are shown in figure 3.8. We basically characterize samples by first observing them with an optical microscope, then we confirm the chemistry of the compound through Raman and EDX analysis before analyzing their crystallinity through X-ray laue transmission and phi scan or pole figure analysis. The setups are summarized below.

Observation of the single crystalline samples with an optical microscope already yields a decent amount of information about the crystal growth process. For the case of Cr_2AlC, adjacent single crystals are found to grow very close to one another, one crystal touching another as the growth goes on. The competition between

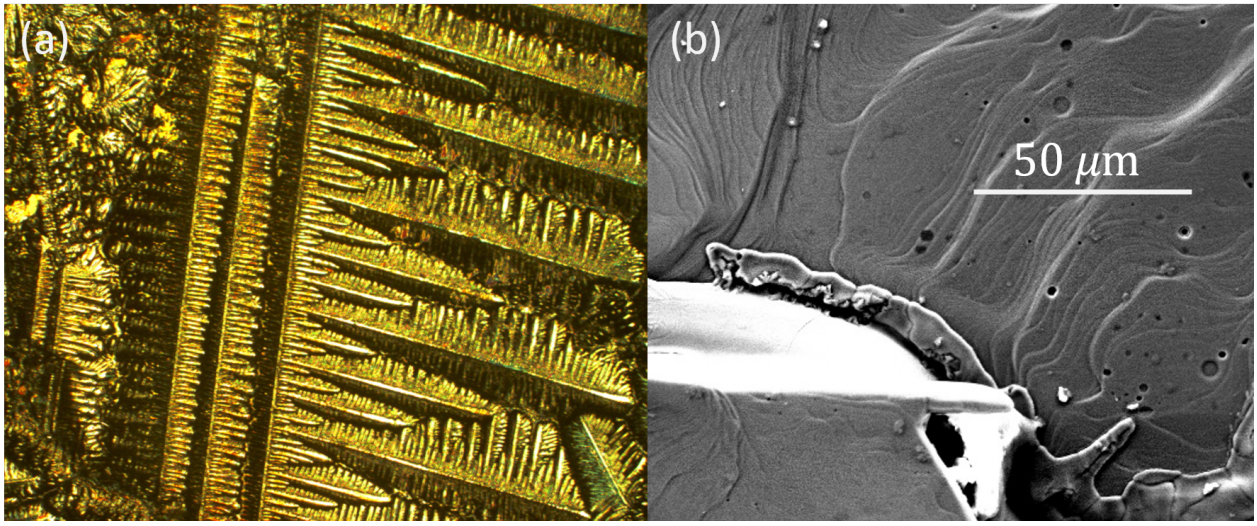

FIGURE 3.10: (a) Zoom over a dendrite on Cr_2AlC surface, a morphologic trait characteristic of surface instabilities arising during growth (as extensively described in [157]). (b) Cr_2AlC growth terraces observed by scanning electron microscopy

bordering nucleations centers leads to a characteristic morphologic defect at the surfacer of these crystals, the so-called dendritic structures (see figure 3.10). Such features arise from surface instability induced during the growth, for example one single crystal touching the surface of another as in the case of the product of Cr_2AlC growth shown in figure 3.7 . Growth terraces are also observed at the surface of all MAX phases single crystals. The overall surface morphology of MAX phase single crystals was highly detailed in the pioneering work of *Mercier et.al* on as grown Ti_3SiC_2 [35].

Following optical microscopy, chemical identification of the crystals is performed by the combined use of several techniques:

-Micro-Raman measurement were performed at room temperature on several crystals using a He-Ne laser as the exciting line (λ=632.8 nm) of a Jobin Yvon/Horiba LabRam spectrometer equipped with a liquid nitrogen-cooled CCD detector. The experimental spectra, as well as the characteristic peak of each elements are compared to the literature for the expected phase [35, 123].

-The chemical composition of the crystals were analysed by energy dispersive X-ray spectroscopy (EDS) using a BRUKER silicon drift detector (SDD) mounted on a Quanta 250 FEI field emission gun (FEG) scanning electron microscope (SEM) operated at 10 to 15 keV.

Finally, X-ray diffraction allows the extraction of more information about the crystal structure and the degree of crystallinity of the as-grown samples. X-ray Laue transmission permits a preliminary confirmation of whether the crystals are indeed single crystals or rather polycrystals. Laue patterns were collected with a Philips PW1730 source with a Tungsten anode at 50kV and 35mA. Tungsten X-ray source allows to obtain a very white source for Tungsten brehmstrallung radiation. This image plate was read with a Fuji BAS1800II scanner.

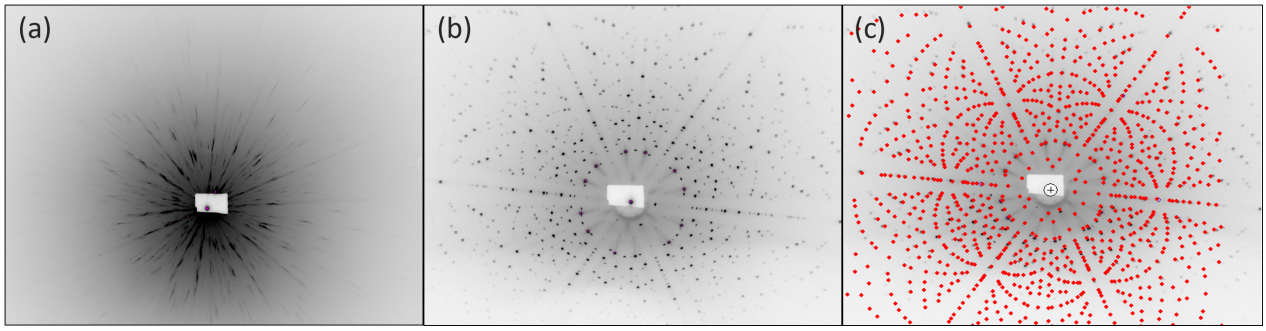

FIGURE 3.11: (a) Laue pattern of a sample of very low quality. (b) Laue pattern of a 10cm large Cr_2AlC crystal used for Neutron inelastic scattering experiments at the Institut Laue Langevin [176]. The symmetry of the system and its orientation can be determined using the Orient Express software(c).

MAX phase single crystals would exhibit characteristic hexagonal patterns for their laue images, as highlighted in figure 3.11, while polycrystals laue would show a blurred, unclear image. iMAX phases shows more complex laue patterns due to their lower degree of symmetry. If the laue pattern does not appear clean enough, then the crystal will not be used for further photoemission experiments (figure 3.11a). If the Laue pattern image is clear enough, one can use software to simulate Laue patterns taking the space group, lattice parameters, experimental conditions and the experimentally determined Laue pattern as an input. The simulated laue which matches that of the experiments allows us to recover the crystal vectors directions, knowing that c-axis is perpendicular to the surface. One can then reorientate the single crystals for further experiments. ϕ scan and pole figure analysis are achieved by X-ray diffraction, using a Siemens- Bruker D5000 diffractometer (Cu, Kα1 radiation). The X-ray source is a copper anode, and diffraction at the Cu Kα1 and Kα2 lines is measured. The data is collected in the 2ϑ range 10°-115°, with a step size of 0.05°, and a duration of 2s per step. The pole figures are recorded using a four-circle goniometer (Schultz geometry), featuring an incident beam with a diameter of 1 mm, a nickel filter for attenuating the Cu Kβ radiation, and a point scintillation detector. The full width at half maximum (FWHM) of the diffraction peaks obtained in phi scan mode is a measure of the crystalline quality of a sample. When performing a phi scan of MAX phase in the $20\bar{2}3$ plane, the FWHM of the peaks are in the 0.25-0.5° range, which is significantly bigger than the industry standard of 0.05-0.1 FWHM for semiconductors. We attribute this value to imperfections at the surface and to residual defects within the bulk of the single crystals.

3.2 Angle resolved photoemission spectroscopy

Photoemission spectroscopy techniques are invaluable tools for probing the electronic states of matter. They are based on the photoelectric effect, discovered by Einstein in 1905 [177], and later put to application by Kai Siegbahn in the 1950s [178] for the development of the first X-ray photoelectron spectroscopy (XPS) experiments. Both discoveries were awarded Nobel prices. The basic principle of a photoemission experiment is

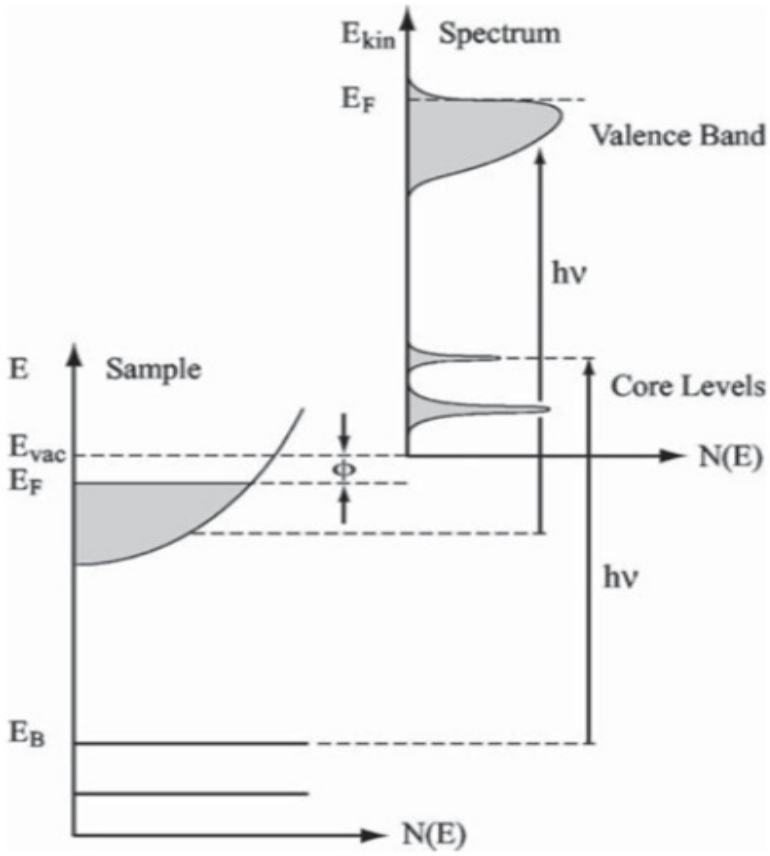

FIGURE 3.12: Illustration of the relation between the electronic structure of a given sample($E_B = E - E_F$) to the energy distribution of photoelectron extracted by electromagnetic radiation $h\nu$. Only the occupied states are being probed (apart for a small energy range of thermally activated states sligthly above E_F) and a broadening of the core states arise from photoemission final state effects and from a limited experimental energy resolution. This figure is taken from *Damascelli* review [180]

to irradiate a sample of the material one wants to probe by electromagnetic radiation (generally X-rays) of energy $h\nu$ sufficiently high to extract electrons occupying the energy bands below the Fermi energy. Once out of the crystal, these photo-electrons will propagate as free electrons until they eventually reach an electron analyzer that permits to measure their kinetic energy E_{kin}. One will obtain a certain electron intensity vs kinetic energy distribution for the emitted photoelectrons. The (simplified) energy conservation throughout the photoemission process in the solid can be written as [179]:

$$E_{kin} = h\nu - \phi + (E - E_F) \tag{3.1}$$

Where ϕ is the workfunction of the solid and the difference $E - E_F$ is often referred to as *binding energy*. It means that knowing $h\nu$ and E_{kin}, one can determine the intrinsic energy spectra of a system. The measured kinetic energy distribution of the photoelectron shall be, at the first approximation, related to the electronic density of states of the solid below the Fermi energy, as illustrated by figure 3.12.

Bands above E_F cannot be probed by the means of standard direct photoelectron spectroscopy as they

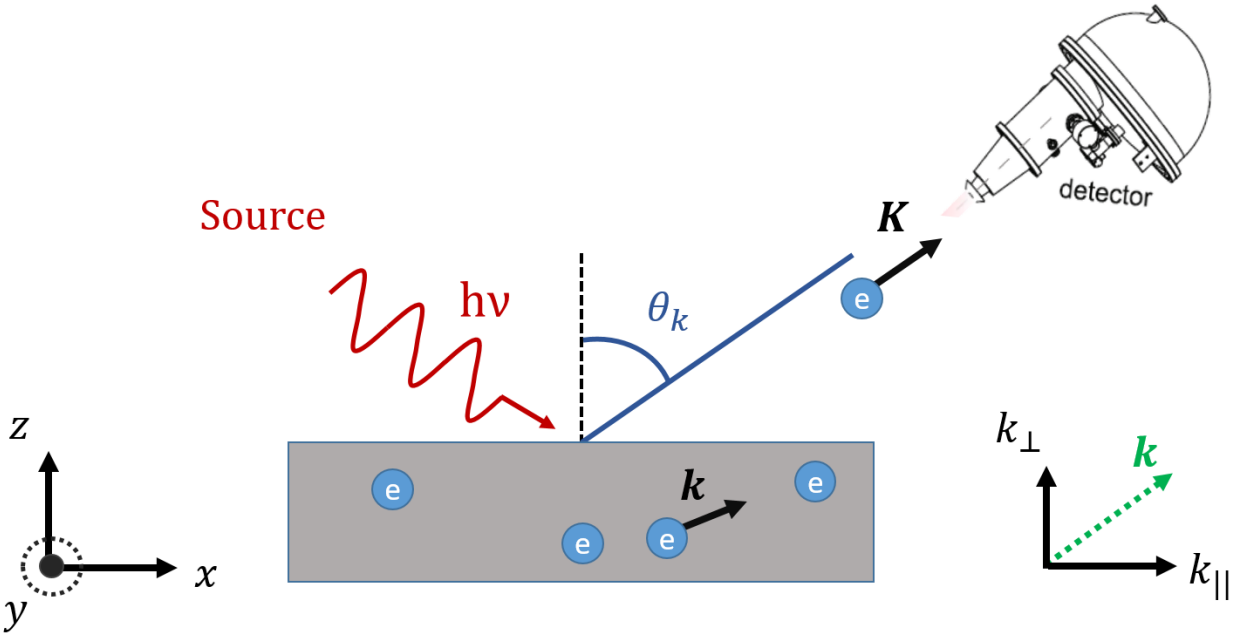

FIGURE 3.13: Basic illustration of an ARPES experiment. The in plane and out of plane component of the wavevectors are given in the lower right of the figure.

are unoccupied. Inverse photoemission spectroscopy (IPES) is used to probe unoccupoed energy states [179], but such experiments are more complex and remain out of the scope of this manuscript. The relationship between the measured spectra and the intrinsic electronic band structure of a solid is naturally more subtle than this straightforward description and it will be discussed with more care in section 3.2.3. Not only is it possible to probe the photoelectron energies, but their wavevectors can also be probed and this is the purpose of angle-resolved photoemission spectroscopy (ARPES). We will now present in greater detail the principles of a standard ARPES experiment as well as the underlying processes that arise when the photoelectrons are extracted from the surface of a single crystalline sample. It must be specified that while XPS does not require a single crystalline sample, one of the constraining criteria for ARPES experiments is to work with properly aligned single crystals. Note that there are many more photoemission techniques derived from XPS [179, 181], but describing them all is beyond the scope of this manuscript

3.2.1 Elementary portrait of a photoemission experiment

As its name suggests, angle-resolved photoemission spectroscopy allows not only the observation of electronic spectra in energy space but also to explore these spectra through the angular degree of freedom of the emitted photoelectrons.

To understand the latter, one first needs to look at the kinematics of the photoelectron and to the momentum conservation laws at the crystal-vacuum interface.

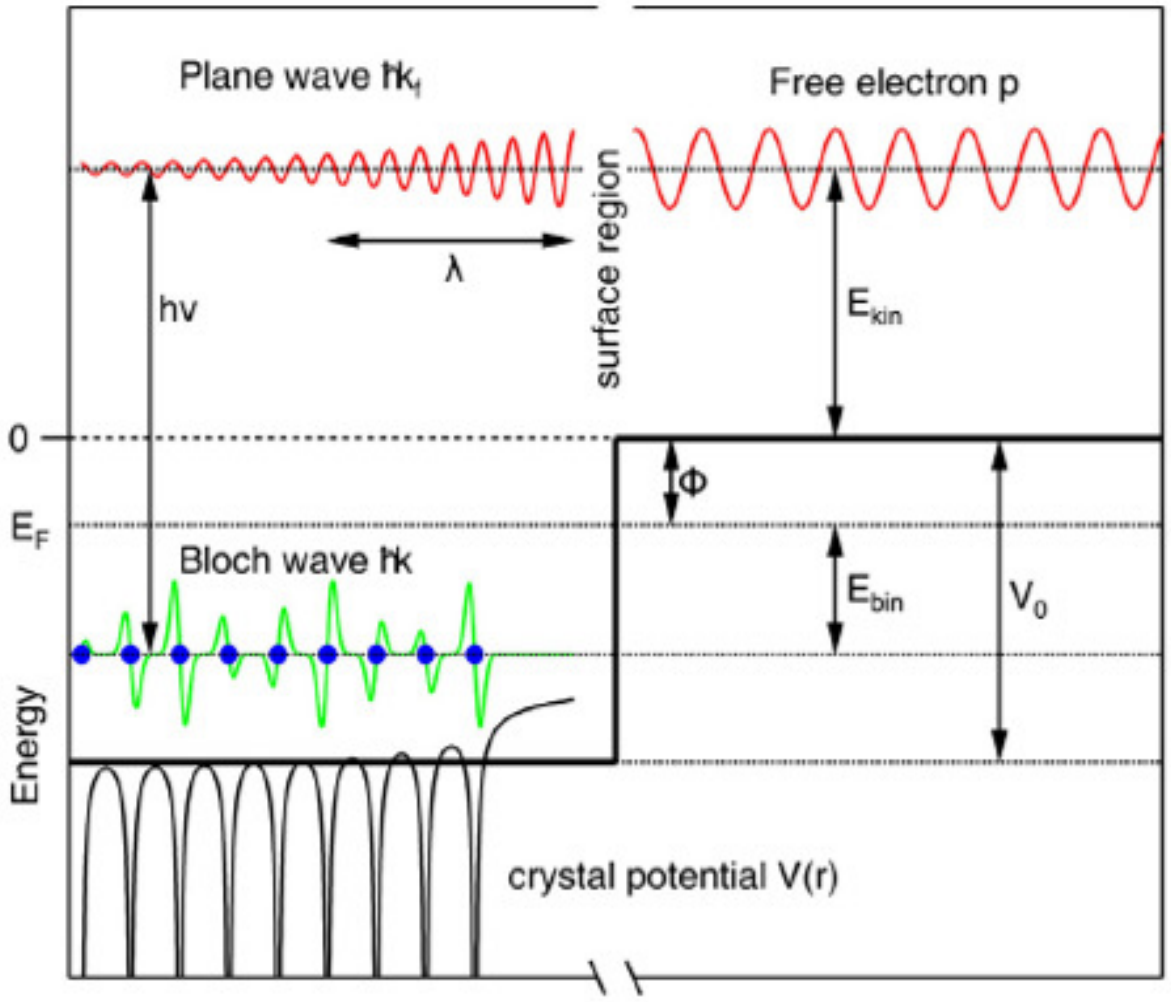

FIGURE 3.14: During the photoemission process, electrons are excited from their initial block states to the so-called final states, above the vacuum level. Electron wavefunctions in these states are damped planwewaves that will cross a potential barrier V_0 at the surface of the solid to be expelled to vacuum. From *Moser* [182].

Let us consider a generic crystal-vacuum interface, with x and y axis defining the horizontal plane of the sample and z the direction perpendicular to the interface (see figure 3.13). Regardless of the finite state effects that will be discussed further, it follows from the translational symmetry over the x,y plane that the k_x, k_y component of the momentum must be conserved when the electron is extracted from the solid [180]. Then, if we define $\mathbf{k}$ as the wavevector of an electron occupying a band of the solid at an energy E, and $\mathbf{K}$ the wavevector of the photoelectron once extracted in vaccum and with an energy $E_{kin} = \frac{\hbar^2 \mathbf{K}^2}{2m}$, we have:

$$\left\{ \begin{array}{l} K_x = k_x \\ K_y = k_y \\ \mathbf{k}_{||} = \mathbf{K}_{||} \end{array} \right\} \tag{3.2}$$

for $k_{||} = k_x + k_y$

If one recalls the propagation of an electron through a potential barrier $V(r)$:

$$V(r) = \left\{ \begin{array}{ll} 0 & \text{if } r > 0 \\ -V_0 & \text{if } r < 0 \end{array} \right\} \tag{3.3}$$

In the case of ARPES, V_0 represents the energy loss of the electron when crossing the crystal-vacuum interface as highlighted in figure 3.14 . Prior to being transported out of the solid, the future photoelectrons are brought up to an excited state above the vacuum level of the solid, known as *the final state* (see figure 3.14). As a first approximation, and since electrons in this state are much less tightly bound to the solid, we consider the final state dispersion to be parabolic, also neglecting electron-electron interactions. Then, one can show that, due to the very small value momentum of the photons, the electrons momentum is mainly conserved when they go from their initial bulk state to their final state within the solid [180, 183, 184]:

$$\mathbf{k} \approx \mathbf{k^{final}} \tag{3.4}$$

where $\mathbf{k^{final}}$ is the wavevector of the electron occupying the final state while, as mentionned above, $\mathbf{k}$ is the wavevector of the electron in the bulk inital state. Due to the conservation of the in-plane momentum component in equation (3.5), the energy loss arising when crossing the interface must only impact the out of plane component of the momentum, labelled $k_\perp$. One then finds the relation:

$$\frac{\hbar^2 (k_\perp^{final})^2}{2m} \approx \frac{\hbar^2 (K_\perp)^2}{2m} + V_0 \tag{3.5}$$

Essentially, the out of plane component of the moment is not conserved through the photoemission process. This fact is often described by stating that $k_\perp$ is not a good quantum number [182, 184].
Electrons that are emitted through *photoelectric effect* escape in vacuum in all directions before being later collected with an electron energy analyzer tuned to discriminate the emission angles of incoming electrons, roughly described in section 3.2.2. The emission angles are typically labelled as θ_k and ζ_k, respectively, though we will henceforth be neglecting the latter. By considering the polar decomposition of the wavevector of the emitted free photoelectrons $\mathbf{K}$, as well as (2.4) and (2.5), one would obtain both components of the initial state wavevector $\mathbf{k}$ [182]:

$$k_{||} = \frac{1}{\hbar}\sqrt{2mE_{kin}} sin(\theta_k) \tag{3.6}$$

$$k_\perp \approx \frac{1}{\hbar}\sqrt{(2mE_{kin} cos^2(\theta_k) + V_0)} \tag{3.7}$$

This implies that with an electron analyzer capable of recording both the angular coordinates and the kinetic energy spectrum of the emitted photoelectrons, one can have access to their prior energies and wavevector inside the crystal and thus experimentally reconstruct the band structure of a material. This

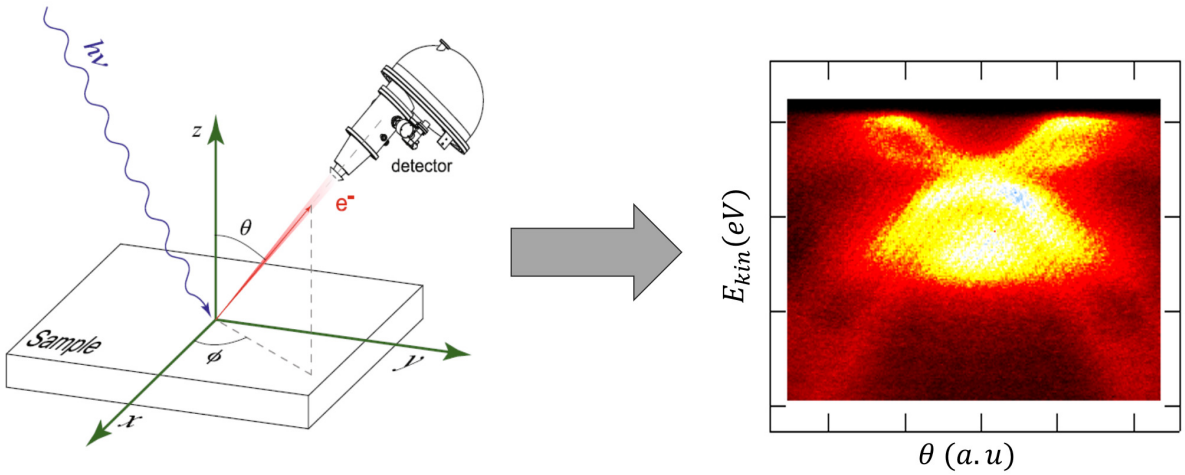

FIGURE 3.15: Output of a "snapshot" ARPES E_{kin}, θ_k BS mapping of V_2AlC for a single crystal properly oriented over ΓK

is the fundamental goal of an ARPES measurement, and the key here is the direct relationship between the electron wavevectors and the emission angles of the photoelectron. Yet, and as stated above, several conditions need to be met to ensure that a measured ARPES spectra as in figure 3.15 does indeed correspond to the intrinsic band structure of the solid. These conditions will be listed in section 3.2.3. We will now briefly describe the different element of an ARPES setup as well as the procedures to perform band structure and Fermi surface mappings.

3.2.2 Setup of an ARPES experiment

The essential elements of ARPES setups for the experiments that were performed on MAX phase single crystals are portrayed in figure 3.16 and outlined as follows :

- The chamber within which the experiment takes place is under ultra high vacuum (10^{-9} Pa) in order to prevent incoming X-rays or the photoelectron to interact with anything but the sample or the detector. Prior to each experiment, MAX phase single crystals are cut with a diamond wire saw and cleaved in the form of parallelepipeds with an area of 3 × 3mm and a thickness around 500µm. Samples are then cleaved again *in situ* within the chamber for the ARPES experiments in ultrahigh vacuum and at temperatures from around 8 K to 13K for experiments on MAX phases, depending on the synchrotron beam line where the experiment takes place.

- The X-ray source (though ARPES can also be performed in the UV range) is a beam of monochromatized radiation supplied either by a gasdischarge lamp, a laser, or by a synchrotron beamline incident on the sample (which must be a properly aligned single crystal in order to perform angle or, equivalently, momentum-resolved measurements).

The main advantage of using synchrotron radiation is first the larger accessible ranges of energy frequency it possesses [181, 179, 184]. Higher brilliance and a greater control over the polarization of the beam

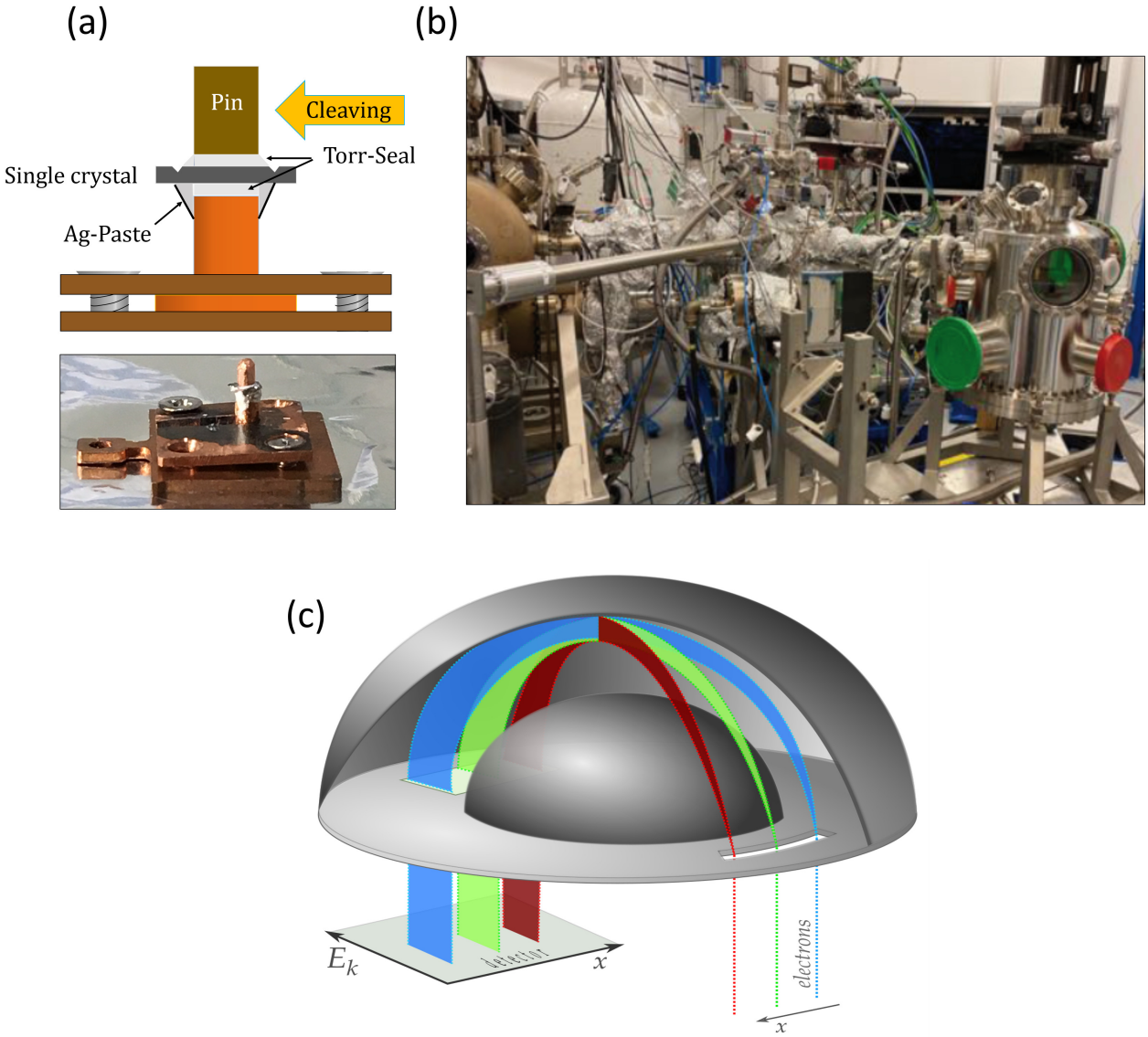

FIGURE 3.16: (a) Schematic of a $3mm \times 3mm$ single crystal mounted on a sample holder and glued with a copper pin used for cleaving under ultra high vacuum. (b) SOLEIL cassiopée Beamline and (c) hemispherical multi-channel electron energy analyzer allowing to record snapshots (E_{kin}, θ_k) maps.

are other elements that favor synchrotron sources for ARPES experiments. All of the measurements on MAX phases described within this manuscript were performed at various synchrotron sources: AichiSR and UVSOR in Japan and/or SOLEIL in France. A picture of SOLEIL Cassiopée line is given in figure 3.16.

-Among the available photoelectron detectors, hemispherical multi-channel electron energy analyzers have become the most widespread in synchrotron ARPES lines. The following description is highly inspired by the review of *Damascelli et.al* [184]. The central piece of the analyzer is the deflector [185] which consists of two concentric hemispheres of radiuses R_1 and R_2 (See figure 2.16) kept at a potential difference V; so that only electrons reaching the entrance slit with a kinetic energy within a range centered at $E_{pass} = eV/(R_1/R_2 - R_2/R_1)$ will pass through this hemispherical capacitor, and then reach the detector where the

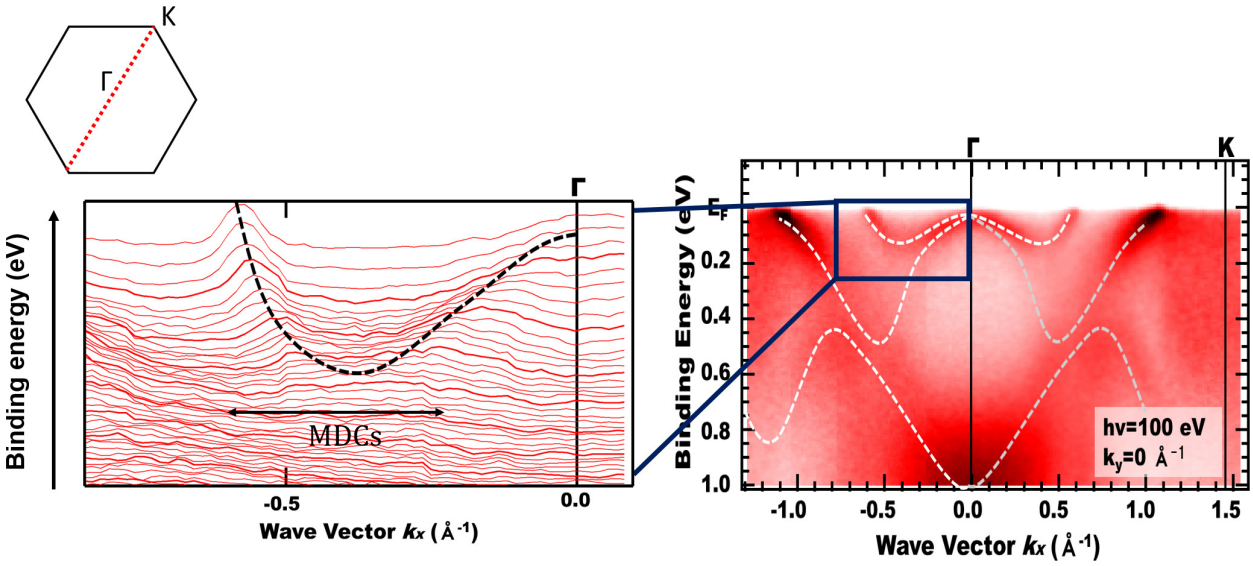

FIGURE 3.17: Band structure mapping of a Cr_2AlC single crystal oriented over ΓK and its decompositions into a set of MDCs. The bands are defined as the curves that follow the respective maxima of the MDCs. ARPES band structure maps can also be decomposed as a multitude of EDCs, each associated with a given angle (or momentum)

intensity is recorded. It is thus possible to discriminate the photoelectrons by their energy. An electrostatic lens located ahead of the deflector is used to slightly decelerate and focus the photoelectrons onto the entrance slit without altering their energy spread. The most recent detectors feature a set of two micro-channel plates and a phosphor plate, coupled to a CCD camera for data recording. In this case, the electrons are dispersed along one of the axes of the phosphor plate as a function of their kinetic energy after travelling through the hemispherical capacitor, and are thus all measured in parallel. Furthermore, position-sensitive electron detectors can be operated in angle-resolved mode, which provides energy-momentum information not only at a single angle or k-point but along an extended cut in k-space. In particular, photoelectrons within an angular window in the order of θ_k within roughly -15° to 15° along the direction defined by the analyzer entrance slit are focused on different x positions on the detector (figure 3.16). It is thus possible to measure a snapshot of kinetic energy versus angle map in one single measurement.

These snapshots can be seen either as a combination of multiple angular distribution curves (ADC) or momentum distribution curves (MDC, that one gets after converting angular units to wavevectors) obtained for several energies or as a combination of energy distribution curves (EDC) obtained at different angles (see figure 3.17). From the application of (3.6), (3.7) and (3.1), and knowing the work function of the material, one can convert the maps in angle and kinetic energy to reveal the $E(\mathbf{k})$ band structure. The direction of reciprocal space being probed is then a function of the single crystal orientation. The sample can be azimuthally rotated or tilted in order to probe different directions within the BZ and the rotations are controlled by several goniometers.

Recording a large number of BSs obtained for a large range of sample tilts and combining them gives

access to a continuous set of isoenergy surfaces over several BZ (see figure 3.18), from the minimum of the recorded energy range to the Fermi energy and its associated isoenergy surface, the Fermi surface.

But, as a first approximation, these mappings can be seen as in plane 2D cuts of a 3 dimensional-isoenergy surface or Fermi surface at a given $k_\perp$ value, naturally labelled as k_z. This k_z value would be fixed by (3.1) and (3.7) as [184]:

$$k_\perp \approx \frac{1}{\hbar}\sqrt{2m(h\nu - \phi + (E - E_F))cos^2(\theta_k) + V_0)} \tag{3.8}$$

Thus the k_z for which one probes an in-plane band structure or Fermi surface is fixed by the energy $h\nu$ of the X-ray source. On can perform an out-of-plane mapping of the Fermi surface by performing many BS snapshots for a single orientation and several $h\nu$ values [186, 187] . By considering the overall symmetry of the resulting out-of-plane FS map, it is possible to deduce the whereabouts of the Γ or A plane and then fix the $h\nu$ value in order to be in a chosen plane within the first BZ for further experiments. Yet, and whether it is for BS, in plane or out of plane FSs, the complexity of experimental ARPES data makes them difficult to interpret without the input of an electronic structure obtained from theoretical calculations. It is even more crucial when considering that there are several physical phenomena that may more or less strongly alter the ARPES spectra from the actual band structure of the solid. Some of the underlying assumption assuring the direct correspondence between (θ_k, E_{kin}) of the photoelectrons (figure 3.15) and the intrinsic band structure of the material are unfortunately not always valid.

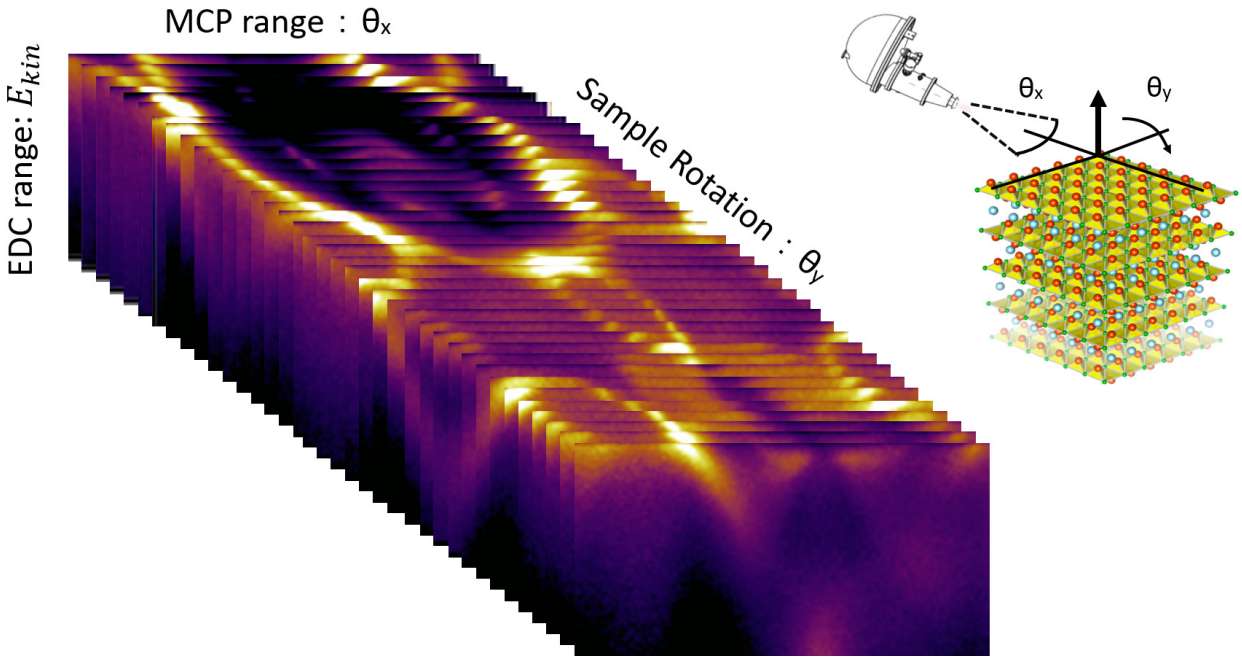

FIGURE 3.18: The construction of Cr_2AlC FS from a set of ARPES band structure snapshots is shown. The single crystal here oriented over ΓM is rotated of a given angular step multiple times and a snapshot of the BS is taken at each of these steps. Combining all these BSs gives a (E, k_x, k_y) in-plane map of the ARPES spectra, thus giving access to all the in-plane isoenergy surfaces within the experimental energy range, including the FS.

3.2.3 Limitation of ARPES

Two fundamental assertions have to be valid in order to ensure the applicability of the ARPES analysis scheme given above.

- The sudden approximation must be verified for the material studied. Its significance can be expressed by the equivalent statements: "the ejected electron escapes fast enough not to interact with the photo-hole generated within the bulk during the photoemission process" [183] or "the photoelectron must not interact with the remaining N-1 electron within the bulk" [184]. These conditions depend on the characteristic electron-electron interaction scattering time τ_{ee} and on the escape time of the photoelectron τ_{escape}, with:

$$\tau_{escape} \approx \frac{\lambda_{escape}}{\sqrt{\frac{2E_{kin}}{m}}} \tag{3.9}$$

Where λ_{escape} is the escape depth of the photoelectron. For the sudden approximation to be met, one requires $\tau_{escape} << \tau_{ee}$, which means:

$$E_{kin} >> \frac{1}{2}m(\frac{\lambda_{escape}}{\tau_{ee}})^2 \tag{3.10}$$

This condition is met for most systems that are not exhibiting strong electron-electron interactions and for $h\nu$ values that are not too low. They are certainly met in the case of most MAX phases -MAX phases are not strongly correlated materials- and for which ARPES experiments took place at energies in the 70-120 eV range. It is yet different for the case of iMAXs and 4473 mentioned above where the influence of 4f orbitals may lead to strong electron-electron interactions.

- The three-step model of photoemission allows to significantly simplify the interpretation of a set of ARPES data . It basically states that the whole photoemission process is made up of 3 distinct steps (see figure 3.19):

.1:Optical excitation of the electron inside the solid, from their initial i to their final state f, above the vacuum level (see figure 3.14).

.2:Transport of the photoelectron to the surface.

.3:Escape of the photoelectron into the vacuum.

In reality, all these steps happen simultaneously in a single step, but a one-step photoemission model would prove to be too complex to be used for a tractable ARPES analysis [180], while for most systems, the three-steps model gives a reasonable description of the whole photoemission process [179].

If both the sudden approximation and the three step model are justified for a given material, it is possible to formally derive the photoelectron intensity, following here the description given by *Damascelli et.al* for a given N electrons system [184]. Let us start by considering the Fermi golden rule that gives the probability rate of transitions from one of many N electrons initial states ψ_i^N to one of the many possible N electrons

final states ψ_f^N [180, 184, 182]

$$w_{f,i} = \frac{2\pi}{\hbar} | < \psi_f^N | H_{rad} | \psi_i^N > |^2 \delta(E_f - E_i - h\nu) \tag{3.11}$$

Where $H_{rad} = \frac{e}{mc}\mathbf{A}.\mathbf{p}$ is the hamiltonian for the dipolar electron-photon interaction (here treated as a perturbation), $\mathbf{A}$ the vector potential of the electromagnetic field, and $\mathbf{p}$ the momentum of the electron. One can then write the photoelectron intensity as [180, 184, 182]:

$$I(\mathbf{k}, E) = \sum_{f,i} w_{f,i} \tag{3.12}$$

$$I(\mathbf{k}, E) = \frac{2\pi}{\hbar} \sum_{f,i} | < \psi_f^N | H_{rad} | \psi_i^N > |^2 \delta(E_f - E_i - h\nu) \tag{3.13}$$

As the sudden approximation applies, it is possible to factorize the N electrons wavefunction final state as a product of the wavefuction of the emitted photoelectron that behaves as a plane wave in vacuum and the final state for the remaining N-1 electrons in the solid [180, 184]:

$$\psi_f^N = \mathfrak{A} \phi_f^k \psi_f^{N-1} \tag{3.14}$$

where $\mathfrak{A}$ is an antismmetry operator that ensures Pauli principle is respected by this product, $\phi_f^{\mathbf{k}}$ is the free

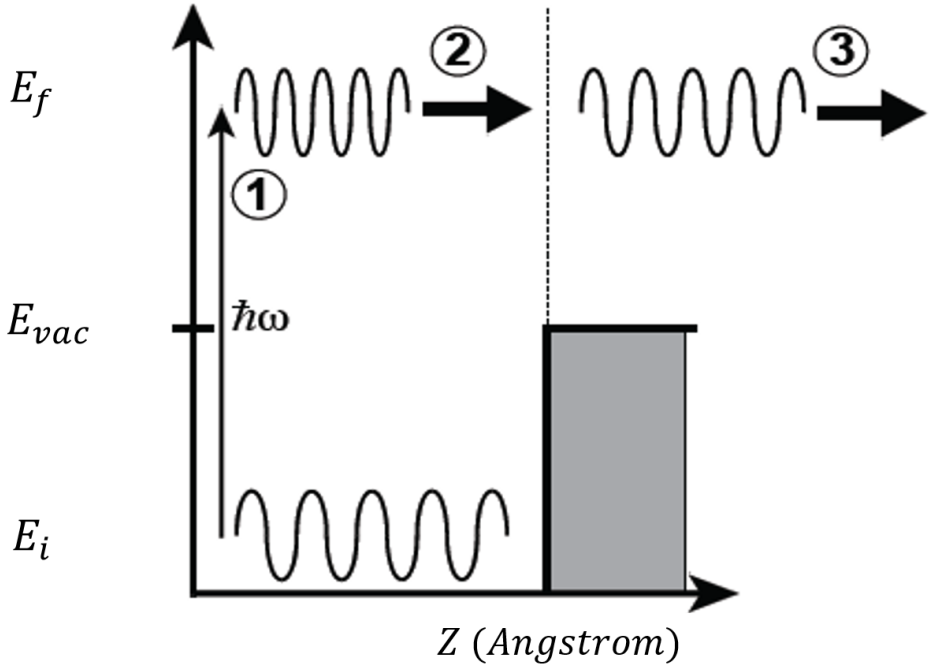

FIGURE 3.19: Outline of the three step model of photoemission, with (1) the optical excitation of the electron inside the solid, from their initial i to their final state f, (2) propagation of the final state electrons to the interface and (3) expulsion of the photoelectrons to vaccum. This figure is taken from *Damascelli et.al.* [180]

photoelectron wavefunction and ψ_f^{N-1} is the final state wavefunction for the remaining N-1 electrons in the solid. As ψ_f^{N-1} is now an excited state, it can be later decomposed within a basis of ψ_b^{N-1} eigenstates for the system with N-1 electron [180, 184]:

$$\psi_f^{N-1} = \sum_b l_b \psi_b^{N-1} \tag{3.15}$$

One also has $E_f = E_{kin} + E_b^{N-1}$ for the final state decomposition. Then, if one approximates the initial state as a slater determinant, one can now factorize ψ_i^N as the product of a single one-electron orbital state ϕ_i^k and ψ_i^{N-1} the wavefuction of the other N-1 electrons [180, 184]:

$$\psi_i^N = \mathfrak{A}\phi_i^k \psi_i^{N-1} \tag{3.16}$$

From there, one can write [180, 184]:

$$I(\mathbf{k}, E) = \frac{2\pi}{\hbar} \sum_{f,i} | < \phi_f^{\mathbf{k}} | H_{rad} | \phi_i^{\mathbf{k}} > |^2 \sum_b l_b | < \psi_b^{N-1} | \psi_i^{N-1} > |^2 \delta(E_{kin} + E_b^{N-1} - E_i - h\nu) \tag{3.17}$$

with $M_{f,i}^{\mathbf{k},E} =< \phi_f^{\mathbf{k}} | H_{rad} | \phi_i^{\mathbf{k}} >$ the one electron dipolar matrix element for the orbital state $\phi_i^{\mathbf{k}}$ and $|c_{b,i}| = \sqrt{l_b} < \psi_b^{N-1} | \psi_i^{N-1} >$

$$I(\mathbf{k}, E) = \frac{2\pi}{\hbar} \sum_{f,i} |M_{f,i}^{\mathbf{k},E}|^2 \sum_b |c_{b,i}|^2 \delta(E_{kin} + E_b^{N-1} - E_i - h\nu) \tag{3.18}$$

If one takes into account the Fermi-Dirac distribution (as only the state below the Fermi energy can be observed through photoemission) one can rewrite the photoemission intensity for all transitions:

$$I(\mathbf{k}, E) = \frac{2\pi}{\hbar} \sum_{f,i} |M_{f,i}^{\mathbf{k},E}|^2 f(E) A_{f,i}(\mathbf{k}, E) \tag{3.19}$$

Where $A_{f,i}$ is part of the one particle spectral functions that account for the deviation of the electronic structure from the independant particle picture [179, 183] . Removing one electron from a strongly correlated system may have a non-negligible effect on its band structure. Despite its complexity, a simplified read of the spectral function can be given as follows: If one deals with a system where electronic correlation are not too large, the $A_{f,i}$ will be the Dirac distributions that follow the band dispersions of the various initial states, thus giving back nearly discrete bands when sweeping over k-space. If not, the $A_{f,i}$ will be functions that spread in energy and momentum, imposing an intrinsic broadening of the bands from the final states. In that case, the observed ARPES spectra can be seen as a renormalization of the initial state band structure. For the simpler case of a one sole initial state band, the one electron spectral function holds the information

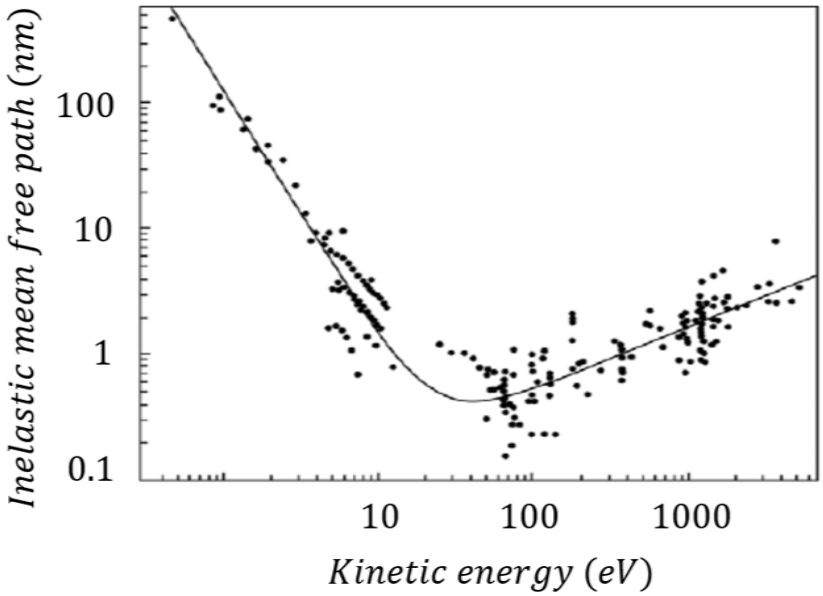

FIGURE 3.20: Kinetic energy dependence of the 'universal' MFP for excited electrons in solids, from [191]

regarding interactions in presence . According to Green's function formalism, it can be written as [184, 188] :

$$A(\mathbf{k}, E) = -\frac{1}{\pi} \frac{\sum''(\mathbf{k}, E)}{[E - \epsilon(k) - \sum']^2 + [\sum''(\mathbf{k}, E)]^2} \tag{3.20}$$

So, if no other effect such as k_z broadening (described in chapter 5 and 7) is present, the FWHM of an EDC of the ARPES spectra gives $\sum''(\mathbf{k}, E)$, the imaginary part of the self energy, which is an image of the interaction at a given $(E, \mathbf{k})$ coordinate [184, 187, 189, 190]. We will make use of this formula when deciphering the influence of electron-phonon coupling on Cr_2AlC spectrum in chapter 4.

The matrix elements $M^{\mathbf{k}}_{f,i}$ will be very important for the various MAX phase photoemission studies described here. They contain the effect of polarization on ARPES experiments and the local orbital information [182]. They also dictate in-plane momentum conservation and out-of-plane k_z broadening [182, 187]. Within chapters 4, 5 and 7, we will rather focus on a quantity derived from these: the photoemission cross section, which encompasses most of the orbital effect to be observed within ARPES spectra.

Another crucial parameter to take into account is the photoelectron mean free path (MFP). The larger it gets, the more photoelectron are extracted from the bulk to vacuum, thus ensuring the obtained ARPES mappings correspond to the electronic structure of the bulk solid. Having a smaller MFP means that the contribution of potential surface states will be more important to the ARPES spectra.

The so-called 'universal curve' [179, 191] describes the dependence of the MFP on the energy of the source $h\nu$. It is given in figure 3.20. A minimum is located in the 70-120 eV range, precisely where the ARPES experiment described within this manuscript took place. It makes for a mean free path of about 1 nm, roughly one 211 MAX phase unit cell, thus a non-negligible surface contribution. The effects described

here as well as the complexity of an ARPES data analysis to be performed and interpreted emphasize the importance of pairing this experimental technique with band structure calculations [181, 179, 183]. Among *ab initio* calculation techniques, Density Functional theory frameworks have been widely used over the past 30 years and it is the class of calculation that was performed in order to understand in greater detail the ARPES spectra of MAX phases.

3.3 Density functional theory

As mentioned earlier, one of the pillars of materials science and condensed matter physics is the many body problem of electrons in a solid (2.8), and with it comes the understanding of the many features of interacting electrons and nuclei as well as the emergent phenomena arising from such interactions [40, 192]. Over the past 50 years, the constant increase in performance and availability of computer workstations and clusters have rendered the resolution of complex and intricate physical problems such as (2.8) possible for many systems . Calculations that required the most powerful cluster in the 1980s can now be performed routinely from almost any location. However, technological advances were not the only requirements to render the solvability of systems made of a large number of atoms numerically accessible. The constant development of quantum mechanical methods for simplifying and diagonalizing the many body Hamiltonian of solid state physics was also central to these advances . Among the first and foremost important computational methods were the self consistent Hartree-Fock (HF) methods based on the Hartree Fock Hamiltonian [193, 194, 195]. It was formulated to take into account correlations from Pauli's exclusion principle, starting from antisymmetric N electrons wavefunction constructed with Slater determinant of individual orbitals [196]. The HF Hamiltonian can be read as:

$$H_{HF} = [-\frac{1}{2}\nabla^2 + V_{ext}(r) + V_{hartree}(r) - V_X(r)] \tag{3.21}$$

With V_{ext} the nuclei lattice coulomb potential, $V_{hartree}$ the coulombian electron interaction potential and V_X the exchange potential describing electron-electron interaction arising when taking into account the Pauli exclusion principle. Despite its success in capturing the essential features of elementary metals [197], semiconductors [198, 199] and more complex materials [200, 201], and thus leading to the determination of their electronic structure, charge densities and more, pure HF methods remain scarcely used in modern computational physics for material science. The strongest argument against them is purely practical as the computation times they require are extremely high compared to other available *ab initio* techniques (from 1000 times slower). Another argument is that HF methods cannot fully portray electronic correlations [192].

Density Functional Theory (DFT) -whose most famed contributors are Kohn, Sham and Hohenberg - stands as one of the direct successors to HF methods. DFT is currently among the most widely used computational

method in solid state physics, chemistry and material science. More than 12000 DFT studies were published in scientific journal as of 2016 [202]. Furthermore, the total number of DFT publications was at this time found to double every 5-6 years since 2000. It is a powerful self-consistent method for constructing and solving an approximate many body Hamiltonian that captures surprisingly well the essential characteristics of an extremely large number of systems, from bulk solids to interface, bidimensional systems and molecules [192]. DFT is routinely used to calculate various properties such as density of states, band structure, Fermi surface, Phonon structure, phase stability, magnetic ordering, optical properties and more [192]. We will now succinctly review the fundamental principles of Density Functional Theory as well as its shortcomings before describing the specificity of the DFT code used to numerically determine MAX phases electronic structure: WIEN2K.

3.3.1 Fundamentals of DFT

Density Functional Theory is grounded on one fundamental theorem from Hohenberg and Kohn. It states two propositions [203]:
-The total energy of a system of many electrons in an external potential (in our case the Couloumbian potentials from the nuclei) is given as an exact functional of the ground state electron density ρ:

$$E = E[\rho] \tag{3.22}$$

-The ground state of the system is given by the ground state density that corresponds to an absolute minimum of the functional above. All other ground state properties will be directly related to the electron density that minimizes E.

The Hohenberg-Kohn theorem does not provide any clue as to the expression of the energy functional for the electron density. Therefore, the effeciency of DFT relies on the approximation taken to build an efficient energy functional [204]. The unknown E is written as a sum of terms which includes the kinetic energy functional T_s for the many body electron density, the Coulomb interaction between electrons and nuclei E_{ei}, the nuclei nuclei interaction E_{ii} (A term generally ignored for basic calculations) and a Hartree term E_H that stands for the coulombian part of the electron-electron interaction :

$$E[\rho] = T_s[\rho] + E_{ei}[\rho] + E_H[\rho] + E_{ii}[\rho] + E_{xc}[\rho] \tag{3.23}$$

Another unknown functional E_{xc} is added and represents the non-coulombian, non-local and many body electron-electron interaction contribution. E_{xc} is labelled as the exchange-correlation functional. Contrary to this functional, the Hartree functional dependance to the electron density is well known:

$$E_H[\rho] = \frac{e^2}{2} \int \frac{\rho(\mathbf{r})\rho(\mathbf{r}')}{|r - r'|} d^3\mathbf{r} d^3\mathbf{r}' \tag{3.24}$$

Several approximations exist for the exchange and correlation functional [205]. The simplest one is the LDA (local density approximation) which gives:

$$E_{xc}[\rho] = \int \rho(\mathbf{r})\epsilon_{xc}(\rho(\mathbf{r}))d^3\mathbf{r} \tag{3.25}$$

where ϵ_{xc} is taken here as a sole function of the local charge density. The most elementary LDA functionals take the HF energy for a uniform electron gas as ϵ_{xc} [206]. Today's most commonly used approximation for the exchange-correlation functional is the general gradient approximation (GGA). One then has a dependency of ϵ_{xc} on the gradient of the density, loosening a part of the "local" character of LDA:

$$\epsilon_{xc} = \epsilon_{xc}(\rho(\mathbf{r}), \boldsymbol{\Delta}\rho(\mathbf{r})) \tag{3.26}$$

There are several GGA functional which are widely used throughout the literature of DFT studies of materials, such as Perdew–Burke–Ernzerhof (PBE) [207] or Wu Cohen GGA's [208]. More advanced functionals such as meta GGA's or hybrid functional that include a HF exchange-correlation term are also used (a popular one being HSE06), but they will not be mentioned further within this manuscript.

From the minimization of the functional (3.23), and writing the many body electron density as a sum over occupied orbitals, one obtains the following set of equation known as Kohn-Sham (KS) equations [209]:

$$H_{KS}\varphi_i(r) = [T + V_{ei}(r) + V_H(r) + V_{xc}(r)]\varphi_i(r) = \epsilon_i\varphi_i(r) \tag{3.27}$$

where the potential depend on the electronic density, and with the density taken as a sum over occupied orbitals:

$$\rho(r) = \sum_{occ.states.} \varphi_i^*(r)\varphi_i(r) \tag{3.28}$$

The trick here is that this set of independant equations stands for one hamiltonian whose eigenvectors are called the Kohn-Sham (KS) orbitals. They are not the eigenvalues of the real hamiltonian of the system but are another set of functions that give the ground state electron density $\rho(r)$ that minimizes the energy functional of the system through (3.22). Here T is the kinetic energy operator, V_H the Hartree potential and V_{xc} the exchange and correlation potential. These last two are given as:

$$V_H(r) = e^2 \int \frac{\rho(\mathbf{r}')}{|r - r'|} d^3\mathbf{r}' \tag{3.29}$$

$$V_{xc}(r) = \frac{\delta E_{xc}[\rho]}{\delta\rho(r)} \tag{3.30}$$

Rather than having a complex functional minimization to deal with with, the problem becomes significantly simpler as one only has to diagonalize a set of Schrodinger-like equations. From Bloch theorem, and as the charge density follows the periodicity of the lattice, one can demonstrate [210] that one only needs to solve the system (3.27) within a restricted fraction of the Brillouin zone called the irreducible Brillouin zone (IBZ).

An important step before solving (3.27) is the choice of a basis set $(\eta_{i,\alpha})$ for the diagonalization:

$$\varphi_i(r) = \sum_{\alpha} c_{i,\alpha}(\eta_\alpha) \tag{3.31}$$

There are several possible bases one can take for the decomposition of KS orbitals [210], such as a plane wave basis, the Linear Augmented Planewaves (LAPW) basis or the APW+LO's described in more detail in section 3.3.3. Each of them has its own advantages and shortcoomings. Various DFT codes are based on different basis sets.

Then, defining the overlap matrix $\mathbf{S}$ in the chosen basis set, one gets the equation to solve for the KS hamiltonian $\mathbf{H_{KS}}$ [210]:

$$(\mathbf{H_{KS}} - \epsilon_i \mathbf{S})\mathbf{c_i} = 0 \tag{3.32}$$

This equation is then solved for each k-point of the IBZ and from the $\mathbf{c_i}$, one can get the KS orbitals φ_i and then the electron density from equation (3.28). The Kohn-Sham orbitals have to be summed up to the last occupied state. For this, one need to determine the Fermi energy of the system. It can be done numerically for a calculation at 0K by considering that the integrations of all the bands up to E_F must be equal to the total number of electrons [210].

To ensure the obtained density is actually a minimum of the approximate functional defined by (3.23) , a self consistency cycle has to be set [192]. It is given in figure 3.20 and it outlines as follow:

Before the DFT cycle is being launched, a number of initial parameters are set such as the density of k-points chosen within the IBZ, the exchange-correlation functional to be used (for most cases, GGA PBE) and more. The input of the DFT cycle is essentially an electron density, from which all the potential terms of KS equations are computed. The secular equation is then solved for all the k points within the IBZ and the KS orbitals are computed. After that, one compute the Fermi Energy. Finally, one calculates the new electron density from the KS orbitals as well as the total energy for the nth loop of the SCF cycle. Then, if the ΔE difference between the energies at the nth and for the previous cycle is smaller than a fixed value ϵ (typically of the order of 0.1 to 0.01 meV), the calculation is stopped and all the DFT calculations parameters are saved. If convergence is not met, a mixture of the n^{th} and the previous density is taken as a new input electron density for the next cycle.

Following Rayleigh-Ritz variational principle, the DFT self-consistency cycle, also referred to as self consistency field (SCF) allows one to recover the ground state electron density as well as the corresponding

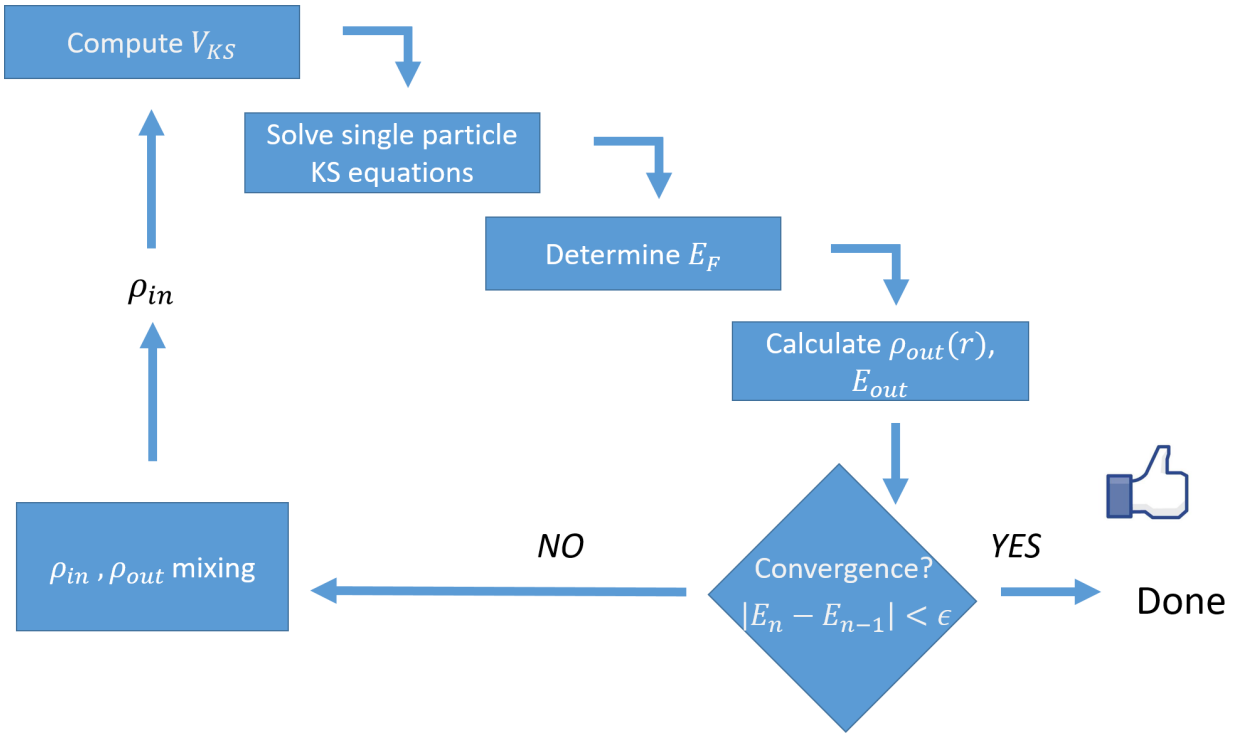

FIGURE 3.21: All the main steps of DFT calculation cycles, with the first input for the electron density generally extracted from a .cif or a structure file containing atomic position within the unit cell of the material to be studied. Typical levels of energy convergence we choose are in the 0.1-0.01 eV range

energy and Kohn-sham Hamiltonian and orbitals, all along with many other observables which include the 'KS band structures' given by the **k** dependence of the eigenvalues of $\mathbf{H_{KS}}$.

3.3.2 Shortcomings of DFT calculations

An absolute numerical method that would perfectly model any physical phenomenon does not exist and of course DFT calculations do not escape this rule. They indeed harbor intrinsic limits and a few are outlined below :

-Hohenberg-Kohn theorem states that the electron density which minimizes the energy functional is the ground state density of the system. Yet it is important to state that the densities obtained by practical DFT calculations are not exact as the real functional to which Hohenberg-Kohn theorem applies is not known [204]. Furthermore, it gives no guarantee that excited states further away from the Hohenberg-Kohm ground state shall be correct. It is of great importance for semi-conductors, where the bands above E_F do not enter within the sum that gives the ground state electron density in the SCF calculations. Thus, the position of these excited states in energy and their morphology in k-space are not necessarily correct. As a matter of fact, one of the most spectacular failure of standard DFT comes with semiconductors and insulators. LDA predicts most semiconductors bandgaps to be 40 percent smaller than their real values [211]. For example ZnO bandgaps

calculated by LDA and GGA DFT fall in a range of 0.23-2.26 eV while ZnO experimental bandgap is equal to roughly 3.3 eV [212]. The difference between experimental bandgaps and DFT will strongly depends on the choice of the exchange correlation functional. One should also note that as excited states are not necessarily well modelled by standard DFT methods, the same problem should arise when modelling optical properties of semiconductors. Many advanced exchange correlations functionals or even advanced DFT based methods such as time dependant DFT [213] or even the more sophisticated DFT+GW [214, 215] lead to significant improvements when dealing with the modelling of excited states as well as more complex phenomena.

-The KS orbitals and the dispersions of their respective eigenvalues are the bands featured on the plots of DFT band structures. But the KS orbitals are not the true eigenstate of the system and thus, similarly to what is mentioned above, there is no formal guarantee that the obtained DFT bands will match the real electronic structure as one goes away from the Fermi level, either below or above [192, 204]. Yet, DFT calculations have shown great successes in modelling the valence and conduction bands of many metals [204, 210].

- Strong and localized correlations from localized f or in some cases d states are often beyond the scope of standard DFT calculations [216]. Rare earth based compounds and transition metal Mott insulators typically fall into that category and the nature of interactions in these system is totally different from the homogenous electron gas like behaviour upon which LDA or GGA DFT are based [204]. To rigorously circumvent such shortcomings, one needs to go one level of abstraction ahead of DFT with Density Mean Field Theory calculations [217], though these calculations are significantly more complex and impose very high calculations times. A more pragmatical approach, though less "physically accurate", is to incorporate on site correlation within DFT calculations. One adds an Hubbard like on site repulsion term [218] to the KS Hamiltonian:

$$E_U = \frac{U}{2} \sum_{i \neq j} n_i n_j \tag{3.33}$$

Where the $i = (l, m_l)$, $j = (l^{'}, m_l^{'})$ are the orbital and magnetic quantum numbers for the relevant atomic shells (here, we only consider the non spin polarized expression of U) and n_i the relevant orbital occupations. Therefore, U potential will be orbital dependent and will only affect a relevant set of orbitals chosen by the user of the DFT code. The value of U is also a parameter to be set by the user. This method is called DFT+U and it has allowed to obtain good approximations of the correct ground states of many correlated systems [218, 219]. It must be noted that the U value may or may not hold a signification for a given material. The choice of U is left to the judgement of the user. Adding an unphysically too large U will favor an unphysical insulating state over a metallic one for some moderately correlated metallic system [210], while standard GGA would give a more accurate ground state. One of the biggest drawback of DFT+U is that the choice of U which would give a better fit between experiment and theory may very well be empirical and

deviate from any physical considerations .

- DFT can effectively cope with magnetism and resolve ferromagnetic, antiferromagnetic or even ground states featuring non collinear magnetism [192]. These calculations go beyond the scope of this manuscript as merely no magnetic DFT calculations are presented within the upcoming chapters.

-Standard DFT calculations are performed for T=0K and more advanced technics [192, 213] allow to take into account the influence of temperature on the ground state.

3.3.3 WIEN2K, APW+lo and applications to MAX phase electronic structure

WIEN2K is a DFT code as well as a plateform to compute various observables from the outputs of calculations [220]. It was developped in Vienna by the group of *Peter Blaha*, and software license is available for purchase and can be used for either academic or industrial use [220, 221, 222]. There are several other similar DFT plateforms available, such as VASP , quantum espresso or Abinit. WIEN2k is the code that was used to obtain all the theoretical results on MAX phase described within this manuscript -Band structures, Fermi surfaces, charge transfers and so on- so its basic structure deserves to be outlined. We will overly simplistically describe it, in order not to delve too far from the main scope of this work.

What differentiates WIEN2k from other available softwares is its basis for the KS orbital decomposition: the Augmented Plane Waves (APW) + Local Orbitals (lo) [223]. Another of its specificities is that, contrary to VASP and other codes [224], the KS potentials in WIEN2k are fully computed at all SCF cycles, thus being referred to as a full potential code. WIEN2k is also an all electron code, which means that all electrons, from the $1s$ to the last occupied orbitals, are considered within the calculations. Other codes may include the influence of inner electron shell within an effective pseudopotential [225].

The electron density ρ, the KS potential $v^{KS} == v_{ei}(\mathbf{r}) + v_H(\mathbf{r}) + v_{xc}(\mathbf{r})$ as well as the basis set onto which KS orbitals are decomposed are all defined within two different areas [210]: The atomic spheres (S_i), where i is an index for different atoms of atomic numbers Z_i, and the interstitial area I between them. These two zones are sketched in figure 3.21 for 3 different atoms in one unit cell. The spheres of radius R_{MT} vary depending on the atomic number Z_i. The choice of R_{MT} values is left to the user, though some standard values are recommanded by WIEN2K.

The electron density and KS potential are defined differently within these two domains, though continuity conditions are set at the frontier between I and $\cup_i S_i$ [222]:

$$\rho(\mathbf{r}) = \left\{ \begin{array}{ll} \sum_{S_i,L,M} \rho_{S_i,L,M}(\mathbf{r}) Z_{S_i,L,M}(\mathbf{r}) & , \mathbf{r} \in \cup S_i \\ \sum_{\mathbf{K}} \rho_{\mathbf{K}} e^{i\mathbf{K}.\mathbf{r}} & , \mathbf{r} \in I \end{array} \right\} \tag{3.34}$$

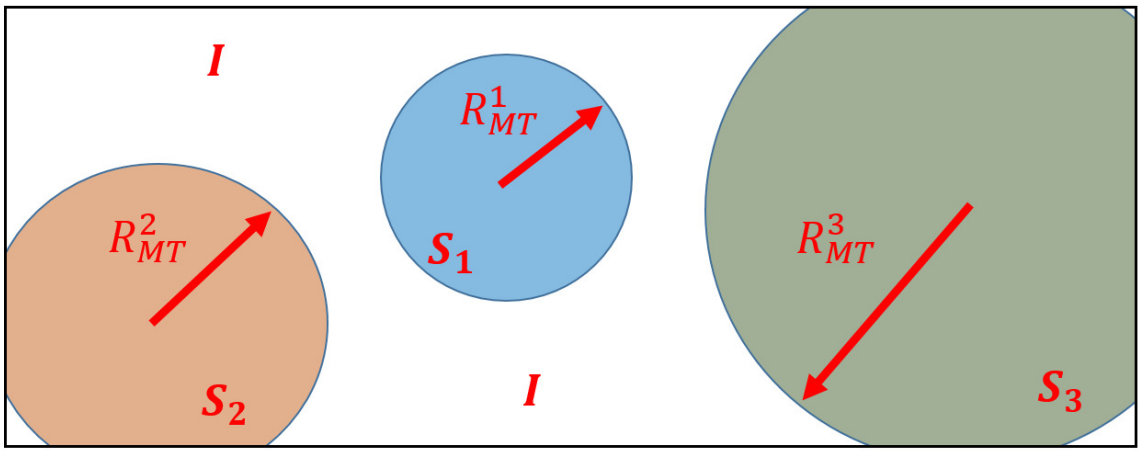

FIGURE 3.22: Example of three different atomic region S_1, S_2 and S_3 respectively corresponding of atoms of increasing atomic numbers Z_1, Z_2 and Z_3. The interstitial I region where APWs are defined as planewave decomposition stands between all the atomic spheres.

$$v^{KS}(\mathbf{r}) = \left\{ \begin{array}{ll} \sum_{S_i,L,M} v^{KS}_{S_i,L,M}(\mathbf{r}) Z_{S_i,L,M}(\mathbf{r}) & , \mathbf{r} \in \cup S_i \\ \sum_{\mathbf{K}} v^{KS}_{\mathbf{K}} e^{i\mathbf{K}.\mathbf{r}} & , \mathbf{r} \in I \end{array} \right\} \tag{3.35}$$

Within the spheres, ρ and v^{KS} are decomposed within the lattice harmonics basis $Z_{S_i,L,M}$ (a combination of adapted spherical harmonics) times radial components $\rho_{S_i,L,M}$ and $v_{S_i,L,M}$. Outside the spheres, in the interstital region, they are expanded as Fourier series in reciprocal space, $\mathbf{K}$ being a reciprocal space vector.

This decomposition of the potential and density comes very handy knowing that the APW basis elements $\phi^{APW}_{\mathbf{k}+\mathbf{K}}$ will also be defined within the two domains defined above [222] :

$$\phi^{APW}_{\mathbf{k}+\mathbf{K}}(\mathbf{r}) = \left\{ \begin{array}{ll} \sum_{l,m} B^{\mathbf{k}+\mathbf{K}}_{S_i,l,m} u_{S_i,l}(\mathbf{r}, E_{S_i,l}) Y_{l,m}(\mathbf{r}) & , \mathbf{r} \in S_i \\ \frac{1}{\sqrt{\Omega}} e^{i(\mathbf{k}+\mathbf{K}).\mathbf{r}} & , \mathbf{r} \in I \end{array} \right\} \tag{3.36}$$

Whew $\mathbf{k}$ lies within the first BZ, $u_{S_i,l}$ are radial atomic functions of energies $E_{S_i,l}$ and $Y_{l,m}$ spherical harmonics. $B_{S_i,l,m}$ coefficients are chosen in so as to have a continous matching between the interstitial and atomic part of $\phi^{APW}_{\mathbf{k}+\mathbf{K}}$ at the boundary. The obvious advantage of this basis set is that it follows simultaneaously a free electron like behaviour in the interstitial region as well as an orbital,"tight-binding like" behaviour in the atomic sphere region, which makes them more adaptative than other basis sets [210, 222]. Yet they show a significant drawback that renders them unpractible for DFT calculations if used on their own. The $E_{S_i,l}$ energies do not depend on k-points coordinate that should vary as one sweep accros the band, thus the atomic part of the APW lacks the variational freedom to modify the atomic part of the wavefunction as E evolves during the SCF cycle. It is also impossible to get the energy bands from a single calculation as their radial decompositions are fixed in energy.

To overcome this difficulties, local orbitals called lo's are added to the APW basis [222, 223]:

$$\phi^{lo}_{S_i,l,m}(\mathbf{r}) = \left\{ \begin{array}{ll} [B^{lo}_{S_i,l,m} u_{S_i,l}(\mathbf{r}, E_{S_i,l}) + C^{lo}_{S_i,l,m} \dot{u}_{S_i,l}(\mathbf{r}, E_{S_i,l}] Y_{l,m}(\mathbf{r}) & , \mathbf{r} \in S_i \\ 0 & , \mathbf{r} \in I \end{array} \right\} \tag{3.37}$$

The term $\dot{u}_{S_i,l}(\mathbf{r}, E_{S_i,l}]$ is a first energy derivative of a radial function, and it allows the eigenvalues to evolve within a continuum of energy values different than the discrete $E_{S_i,l}$'s.

The combination of APWs and lo's permits to significantly reduce the number of basis elements compared to other basis sets previously used with WIEN2k. The number of cycle needed before reaching convergence is then reduced [222].

APW+lo are yet not efficient at treating semi core states, i.e. states of intermediate energies that are not completely localized on an atomic site [222]. To circumvent this issue, other local orbitals called LO, $\phi^{LO}_{S_i,l,m}$ are added to the APW+lo basis set:

$$\phi^{LO}_{S_i,l,m}(\mathbf{r}) = \left\{ \begin{array}{ll} [B^{LO}_{S_i,l,m} u_{S_i,l}(\mathbf{r}, E_{S_i,l}) + C^{LO}_{S_i,l,m} u_{S_i,l}(\mathbf{r}, E_{S_i,l})^{LO}] Y_{l,m}(\mathbf{r}) & , \mathbf{r} \in S_i \\ 0 & , \mathbf{r} \in I \end{array} \right\} \tag{3.38}$$

Basic WIEN2k routines fix automatically the $E_{Si,l}$ values before combining APW+lo's to build the KS orbital decomposition.

The basic input of a WIEN2k is a structure file, typically generated from a .cif file,i.e. a file that contains the atomic positions of each atom within the unit cell of the material for which the ground state will be computed. It allows to set the input density for the first SCF cycle through a program called -initlapw.

The WIEN2k SCF cycle consists of a complex workflow build up from different programs. The main steps are outlined as follows [222]:

-*lapw0*: Computes the Hartree and exchange correlation potential from the density.

- *lapw1*: Diagonalizes the KS hamoltonian to obtain the valence and semi-core eigenvalues and eigenvectors at all requested k-points

-*lapw2*: Calculates the Fermi energy and the valence electron density

- *lcore*: Calculates the core levels eigenvalues and the core electron density

- *mixer*: Adds up the core and valence densities, compute the total energy and later mixes the total density with densities from previous iterations.

Convergence critera can be set on the total energy, but also on the charge or other quantities. Convergence in atomic position, force minimization and structure relaxation can also be performed in parrallel to the SCF cycle but these aspects will not be discussed within this manuscript.

Additional steps can be added to the SCF of WIEN2k if one performs a DFT+U calculation or if one takes spin orbit coupling into account.

Band Structures and Fermi surfaces are calculated from the KS Hamiltonian after the DFT convergence is reached. A klist file, or set of k-point coordinates corresponding either to a line cut through the BZ for a band structure or to a mesh of the IBZ for fermi surface plot, is generated prior to the calculation. Then from the final KS hamiltonian, one performs once again lapw1 and lapw2. A program labelled as Spaghetti generates the band structure file as a readable .text file ready for a plot. FSs 3D plots are generated through a complex program called Xcrysden, which will not be detailled further within this chapter.

Particular operations, parameters and other details related to each specific MAX phase are specified whenever necessary in all upcoming chapters.

The last point to be briefly discussed in this section is the treatment of spin orbit coupling in WIEN2k.

Spin orbit coupling (SOC) is expressed as a coupling between the electrostatic field and the spin of the electrons [142]:

$$H_{SO} = \frac{1}{2m_0c}(\nabla V(r) \times \mathbf{p}).\mathbf{S} \tag{3.39}$$

where $\mathbf{p}$ is the momentum operator for the electron, V is the overall electronic potential and $\mathbf{S} = (\frac{\hbar}{2})\boldsymbol{\sigma}$ the spin operator.

But this term is actually among the firsts of a serie expansion of the Dirac Hamiltonian. As a reminding note, the Dirac equation is the relativistic version of Schrodinger equation for the electron [226]. Its solutions are not wavefuctions but 2 dimensional spinors [227]. It is possible to set up a DFT scheme based on Dirac equation to take into account spin orbit coupling or other relativistic effects that may become of importance for heavy elements and for specific materials. In this "Dirac DFT" calculation scheme [210, 222], one consider that the Dirac equation holds within the atomic spheres S_i, while relativistic effects are ignored in the interstitial region [222].

From there, we have an eigenvalue problem for which all relativistic terms are included within the main Kohn-sham potential of a DFT scheme without altering much the overall procedures [222]. These terms are taken into account for core states calculations [222].

The spin orbit term, on the other hand, will be treated differently, as it leads to a lift of degeneracy of the two components of the spinor, the up and down spin states.

For a set of n KS eigenvectors without SOC, one has to resolve a $n \times n$ matricial secular equation . Adding spin orbit coupling for each of the orbitals leads to a degeneracy lifting and one obtains a $2n \times 2n$ secular equation for which computation time is significantly increased [210]. In WIEN2k, the program that deals with SOC is *lapwso*. It only sets SOC for shells defined by the code user ($3d$ for the case of "simple" MAX phases). After a first non relativistic diagonalization *lapw1*, another diagonalization is launched , but with a larger matrix where relativistic orbitals (relativistic version of the Kohn-sham orbital) and SOC hamiltonian terms are only considered for the shell of interest. One doubles the number of matrix elements only for a

subpart of the secular Hamiltonian and the computation time is not critcally altered. After this step, the relativistic eigenfunctions are reexpanded within APW+lo basis and the SCF cycle moves forward.

We so far described all the method we employed to get an insight into MAX phase electronic structure. High temperature solution growth is used to synthetize MAX phase single crystals, Angle resolved spectrosopy to determine their electronic spectra in $(E, \mathbf{k})$ space and finally DFT calculations performed with WIEN2k code to numerically resolve MAX phase electronic ground states and compute their band structures and Fermi surfaces. Each of the next chapters will be devoted to one of the main scientific outputs of this work regarding MAX phase electronic structure.

Chapter 4

Cr_2AlC: Electronic states and magneto-transport

This chapter treats solely of Cr_2AlC and is highly inspired by the following references [228, 229]. The author of this thesis made significant contributions to these two articles.
Cr_2AlC is quite a peculiar case among 211 MAX phases. It exhibits a substantially higher resistivity than most other phases [159], and even more surprisingly, it follows a magnetotransport scaling law [154], which is in general observed in highly correlated electron systems such as high T_c cuprates [230] and pnictides in their normal state [231] or heavy Fermion compounds [232].

In order to decipher such a behaviour, it is needed to get an insight on the BS and FS of this phase, if possible from both experiments and calculations. Additionally, one needs to confirm that the strong transport anisotropy measured from Cr_2AlC single crystals are consistent with its electronic structure.

There has been a certain level of controversy over the nature of Cr_2AlC ground state. While it has been predicted to be antiferromagnetic (AFM) at low temperature [233, 234], other studies suggest that it would remain paramagnetic [234, 235]. No clear experimental confirmation of an AFM transition has been given yet, but it was hinted that a magnetic transition takes place at 73.5 K [236].

From trial experiments at the High magnetic field laboratory in Grenoble, it appears that available Cr_2AlC single crystals do not exhibit *de Haas–van Alphen* or *Shubnikov–de Haas* oscillations at magnetic fields below 12 T and at low temperature. Therefore, ARPES remains the only method available for the experimental assessment of the band structure and the FS.

As in some previous work [182, 237, 238] "matrix element effect" or photoionization cross sections effect allows us to confirm the local orbital character of the observable bands close to the Fermi level, as predicted by DFT calculations. We also measure a quasi-2D dispersion for both hole and electron bands, and prove that the electronic states close to the Fermi level are dominated by the d-orbital contribution of the transition-metal atoms, as predicted for all MAX phases.

There is a remarkable agreement between the ARPES data and calculations. However, some discrepancies

are found with the presence of an additional FS tube appearing around Γ and some band renormalization effects for other bands. Physical effects that possibly lead to these discrepancies are briefly described.

Another surprising result is how well spinless GGA reproduce the experimental bands, without taking into account any antiferromagnetic ordering (depsite controvesies over the magnetic nature of the Cr_2AlC ground state). Neutron diffraction experiments performed on Cr_2AlC powders did not give clear signs of antiferromagnetic transition.

Finally we show that a realistic analytic approximation of the DFT Fermi surface allows one to recover the main features of the in-plane magnetotransport (temperature variations of the Hall coefficient, in-plane resistivity and magnetoresistance). The temperature variations of electric transport coefficients are explained by the combined contribution of electron and hole bands, taking into account the local curvature of the FS and an appropriate temperature variation of the relaxation times for each band.

4.1 Specificity of Cr_2AlC analysis

4.1.1 Experimental details and computational outputs

Single crystals of Cr_2AlC were prepared by high temperature solution growth following the procedure detailed in chapter 3. The growth process involves a slow cooling step, allowing us to reduce the number of growing crystals in the solution by Ostwald ripening. Typical Cr_2AlC platelets have an area of several square centimeters and a thickness around 1 mm. They were cut with a diamond wire saw and cleaved in the form of parallelepipeds with an area of 3 × 3mm and a thickness around 500µm. Samples were then cleaved again in situ for the ARPES experiments, which were carried out either at the UVSOR or Aichi lines in ultrahigh vacuum and at temperatures around 8 K. Photon energy was ranging from 50 to 100 eV. Linearly polarized x-ray light was used for the two setup configurations described in figure 4.1, which we defined as the S-pol mode [figure 4.1a] or the P-pol mode [figure 4.1b], respectively. All angles and axes are described in Fig. 4.1. The angle between the light beam and the detector was set to 45°. The polarization vector was lying in the horizontal plane(defined in figure 4.1).

All calculations were performed with the full potential LAPW+lo method implemented within WIEN2K and described in section 3.3.3. The nonpolarized PBE GGA functional was chosen. The *RKM* cutoff parameter -the product of the smallest atomic radius within the unit cell with the maximum K value taken for the calculation- is fixed at 7.5. For computation, we took the standard Cr_2AlC hexagonal unit cell from [239] containing eight atoms for computation . It is the standard 211 MAX phase unit cell described in chapter 2 (figure 2.1), for M=Cr and A=Al. The integration of the BZ was performed with a very dense k-mesh. Following the Monkhorst-pack scheme, we took a 73 × 73 × 14 mesh for the IBZ. The Fermi surfaces were plotted using XCRYSDEN [240]. The choice of a very dense k-mesh is justified by the disappearance of artefacts on the Fermi surface that arise when using a high number of points. Only a linear interpolation was

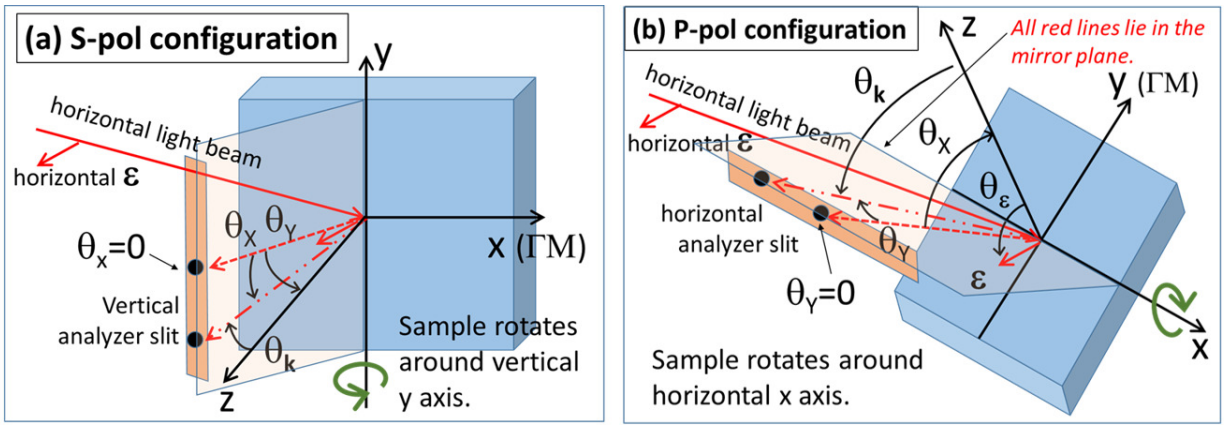

FIGURE 4.1: (a) Schematics of the ARPES experimental setup configuration in the S-pol mode and (b) configuration in the P-pol mode. In both configurations the light beam and polarization stay horizontal, and the x, y, and z axis are attached to the sample; z is always normal to the sample. In (a) the y axis stays vertical and the sample is rotated around it, so that the x and z axis move with respect to the light beam and the detector slit. The detector slit is vertical. θ_y is the angle between the line defined by the emitted electron beam detected in the middle of the detector slit and the z axis. θ_x is the angle between the same line and an electron beam line detected in another, given part of the slit. In (b) the sample is rotated around the x axis so that both the y and z axis move with respect to the light beam and slit. The detector slit is horizontal. θ_x is now describing the sample rotation and θ_y the angle between the mid-position line and an arbitrary one in the detector slit. θ_k is the angle between the emitted electron beam and the normal to the sample (z axis).

needed to get the FS plots in figure 4.3. Orbital characters of the bands were obtained with the spaghetti PRIMA code.

Cr_2AlC BS has already been studied in [241], and the band structure is predicted to form electron bands centered around Γ and smaller hole pockets centered at the M points. The FS was not computed in [241]. Repeating those calculations leads us to very similar results (figure 4.2). A difference with the treatment expounded in [241] is that we chose a much denser k-mesh in order to improve the definition of the band structure (figure 4.2) and compute the FSs (figure 4.3).

Cr_2AlC is predicted to be quasi two dimensional, as shown in figure 4.3, where all FSs' form open, bulged tubes along k_z (k_z is parallel to c). Due to the presence of the Cr atoms, magnetic properties could be expected and are indeed predicted in a previous work [233], which showed that an antiferromagnetic (AF) state with magnetic vector (1/2,0,0) exhibits a slightly lower energy than the nonmagnetic configuration. Even though our own calculations do not take magnetic interactions into account, their comparison with the ARPES data of section 4.2.1 show that neglecting magnetism does not preclude a first-order, acceptable fit of the experimental ARPES data. Also, as highlighted in section 4.2.2, our neutron diffraction data do not allow to state whether a magnetic transition indeed occurs at low temperature.

A qualitative analysis of the orbital character of each band is given by the colored plots of the band structure in figure 4.2. At the Fermi level E_F and in the Γ plane (i.e., $k_z = 0$), the hole pockets are dominated by a d_{z^2} character in the FS parts crossing the major axis of the ellipsoidal FS shape (see figure 4.2), and a $d_{xz} + d_{yz}$ character prevails in the parts crossing the minor axis. The situation is a bit more complex for the

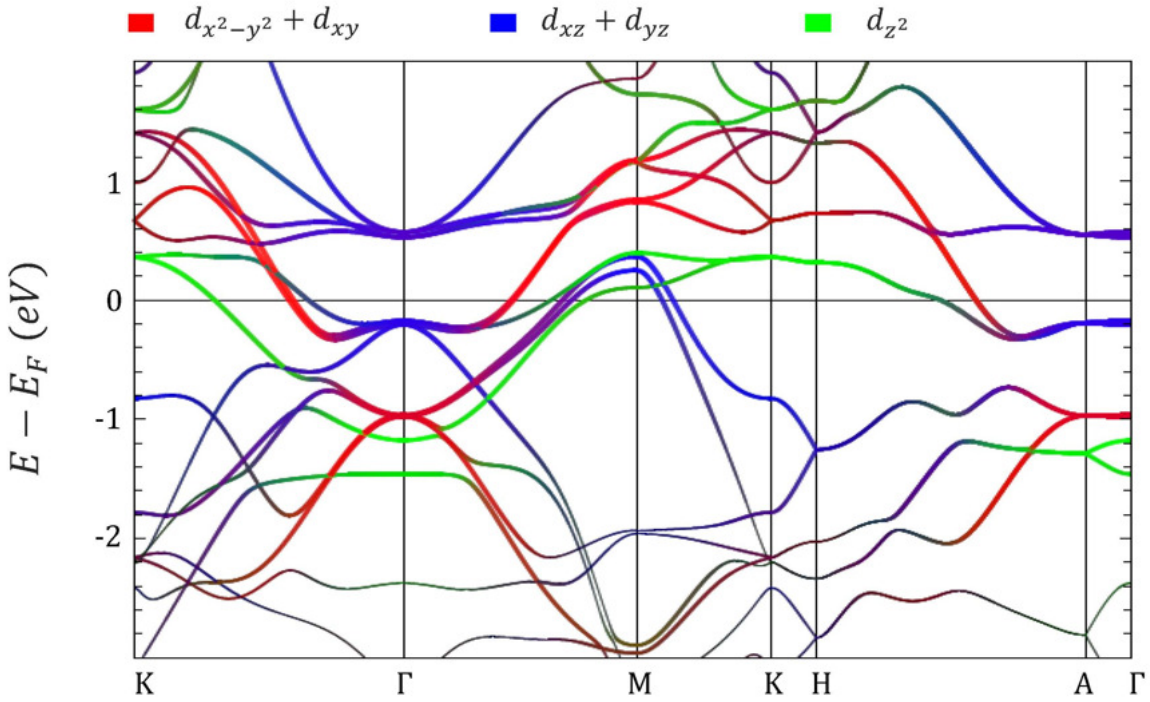

FIGURE 4.2: Cr_2AlC band structure calculated from the WIEN2K software. E_F is taken as the energy origin. The main orbital character of each band is indicated by the color code defined above the figure.

electron bands. The orbital character expected to be dominant for each band crossed by E_F are summarized by the schematics of figure 4.4, both for a FS cross section in the Γ and A planes. We shall put figure 4.4 to good use in order to interpret ARPES datas.

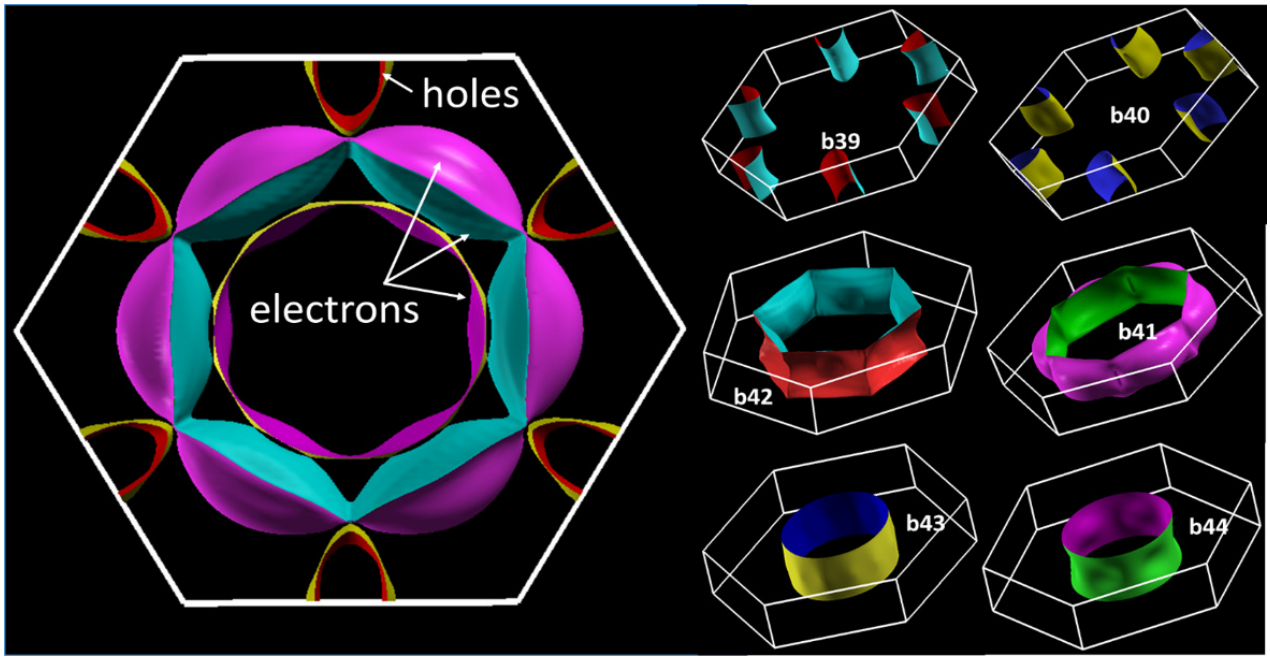

FIGURE 4.3: Cr_2AlC Fermi surfaces, as predicted from DFT calculations performed with WIEN2k and XCRYSDEN software.

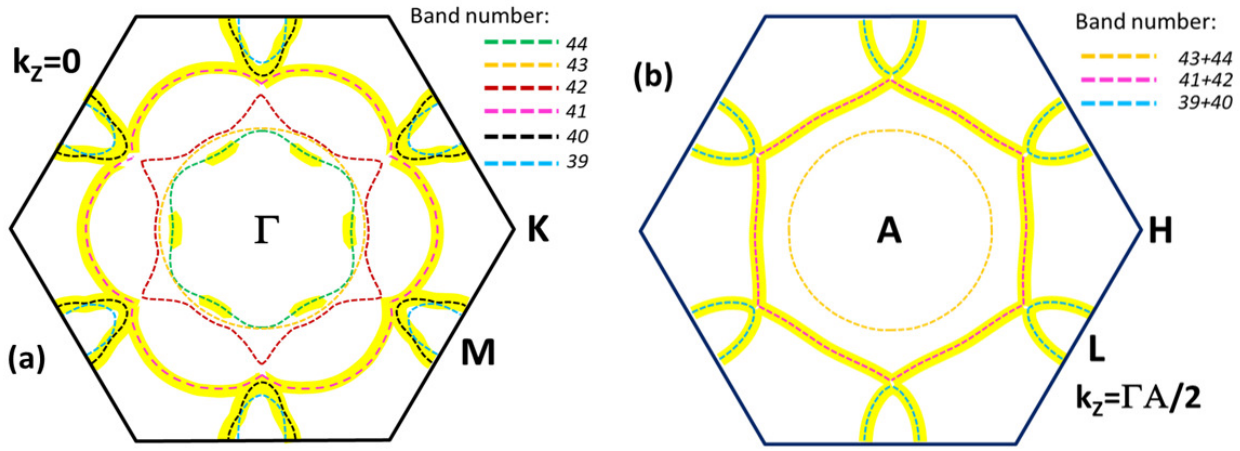

FIGURE 4.4: (a) Predicted cross section of the FS in the Γ-plane ($k_z = 0$). The yellow halo schematically indicates which bands should give a substantial ARPES signal in the S-pol mode if $\Gamma = (\theta_x = 0, \theta_y = 0)$. The halo is obtained by comparing the orbital characters indicated in figure 4.2 with the photoionization cross sections estimated in figure 4.5; we make it appear whenever there is a marked d_{z^2} character, or when there is a $d_{xz} + d_{yz}$ character and substantial angle values. (b) FS cross section in the A-plane and P-pol mode. It is worth noting that a general asymmetry in the ARPES signal should be obtained along the wave vector direction parallel to θ_y.

4.1.2 Prevailing contributions to the ARPES spectra

Matrix elements effects can be encompassed within one quantity: The differential photoionization cross section $\frac{d\sigma}{d\Omega}$ [237]. Since the photoionization cross section highly depends on the orbital character, predicting the photoemission intensity requires one to get a minimum idea of their respective values as a function of the experimental configuration. We calculated it in two ways. First, in the roughest approximation, we just consider the orbital dependence from the inital state and assume a plane-wave final state so that the photoionization differential cross section is approximated as [237]:

$$\frac{d\sigma}{d\Omega} \propto (\mathbf{E_{pol}}.\mathbf{k})^2 |Y_{l,m}(\theta_k, \varphi_k)|^2 \tag{4.1}$$

$\mathbf{E_{pol}}$ being the light polarization vector, $\mathbf{k}$ the photoelectron wavevector, and $Y_{l,m}(\theta_k, \varphi_k)$ the spherical harmonic that makes for angular part of the orbital wave function. Secondly, we take into account more complex matrix elements as detailed, e.g., in [237], accounting for the two angular momentum values allowed by the dipole approximation for a photoelectron excited from a single orbital state. Staying at a rather qualitative level, we summarize here only the predictions of the most basic approach and use the more complex expressions established in [237] in one case only, for which going beyond the plane-wave final-state approximation is revealed to be necessary (See section 4.2.1). We totally neglected the effect of the mean free path on the cross section. Such effects are detailed in [182] and briefly mentioned in chapter 3. Figures 4.5a and 4.5b show the variation of the differential cross section in the two ARPES configurations that were used (P-pol and S-pol configurations, given in figure 4.1).

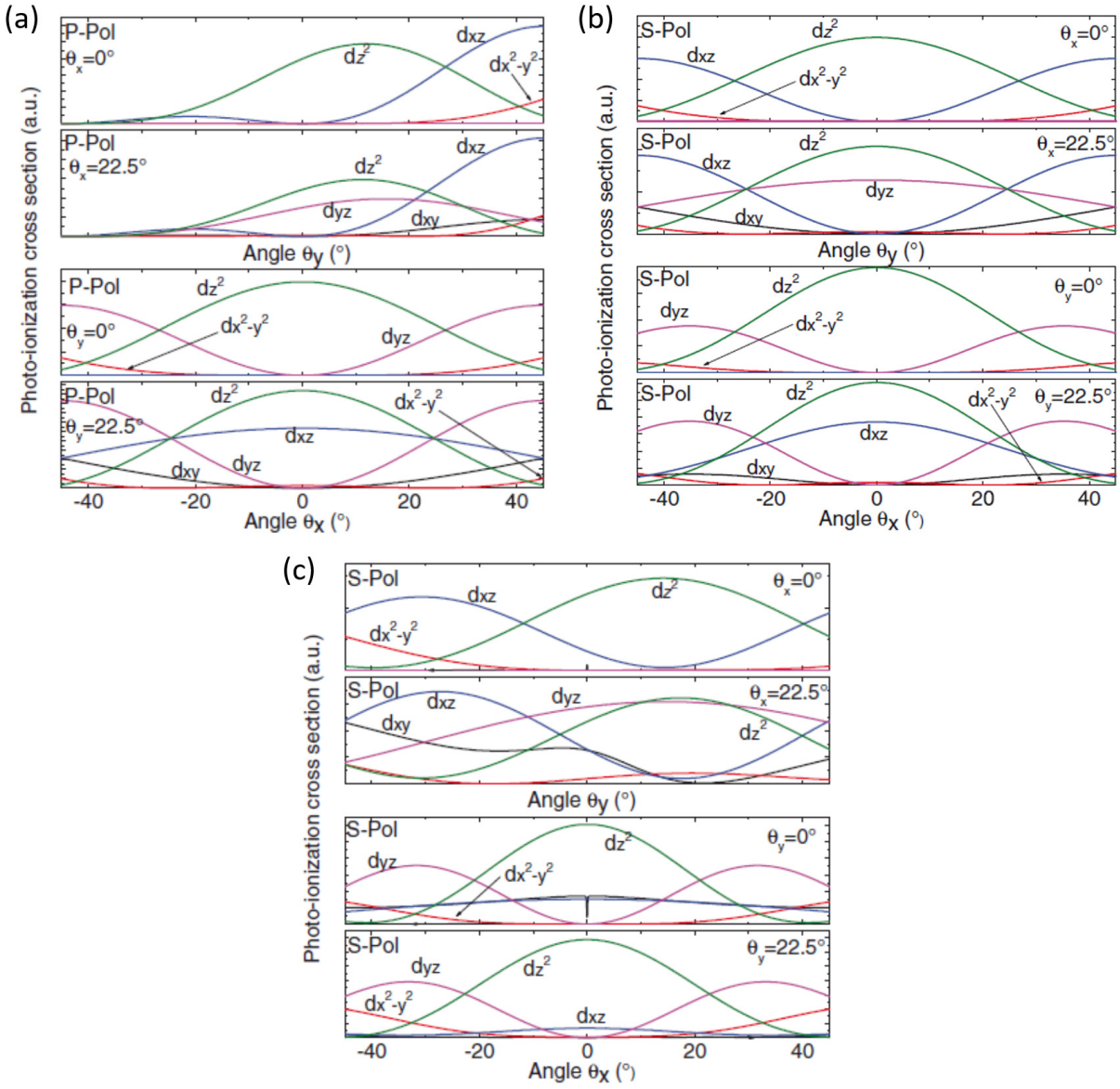

FIGURE 4.5: (a)Orbital components of the photoionization differential cross section as a function of the angles, calculated in the P-pol (a) and S-pol (b) configurations and the simplest level approximation. In (c), it iscalculated in the S-pol configuration but this using the more complex closed-form expression of Ref. [182].

It is clear that the dz^2 orbital always prevails for low θ_x and θ_y angles. When these angles exceed some 10◦, other orbitals may also substantially contribute to the ARPES signal. As already reported, P polarization induces a dissymmetry along the θ_y axis [182]. Comparing those plots to figures 4.2 and 4.4 allows us to qualitatively predict which band regions should lead to a prominent ARPES signal, depending on the values adopted for the θ_x and θ_y angles. It is worth noticing that taking into account the selection rules of the dipole approximation induces a dissymmetry which can make some orbitals exhibit a substantial contribution to the photoionization signal at vanishing angles, even if Eq. (4.1) would predict no contribution at all (see, e.g., the d_{xz} orbitals in figure 4.5c).

4.2 Results and discussions

4.2.1 Band structures and Fermi surfaces

Experimental FS cross projections have been obtained at two different energies and for two different polarization modes [$h\nu = 100eV$ and P-pol configuration at the UVSOR line, figure 4.6b, and $h\nu = 50eV$ and S-pol configuration at the AichiSR synchrotron, figure 4.6a]. Comparing these ARPES images to figures 4.3 and 4.4 clearly shows that there is a remarkable agreement between both. The FS parts expected to show a prevailing d_{z^2} character are all represented and both the theoretical and experimental shapes favorably match. Figure 4.6a seems to be well described by figure 4.4a, and figure 4.6b seems to sit in between figures 4.4a and 4.4b, somewhat closer to 3.4b. This is therefore an interesting and direct experimental confirmation of two past predictions from DFT: (i) the electrons at the Fermi surface of MAX phases mainly exhibit a d-orbital character and (ii) their wave functions are localized at the transition-metal atom sites. As demonstrated in chapter 3 using a nearly free approximation to describe the photoexcited electron in the final state inside the solid, let us remind the relation (3.7) between the transverse wave vector of the electron and the polar angle of the detected photo electron [180]:

$$k_{\perp} \approx \frac{1}{\hbar}\sqrt{(2mE_{kin}cos^2(\theta_k) + V_0)} \tag{4.2}$$

For the in-plane wavevector, one has once again (3.6)[180]:

$$k_{||} = \frac{1}{\hbar}\sqrt{2mE_{kin}}sin(\theta_k) \tag{4.3}$$

An interesting point is that as long as θ_k is not too large, probing the FS with a given photon energy roughly amounts to scanning a cross section of the FS at a constant value of k_z, as indicated by Eq. (4.2). Comparison of figures 4.6a and 4.6b to figures 4.4a and 4.4b thus indicates that most probably, the average k_z value in the first image is very close to define the Γ plane, and that of figure 4.6b is closer to an A-plane cross section. Focusing on figure 4.6a and comparing its high-intensity regions with the yellow shaded areas in figure 4.4a, one can observe all d_{z^2} contributions predicted by the analysis in section 4.1, but also the totality of the hole pocket FS projection. This should come as no surprise, since the hole pocket parts not characterized by a prevailing d_{z^2} contribution are predicted to have a $d_{xz} + d_{yz}$ character, the photoionization cross section of which becomes appreciable at larger angles (see Figure 4.5).

Recording the photon-energy-dependent ARPES trace in the (k_x, k_z) plane (i.e., in the ΓALM plane) also demonstrates the lack of appreciable energy dispersion of the detected bands (figure 4.7), confirming experimentally the quasi-2D character of the Cr_2AlC phase. This is in strong support of the large resistivity anisotropy deduced from the magnetotransport measurements reported in [159].

The main difference between theory and experiments lies in the detection of an additional, small hole pocket

in the center of the Brillouin zone (see figures 4.6 to 4.8). In figure 4.8a, it can be seen that this hole pocket appears thanks to a shift of the upper band centered around Gamma, whose camelback structure slightly crosses the Fermi level. Theory predicts that this band should remain unoccupied. As shown in figure 4.7, this additional band is delocalized along c, too. If the observed band does correspond to the camelback structure predicted to occur inside the central electron bands (compare figures 4.2 and 4.8), either because the band itself is shifted or because E_F is shifted across it, it should mainly exhibit a $d_{xz} + d_{yz}$ character. As a consequence, a naïve application of Eq. (4.1) should lead to no visible intensity as compared to the d_{z^2} contributions in other areas, because any other orbital contribution should be almost zero (see figure 4.5). A way to explain this result is to go beyond the plane-wave final-state approximation, the one which led to equation (4.1). taking into account the two allowed values of the photoelectron angular momentum ($l' = l + 1$ or $l' = l1$) leads to expressions for the differential cross sections which were computed and detailed in [237]. Applying these closed-form expressions to our two configurations leads to asymmetries and shifts, the one portrayed in 3.5c, which make the d_{xz} contribution non-negligible, but still appreciably smaller than that of the d_{z2}. This is in agreement with the ARPES images of figure 4.6.

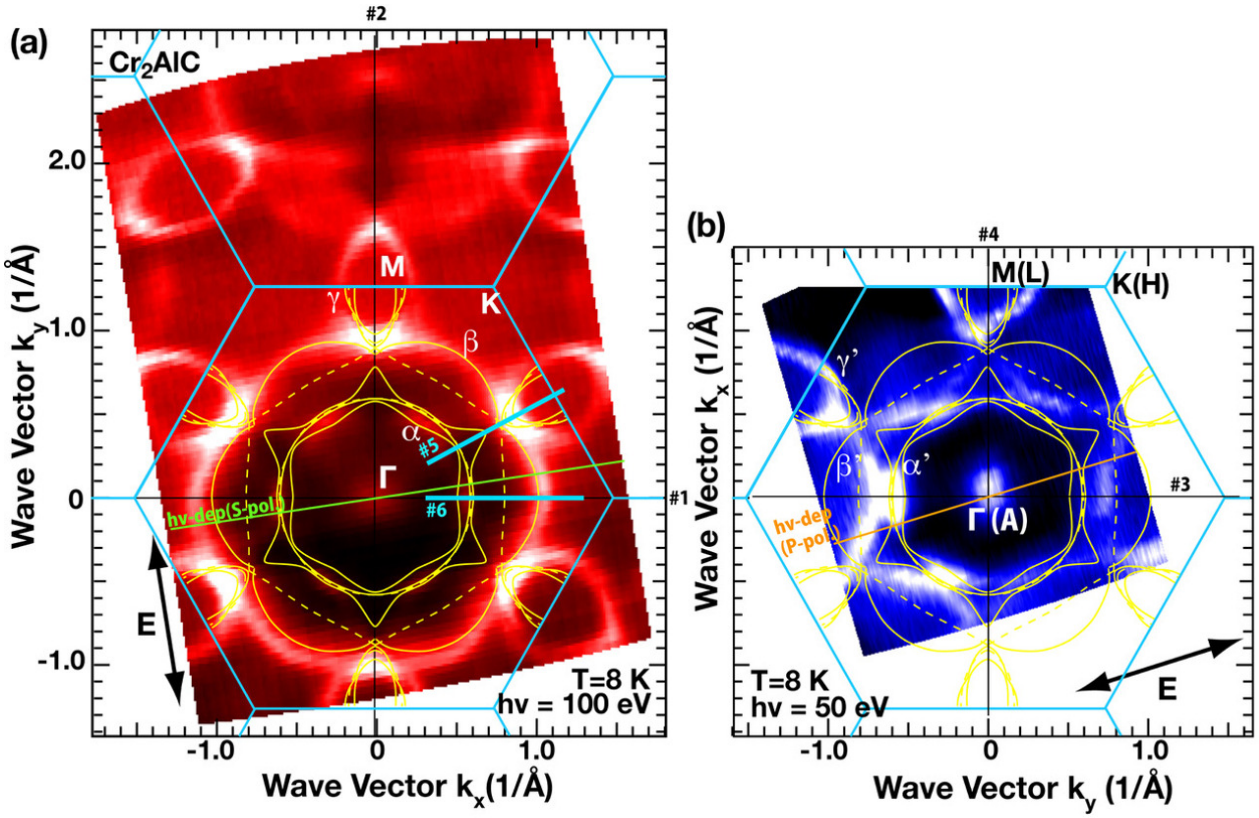

FIGURE 4.6: Fermi-surface images of Cr_2AlC obtained by ARPES with S-pol configuration and $h\nu = 100eV$ photons (a) and with P-pol configuration and $h\nu = 50eV$ photons (b), respectively. Polarization directions are indicated with arrows. Yellow solid and dashed lines are outputs of DFT calculations in ΓKM and AHL plane, respectively. ARPES measurement lines in figures 4.7, 4.8, and 4.9 are indicated with indices ($h\nu$-dep (S/P-pol), following figures 4.1 to 4.5). Experimentally observed Fermi surfaces in the S (P)-pol modes have been indicated as α (α'), β (β'), and γ (γ').

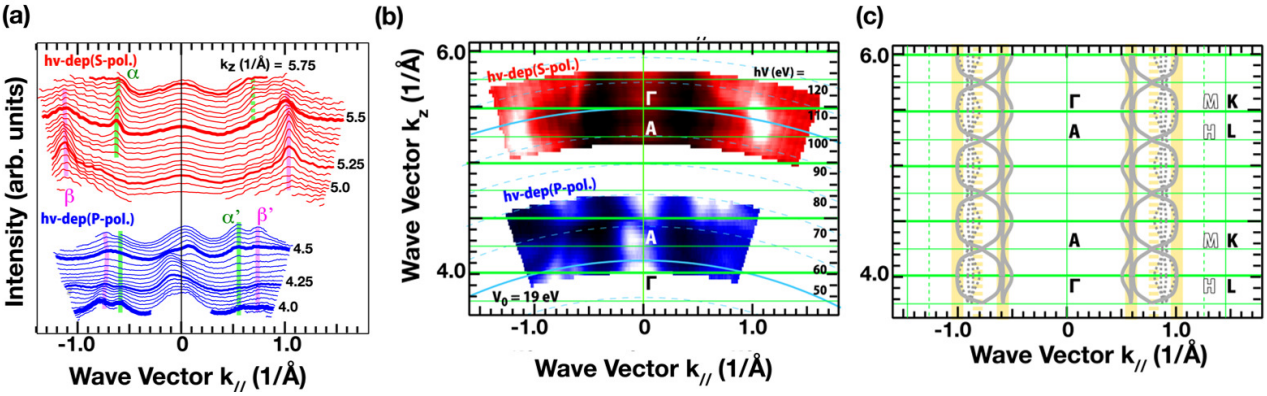

FIGURE 4.7: kz dependence of MDC spectra at EF (a) and Fermi surface image (b) obtained by photon-energy-dependent ARPES performed at the slices indicated in figure 4.6. (c) Interplane Fermi surface calculated by DFT along $\Gamma K - LH$ (gray solid lines) and $\Gamma M - HA$ (gray dashed lines), respectively. Quasi 2D topology of the calculated Fermi surface has been expected as shown with yellow shaded lines. Though the observed Fermi surfaces show little k_z dependence at this $k_{||}$ position, we have estimated the inner potential as $V_0 = 19eV$ in Eq. (4.2) from the systematic intensity variations.

As detailed above, there is a good overall agreement between the expected and measured data. The most striking discrepancy is the apparent shift of the Fermi level through the camelback band structure predicted at the zone center. Although we cannot give a definitive explanation, it is worth noticing that the photon energy range is the same as the one for which we expect a minimum in the photoexcited electron inelastic mean free path. This implies that the photoexcited electrons come from no deeper than a very few layers from the surface (See Chapter 3). As predicted and discussed both in chapter 2 and above within this section, the electrons at E_F are confined in the Cr_2C planes, and Cr_2AlC is quasi-2D compound. However, the electron densities in each band and Fermi-level position are in part determined by some electron transfer from the Al atoms.

This is a general feature of MAX phases and is obvious from the fact that, e.g., the carrier density and even the band structure of MXene materials with the same M_2X layers substantially depend on the nature of the surface termination (See chapter 2). Yet the electrons at E_F are confined in the M_2X planes. This implies that the Cr_2C layer closest to the surface might be affected by surface effects. We can therefore suspect that the surface could exert some influence on the ARPES signal. As a consequence, one cannot exclude the possibility of a slight surface-induced Fermi-level shift due to band bending at the interface. It is worth noticing that from the DFT calculations, a minimum of 130 meV is required for making the Γ camelback band to cross E_F. We note that if we directly compare the band structure obtained by ARPES to the theory exposed in section 3.1 and to the DFT results obtained after shifting E_F by 160 meV, the electron bands around EF are indeed still more satisfactorily fitted than when using the rough DFT predictions, but then the discrepancy with the hole bands noticeably increases. That the Fermi level is shifted with respect to DFT predictions is also supported by an examination of bands at a lower energy. The set of bands starting from 1.3 to 0.9 eV from *Gamma* and rising when going towards K is also better fitted with the same Fermi-level shift. The

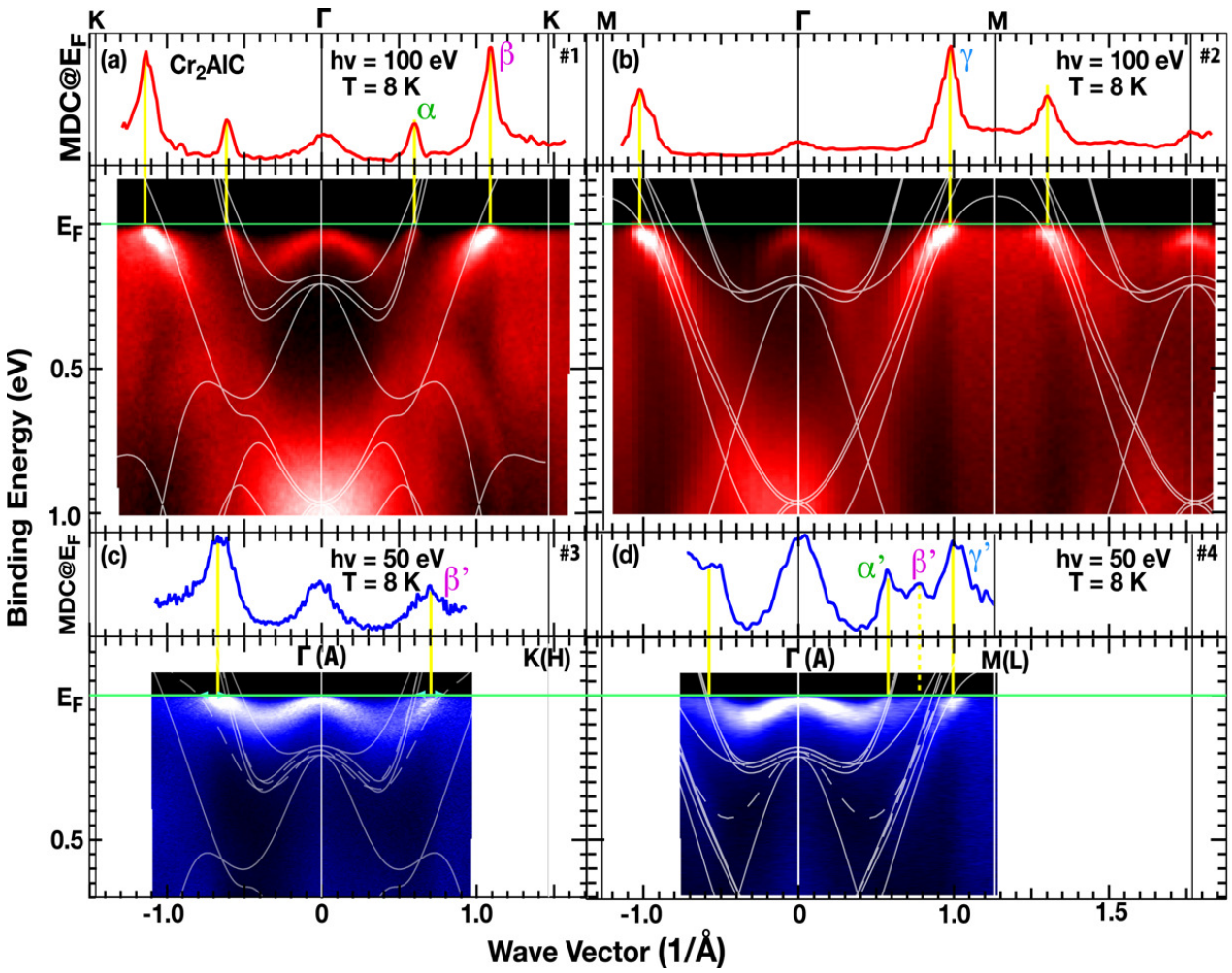

FIGURE 4.8: Band structure images of Cr_2AlC obtained by ARPES along no. 1, ΓK (a); no. 2, ΓM (b); no. 3, $\Gamma K(AH)$ (c); and no. 4, $\Gamma M(AL)$(d) slices indicated in figure 4.6, respectively. MDCs at E_F are indicated at the top of each image to estimate the k_F points. White solid and dashed lines are results of DFT calculation along $\Gamma K, \Gamma M$ and AH, AL lines, respectively.

two lower bands of the set, which exhibit a d_{z^2} character around Γ , exactly correspond to the high ARPES intensity in that range after operating the Fermi-level shift. Besides, the observed ARPES splitting observed for those bands when going towards ΓK also corresponds to the band variations in regions with a prevailing d_{z^2} character.

4.2.2 Electron-phonon coupling and absence of antiferromagnetic signature

The main remaining discrepancy is then an apparent overestimation of the band curvature of the hole pockets by DFT and a general increase of the extracted effective masses in all bands as compared with the DFT predicted values. The dispersion observed for the hole pockets around E_F is definitely larger than the predicted one. It is worth noticing that: (i) any hole pocket exhibits a partial nesting with a neighboring one upon a translation of vector (1/2 0 0), which is the magnetic vector predicted for AFM in Cr_2AlC [233] (the

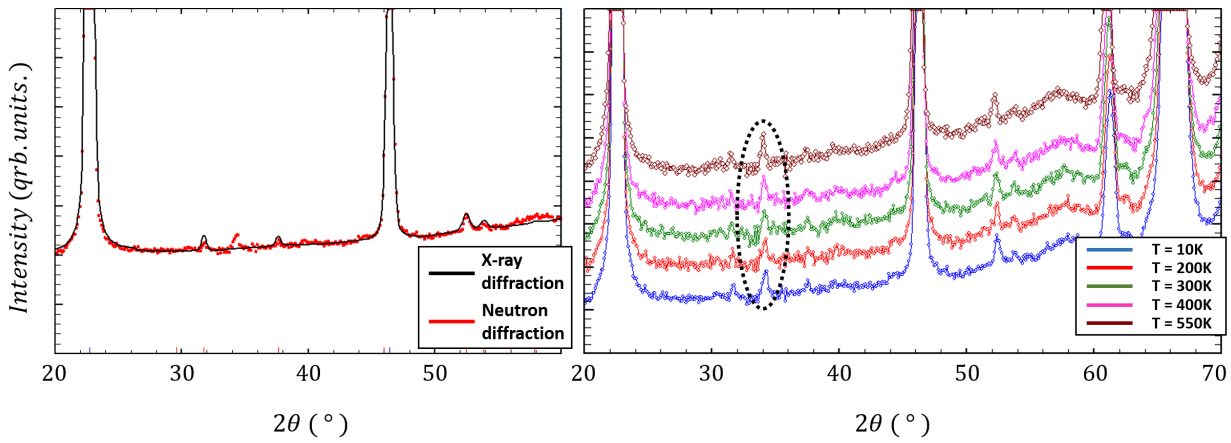

FIGURE 4.9: (a) X-ray vs neutron diffraction diagram, recorded at the Institut Laue langevin by Claire Collin from a powder of mashed, pure Cr_2AlC single crystals. An additional peak on the neutron spectra appears at 34°. It corresponds to an hypothetical $(1/2, 0, 0)$ magnetic vector. Yet, this peak does not shift nor disappear or evolve in any manner in a very large range of temperature, from 10K to 550K. It may not correspond to any magnetic order (b).

hole pocket being isotropic in the Γ plane, nesting would be perfect [242]); (ii) besides, the particular scaling law observed for magnetotransport might also indicate the presence of electron correlations [154]; and (iii) since the d waves are quite confined on the Cr atoms, Mott-Hubbard-like interactions could also come into the play. Each of these three effect might be responsible for a modification of the hole bands around the M points, as compared with our DFT calculations. Besides, many-body effects associated to magnetic or electron-phonon coupling are often responsible for substantial band renormalization effects. The spectral function should incorporate those additional couplings, which modify accordingly the dispersion observed from ARPES and introduce a self energy term, finite excitation lifetime and ARPES intensity bandwidth as defined in chapter 3 [184, 243]. This is discussed below.

In order to discriminate among the possible scenarios for the band renormalization mentioned just above, neutron scattering experiments were performed to investigate for possible magnetic structures that would fulfill (i). As neutrons possess a spin, they interact with atoms not only through their charge but through their spin degree of freedom. Thus neutron diffraction techniques can resolve diffractions peaks to be associated both with the regular unit cell as well as with the magnetic supercell [40]. Such experiments were performed by *Claire Colin* on a powder made from grinded, pure Cr_2AlC single crystals brought to the D1B Two-Axis Powder Diffractometer of the Institut Laue Langevin. Both X-ray and neutron diffraction patterns are respectively given in figure 4.9a. An additional peak appear on the neutron curve, at a coordinate of $2theta = 34$. From a magnetic group analysis also performed by *Claire Colin*, this peak is found to be compatible with a (1/2, 0, 0) magnetic vector for an AFM structure. But when sweeping the temperature from 10K to 550K, recording neutron diffraction spectra for several temperatures as indicated in figure 4.9.b, neither the amplitude, the width nor the position of the peak seemed to change. Also, no sharp variation were found on the dependence of the measured unit cell parameters and volume with temperature (given in figure 4.10),

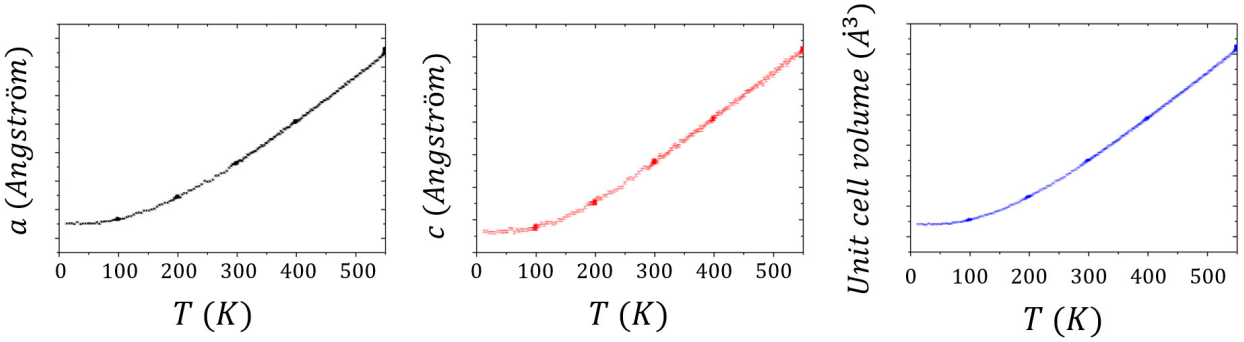

FIGURE 4.10: Evolution of Cr_2AlC lattice parameters a (a) and c (c) as well as the overall unit cell volume (c) with temperature. No notable sign of a sudden variation in volume (to be linked to a magnetic transition) is observed.

while an AFM magnetic ground state was found in previous calculations [233] and an magnetic transition Tc= 73.5K was hinted by a previous experimental study on polycrystalline Cr_2AlC samples [236]. One must mention that elemental chromium is antiferromagnetic and it exhibits a complex ordering, featuring spin density waves [242]. Considering the lack of a clear experimental signature of a magnetic ground state as well as the good agreement between nonmagnetic DFT calculations and ARPES spectra, we presume that AFM will likely not be the origin of the band renormalizations observed for Cr_2AlC.

Going back to the electronic band structure of Cr_2AlC, we computed a partial set of Fermi velocities and effective masses, corresponding to the electron and hole bands crossing the Fermi level. In figure 4.11, they are compared to the values extracted from the ARPES data following methods similar to those described in [244] (figure 4.12). The Fermi velocities in the outer, Γ centered electron band (b41) and those of the holes in the direction (b39,40) are respectively around 1.41×10^5 and $9.15 \times 10^4 ms^1$, as deduced from the slope of the experimentally observed dispersion. The inner electron tube (b44) exhibits a Fermi velocity around $1.9 \times 10^5 ms^1$, closer to that of Cr ($2.7 \times 10^5 ms^1$ [242]). These values are much lower than those of ordinary metals, and due to the d-orbital character of the carriers at the Fermi energy. Extracted masses of the hole pockets and of the electrons of b41 are much heavier than predicted by theory, with, e.g., a hole mass $m_h \approx 3.21 m_0$ for band 40, instead of a predicted value of $1.92 m_0$. Band renormalization effects are also observed in the momentum distribution curves (MDC) shown in figure 4.12.

Although it is difficult to put it on a precise quantitative basis, assessing whether phonons are responsible for the observed band renormalization can be achieved as follows: First, we compute the electron-phonon coupling constant as $\lambda = (m^{renorm}_{ARPES}/m_{DFT}) - 1$ [245], where m^{renorm}_{ARPES} is the renormalized mass evaluated close to E_F , and m_{DFT} the DFT values. Second, we compare those values to the averaged value deduced from specific heat measurements versus temperature. (In the latter case a comparison was made between the density of states at the Fermi energy $D(E_F)$ extracted from specific heat measurements and the predicted DFT value, assuming that λ is a simple function of their ratio [1].) For the γ hole band along ΓM, we found $\lambda = 0.67$. For the corresponding electron band b41 along ΓK we also found $\lambda = 0.67$. The inner α electron

	m^*/m_e	carrier	k_F (Å^{-1})	v_F (m/s)
DFT //ΓM (//ΓK)				
band44	2.71 (3.28)	electron	0.587 (0.517)	2.51×10^5 (1.82×10^5)
band43	2.55 (2.00)	electron	0.599 (0.598)	2.71×10^5 (3.47×10^5)
band42	6.32 (2.17)	electron	0.804 (0.622)	1.47×10^5 (3.33×10^5)
band41	3.97 (-5.31)	electron	0.867 (1.03)	2.53×10^5 (2.24×10^5)
band40	1.92	hole	0.343	2.10×10^5
band39	2.34	hole	0.276	1.36×10^5
ARPES				
$\alpha_{//\Gamma K}$ b44	3.68	electron	0.595	1.87×10^5
$\beta_{//\Gamma K}$ b41	-8.86	electron	1.08	1.41×10^5
$\gamma_{//\Gamma M}$ b40	3.21	hole	0.254	9.15×10^4

FIGURE 4.11: Fermi velocities and effective masses obtained by fitting the first and second derivatives of the dispersion curve. The Fermi momenta k_F 's are defined by the distances from the $\Gamma(M)$ point with respect to the electron (hole) carriers. The observed effective masses as well as the Fermi velocities of the α, β, and γ bands correspond to the DFT bands 44, 41 along ΓK and 40 along the ΓM axis, respectively. All experimental bands display a significant mass enhancement (1.14 to 1.7 times) relative to the DFT calculations.

band gives $\lambda = 0.12$. Specific heat measurements give a value around 1.45, but for a complex average over all bands (see Fig. 4.18 in [1]). Notwithstanding the fact that all three methods are imprecise and rely on the approximate (in this case) Debye model, finding the same order of magnitude in the three cases makes electron-phonon coupling as a reasonable candidate in order to explain the observed band renormalization. It is important to note that the MDC values are much smaller in the case of the α band than for the β and γ bands, corroborating the conclusion drawn above that electron-phonon coupling should be prominent for the two latter bands. Figure 4.12d displays the variation of the momentum dispersion curve as a function of energy. As seen in figure 4.12d, and even if a direct relationship between the phonon density of states and the MDC signal farther away from E_F is not entirely obvious, the observed peaks or thresholds observed close to E_F roughly correspond to the regions where a high density of phonon modes is expected [yellow areas in fgure 3.12d]. Besides, renormalizing the MDC by multiplying it by the Fermi velocity gives curves lying close to one another around E_F , also in agreement with the assumption that phonon-electron coupling plays a significant role.

It is worth noticing that all data and references dealing with electron-phonon coupling in Cr_2AlC agree upon the fact that it is much stronger than for most other MAX phases [1], some similar Cr-based MAX

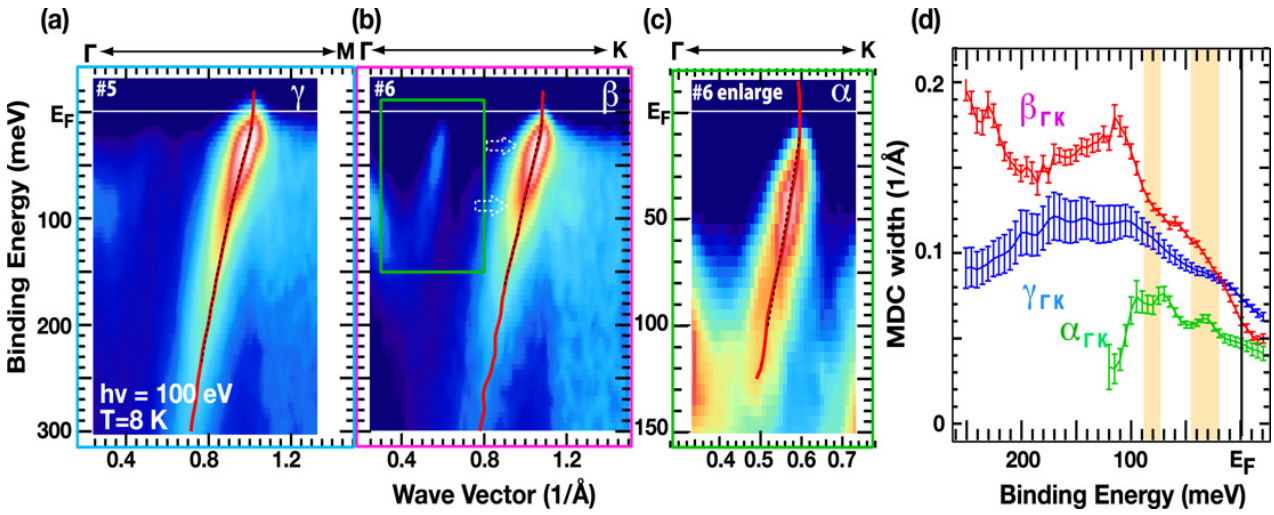

FIGURE 4.12: (a–c) Detailed band dispersions at the holelike FS around the M point (a), the large (b), and small (c) electron-like FSs around the point, respectively. Red solid and black dashed lines are the peak positions of MDC spectra and the fitting curves based on a standard free-electron model. (d) Comparison of the width of the MDC spectra obtained by the fitting with Lorentz functions, which should correspond to the spectral function. Yellow shaded energy ranges around 30 and 80 meV correspond to intervals where the calculated phonon density of state is predicted to be high (from [239]).

compounds such as Cr_2GeC omitted. This large coupling, combined with the fact that most carriers occupy the bands with a lower Fermi velocity, explain the higher resistivity values of the Cr_2AlC compound in the phonon-controlled temperature range, as compared to most other MAX phases and many transition metals .

4.2.3 Modelling Cr_2AlC in-plane magneto-transport

Omitting the effect of electron-phonon coupling, the FSs computed by DFT can be used to compute electronic transport coefficients and charge carrier densities, owing for the relationship between the morphology of the Fermi surface and Onsager coeficients such as electronic conductivity (given by equation (2.21)). Such analysis was performed by *Thierry Ouisse* using the as computed Cr_2AlC DFT FSs as an input. These results are detailed in [229]. The whole formalism and methodology used in [229] follow former work on the nearly free electron description of Ti_2AlC electronic structure [159]. We will briefly describe these results, their level of consistency with magnetotransport experiments on bulk single crystals and, following the discussion in section 2.1.3, illustrate how the two band Drude models erroneously describe electronic transport in MAX phases (specifically for the Cr_2AlC case). The model described here cannot describe the very specific violation of Kohler Rule recently observed for Cr_2AlC, where magnetoresistance exhibits a scaling law in Hall angle when varying Temperature, rather than a scaling law with magnetic field [154].

The first step of the model is to approximate the FSs from DFT as completely bidimensional (As partially justified in section 4.2.1.). It allows to replace the three dimensional FS by Fermi lines (FLs) corresponding to the FS cut in the Γ plane. These lines are approximated by a sum of fully analytical functions given by Gielis [246]:

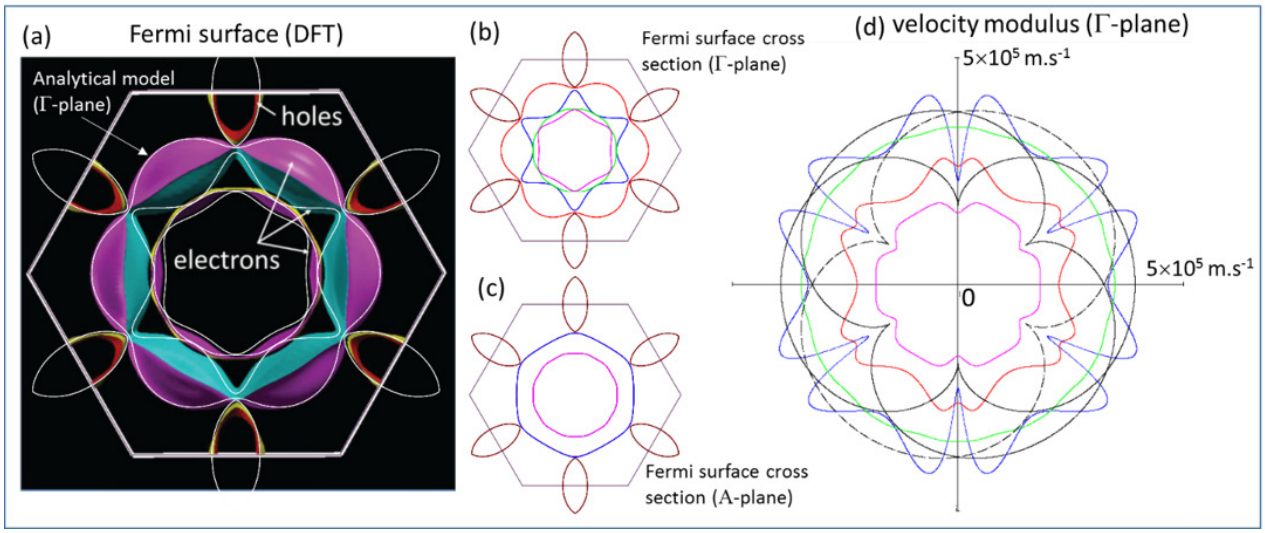

FIGURE 4.13: (a) Top view of the FS projection onto the Γ-plane as computed by DFT , onto which is superimposed the fit of the Fermi lines in the Γ-plane using Eq. (4.4) (white solid lines), (b) Fit of the Fermi lines in the Γ-plane using Eq. (4.4), (c) Fit of the Fermi lines in the A-plane. (d) polar plot of the corresponding Fermi velocities in all bands. In (d) the color code is the same as in (b), but for the hole pockets, which give rise to 3 equivalent but differently oriented polar plots, 2 of them being represented by black solid lines and the third one by a black dashed line.

$$k_F(\vartheta) = \xi k_M(|\frac{1}{a}cos(\frac{p}{4}(\vartheta+\varphi))|^{n_2} + |\frac{1}{b}sin(\frac{p}{4}(\vartheta+\varphi))|^{n_2})^{-\frac{1}{n_1}} \tag{4.4}$$

with k_F the modulus of the Fermi wavevector, ϑ the polar angle, k_M the wavevector modulus at the M point and ξ, a, b, p, n_1, n_2 and n_3 are fit parameters used to find an acceptable fit of the Fermi lines at Γ. The fits to the in plane (Γ plane) FS from DFT are given in figure 4.13 (An A-plane FS cut was also approched by a set of angular function and used to compute transport parameters, as seen in 3.13c. Little differences are found between the obtained parameters for Γ and A-plane sets of FLs). In order to calculate energy derivatives such as the Fermi velocities, one approximate the local near E_F dependance of the energy on momentum as [229]:

$$E = \hbar v_0 k_0 \frac{(k^2 cos^2(\vartheta) + k^2 sin^2(\vartheta))}{2k_F^2(\vartheta)} \tag{4.5}$$

Where v_0 and k_0 are respectfully the fermi velocity and Fermi wavevector along ΓM for electron bands or ΓK for hole bands. Then, one can calculate the Fermi velocities map as $\mathbf{v_F} = \frac{1}{\hbar}(\frac{\partial E}{\partial \mathbf{k}})_{E=E_F}$ (See figure 4.13d). From there comes the second step of the analysis, relying on semi classical transport formalism.

When applying a magnetic field **B** parallel to z axis and an in plane electric field $\mathbf{E_{el}}$ along x axis, one get the out of equilibrium distribution function from Boltzmann equation as [40]:

$$\Delta f = -(1 + \frac{e\tau}{\hbar}(\mathbf{v} \times \mathbf{B})\frac{\partial}{\partial \mathbf{k}})^{-1} e\tau \mathbf{v}.\mathbf{E_{el}} \frac{\partial f}{\partial E} \tag{4.6}$$

Which becomes, in the Jones Zener approximation [247]:

$$\Delta f = -(1 - \frac{e\tau}{\hbar}(Bv_y\frac{\partial}{\partial k_x} - Bv_x\frac{\partial}{\partial k_y}) + order2)e\tau\mathbf{v}.\mathbf{E_{el}}\frac{\partial f}{\partial E} \tag{4.7}$$

with τ the relaxation time. The first term will account for the direct conductivity σ_{XX} while the second term in v gives the transverse Hall conductivity σ_{XY} while higher order terms give rise to the magnetoresistance [159].

One can extract σ_{XX} and σ_{XY} by calculating the integral that give the full current [154]:

$$\mathbf{j} = \frac{e}{2\pi^2}\int \mathbf{v}(\mathbf{k})\Delta f d^2\mathbf{k} \tag{4.8}$$

There, j_x component gives σ_{XX} (and the magnetoresistance) while j_y leads to σ_{XY}. These integrals can be approximated as integrals along the Fermi lines [159].More detail on their computation are given in [248].

One then have the in plane resistivity ρ_{ab} and Hall constant R_H (by summing over the band indexes i) [159]:

$$\rho_{ab} = \frac{\sum_i \sigma XX^i}{(\sum_i \sigma XX^i)^2 + (\sum_i \sigma XY^i)^2} \tag{4.9}$$

$$R_H = \frac{1}{B}\frac{\sum_i \sigma XY^i}{(\sum_i \sigma XX^i)^2 + (\sum_i \sigma XY^i)^2} \tag{4.10}$$

All the dependancies on ϑ of the term within equations (4.7) and (4.8) are known but the relaxation time. It is within the relaxtion time τ that most of the temperature dependance of σ_{XX} and σ_{XY} will lie. The relaxation time is chosen as follows, taking into account impurity scattering prevailing at low T [40, 247], phonon-limited Bloch-Gruneisen contribution at intermediate T [40, 247] and the standard phonon-limited linear dependence [40, 247] at high T [229]:

$$\frac{1}{\tau} = \frac{v_F(\vartheta)}{\lambda_{imp}} + (\tau_{ph}(\frac{T_A}{T} + (\frac{T_B}{T})^5))^{-1} \tag{4.11}$$

With λ_{imp} the impurity mean free path, τ_{ph} a phonon-related characteristic time and T_A and T_B characteristic temperatures that vary from band to band. These four parameters are used as fitting parameters in the overal model and were adjusted to obtain the fit of the temperature dependence of experimental transport parameters given in figure 4.14 [229].

In figure 4.14, the experimental data points are retrieved from [159]. It is worth noting that the approximation procedure is not easily automated, because the fitting parameters are the entire T dependencies of the relaxation times in each band (see reference [229], figure 2).

To obtain the all-important parameters, one first estimated λ_{imp} to be compatible with the saturation of ρ at low T (visible in figure 4.14a).Remarkably, these values also give a satisfying approximation of R_H (figure

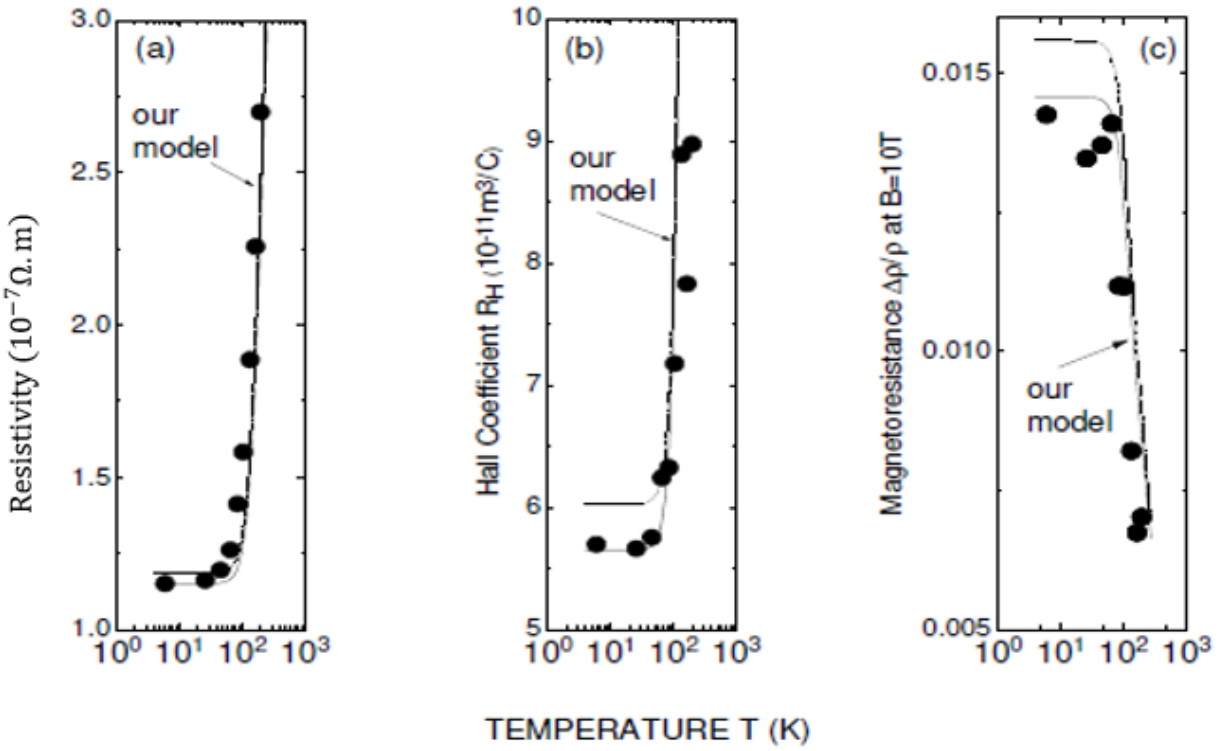

FIGURE 4.14: Temperature dependencies of, (a) ρ, (b) R_H, (c) and MR for B=10T. Data points are taken from [159], using the same set of experimental data. Solid and dotted lines are the fits using the extremal Fermi line cross section respectively in the Γ and A planes.

4.14b). The second key ingredient is to select relaxation times τ_{ph}, the temperature variations of which, that render the relative balance between electron and hole contributions to vary with T [229]. We note that due to the fitting procedure, we cannot ensure that no other set of relaxation time values could lead to a satisfying fit of the experimental data. Yet, the agreement between model and experiment is good enough as to support the validity of the model: not only the variations of ρ with T (figure 4.14a), but also the variations in R_H (figure 4.14b) and MR (figure 4.14c) with T. In our framework, the carrier densities n_e and n_h in the different bands are constant with T, and the temperature dependencies of the transport parameters are entirely due to variations of the relaxation times. The latter are obtained by summing the areas enclosed by the FLs in k-space and are equal to $n_e = 2.54 \times 10^{22} cm^{-3}$ and $n_h = 4.56 \times 10^{21} cm^{-3}$, respectively [229].

Thus, these results illustrate that in the case of MAX phases, the parameters extracted by either the single or double-band methods bear no relation with transport parameters.

4.3 Summary

Despite the discrepancies mentioned in section 4.2.1, the reasonable agreement obtained between ARPES data and DFT calculations makes one confident in the fact that the FS deduced from the ARPES image in figure 4.6 does reflect most of the expected bulk FS properties and is not seriously affected by surface features.

The FS is formed by a complex combination of hole and electron bands, as expected for all MAX phases. The ARPES signal is in very good agreement with the expected orbital character of each band. The dispersion of the most populated bands at E_F is large, resulting in large effective masses and low Fermi velocities. It could explain the relatively higher electrical resistivity values previously mentionned in the literature, as compared with non-Cr-based MAX phases.

Using an approximation of the DFT FS shape and Boltzmann's equation, we retrieved the temperature variations of R_H and ρ_{ab} determined by transport measurements on single crystals [159]. Our results illustrate that the parameters extracted by either the single or double-band methods bear no relation to the real transport parameters. A Fermi-level shift induces the population of an additional hole band, but our experiments do not allow to determine whether this is due to a surface effect. The anomalous dispersion of the hole bands and of the electron bands closest to them, as compared with the DFT bands, possibly result from a substantial electron-phonon coupling-induced band renormalization. Renormalization effects arising from AFM coupling are most likely to be ruled out due to the lack of a clear AFM signature on neutron diffraction patterns measured over a very large range of temperature. This is consistent with the fact that spinless DFT calculations alone proved to bring a satisfactory fit to the ARPES spectra.

Comparison with ARPES data obtained from other MAX phases should allow one to determine whether the band renormalizations observed are specific to the case of Cr_2AlC or would be observed in other MAX phases. It should also allow one to verify whether if all MAX phases are identically quasi bidimensional, as our ARPES measurements confirm it in the case of Cr_2AlC, or delocalized in all three directions of space. It thus brings us to the electronic structure of another MAX phase to be explored: the one of V_2AlC.

Chapter 5

V_2AlC: Near Fermi Fermi level bands, out of plane dispersions, surface states

This chapter is dedicated to the electronic structure of another 211 MAX phase, V_2AlC. It is based on another article that the author of this manuscript published as first author [249].

In the course of chapter 3, we illustrated how Cr_2AlC electronic structure quasi-2D nature was confirmed by ARPES and DFT calculations [228]. While Cr_2AlC (together with other Cr based MAX phase) lies aside from other MAX phases for having a significantly higher resistivity [1, 38, 159] ,V_2AlC is known to exhibit a very low resistivity compared to most MAX phases [1, 38]. One must note that recent transport measurements on both Cr_2AlC and V_2AlC single crystals found the latter's transport anisotropy $\frac{\rho_c}{\rho_{ab}}$ to be an order of magnitude higher [159]. From this argument, V_2AlC Fermi surface ought to show even less dispersion over k_z than its Cr_2AlC counterparts.

It thus makes it a perfect candidate to test how far the conclusions of chapter 3 regarding Cr_2AlC electronic structure can be generalized to other MAX phases.

Here, our ARPES analysis of V_2AlC single crystals is outlined. The resulting BS and FS maps have been systematically confronted to the output of DFT calculation. The scheme we followed is similar to the one for Cr_2AlC, described in chapter 3 [228].

We confirm that V_2AlC features the same predominance of the d orbitals at E_F . Unexpectedly, DFT calculations seem to show that the V_2AlC FS would be less 2D than that of Cr_2AlC. We consistently observe a rather large broadening of the ARPES signal in the areas of the BZ where DFT predicts the strongest three-dimensionality. As it has been discussed for other materials [250, 251, 252], one can relate such large broadening of the ARPES signal in some restricted reciprocal space areas to a non-negligible k_z dependence of the FS topology. We also provide experimental evidence of the existence of a volatile surface state, the signature of which progressively disappears within hours after cleaving V_2AlC samples in UHV. Once those effects are taken into account, a remarkable agreement between the ARPES data and the theory is found.

5.1 Preliminary analysis

5.1.1 Experimental and computational methods

V_2AlC single crystals were prepared by a high-temperature solution growth following the procedure detailed in chapter 3. Platelets have an area below 1 cm^2 and a thickness going up to 50 µm. As mentioned earlier, they were cut in 3×3 mm squares by using a diamond wire saw and later cleaved in situ for ARPES experiments performed at AichiSR on the BL7U line.

This line is equipped with a MBScientific A-1 electron analyzer (see section 3.2.2). Base pressure was set below 3×10^9 Pa. Temperature was set in the 10–20 K range (roughly 10 K for figures 5.4a and 5.8, and 20 K for the measurement of figures 5.4b and 5.5–5.7). Energy and angular resolution were set at $E \approx 35$ meV and $\theta \approx 0.38$, with an acceptance angle of ± 16 for θ_x (pass 20). We probed a wider θ_y range by tilting the sample holder relatively to the detector. Energy dependent ARPES was performed using photons with energies from $h\nu = 70\neg 150$eV and $h\nu = 85\neg 115$ eV. Linearly polarized lightwas used in the so-called S-pol mode, as described in detail in chapter 3 [228] (See figure 5.1). The angle between the light beam and the detector was set to 45° .

All calculations were carried out with the full potential LAPW+lo method implemented within the WIEN2K software (version 17.1). The non-spin-polarized PBE GGA functional was chosen [207]. Wave functions were expanded up to a RKM cutoff parameter of 7.7 (As mentioned in section 4.1.1, RKM refers to the product of the smallest 'atomic sphere radius' times the largest K vector of the APW expansion used [222]). We selected the V_2AlC unit cell from [5] for our computations. Similarly to [228], we took a very dense k-mesh in order to map fine details of the FS without using interpolation of order higher than 1. We used a $93 \times 93 \times 17$ Monkhorst-Pack meshing of the IBZ for the whole calculation. The FSs were calculated using X-CRYSDEN [240]. An even denser mesh of 3200×48 was used to get the 2D FSs cuts over ΓK and ΓM in figure 5.5. Orbital character plots were obtained with the PRIMA.PY code .

5.1.2 Fermi surfaces, bands and orbital characters from DFT

A few studies already report V_2AlC band structure DFT calculations [253, 254], but they do not show the FS. When plotted only in the first BZ, the FS as given by X-CRYSDEN shows only two occupied bands at the Fermi energy E_F, in contrast to what was found for other MAX phases [154, 228]. Figure 5.1 shows the whole FS calculated from DFT in the first BZ (figure 5.1a) and the band 39 and 40 FSs in a cell centered on the M (L) point (figure 5.1b). Band 40 exhibits the following features: Electron tubes centered on and parallel to the c axis, tripod tubes centered on K (H) points parallel to the c axis, and transverse tubes directed along AH and perpendicular to the c axis. The two tubes directed along k_z are connected through the tubes directed along AH, making the whole structure fully connected and definitely three dimensional, even if the tubes

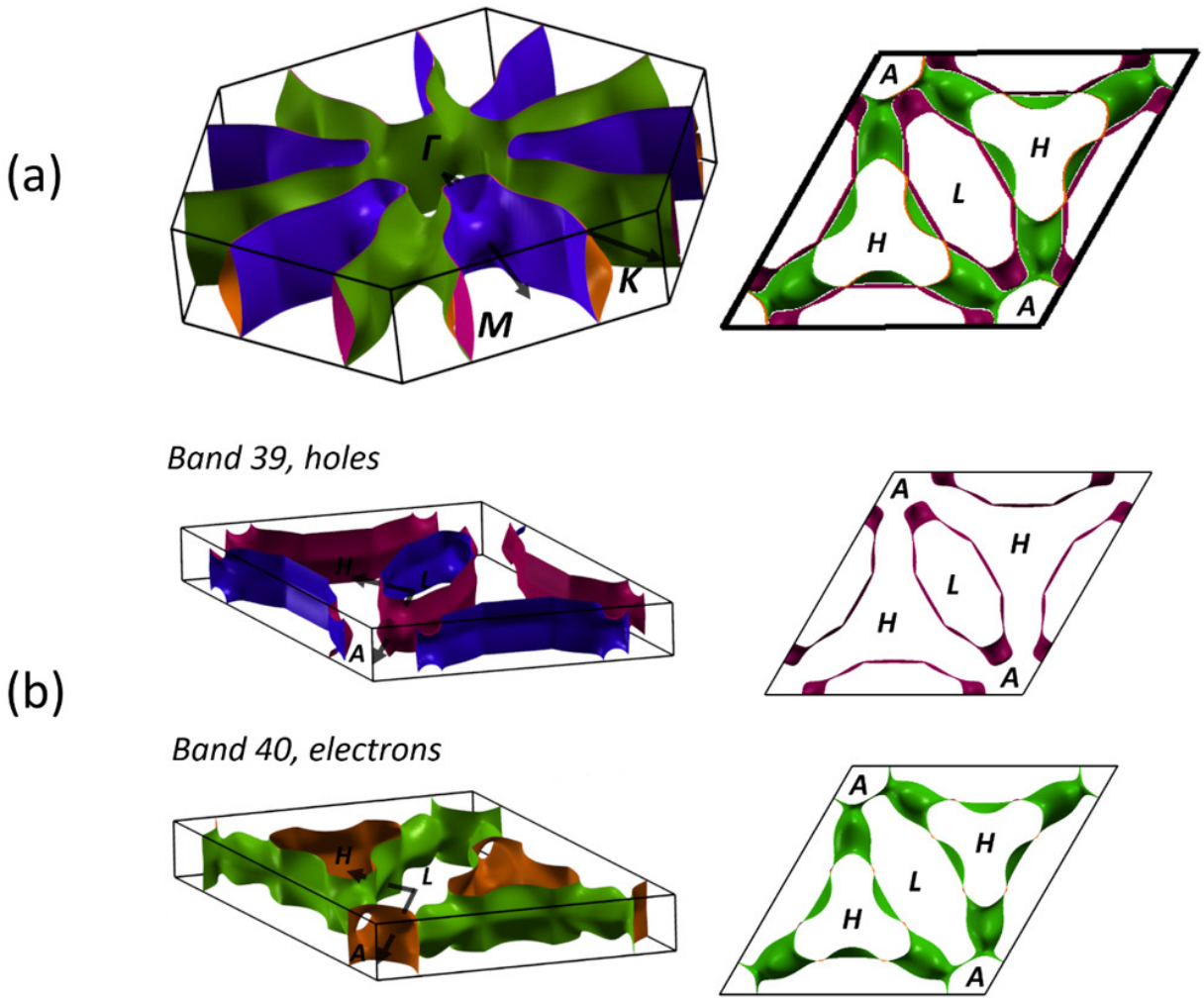

FIGURE 5.1: (a) V_2AlC FS calculated with WIEN2k, plotted in the first BZ (left figure) and in a cell centered on A (right figure). Only one electron band and one hole band are crossing E_F , and (b) shows the two bands separately. The overall morphology of the FS is rather complex, band 40 exhibiting 3D features with tubes perpendicular to the c axis (directed over AH) and tubes parallel to the c axis connected altogether.

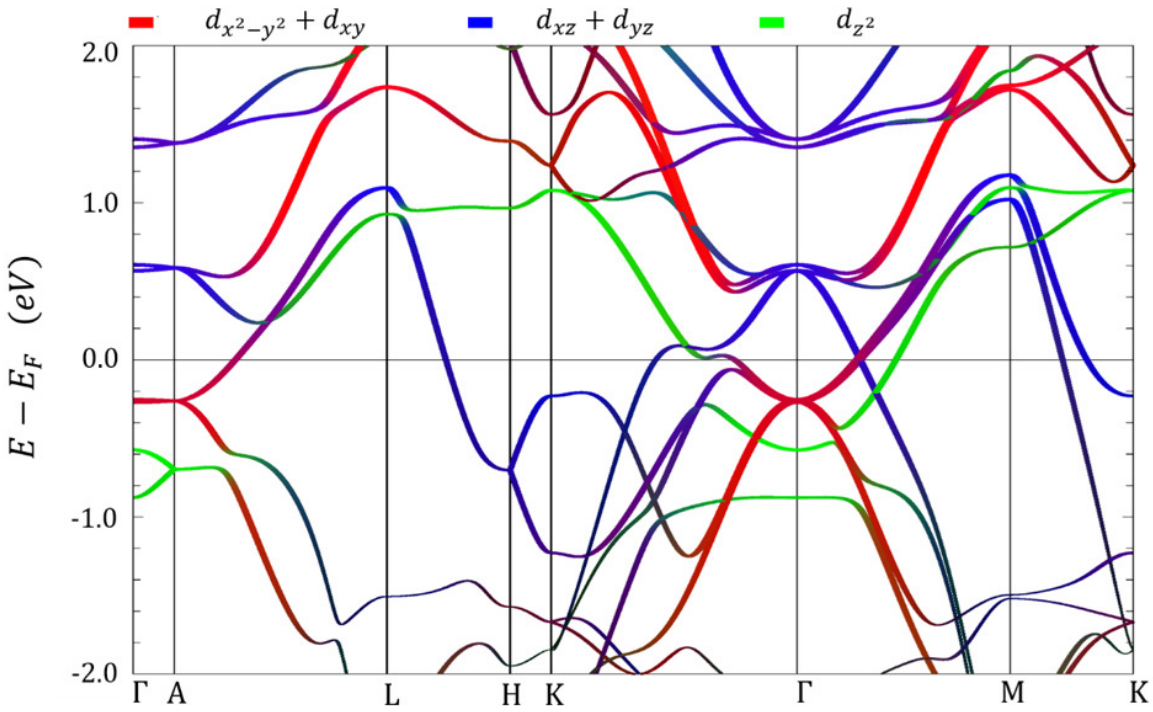

FIGURE 5.2: V_2AlC band structure as calculated by the WIEN2k software. E_F is chosen as the origin of energy. Colors refer to the orbital character of each band.

perpendicular to the c plane remain much smaller than the ones parallel to c. In contrast, band 39 exhibits quasi-2D features with tubes centered on M (L) points and a closed-loop-like feature between Γand M.

A qualitative analysis of the orbital character of each band is given by the colored band structure plots of figure 5.2. Since in MAX phases the electronic properties of the electrons at E_F are mainly determined by the d orbitals of the M atoms [1], those are the only ones considered here. The $\Gamma(A)$ centered tubes and the AH transverse tubes of band 40 show a mixture of vanadium d_{z^2} , $d_{xy} + d_{x^2y2}$, and $d_{xz} + d_{yz}$ orbitals. The inner part of the closed-loop feature of band 39 exhibits a strong d_{z^2} character. All other bands have almost no d_{z^2} contribution at E_F .

Regarding matrix element effects, phrased here as the angular and orbital dependance of the photoionization cross section, we followed the procedure we previously applied to the study of the Cr_2AlC electronic structure in chapter 3 [228]. As a first approximation, we only considered the d-orbital contribution to the ARPES signal and assumed a plane-wave final state to extract the differential photoionization cross section using the expression in equation (5.1).

As it is described in [228], d_{z^2} orbitals are the ones mainly contributing to the photoemission intensity at low angles. As our ARPES experiments were mainly performed for angles below 15°, we can expect that we would have an ARPES signal mainly for areas where the DFT FSs show a pronounced d_{z^2} orbital character. From a calculation of the photoemission cross section going beyond the plane-wave final-state approximation [228], one shows [182, 228, 237] that the d_{xz} and dyz photoionization cross sections are not totally negligible and may also contribute to the ARPES signal, especially near the edges of the first BZ and

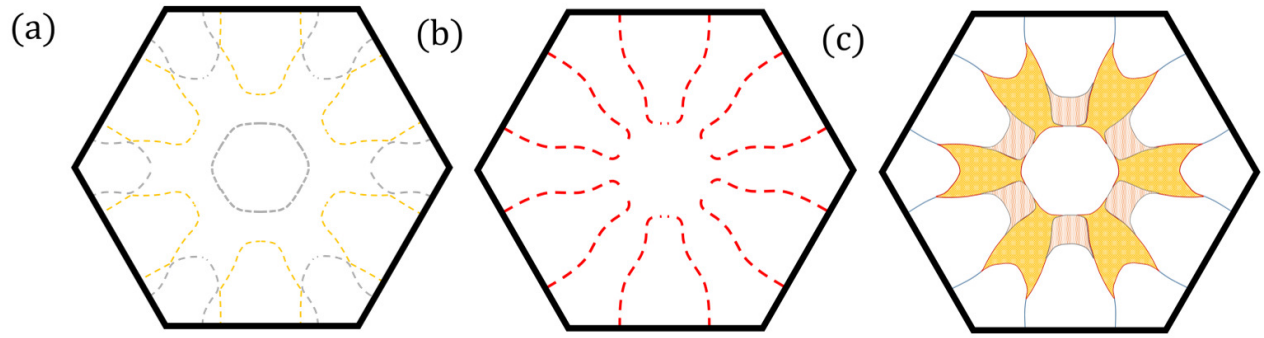

FIGURE 5.3: V_2AlC FS cut over Γ (a) and A (b) planes, respectively, both issued from DFT calculations. Yellow lines stand for band 39. Gray lines in (c) stand for band 40, and red lines stand for the degenerate bands 39 and 40 in the A plane. (c) The projection of the full V_2AlC FS with a d_{z^2} orbital character onto the horizontal plane. Areas with $d_{xz} + dyz$ character near the BZ boundaries are also represented.

beyond.

From those considerations, we are able to predict the output of ARPES experiments directly from the DFT FS. These expectations are summarized in figure 5.3, where we show a FS cut over the Γ (figure 5.3a) and A (figure 5.3b) plane and a projection onto the first BZ of the areas of the FS with a d_{z^2} character, plus the one with a $d_{xz} + dyz$ character located near the edges of the first BZ (figure 5.3c). All colored areas and lines appearing in figure 5.3c are expected to lead to a measurable ARPES signal.

5.2 Results and discussion

5.2.1 A three dimensional Fermi surface

As detailed below, our fairly simple DFT calculations with a standard GGA functional seem to give a very decent fit of the ARPES data, the main features of the FS, and of the BS near E_F being successfully reproduced (see figures 5.4–5.6). The ARPES cross section at E_F has been obtained for a polarization in the S-pol configuration and for an energy $h\nu = 100$ eV . The first striking feature of figure 5.4 is the wide broadening of the FS. It does not fit either the DFT FS cut across the Γ (figure 5.3a) or A plane (figure 5.3b). Rather than just exhibiting narrow Fermi lines as for Cr_2AlC [228], the FS signal rather appears as a whole surface in the (k_x, k_y) plane, and figure 5.3c seems indeed to reproduce the features of the experimental FS map of figure 5.4 in a very convincing way. As we mentioned before, figure 5.3c represents the FS projection onto a 2D plane of the full, 3D FS that is expected to give a substantial contribution to the ARPES map. The good matching between figures 5.4 and 5.3c, also shown in figure 5.4b, seems to corroborate two predictions from DFT: (i) there is a non-negligible k_z dispersion of the V_2AlC electronic structure in two restricted regions, and (ii) the d orbitals of the M atoms dominate electronic properties at E_F , as predicted for most MAX phases. It is worth noticing that the influence of k_z dispersion on the broadening of the ARPES signal has already been

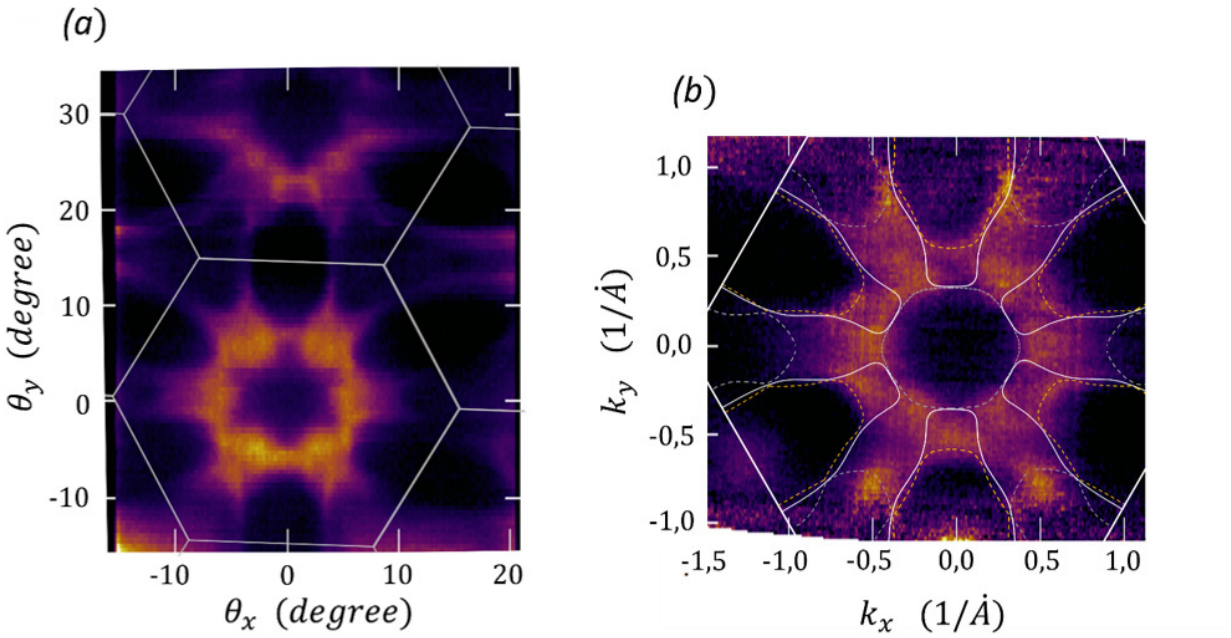

FIGURE 5.4: FS images of V_2AlC obtained by ARPES with S-pol configuration and $h\nu = 100eV$ photons. The image in (a) is the raw Fermi surface data for a high angular range in order to display several BZs. Image in (b) shows the FS in wave-vector units over a single BZ, along with a cut of the DFT FS across the Γ plane (dotted lines; the yellow one stands for band 39 and the white one for band 40) and across the A plane (full white lines).

extensively described by several authors [250, 251], but it is sometimes ignored for the study of 2D and even quasi-2D materials.

Damping of the photoelectron at the metal/vacuum interface and the finite value of the photoelectron mean-free path are effects that might account for the k_z broadening we observe [182, 250, 251, 252, 238, 184].

For the sake of further clarity, let us recall one last time the relationships between the electrons in plane and out of plane wavevector components ($k_{||}$ and $k_\perp$) and the angle at which photoelectrons are detected θ_k:

$$k_{||} = \frac{1}{\hbar}\sqrt{2mE_{kin}}sin(\theta_k) \tag{5.1}$$

$$k_\perp \approx \frac{1}{\hbar}\sqrt{2m(h\nu - \phi + |E - E_F|)cos^2(\theta_k) + V_0)} \tag{5.2}$$

We extracted a V_0 value of 22.5 eV from the period of the E vs $h\nu$ curve (see figure 5.6b) and took the work function ϕ equal to 4.3 eV for our calculations. The validity of equation (5.1) does not depend on the dimensionality of the electronic structure of the observed material. In contrast, equation (5.2) is in some cases not straightforwardly applicable to materials exhibiting a three-dimensional electronic structure [250, 251, 252, 184].

Assuming a FS with merely no three-dimensional features, the probed k_z component would then be a univocal function of $h\nu$ and one could be able to measure FS cuts for various k_z values by playing with the

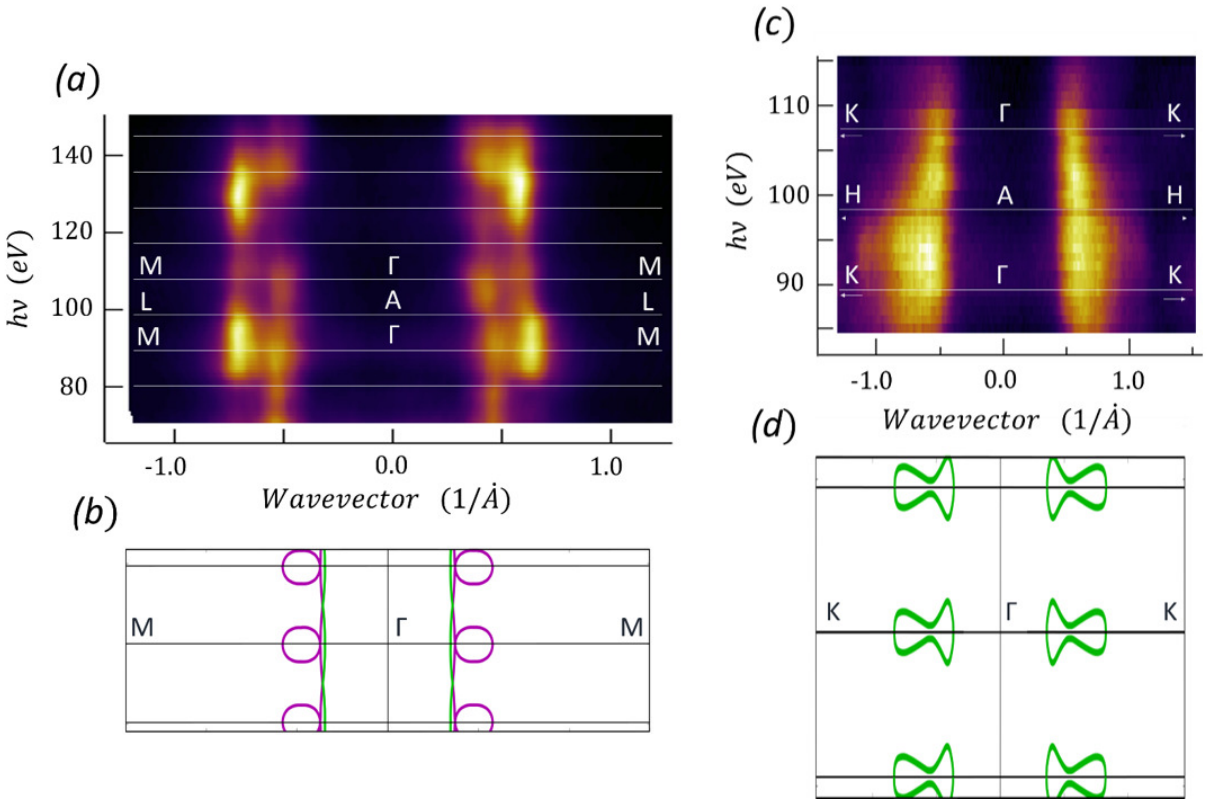

FIGURE 5.5: $A\Gamma ML$ (a, b) and $A\Gamma KH$ (c, d) ARPES photoemission maps and FS cuts from WIEN2K. Purple lines stand for band 39 and green lines for band 40. An acceptable matching between DFT and ARPES is found for ΓM, while photon-energy-dependent ARPES data over ΓK (c) fails to reproduce features from DFT, therefore corroborating the three-dimensional character of V_2AlC electronic structure along this direction.

photon energy. ARPES and DFT $A\Gamma ML$ and $A\Gamma KH$ cuts of the FSs are respectively given in figures 5.5a–5.5d. DFT and ARPES match for the $A\Gamma ML$ k_z cut, where the 2 FSs predicted by theory clearly appear on the experimental data. It therefore suggests that this part of the FS is quasi-2D. The enclosed loop structure we observe with DFT in the Γ plane could match the wide dots we observe in the ARPES map (see figures 5.5a and 5.5b). On the other hand, the lack of similarity between the $A\Gamma KH$ photoemission map and its DFT FS cut counterpart confirm that here equation (5.2) is not straightforwardly applicable in order to determine the k_z dependence of the FS topology (see figures 5.5c and 5.5d). The overall ARPES signal for the $A\Gamma KH$ map has roughly the same width as the maximum width of the DFT FS. We suggest that figure 5.5c would actually correspond to the DFT out-of-plane FS cut of figure 5.5d being broadened up to a point for which the signal of each FS tube perpendicular to the c axis (see figure 5.1) would sum up in order to form a continuous stripe over k_z. This argument comes in support of the 3D k_z dispersion of the FS we inferred from figures 5.3 and 5.4.

To ensure the bulk origin of the observed interplane FSs, we determined the ARPES band structure along the ΓA axis as shown in figure 5.6b. We observed a combination of intense (DFT calculation plot with solid line) and weak (DFT calculation plot with dashed line) dispersive features from 0.6 to 0.9 eV with a $\frac{4\pi}{c}$ periodicity along k_z axis. A similar intensity variation with the same $\frac{4\pi}{c}$ periodicity also appears on the

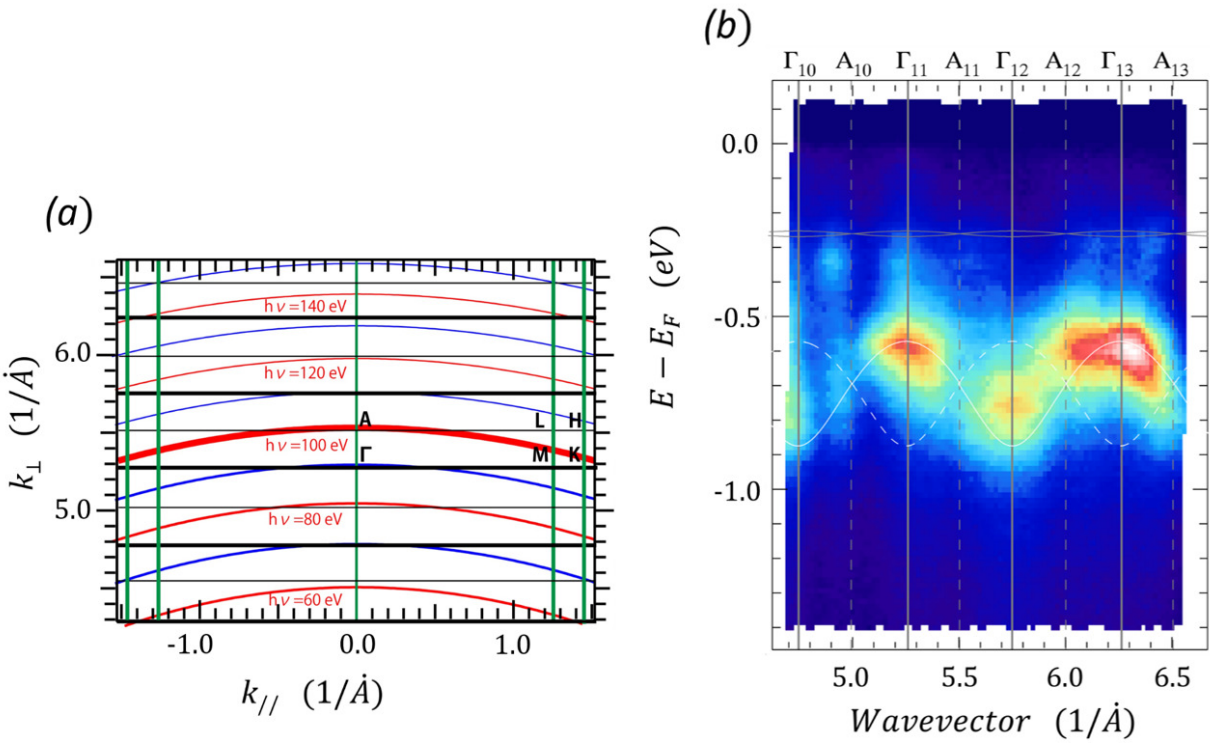

FIGURE 5.6: (a) Indicates which $k_\perp$ value is probed at a given $k_{||}$ value, for various values of photon energy $h\nu$. 100 eV corresponds to a $k_\perp$ wave-vector component lying between A and Γ planes. (b) V_2AlC band structure along ΓA. The good matching between ARPES data and calculations shows that bulk electronic states are observed. V_0 was extracted from the half period of the band.

$A\Gamma ML$ FS mapping. ARPES intensity variations with twice the periodicity of the expected band structure have frequently been observed in layered materials, owing to the difference of the transfer integral between the layers [255]. Thus, the ARPES band structure along the ΓA line shows a good correspondence with bulk DFT calculations.

As detailed above, there is a good overall matching between FS calculations and experimental ARPES data. Same conclusions are to be drawn for the band structure plots given in figure 5.7. DFT and ARPES bands seem to fit pretty well near E_F, both for $\Gamma K(AH)$ and $\Gamma M(AL)$ directions. Nearly all the DFT bands presenting a d_{z^2} character fit the ARPES signal, as well as the $d_{xz} + d_{yz}$ ones for higher angles. A few discrepancies between calculated bands and the ARPES signal are observed for lower energies. Due to k_z broadening, it is complicated to quantitatively assess these discrepancies. Furthermore, bands showing a strong $d_{xy} + d_{x^2-y^2}$ should barely not be observable by ARPES with our experimental configuration, as detailed in section 4.1.2.

5.2.2 Evanescent surface states revealed

In addition to the band structure results described above, we systematically observe a transient ARPES signal visible immediately after cleavage, the intensity of which continuously decreases until it almost totally

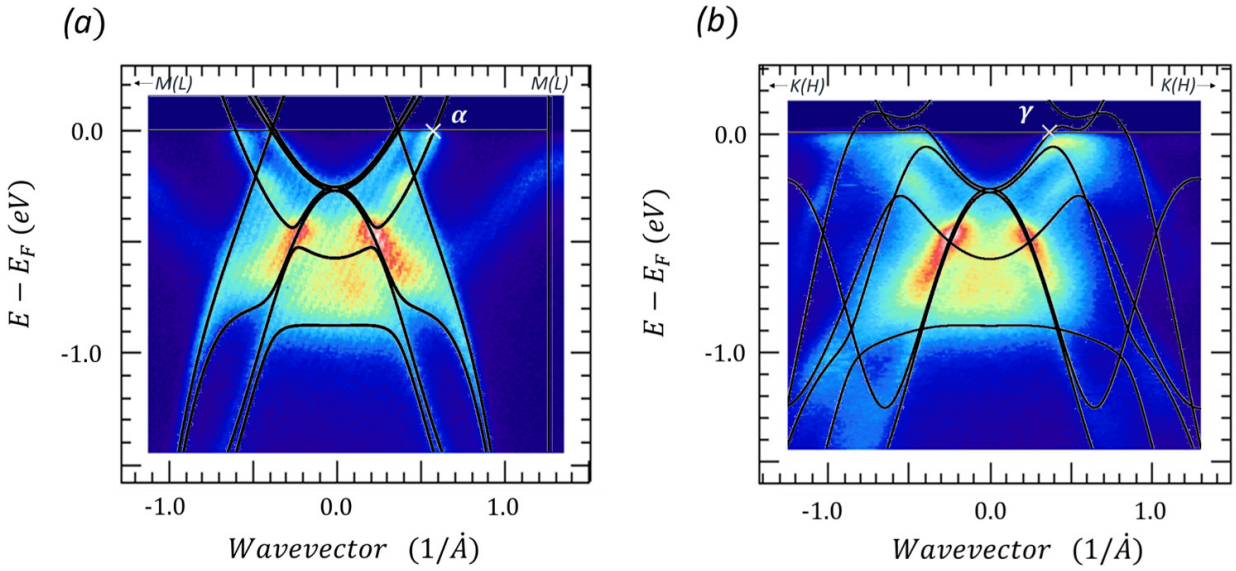

FIGURE 5.7: Band structure from ARPES over ΓM (a) and ΓK (b). Black lines are the output of DFT calculations. Experimental and theoretical Fermi velocities and effective masses are compared at the α and γ points.

vanishes, after several hours of exposure of the cleaved surface in UHV conditions. Figure 5.8a shows an ARPES image of the FS measured immediately after crystal cleavage and with a low pixel resolution so as to reduce the acquisition time (about 30 min). Figure 5.8c shows the band structure measured in the same conditions along a line crossing two M points, as indicated by the blue dotted line in figure 5.8a. Figures figure 5.8b and 5.8d are similar plots as in figure 5.8a and 5.8c, respectively. But, in contrast to the latter, they were acquired about 7 h after cleavage, with a better pixel resolution and thus a longer acquisition time (2 h). Immediately after cleavage a pattern appears at all three M points corresponding to measuring angles $\theta_y < 0$. In contrast, for positive values of θ_y , the intensity of these points becomes hardly measurable. This disappearance may be due to two different factors: on the one hand, positive θ_y values lead to a lowered intensity, due to the asymmetric dependence of the photoionization cross section of the d_{z^2} contributions on θ_y (See figure 4.5 in chapter 4, which shows the dependence of the cross section versus angle, and where the sign convention is reversed with respect to the one chosen in the present chapter). Figure 5.4 also gives a nice illustration of this cross-section effect: the permanent patterns of the second BZ (upper region of the ARPES image), obtained using positive θ_y values, show a marked decrease in intensity with respect to the ones obtained in the first BZ and for negative values. (Also note that none of the band structure patterns observed in figure 5.4 is subject to appreciable variations with time.) On the other hand, the disappearance of the signal at the M points with $\theta_y > 0$ could also be due to the instability of the pattern, assuming that it is the manifestation of an unstable surface state.

Interestingly, figures 5.8b and 5.8d show that after several hours, all band structure patterns taking place around the M points almost disappear, even for $\theta_y < 0$. They start vanishing about an hour after cleaving. This is a strong indication that those patterns are due to the existence of an unstable surface state. Its

passivation after some time and/or the cross-section effect makes it difficult to observe it in the upper BZ, but the three patterns observed after 30min at three M points demonstrates that it has a sixfold symmetry and that it contributes to form a band conserving the original lattice periodicity. It is therefore reasonable to attribute those patterns to the breaking of the d-orbital contributions of the unreconstructed V atoms, pointing perpendicularly to the cleavage surface and resulting in the formation of a surfacestate energy band. As expected in such a frame, it is worth noticing that the surface state contribution to the bands visible in figure 5.8b around the M points is also the only one not predicted by DFT calculations. Unfortunately, our data do not allow us to determine the nature of the passivation effect. A plausible origin might be oxidation of the unreconstructed V atoms.

5.2.3 Fermi velocities and anisotropies

From the band structure, we could extract the Fermi velocities and the effective masses at α and γ (see figure 5.7 for the respective positions of these points). Those values were extracted from the ARPES data following methods similar to what is described in [244] and in chapter 4 for Cr_2AlC. We also computed Fermi velocities and the effective masses from DFT calculations for various directions, and a summary of the DFT and the ARPES data is given in figure 5.9.

From the experimental slope at the Fermi level, we found a Fermi velocity of $2.81 \times 10^5 ms^1$for the main tubular FS of band 39 over $\Gamma M(AL)$ (α point), and $1.03 \times 10^5 ms^1$ for the central almost tubelike FS over $\Gamma K(AH)$ (γ point). They are of the same order of magnitude as the one found for Cr_2AlC [228], and significantly lower than for "good," ordinary metals. The discrepancy between DFT and ARPES is found to be less than 10 percents, the value extracted from ARPES being smaller. We extracted an effective mass of 0.719 m0 at γ for band 40, again quite close to the one given by DFT calculations. It is 5–10 times smaller than the Fermi level effective masses found for Cr_2AlC [228]. The very good agreement between the transport parameters extracted from DFT and ARPES gives confidence in the overall validity of this study. This again has to be put in contrast to the case of Cr_2AlC, where stronger evidence of a renormalization has been shown [228], which is believed to be a consequence of a strong electron-phonon coupling.

It is interesting to note that previous specific heat measurements indicate that electron-phonon coupling should be much more important for Cr_2AlC than for V_2AlC [1], a point which seems to be confirmed by our ARPES measurements. It also indicates a certain variety of electronic behavior within the 211 MAX phase family. One would note that the absence of band renormalization, probably accounting for a low electron-phonon coupling, combined with the low in-plane effective mass values found for any DFT or ARPES band of V_2AlC (as compared to those of Cr_2AlC [228]), is consistent with the V_2AlC in plane resistivity $\rho_{ab} = 3.8108\Omega m$ at 300K, about 2 times bigger than ρ_{Cu}, which is known to be the lowest among the MAX phases [159]. It is also worth noticing from figure 5.1a that the electron and hole bands are very closely nested into one another, with a very small separation between them. One therefore expects very similar transport

properties —relaxation time, Fermi velocities, etc.— for both electrons and holes. It is therefore not at all surprising that if used for interpreting magnetotransport, a conventional two-band model gives equal carrier concentrations and mobilities [38], and measurements lead to small Hall coefficients.

Considering the very good matching between DFT and ARPES data, one can try to extract semiquantitative information about the V2AlC FS morphology directly from the DFT data. Although using a software such as BOLTZTRAP would clearly give a better quantitative appreciation, we very roughly estimated the order of magnitude of the conductivity anisotropy from the three dimensional FS topology (see figure 5.1) and the Fermi velocities given in figure 5.9. For σ_{ab}, the products of the surface areas parallel to the c axis to

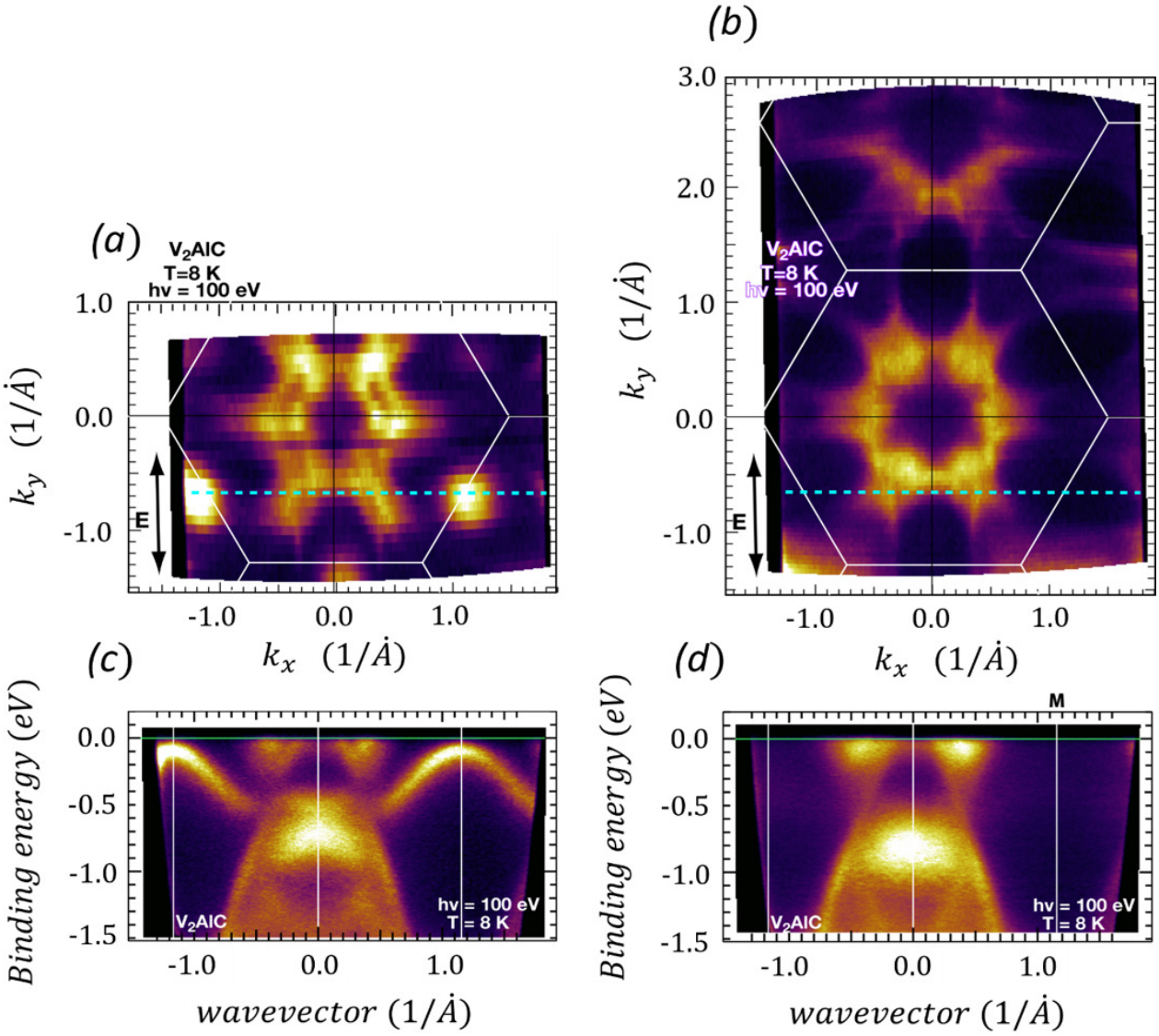

FIGURE 5.8: (a) ARPES FS mapping measured during 30 min with a low angular resolution and immediately after crystal cleavage. (b) FS mapping measured about 7 h after cleavage and during about 2 h on the same sample as in (a). (c) Band structure along the direction given by the blue dotted line in (a), and (d) band structure measured along the direction given by the blue dotted line in (b). A surface state not predicted by bulk DFT is clearly visible in (a) and (c). In (a) and (b), a small energy shift of 10 meV below E_F was chosen in order to enhance the signal due to the surface state, when present.

	Carriers	$v_F\ (m.s^{-1})$	m^*/m_e	$k_F\ (\AA^{-1})$
ΓM (DFT)				
Band 40	Electrons	1.84×10^5	–	0.345
Dirac points (bands 39, 40, 41)	Holes and electrons	$3{,}36 \times 10^5$ (M → Γ) $1{,}79 \times 10^5$(Γ → M)	–	[0.370]
Band 39 (α)	Holes	$2{,}90 \times 10^5$	–	0.670
ΓK (DFT)				
Band 40 (γ)	Electrons	1.11×10^5	−0.769	0.364
Band 40	Electrons	2.20×10^5	−0.725	0.610
Tube along AH (DFT)				
band 40	Electrons	4.1×10^5	−0.65	0.17
L centered tube (DFT)				
band 39	Holes	6.6×10^5	–	0.311
H centered tube (DFT)				
band 40	Electrons	2.79×10^5	1.08	0.27
ARPES				
Band 39 (α)	Holes	2.81×10^5	_	0.69
Band 40 (γ)	Electrons	1.03×10^5	-0.719	0.405

FIGURE 5.9: Fermi velocities and effective masses at E_F from DFT calculations and ARPES experiment. The observed effective masses as well as the Fermi velocities at the α, γ (see Fig. 6) points are compared to DFT bands . We also give the Fermi velocity and effective mass for various other FS parts: the transverse tube directed over AH (see figure 5.1), the triangular tube centered on H and parallel to the c axis, and the tube centered on L and parallel to the c axis (see figure 5.1). Two different values are given for the anisotropic band crossings (see figure 5.10), when one goes respectively from Γ to M and M to Γ.

the Fermi velocities normal to those surfaces were computed, then summed. For σ_c, the same method was applied to the surface areas seemingly parallel to the ab plane. The FS areas significantly contributing to σ_c are the six AH directed tubes of band 40 and the six enclosed looplike structures of band 39.

We then find a ratio σ_{ab}/σ_c roughly comprised in the interval of 17–45. Despite the very crude character of our estimation, it must be noted that our results are extremely far from the experimental anisotropy ratio measured in [159], whose values were ranging from 6000 to 9000. Three factors can possibly explain this apparent discrepancy:

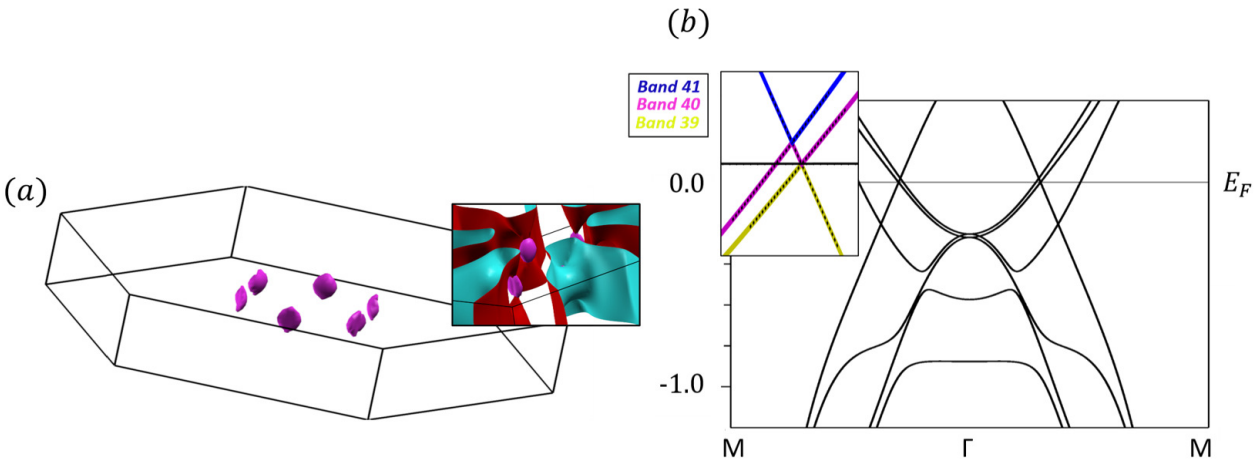

FIGURE 5.10: (a) Location of six linear band crossing points appearing roughly at 0.25ΓM, evidenced on the DFT FS by increasing the energy by 10 meV above EF . [For the sake of clarity, just the Dirac points have been kept in (a).] This shift reveals nearly punctual and anisotropic electron pockets which are located in the FS loop shown in the inset of (a). Those features are due to the presence of "double" band crossings also visible by plotting, e.g., the band structure along ΓM, as achieved in (b). Another band crossing is apparent around 0.27 eV below E_F.

(i) The relaxation time has no reason to be the same in the different tubular regions of the FS. (See, e.g., the interpretation produced in chapter 4 to assess the anisotropy of the electron-phonon coupling in the case of Cr_2AlC.) This might well increase the anisotropy by a substantial, additional factor.

(ii) The V_2AlC crystals measured in [159] were possibly too thin for allowing one to get a precise, quantitative estimation of the anisotropy ratio using the device structure and correction method expounded in [159].

(iii) The V_2AlC crystals investigated in [159] exhibit inplane stacking faults or partial delaminations, which could increase the resistivity value measured along c. (We note, however, that the x-ray diffraction patterns of these crystals (see chapter 3) did not indicate any substantial delamination, which would induce in a Laue pattern a noticeable spreading of the diffraction peaks, or even double peaks.)

Eventually, we briefly describe details observable nearby or at the closed-loop-like structure we obtain from DFT on the FS of band 39, in the ΓM direction. The origin of this strange morphological detail is made clear by the band structure plot over ΓM: A linear crossing-like structure appears at the Fermi level, where we observe the loop structure in the FS. Bands 39 and 40 are involved in the crossing at the Fermi level, and bands 40 and 41 in the one standing 20 meV above E_F . If one plots an isoenergy surface for bands 41 at an energy of around 30 meV above the Fermi level, one gets nearly punctual and anisotropic oval surfaces at the crossing point over ΓM(see figure 5.10; the highest velocity is in the ab plane and in ΓM direction). Further

investigations are needed to confirm the existence of this node, whether it might be considered as a socalled topological node, a potential 3D counterpart to a Dirac point and its possible impact on magnetotransport.

5.3 Summary

We presented an in-depth study of V_2AlC near Fermi level electronic structure. ARPES results are in excellent agreement with the output of our computations. The V_2AlC FS shows a noticable degree of anisotropy but far lower than expected from previous transport measurement studies [159]. The renormalization of the effective masses and velocities at the Fermi level appears to be quite small, in contrast with what we previously observed for Cr_2AlC [228]. This suggests that the electron-phonon coupling is weaker in V_2AlC than in Cr_2AlC. Coming back to the conclusion of chapter 4, we can now state that the quasi bidimensional nature of Cr_2AlC is not shared with its counterpart V_2AlC, nor the influence of electron-phonon coupling

Our results indicate that the hole and electron FSs are tightly nested into one another, possibly explaining the almost perfectly compensated character of this semi-metal, as observed from magnetotransport measurements [159]. We also reported the first observation of the electronic surface state of a MAX phase. Further investigations are needed to address some of its properties, such as the nature of a passivation process which makes the surface state to progressively disappear after several hours in UHV conditions. Despite the very different morphology of the near Fermi level electronic structures of V_2AlC and Cr_2AlC, one can wonder whether it is still possible to find a relation between them. Also, the puzzling linear band crossings spotted near E_F over ΓM ought be studied in greater detail.

Chapter 6

A unified description of (211) MAX phases based on rigid band models

As for chapter 5, the content of this chapter is mainly taken from another article [256] that was written by the author of this thesis. On the contrary to the two previous chapter, that each covered one specific phase, the present one takes a more global approach on MAX phase electronic structure and how the so-called rigid band models can describe whole subclasses within the MAX phase family.

Rigid band models (RBM) are indeed useful for describing families of materials where varying a parameter does not appreciably modify the electronic band structure but results in an appreciable sweep of the Fermi energy across the bands [257, 258, 259]. This parameter is typically a tunable atomic fraction of a given chemical element, which either directly enters into the composition of an alloy or a compound (see, e.g., [257, 258, 259, 260, 261]) or which is used for intercalating a nanolamellar phase (see, e.g.,[262, 263, 264]). Alternatively, it was noticed long ago that simple transition metals belonging to the same or neighboring groups could exhibit quite similar band structures, their electronic structure differing only by a shift in Fermi energy (see, e.g., [265]). Finally (as in this work), changing a chemical element in a compound belonging to a given family while keeping a similar band structure also justifies the use of a RBM [266, 267]. For the latter to be applicable, the symmetry of the crystal structure must not only remain unchanged from one compound (or composition) to the next but electronic correlations effects must also be small with respect to the electronic structure [268, 269, 270]. In contrast, when the structure is maintained the same but a noticeable change within the electronic structure is observed, the failure of the rigid band model is often viewed as a good indication that electronic correlations or other many body effects play an important role (see, e.g., [268, 269, 270]).

The aim of the study we present throughout this chapter is to demonstrate the applicability of rigid band models to the nanolamellar MAX phases. In particular, we focus on the subfamily of the 211 MAX phases, which we described in chapter one (See figure 2.1 for their unit cell). The similarity between the electronic structure of several 211 (and even 312) phases was noticed long ago: the calculated DOS profile

of one compound, once correctly shifted in energy, could be roughly superimposed over the DOS of another compound [1, 144, 151]. Here, we go one step further and combine DFT calculations to ARPES in order to show that not only the DOS but also the topology of the bands in reciprocal space is also conserved. All band structures are similar within a given A group and, quite remarkably, the Fermi surface of a given MAX phase can be deduced from ARPES measurements conducted on another phase simply by selecting the appropriate ARPES isoenergy surface. Additionally, the shift in energy required to obtain this agreement reasonably matches the shift in E_F predicted by DFT calculations. We will see that these results allow one to build a unified description of the electronic structure of MAX phases. Such a unified description was not obvious a priori, because the Fermi surfaces of different MAX phases can differ enormously (as predicted and measured in [228, 249], and described in chapter 4 and 5). It turns out that this difference is mostly accounted for by a simple shift in E_F .

Applicability of the rigid band model to MAX phases offers interesting perspectives. As detailed below, the band structure of those phases exhibits many band inversions, which result in the existence of several nodes or band crossings at different energy levels (As the linear band crossing in section 5.2.3). This leads, e.g., to the prediction of the presence of nodal lines and other topological nodes within MAX phase rigid band structure.

Such topological features were studied very early in the history of quantum and solid-state physics [271]. However, they actually laid dormant in the literature until the last two decades. They then sparked a renewed and now very strong interest (see, e.g., [272, 273, 274] for recent reviews) due to the resulting electronic properties they may generate, e.g., protected surface states, or the specific responses to electromagnetic excitations they may lead to [272]. These include Weyl, Dirac, and nodal line semi-metals [272, 273, 274], as well as other systems featuring intricate band structure specificities (see, e.g., [275] for a hybrid parabolic and Dirac-like dispersion at the degeneracy points or [276] for other semi-Dirac points, or [277] for surface Dirac node arcs). In particular, nodal lines are now actively studied in a number of 3D materials and can be divided into gapped and symmetry-protected lines, depending on whether spin-orbit coupling lifts the degeneracy at the crossing point or not (see, e.g., [274]). In principle, gapped nodal lines positioned at E_F favor the existence of a strong spin Hall effect, a desired property for generating spin currents in spintronic devices [274, 278, 279]. In the last section, we provide detailed theoretical and experimental evidence for the existence of such topological features in the V_2AlC phase (more precisely, a gapped nodal line slightly below E_F and a complex crossing point with some Dirac-like features at E_F). In MAX phases, such nodes are always accompanied by the presence of other, more conventional bands, but the possibility to change E_F appreciably by just changing the M element should allow one to position E_F at a given crossing point (this is predicted, e.g., in the case of the "simple" phases V_2AlC, Cr_2AlC, and Ti_2AlC). Combining conventional bands to nodal lines is indeed not expected to prevent one from obtaining a strong spin Hall effect (see, e.g., [279] and references therein). Hence, combining several M elements could possibly allow one to reach

other interesting topological nodes experimentally. The 211 MAX phases thus form a family of semimetals incorporating a variety of interesting topological features, which could reasonably be described by the use of a restricted number of rigid band models.

6.1 Rigid band model of M_2AlC MAX phases

6.1.1 Methodology

ARPES isoenergy surfaces and band structure mappings from Cr_2AlC and V_2AlC single crystals -corresponding to figures 6.1 and 6.3- are issued from the same experimental run as the data presented in chapter 4 and 5.

Additional ARPES experiments were performed by *Takahiro Ito* at the Institute for Solid State Physics (ISSP), University of Tokyo [280], at T = 35 K using a quasi-continuous-wave laser source ($h\nu = 6.994$ eV) (figures 6.12b, 6.12d, and 6.13b). Here, circularly polarized light was used in order to partially circumvent the low-photoionization cross section of some orbital contributions within the experimental range allowed by the detector. Energy resolution was set at about 5 meV. All calculations were performed with the full potential LAPW+lo method implemented within the WIEN2K software. The non-spin-polarized PBE GGA functional [207] was chosen. The following phases were chosen for computational analysis in this work (together with the references of the .cif files used for computations): Cr_2AlC [239], V_2AlC [5], Ti_2AlC [10], Nb_2AlC [281], Ti_2GaC [19], Ti_2GeC [10], and Ti_2SnC [10]. Wave functions were expanded up to a RKM cutoff parameter of 9 to make sure convergence was reached for all phases. For the same reason, a very dense $73 \times 73 \times 14$ Monkhorst-Pack cell was used. The Fermi surfaces were as usual calculated using X-CRYSDEN [240]. The level of convergence in energy was set to 0.001 mRy for Bader charge calculations with the WIEN2k AIM code.

6.1.2 Electronic structure of M_2AlC (M = Cr, V, Ti, Nb)

As outlined above, the combination of ARPES experiments performed on MAX-phase single crystals and DFT calculations makes it possible to test the RBM beyond the mere assessment of the density of states [228, 249]. This methodology allows us to study how the topology of the bands in reciprocal space (i.e., the band structure and the isoenergy surfaces) would evolve when going from one phase to another. We applied it to first-hand ensure the efficiency of RBMs to picture M_2AlC phases.

Before detailing the first step of our analysis, it is useful to briefly summarize briefly the results of chapter 4 and 5 [228, 249]: Regarding the ARPES spectra of Cr_2AlC, it was found that most of the features of the experimental FS were well reproduced by DFT calculations. It mainly consists of quasi two-dimensional tubes directed along c^*. The most noticeable discrepancy was an additional pocket observed at the point that accounts for a camel-back-like structure located just below E_F . Some renormalization effects were

also observed. V_2AlC FS determined by ARPES showed an even better level of consistency with DFT but was found to be much less bidimensional than Cr_2AlC. For Cr_2AlC as for V_2AlC, all ARPES spectra were found to be consistent with both the angular dependence of the photoionization cross section and the orbital characters of the bands predicted by DFT.

Figure 6.1 displays a section, i.e., a 2D cut or a projection for a specific reciprocal space plane (here the ΓKM plane), of the FS of three MAX phases (Cr_2AlC, V_2AlC, and Ti_2AlC). For each image, the ARPES intensity map and DFT results at ΓKM and AHL planes are plotted together. The specificity of all figures is that we do not directly superimpose the DFT of one phase to the ARPES image of the same phase. For each image, the DFT and the ARPES come from two different phases, but we apply to the DFT datas (or to the ARPES) an overall energy shift which allows us to optimize the matching between the DFT and the ARPES maps. In other words, if we start from the ARPES FS of a given phase, we find the appropriate energy shift in the band structure of another phase, which is required to obtain the best fit of the ARPES image, and plot the resulting DFT isoenergy surface. Alternatively, if we directly plot the DFT FS, then we probe the ARPES isoenergy surface of another phase for an energy value which allows us to fit the DFT FS. The ARPES maps are therefore plotted versus the FS or isoenergy sections over the Γ or A plane. Thus, the ARPES spectra of several phases are directly compared, at and below E_F , to DFT Fermi lines or isoenergy surface lines of other phases.

In figure 6.1a, the measured Cr_2AlC FS is compared to V_2AlC isoenergy lines 0.6 eV above the V_2AlC Fermi level, computed by DFT. They match to a remarkable extent. Even more strikingly, the V_2AlC isoenergy surface shows a pocket centered at Γ, a feature which was actually missing from Cr_2AlC DFT calculations but was spotted by ARPES in chapter 4 [228]. Similarly, in figure 6.1b one can verify that a Cr_2AlC ARPES isoenergy section at $E = E_F 0.56$ eV almost perfectly fits the V_2AlC DFT Fermi surface (The additional features around M are due to surface states appearing just after crystal cleavage, already observed and commented on in chapter 4 [249]). This ARPES isoenergy surface has a form that shows not only well-defined lines but also extended regions due to dispersion bands which are locally 3D, as expected for the V_2AlC FS. One can also check the very strong similarity existing between a direct ARPES measurement of the V_2AlC FS (figure 6.1c) and the shifted Cr_2AlC ARPES image of figure 6.1b. (A 45-degree rotation needs to be applied in order to take into account the difference in orientation of the two crystals for those two measurements.) We summarize DFT FS results in figure 6.2, where V_2AlC FS and isoenergy surfaces are plotted in 3D within the first Brillouin zone (BZ). By shifting upwards by 0.6 eV with respect to the V_2AlC Fermi energy, one obtains an isoenergy surface identical to Cr_2AlC FS, and by shifting downwards by approximately 1.14 eV, one obtains the Ti_2AlC FS.

The band structures (BSs) demonstrate a similar trend (see figures 6.3 and 6.4): the V_2AlC BS is recovered when shifting the Cr_2AlC bands by roughly 0.6 eV downwards. It is worth noticing that despite their strong resemblance, some discrepancies between shifted Cr_2AlC and plain V_2AlC DFT BSs remain [figures 6.3a and

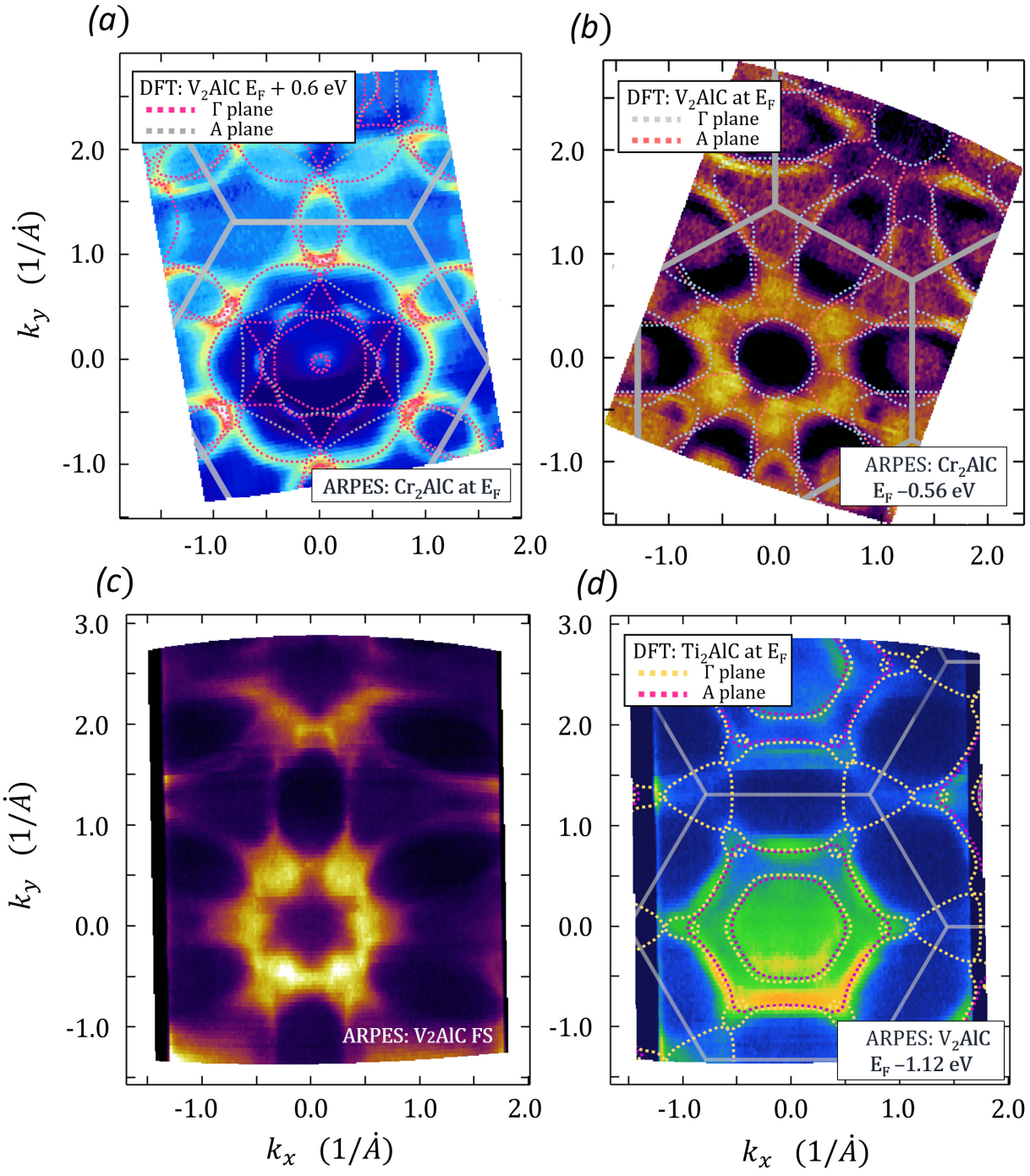

FIGURE 6.1: (a) Cr_2AlC Fermi surface mapping from ARPES plotted together with V_2AlC DFT isoenergy lines 0.6 eV above E_F. On (b), ARPES in-plane mapping of Cr_2AlC at $E = E_F 0.56$ eV is compared with V_2AlC DFT Fermi surface cuts. (c) V_2AlC ARPES Fermi surface mapping. When shifting the energy 1.12 eV below the V_2AlC Fermi level, we obtain the in-plane mapping in (d), which is plotted vs Ti_2AlC DFT Fermi surface cuts. Dotted lines stand for isoenergy lines over the Γ and A planes.

6.3c]. Some bands mismatch by a few meV, up to 160 meV for the camel-back structure centered on Γ. These differences actually correspond to what is observed between the ARPES BS of Cr2AlC and DFT calculations [228]. This means that the shifted V_2AlC band structure would actually be a better fit to Cr_2AlC ARPES BS than the output of previously presented Cr_2AlC DFT calculations (see chapter 4). This is indeed what is observed when directly comparing V_2AlC DFT BS shifted by 0.6 eV upward to Cr2AlC ARPES BS mapping over ΓM and ΓK (figures 6.4a and 6.4b). It also means that it is possible to navigate from V_2AlC to Cr_2AlC electronic structure just by applying an appropriate energy shift of about 0.56–0.6 eV.

Let us now turn ourselves towards what is observed when we shift the V_2AlC spectra below the Fermi energy: For $E = E_F$1.12 eV, we get the ARPES mapping shown in figure 6.1d, which is this time compared to the Ti_2AlC DFT FS. The two tubes centered on Γ (each of them actually stands for two different FSs that are almost degenerate) are electronlike while the plate-like FSs centered on K are hole pockets. We obtain a similar level of matching between the Ti_2AlC DFT FS and shifted V_2AlC ARPES image as for figures 6.1a

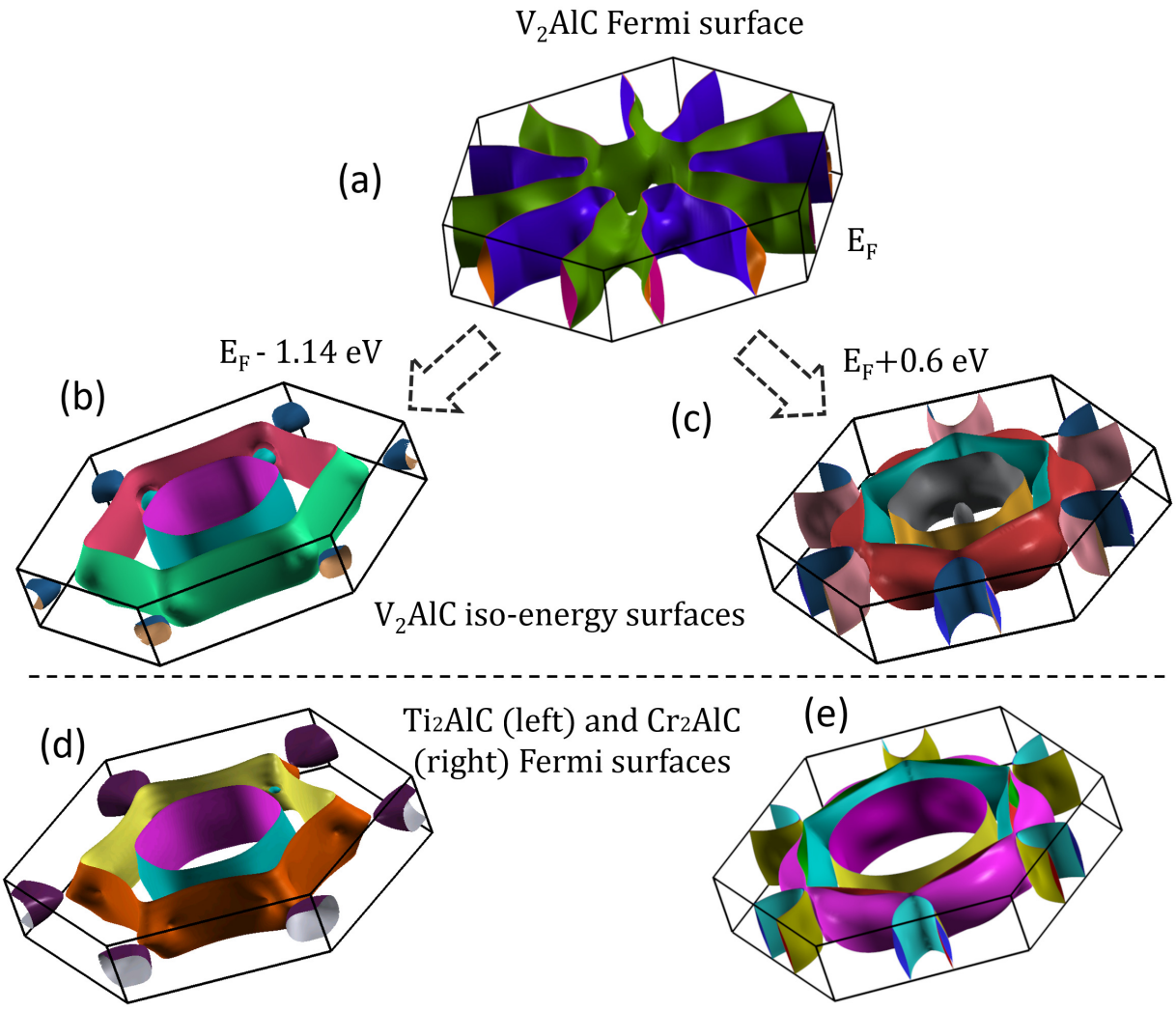

FIGURE 6.2: Overall relations between various M_2AlC Fermi surfaces and the isoenergy surfaces of V_2AlC. All energy shifts and isoenergy surfaces were computed by DFT calculations.

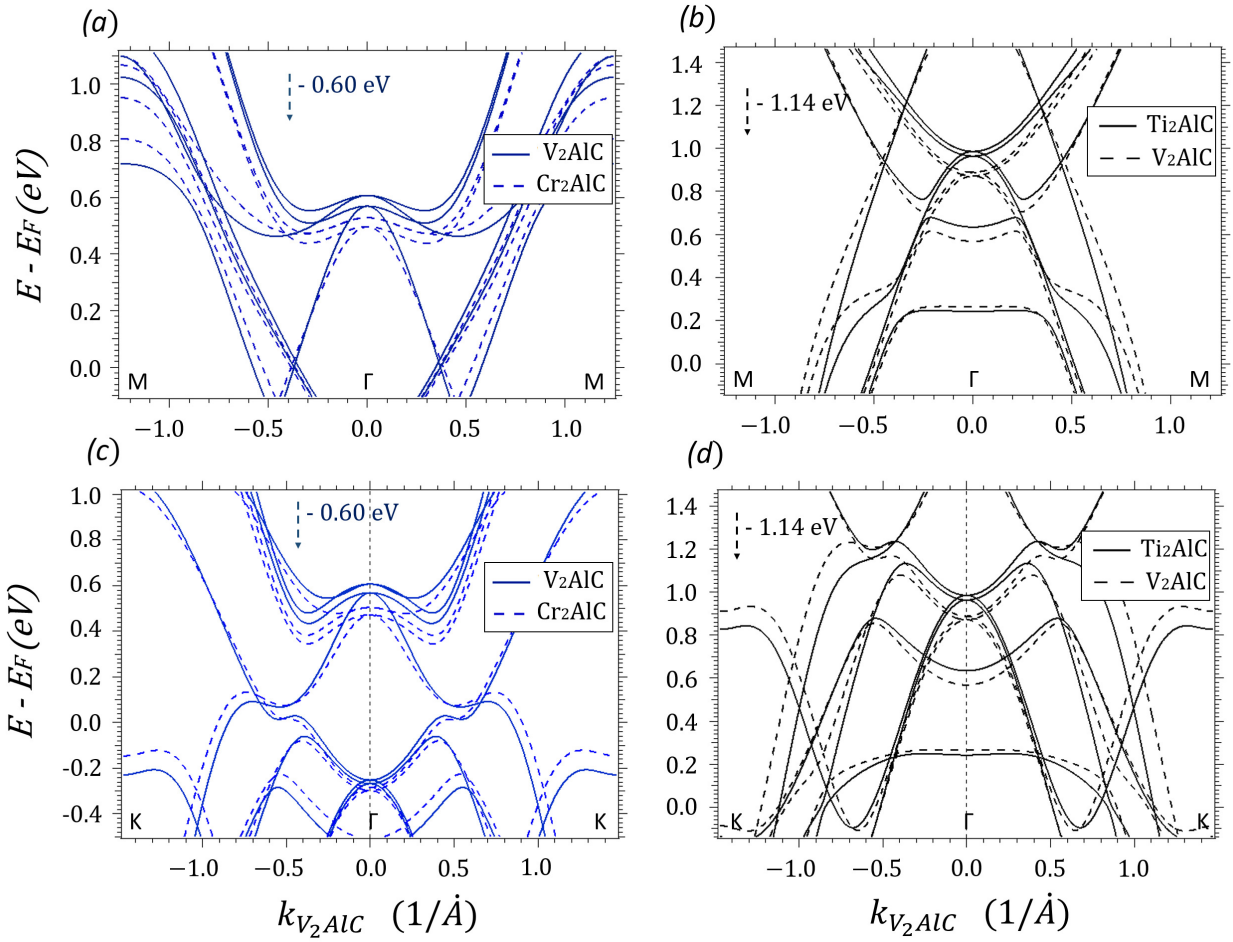

FIGURE 6.3: V_2AlC and -0.6 eV shifted Cr_2AlC band structures from DFT calculations, plotted together over ΓM (a) and ΓK (c). A 160-meV discrepancy is observed for the camel-back structure of Cr_2AlC near Γ, though the bands shape is nearly like V_2AlC. Similarly, Ti_2AlC band structure is plotted together with -1.16 eV shifted V_2AlC bands (b, d). For all figures, the BZs are scaled to that of V_2AlC.

and 6.1b. When shifted by 1.14 eV downwards, the V_2AlC DFT BS also happens to correspond to that of Ti_2AlC (figures 6.3c and 6.3d]. And once again, shifting the Ti_2AlC DFT BS by +1.16 eV accurately renders the ARPES BS map of V_2AlC over ΓM and ΓK (figures 6.4c and 6.4d). The energy required to go from V_2AlC to Ti_2AlC lies between 1.12 and 1.16 eV

These results clearly demonstrate that one can navigate across the electronic structure of the M_2AlC phases just by applying an appropriate energy shift. Figures 6.1 and 6.4 thus constitute a direct experimental verification of the applicability of RBMs to MAX phases.

So far, we only verified the applicability of the RBM when navigating horizontally across the periodic table, going from Ti to Cr, and not horizontally. Figure 6.5 summarizes the similarities found between the BSs and FSs of V_2AlC and Nb_2AlC, all obtained from DFT calculations. (Our Nb_2AlC crystals are presently too small for being probed by conventional ARPES.) The BSs are plotted over ΓM (figure 6.5a), and the Nb_2AlC BS is renormalized to the volume of the V_2AlC BZ. Both show very similar features, but the Nb_2AlC band structure seems to show sharper slopes than V_2AlC. It is almost as if one could obtain the V_2AlC BS from

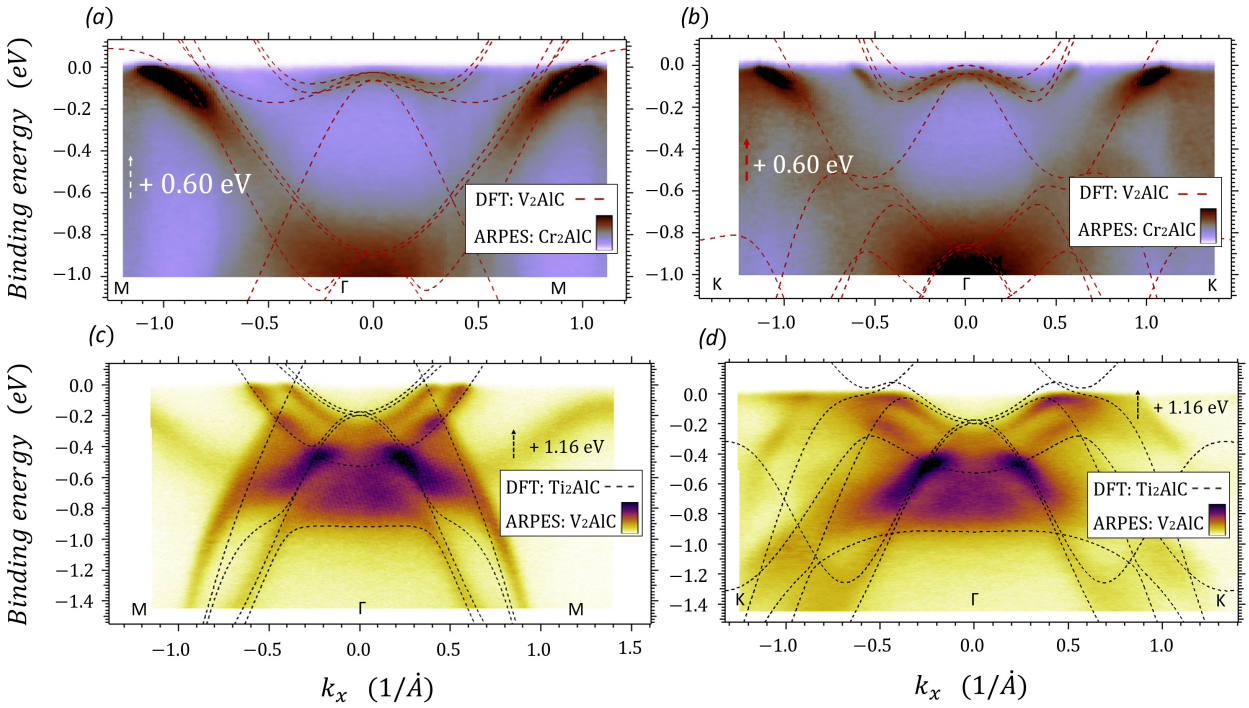

FIGURE 6.4: Cr_2AlC band structure from ARPES vs V_2AlC + 0.6 eV shifted band structure from DFT (red dotted lines) over ΓM (a) and ΓK (b). V_2AlC ARPES mapping over ΓM and ΓK is also compared with Ti_2AlC DFT BS, shifted by 1.16 eV. The energy shifts needed for the band structure to match are nearly the same as in figure 6.1.

that of Nb_2AlC by simply dilating the energy axis and expanding the wave-vector axis. The morphology of their bands at E_F seems quite similar (see figure 6.5b). Nb_2AlC would then share a FS nearly identical to that of V_2AlC. This is reminiscent of the so-called jungle-gym Fermi surface [282] that describes the V, Nb, and Ta elemental metals. Horizontally varying the M atom of MAX phases would leave the FS unchanged but would homogeneously distort the bands.

6.2 Demonstration of the applicability of the rigid band models

6.2.1 Charge transfer and rigid energy shifts

The energy shifts required to go from one M_2AlC phase to another one are large: 0.6 eV for the shift between Cr_2AlC and V_2AlC, and about 1.14 eV between V_2AlC and Ti_2AlC. Such shifts are quite large, as compared to the typical variation of the Fermi level that arises when doping a metal (adding a very high concentration of dopants would move E_F just by a few meV [40]) but of the same order of magnitude as those obtained between some elemental transition metals, when they can be described by the RBM [265]. If the origin of the changes in E_F is quite obvious for a doped metallic system [40], a slightly more involved explanation is needed to make sense of the energy shift values found in section 6.1.2 for the M_2AlC phases, and the corresponding analysis is described below.

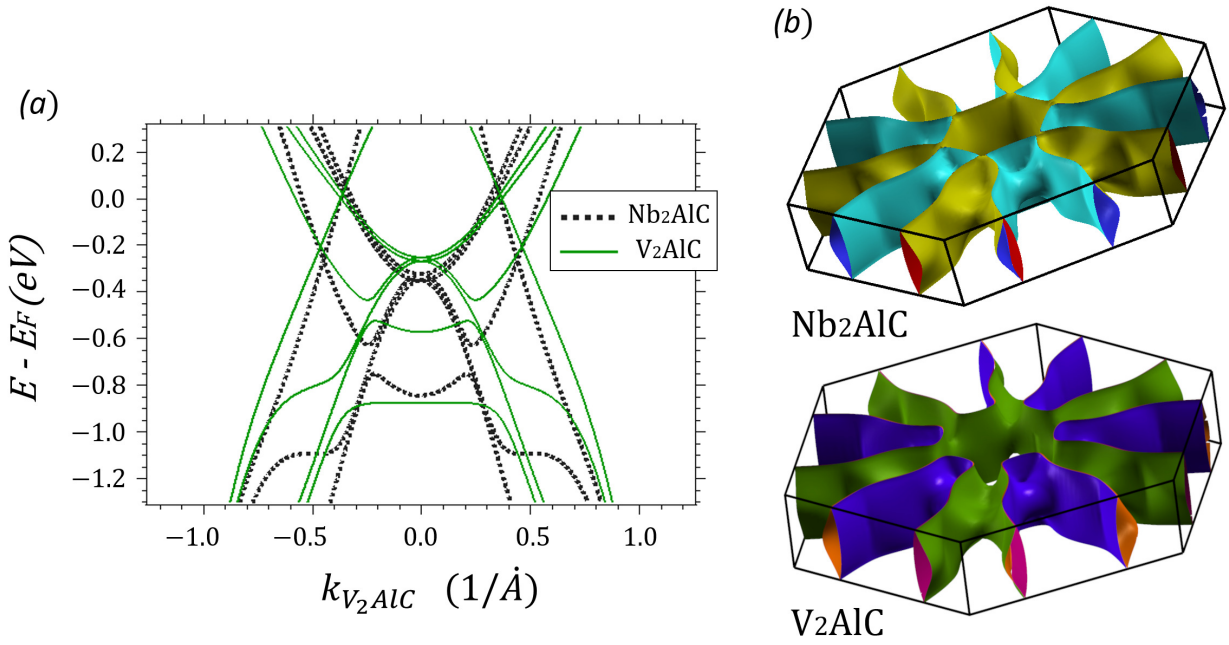

FIGURE 6.5: (a) The band structure of V_2AlC is compared to Nb_2AlC over ΓM. Their respective Fermi surfaces are given in (b).

In figure 6.6, the M atom partial densities of states (pDOS) of Cr_2AlC, V_2AlC, and Ti_2AlC are given. As expected from section 6.1.2, one can recover one of the pDOS from another pDOS by applying the same energy shifts as those required in figures 6.1–6.3. One can also integrate the pDOSs from the Fermi level of V_2AlC (Ti_2AlC) to Cr_2AlC (V_2AlC) and obtain quantities homogeneous to a charge per unit cell. Dividing the latter by the number of M atoms per unit cell (four), we obtain a quantity that would intuitively be considered as the charge variation on the M site when going from one phase to another, which we will refer to as $\delta Q_{DOS}^{M_Z \rightarrow M_{Z+1}}$. To elaborate a proof of this identity, we also compute the charge variations on the M sites by another method involving the computation of Bader charges [283]. We first compute the Bader charge of the different atoms in the M_2AlC, V_2AlC unit cell. As a quick reminder, the Bader charge is defined as the integral of the charge density across the so-called "Bader atom area," which refers to the volume of space within the charge density basin, centered on a given nucleus [283]. Both the charge density basin and the Bader charge are calculated with the AIM code embedded within WIEN2k. The Bader charges of all the atoms considered are then subtracted from their respective atomic numbers in order to obtain a quantity that we call Bader charge transfer or ΔQ^{Bader}. For a given atom Ω , the Bader charge transfer is thus be given by the following expression:

$$\Delta Q_{\Omega}^{Bader} = Z_{\Omega} - \int_{\Omega} \rho(\mathbf{r}) d\mathbf{r} \tag{6.1}$$

where Z_{Ω} stands for the atomic number of Ω, and ρ is the electron density of the system that is being integrated over the charge density basin of the atom Ω . We compile those values for the M_2AlC (M = Ti, V,

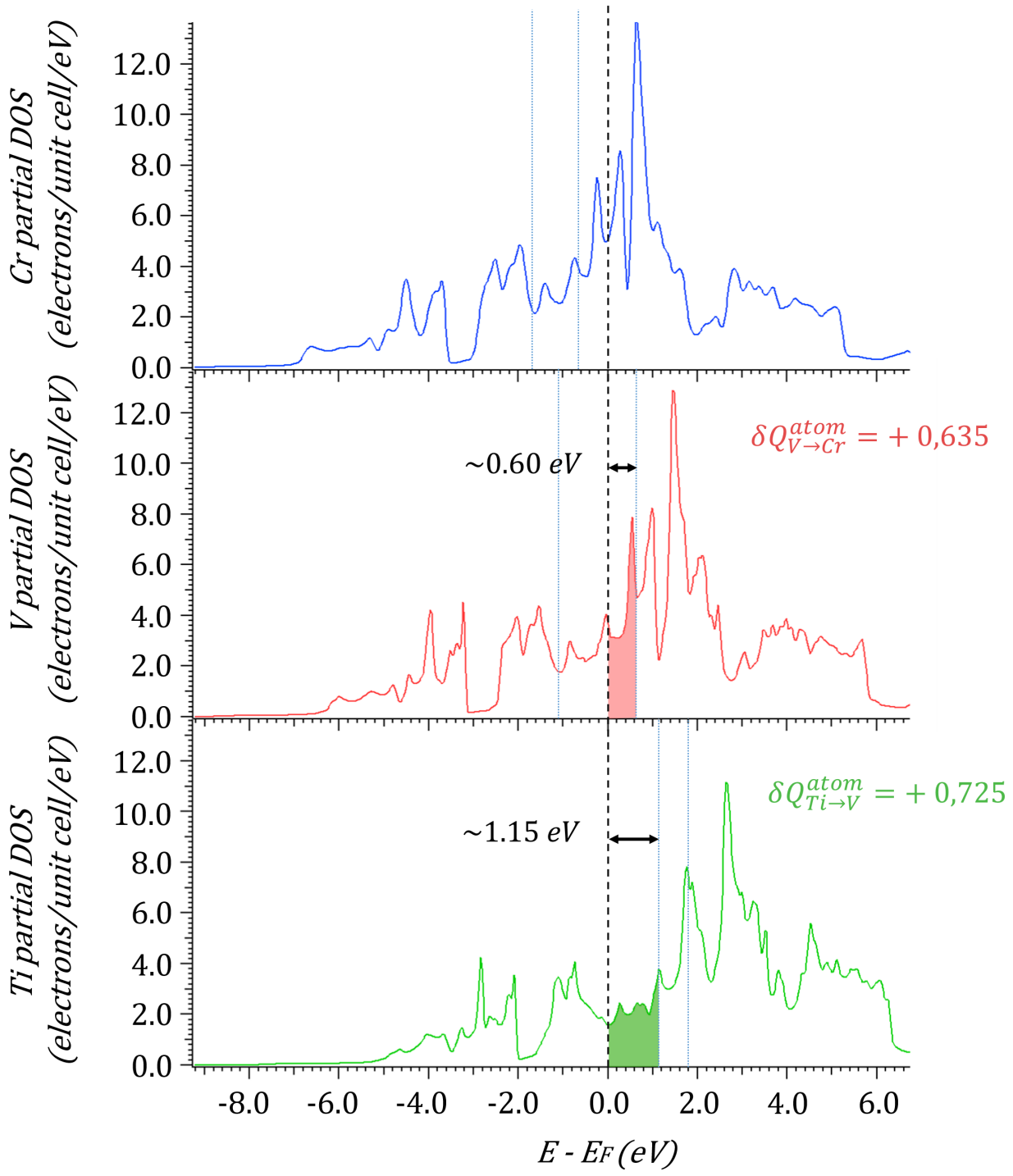

FIGURE 6.6: Various M_2AlC M atom partial DOSs, with M = Cr, V, Ti. DOSs are integrated from the Fermi level of V_2AlC (Ti_2AlC) to Cr_2AlC (V_2AlC) to get quantities homogenous to a charge per unit cell, which are later converted to a charge per M atom unit.

Cr, Nb) phases in figure 6.7 and 6.8.

We observe that we conserve the overall charge neutrality when summing up ΔQ^{Bader} of all the elements within a phase unit cell. In figure 6.7c, we plot the Pauling electronegativities of the M elements [284] against the ΔQ^{Bader} for those phases. A roughly linear relationship is revealed, thus demonstrating the consistency of our charge-transfer analysis.

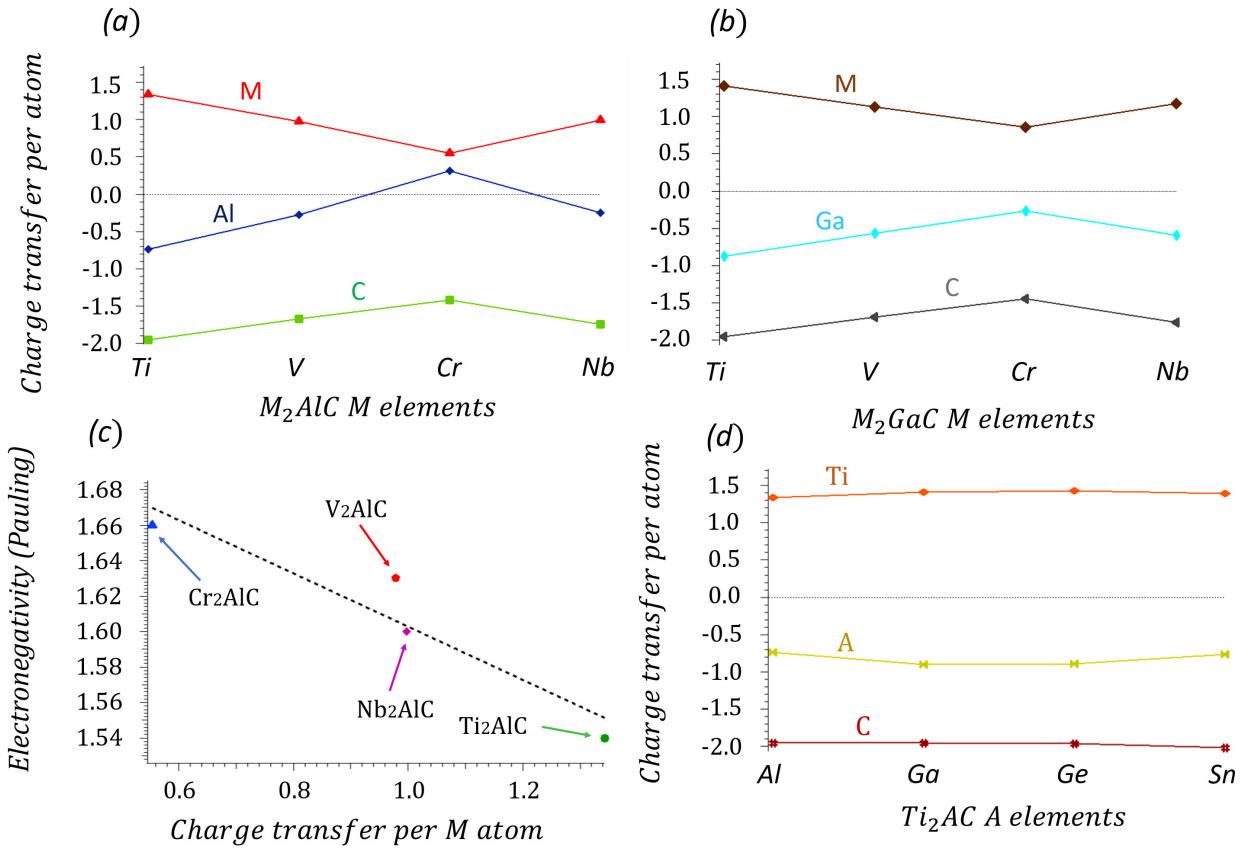

FIGURE 6.7: Charge transfer, or the difference between the electronic charge of atoms within MAX-phase unit cells (computed with the Bader method) and in vacuum, calculated for selected M_2AlC (a), M_2GaC (b), and Ti_2AC phases (d). In (c), a linear relationship is found between the M atom charge transfer for the Al 211 phases and the respective Pauling electronegativity of the M elements.

From the charge transfer on the M atom site, we can compute the local charge variation on the M site arising when changing the M element by one atomic number. It is given by the following expression:

$$\delta Q_{Bader}^{M_Z \rightarrow M_{Z+1}} = 1 + (\Delta Q_{M^{Z+1}}^{Bader} - \Delta Q_{M^Z}^{Bader}) \tag{6.2}$$

where M_{Z+1} and M_Z would, for example, stand for the vanadium and titanium atoms. All values of $\Delta Q_{M^{Z+1}}$ are tabulated in figure 6.8, together with the $\Delta Q_{M^Z}^{Bader}$ of the M elements and the $\delta Q_{DOS}^{M_Z \rightarrow M_{Z+1}}$ integrals of the pDOSs within the energy intervals of $\delta E_{DOS}^{M_Z \rightarrow M_{Z+1}}$. The $\Delta Q_{M^Z}^{Bader}$ differs by less than 0.1 electrons/atom from $\delta Q_{DOS}^{M_Z \rightarrow M_{Z+1}}$ (see figure 6.8). This means that the $\delta Q_{DOS}^{M_Z \rightarrow M_{Z+1}}$ integrals over the $\delta E_{DOS}^{M_Z \rightarrow M_{Z+1}}$ energy shifts intervals can be associated to the charge transferred from the M atom site when going, for example, from Ti_2AlC to V_2AlC.

The energy shifts experimentally determined in section 6.1.2 can thus be understood both in terms of charge transfer and as the occupation of the states of the rigid electronic structure in the $\delta E_{DOS}^{Ti \rightarrow V}$ interval. This opens up the possibility of tuning the position of the Fermi level on the M_2AlC BS over a wide energy range just by changing the nature of the atoms on the M sites. We note that the applicability of the rigid band model

to M_2AlC phases is far from obvious because of the implication of *d* orbitals in M_2AlC's electronic structure. These could intuitively lead to non-negligible electronic correlations and to a dramatic failure of the RBM. But the success of the RBM at describing M_2AlC phases strongly suggests that electronic correlations do not play a key role in the electronic structure of many 211 MAX phases (at least) in a given window around the Fermi energy values, as long as the atomic number of the M atom remains small enough (i.e., 211 phases avoiding, e.g., Ta, W, etc.) [268, 269, 270]. Here, an important word of caution must be offered to readers. In this study, and as for the case of Cr_2AlC in chapter 4, we did not need to account for magnetic ordering nor did we have to use a DFT+U approach for the DFT calculations in order to produce good fits of the band structure and FS as measured by ARPES. However, it must be clear that for some Cr-based compounds such as Cr_2GaC, a nonmagnetic configuration yields very inaccurate results for a range of other properties, notably, elastic (see, e.g., a review of such results in [22] and references therein). And in the case of strongly magnetic MAX phases or derivatives such as iMAXs or 4473 phases (see chapter 2), any property clearly requires taking magnetism in the DFT approach explicitly into account. As a consequence, the RBM approach can in no case be extended to other properties than band structure without a careful comparison of theory and experiment.

6.2.2 Global picture of 211 MAX phase rigid band models

Figure 6.9 is a summarizing picture of the rigid band model that describes M_2AlC phases. The isoenergy surfaces that correspond to Cr_2AlC, V_2AlC (Nb_2AlC), and Ti_2AlC Fermi surfaces are appointed to their relative positions on the rigid band structure. All of them were computed by DFT. Note that several band crossings are observed in figure 6.9, notably at the V_2AlC Fermi level over ΓM (red line) and at the Ti_2AlC Fermi level over ΓK (green line); other crossing points also appear between these two energy positions. In [249], a linear crossing has been predicted within the V_2AlC BS, at E_F. It originates from a band inversion

	ΔQ^{bader} $(e/atom)$	$\delta Q^{bader}_{M^Z \to M^{Z+1}}$ $(-e/atom)$	$\delta Q^{DOS}_{M^Z \to M^{Z+1}}$ $(-e/atom)$	$\delta E^{DOS}_{Z \to Z+1}$ (eV)	$\delta E^{FS}_{Z \to Z+1}$ (eV)	$\delta E^{BS}_{Z \to Z+1}$ (eV)
Ti2AlC	1.343	0.635	0.725	1.14	1.12	1.16
V2AlC	0.979	0.575	0.635	0.60	0.60/ 0.56	0.60
Cr2AlC	0.554	–	–	–	–	–

FIGURE 6.8: In column 1, the charge-transfer values from the Bader method for the M atoms of M_2AlC phases (M = Cr,V,Ti) are tabulated. In column 2, we give the charge variations on the M site when going from one transition metal to another, also calculated with the Bader method. Column 3 stands for the integrals of the M atom partial DOSs over the energy intervals of column 4. These intervals are alternatively extracted from Fermi surface (column 5) or band structure rigid energy shifts (column 6).

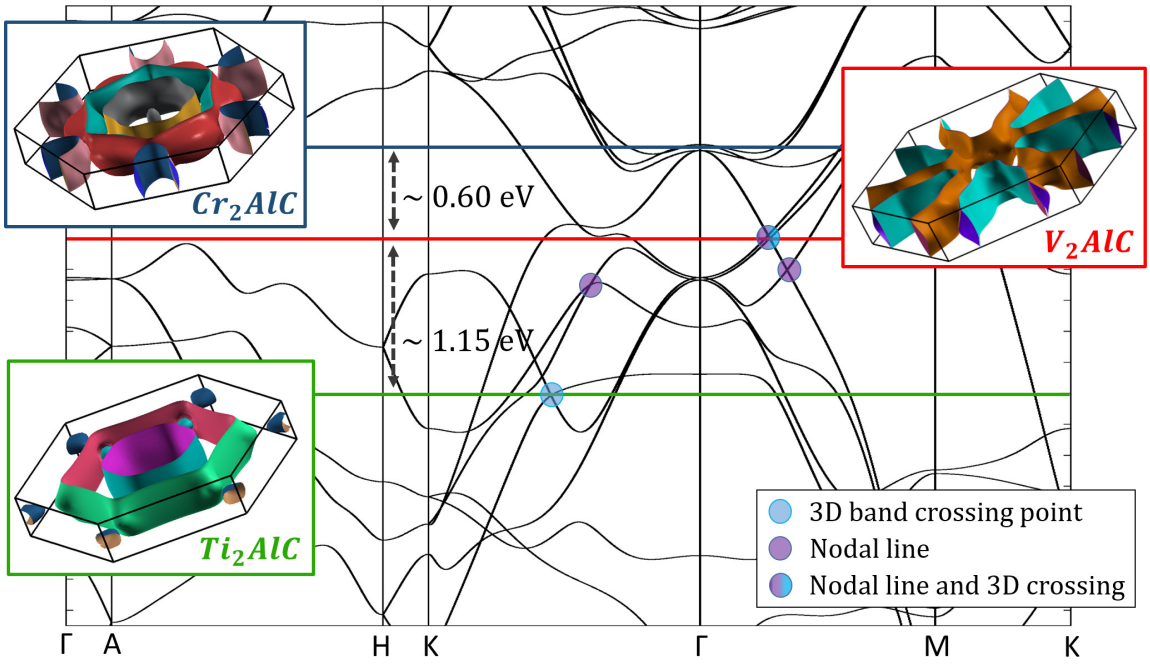

FIGURE 6.9: A summarizing picture of the rigid band model describing the M_2AlC phase's electronic structure. Band crossings are observed at V_2AlC and Ti_2AlC Fermi levels. Crossings that might account for 3D linear crossings or nodal lines are located in between those two energy levels.

involving bands with a $d_{x^2y^2} + d_{xy}$ and a $d_{xz} + d_{yz}$ orbital character, and some tiny weight from p orbital of the Al bands. Similar Ti_2AlC band crossings occurs at E_F, as well as some nodal lines like features which can be observed between the V_2AlC and Ti_2AlC Fermi levels (See section 6.3.1). The bands involved in those band crossings exhibit a mixture of different M d orbitals, also with a small weight of $p_x + p_y$ for some.

Here, we do not want to give an exhaustive description all of these nodes, as the next section is devoted to provide both detailed theoretical and experimental data to show the existence of two such features (a nodal line below E_F and an apparent semi-Dirac-like band crossing at E_F) in the particular case of V_2AlC. If the rigid band approach is valid, alloying on the M site (with Ti or V) or controlling the vacancy concentration would allow one to navigate between several such band crossings by applying simple rigid band shifts. The applicability of the rigid band model could also guarantee that the bands would be conserved even if the M sites were randomly occupied by different transition-metal atoms [260]. One should note that synthesis of 211 phase solid solutions or ordered phases with several and differents Ms is already well described in the literature, as it is well described within the section 2.2.2 of this manuscript and the references therein. These results suggest that MAX phases could open up avenues for physicists to study gapped nodal lines and other Dirac-like band crossings, as the possibility to tune the Fermi-level position on the M_2AlC rigid band structure would make a considerable number of band crossings experimentally accessible (see Fig 6.9). Similar studies have been performed on doped semiconductors, where Dirac points were observed at higher energy [285, 286].

The applicability of the rigid band model to M_2AlCs brings up many avenues for further research and could be generalized to other 211 phases with different atoms on the A site. In figure 6.10, the BSs of Ti_2AC (A = Al, Ga, Ge) were computed over ΓM and ΓK (see figures 6.10a and 6.10b). Ti_2AlC and Ti_2GaC BSs are very similar, sharing bands with the same features at all energies, and nearly no shifts are required for them to match. A few minor discrepancies still remain, as some Ti_2GaC bands are locally displaced upwards or downwards from Ti_2AlC by a few tens of meV. After renormalization of the band structures to the Ti_2AlC BZ, almost no discrepancies in momentum seem to appear between Ti_2AlC and Ti_2GaC bands. Their FSs are also similar, with the same bands being involved at E_F . The main discrepancy appears in the hole pocket centered on K. For Ti_2GaC, it has the shape of a torus centered on K, whereas it is more of a plain triangular plate for Ti_2AlC. The Bader charge transfers were calculated for all atoms involved in Ga-based 211 phases (figure 6.7b), and they follow the same trend as the Al phases (figure 6.7a). In contrast, Ti_2GeC BS diverges from its counterparts. No meaningful energy shift linking it to Ti_2AlC has been found. Even the number of bands involved in its FS is different, as is its overall FS topology. One should note that both Ga and Al belong to column IIIB of the periodic table, and their respective Ti_2AC phases are described by nearly identical BS and FS, while Ge belongs to column IVB and Ti_2GeC show a BS very different from the two others. This implies that M_2GaC and M_2AlC phases will likely be described by a very similar rigid band model, while a very different one would be needed for any M_2GeC phase. The following trends can then be intuited:

211 MAX phase for which the A element belongs to a single column of the periodic table will be described by a single RBM, and keeping the same M element while changing A over this column will not lead to any rigid energy shift. Only five rigid band models, one for each A element column, should then be needed to describe all the existing 211 MAX phases [1]. The charge transfers for the Ti_2AC's (A = Al,Ga,Ge,Sn) have been computed (figure 6.7d), and no significant difference in terms of charge transfer is observed between them.

6.3 Investigating topological nodes within V_2AlC rigid band structure

In this section we wish to illustrate the interest of using the rigid band model for guiding Fermi-level tuning close to one of the particular topological features the model contains. We focus on two particular such points or lines because, being located at or close to E_F, they may be experimentally probed within the ARPES spectra of V_2AlC single crystals. However, it is worth noticing that the RBM is not limited to those two points, as it contains other similar band crossings. V_2AlC is predicted to exhibit a crossing point at E_F (shown in figure 6.9 and hereafter designed as α) and a nodal line predicted by figure 6.9 to cross $A\Gamma ML$ plane about 0.2 eV below E_F. Although the $P6_3/mmc$ space group is nonsymmorphic, this particular nodal line does not lie at a BZ boundary, so that is not symmetry protected against perturbations. This line is thus expected to be gapped by spin-orbit coupling [274, 287]. For similar reasons, the crossing point with Dirac-like features is

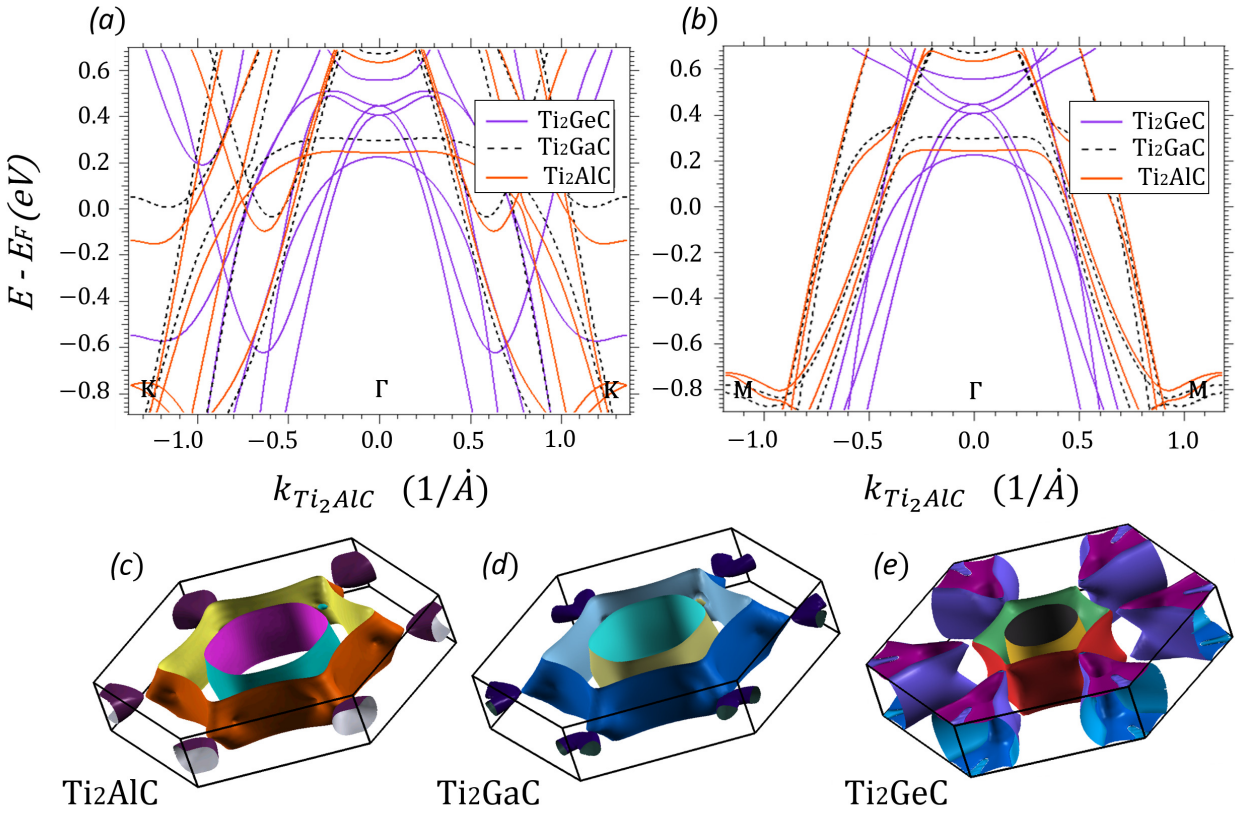

FIGURE 6.10: The band structure of several Ti_2AC phases (A = Al, Ga, Ge) over ΓM (a) and ΓK (b). The FSs of these compounds are plotted in (c), (d), and (e).

also expected to be splitted. Here we use DFT in order to estimate their value and assess whether they have a strong impact on the Dirac-like dispersions evidenced at those particular band crossings. Besides, those gaps are expected to depend on the element M involved in a particular phase, and below we give values corresponding to only M = V.

6.3.1 Evidence of a nodal line within $\mathbf{V_2AlC}$ ARPES and DFT spectra

Let us first focus on the nodal line (labeled as β at its intersection with ΓM). It can be theoretically evidenced by plotting an isoenergy surface located slightly below the purple points observed in figure 6.9 along ΓM and ΓK. The resulting plot is shown in figure 6.11b. In addition to conventional bands, one obtains a closed loop with a slightly varying diameter. The latter variation is due to the fact that although the nodal line lies exactly in the Γ plane, it slightly varies in energy in the (k_x, k_y) plane (see, e.g., its intersection points along ΓM and ΓK appearing in figure 6.9). It is therefore convenient to visualize it in the (k_x, k_y, E) space, as illustrated in figure 6.11a. Such a variation is not an exceptional finding and is, e.g., already described in [277, 278, 279] for other materials. The line is located about 0.2–0.3 eV below E_F .

Before showing experimental evidence for the existence of this line using ARPES data, it is worth describing the BS predicted by DFT, not only as a function of in-plane wave-vector coordinates k_x and k_y but

also with k_z as a parameter. In a 2D system devoid of any dispersion with k_z, a given cut of the ARPES signal along a particular in-plane direction in reciprocal space is formed of "simple" lines which directly correspond to the band structure. However, and as mentioned in chapter 5, for given k_x and k_y values, energy dispersion with k_z gives rise to a signal broadened in energy, the well-known "k_z-broadening" effect [250, 251]. The signal is dispersed over an area in the cut which is limited by the dispersion in k_z over a Brillouin zone. Roughly speaking, a well-defined line indicates that the corresponding band is 2D, and a broad region is the sign that the band is 3D [250, 251]. It is thus important when plotting the DFT band structure along a particular in-plane crystallographic direction, such as, e.g., ΓM, to plot a full set of dispersion lines corresponding to values of k_z ranging from 0 to a value equal to ΓA and not limited to, e.g., $k_z = 0$, as done in figure 6.12. Figure 6.12a shows such a set along ΓM and figure 6.12c along a line intercepting the crossing

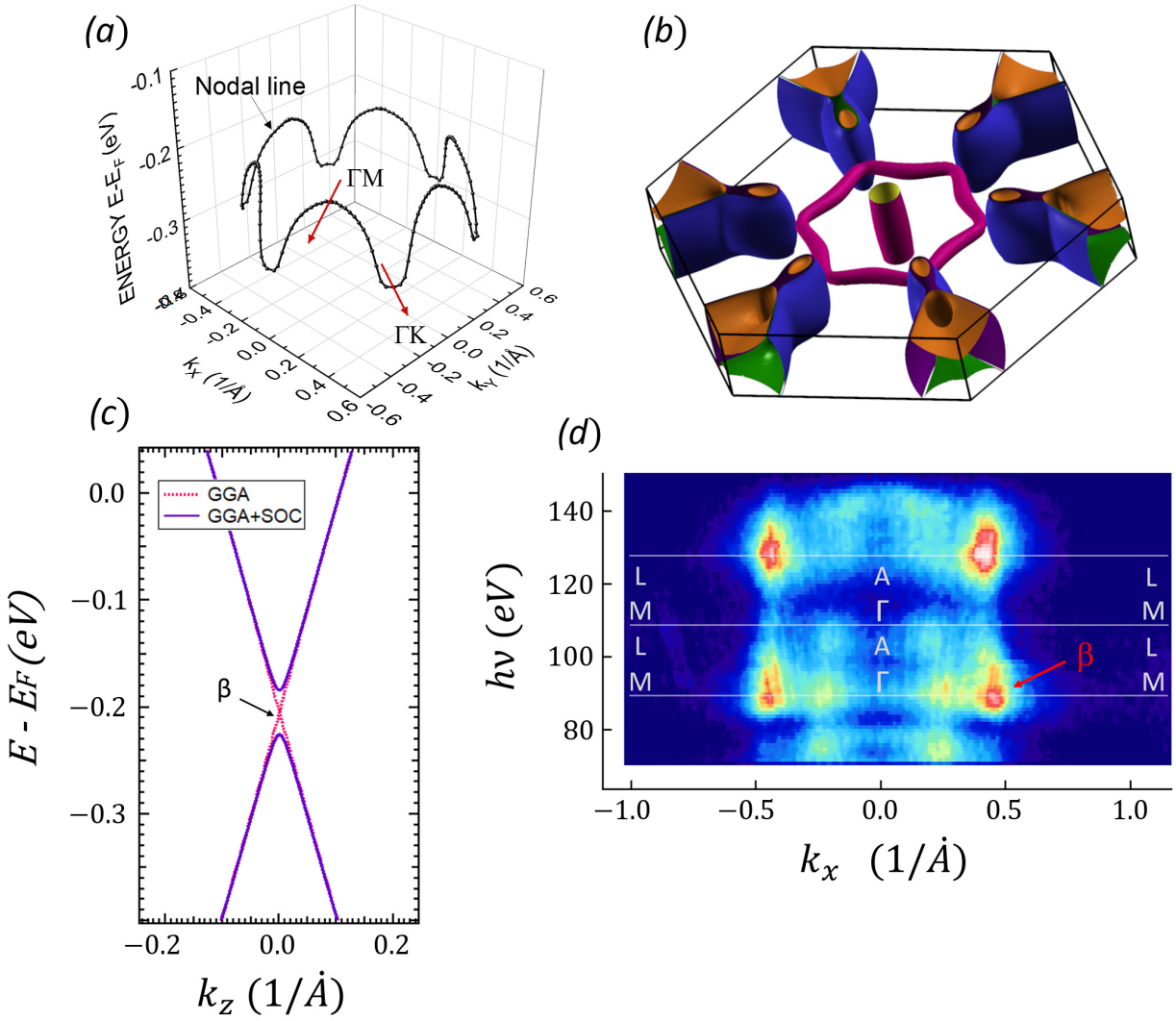

FIGURE 6.11: M_2AlC nodal line features, as calculated from V_2AlC electronic structure, are plotted in (E, k_x, k_y) (a) and within V_2AlC isoenergy surfaces at $E = E_F \neg 0.29$ eV (b). A linear dispersion across the nodal line is found with GGA calculations and becomes 41.0 meV gapped when including spin-orbit coupling (SOC) (c). A V_2AlC ΓMLA ARPES isoenergy surface mapping at around 0.21 eV below E_F reveals k_z broadened points in the ΓMK plane, at the coordinate β where the nodal line is expected to lie (d).

point α at E_F already indicated in figure 5.9 but with a cut direction parallel to k_y (figure 6.12c). In those two figures, dispersion appearing as "bold" lines corresponds to quasi-2D bands (confined along z), and bands where k_z dispersion is appreciable now appear as defining domains. Those domains are bounded by the curves corresponding to $k_z = 0$ and $k_z = \pi/c$. Although photoionization cross-section effects should also be taken into account, figures 6.12a and 6.12c should reflect the overall appearance of ARPES images measured along the same cuts.

As expected from Fig. 5.12a, the nodal line exhibits a strong dispersion in any direction perpendicular to the line. In particular, and as shown in figure 6.11c, since around β the nodal line is locally parallel to k_y, it exhibits a linear dispersion both along k_x and k_z. This should result in the k_z-broadening effect predicted by figure 6.12a, defining an hourglass-shaped region below and above the line. Such an hourglass pattern is easily recognized in the ARPES image of figure 6.12b. Well defined lines are not observed around the nodal line, most probably due to k_z broadening. The blurred hourglass shape visible in the ARPES cut is also well bounded by the extremal dispersion lines predicted by DFT (located respectively in the Γ and A planes, and also shown in figure 6.12a).

To prove the existence of the line requires more than an ARPES cut, and thus additional evidences are given below. Figure 6.13a shows an isoenergy section at an energy value where most of the nodal line is expected to lie. We find the theoretically predicted hexagonal shape, and similarity between figures 6.13a and 6.11b is striking. Additional patterns appearing at the apices of the hexagon are due to the additional bands predicted in figure 6.11b and to the fact that the nodal line slightly varies in energy (see figure 6.11a), so that in those regions the isoenergy plane intersects the lower part of the "hourglass" instead of the crossing point. In order to prove that the hexagon seen in figure 6.13a does not simply represent the energy intercept of a regular band but corresponds to the intercept of the nodal line, we represent in figure 6.13b ARPES cuts parallel to k_x but intercepting points β, β_1, or β_2, defined in the zoomed part of figure 6.13a. As is obvious from the three cuts of figure 6.13b and due to the fact that the nodal line runs parallel to k_y, the ARPES pattern remains almost unchanged. The "hourglass" is always present and lies at the same position. (Here we note that the ARPES line corresponding to the rising band going to α is also almost independent of k_y, and this is the reason why its location is also constant, as for the nodal line; this is discussed below in the section discussing the dispersion around α) DFT dispersion in k_z is illustrated by the k_z-broadening curves of figure 6.13b, but it is also interesting to produce a direct k_z variation by varying the incident photon energy, as shown in figure 6.11d. Location of the DFT nodal line at $k_z = 0$ is compatible with the data shown in figure 6.11d. What cannot be done experimentally is to get a quantitatively accurate estimation of the dispersion line around k_z, but combining the information given by figures 6.11, 6.12 and 6.13 clearly demonstrates the experimental existence of the nodal line. Relativistic SOC DFT calculations predicts a value of 41 meV for the gap in β (see figures 6.11c and 6.14). Positioning E_F close to this line while maintaining its BS pristine should result in spin polarization effects. From the DFT calculations, it is also worth noticing that in spite of

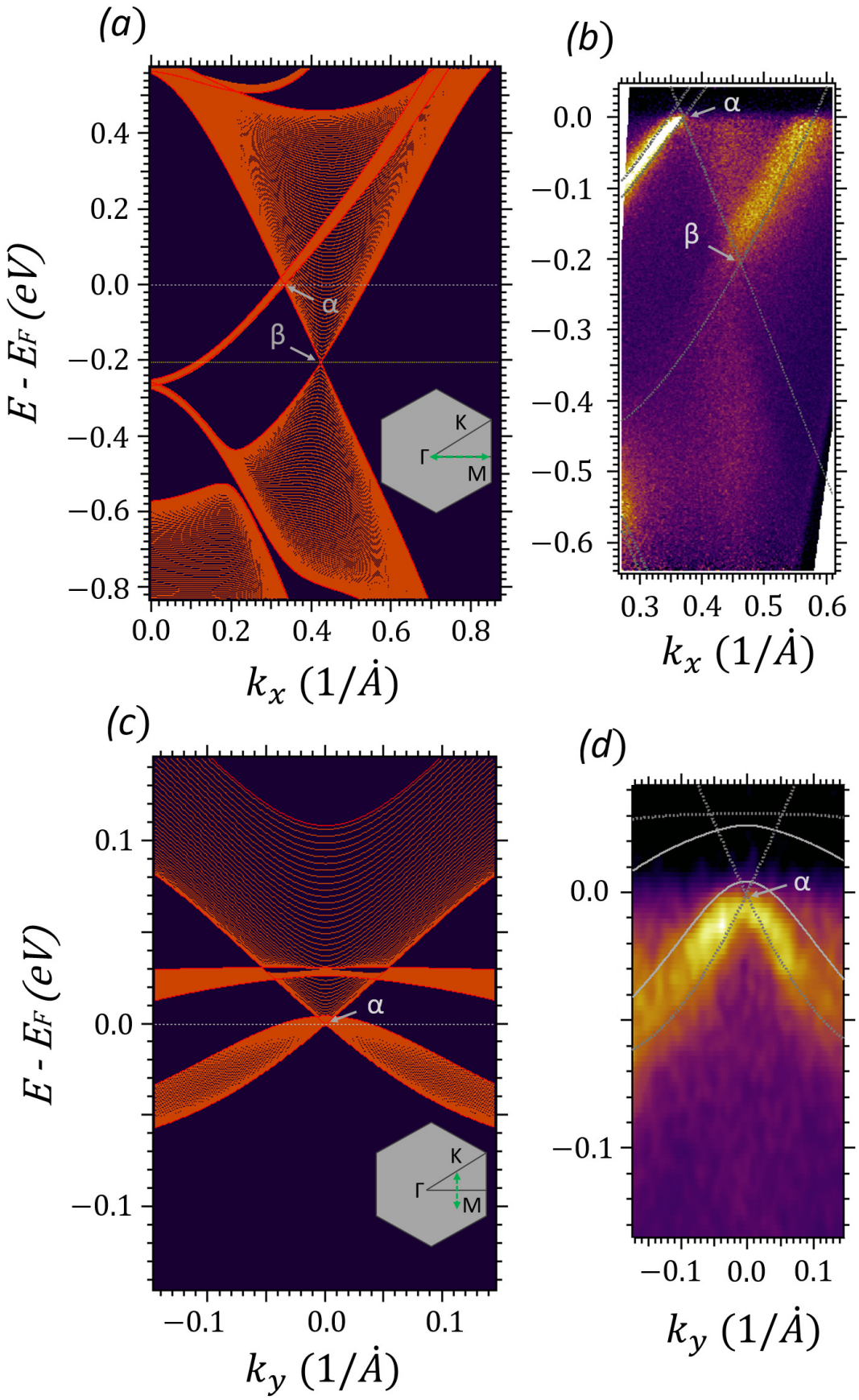

FIGURE 6.12: k_z projected band structure of V_2AlC along ΓM, from DFT (a) and ARPES (b). k_z broadening is considered from $k_z = 0$ to $k_z = \pi/c$ (red curves stand for extremal k_z values). The linear band crossing point at $E = E_F$ is labeled as α and that corresponding to the nodal line as β. The k_z projected band structure centered on α and perpendicular to ΓM from DFT and ARPES measurements is plotted in (c) and (d). In (b) and (d), full and dashed gray lines stand for the band structures in the ΓMK and ALH planes.

the gap induced by spin-orbit coupling, dispersion becomes linear and "Dirac-like" roughly less than 2 meV away from the top of the band.

6.3.2 Other node and effect of spin orbit coupling

Let us now address the bands morphology near point α, which exhibits Dirac-like dispersions in various directions. k_z-broadening not only affects the ARPES cuts of the nodal line but also the bands measured around α, as predicted by figure 6.12c. DFT predictions along various particular directions are given in figure 6.14. Three bands are present around α (bands 39, 40, and 41). When going from Γ to M and from the bottom to the top of the energy window around α, these bands respectively form (i) a quasi-2D Dirac cone before α and linear dispersions along k_x and k_y but massive dispersion along k_z beyond α (see figures 6.12a and 6.14); (ii) a quasi-1D line along k_x (i.e., large effective masses and almost flat dispersion along k_y and k_z, given in figures 6.14b and 5.14c); and (iii) a cone with Dirac-like dispersion along k_x (figure 6.14a) and mixed shapes along k_y and k_z (figures 6.14b and 6.14c). The structure around α is thus quite complex (and is indeed much more involved than what we assumed in chapter 5 for V_2AlC). Below we describe in more detail the topology around this crossing point along with the experimental evidence that can be gained from ARPES.

Figure 6.12a shows the theoretical dispersion and predicted k_z broadening along k_x (i.e., along ΓM), and figure 6.12c shows the same features, but now along the line parallel to k_y intercepting α in reciprocal space. ARPES cuts are shown in figures 6.12b and 6.12d, where extremal DFT lines are superimposed to the ARPES cut. All lines forming the Dirac-like point are distinctly recognized along k_x and k_y, respectively, taking into account effects already discussed for the nodal line. Let us first consider figure 6.12b. The left ascending part is clearly visible as a line, because there is no predicted k_z broadening in this part, and the band is quasi-2D with Dirac-like dispersions along k_x (figures 6.12a and 6.12b) and k_y (figures 6.12c and 6.12d) but at the top of the band, where the crossing point is split by spin-orbit coupling (see figure 6.12). In contrast, the right descending part appears as a blurred region, which is easily explained by two features. On the one hand, and in contrast to all other lines, the main orbital contribution of the "descending" part beyond α is $d_{xz} + d_{yz}$, and it turns out that the available angle range of our experiment makes the photoionization cross section of this part rather small. On the other hand, and most of all, beyond α (see figure 6.12a) there is a strong dispersion along k_z so that the ARPES cut is subject to the well-known k_z-broadening effect in that part [250, 251]. (In fact, beyond α and going towards M, the upper band seen in figure 6.14c crosses E_F and goes down as k_x increases, so that it is responsible for the strong dispersion along k_z in that part.) Experimental dispersions are clearly visible along the line parallel to k_y (figure 6.12d). It is thus clear from figure 6.12 that the crossing point is present where DFT predicts it to lie. The observed line broadening is once again explained by k_z broadening, and is well circumscribed by the domain predicted by figure 6.12c (The extremal band lines defining the domain have also been superimposed in the ARPES cut of figure 6.12d). From the

considerations above, the overall topology of the crossing point can be viewed as the complex result of the intersections of quasi-1D, quasi-2D, and 3D bands, respectively.

Due to k_z broadening, we could not accurately assess the experimental value of the spin-orbit splitting or the band curvature. We did it using DFT calculation only. We found a gap of 20.7 meV at α, to be compared, e.g., to the gap at around 70 meV found in the 3D Dirac semimetal Cd_3As_2 [288]. This small gap makes the dispersion become linear, e.g., Dirac-like, roughly less than 10 meV below the top of the band (see figure 6.14). This is indeed somewhat "better" than what is found in an archetypal 3D material such as Cd_3As_2, where, due to crystal field splitting, 3D Dirac electrons are expected only around 100 meV below E_F [288]. Experimentally, the presence of, e.g., vacancies, could slightly empty the population of the lowest band or fill the upper one. Although this still remains speculative, the presence of a few holes in this valence

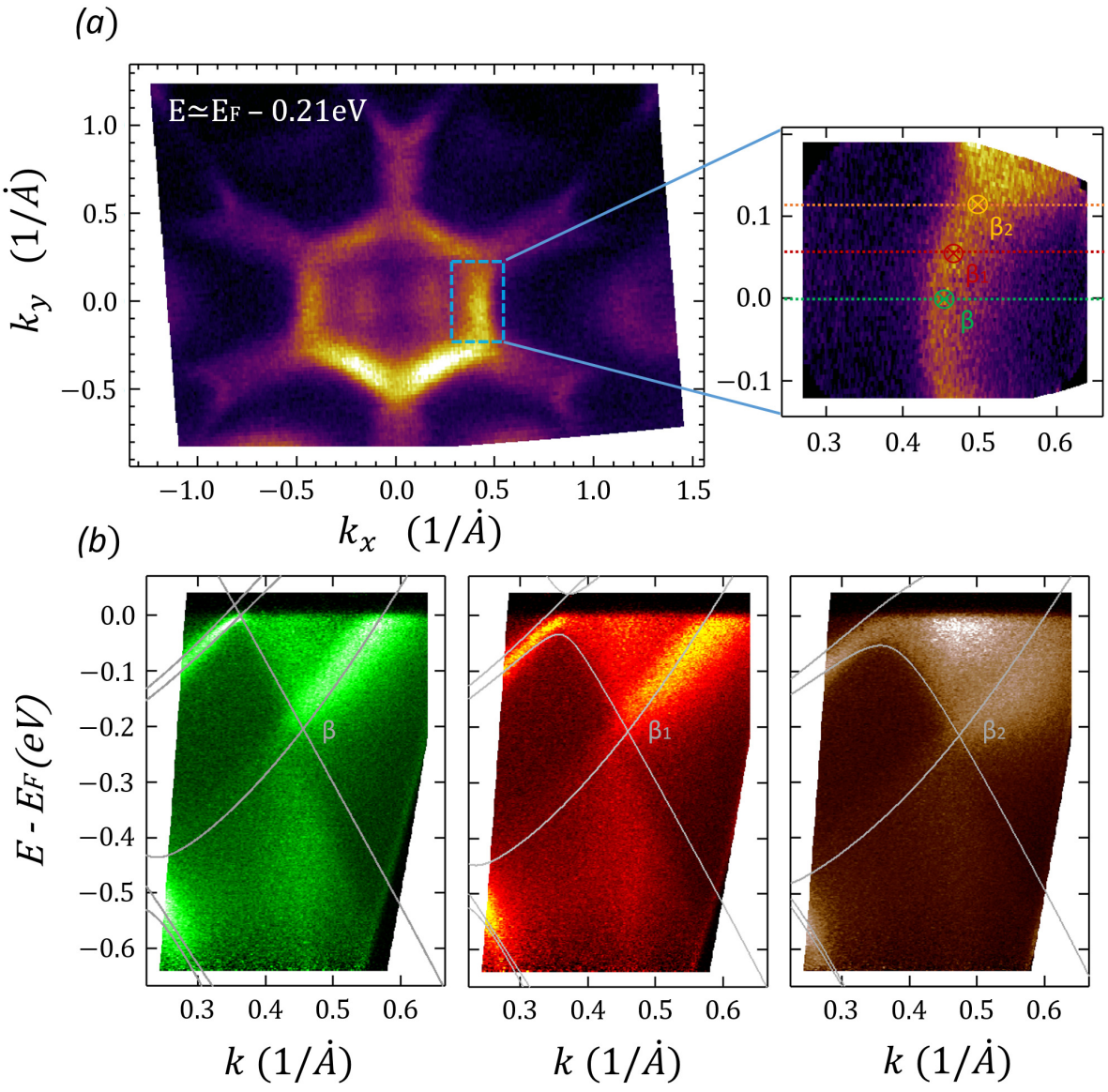

FIGURE 6.13: V2AlC ARPES isoenergy surface mapping at $E = E_F$0.21 eV, a few meV below β. (b) ARPES band structure is plotted vs DFT band structure along three directions parallel to M and respectively crossing the nodal line at β, β_1, and β_2.

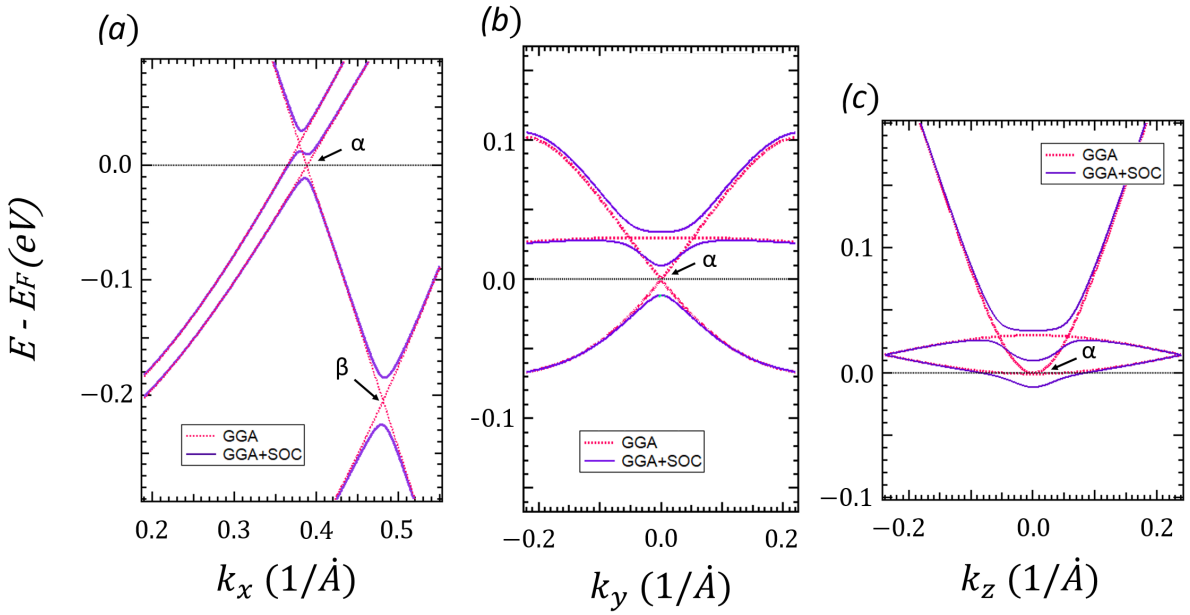

FIGURE 6.14: V_2AlC band structure near α across k_x , k_y, and k_z , with and without spin-orbit coupling.

band could then explain the fact that when measuring magnetoresistance (MR) in similar crystals, we never found a perfect parabolic dependence (V_2AlC MR power exponent was around 1.4) [159]. In V_2AlC, this seemingly anomalous behavior could indeed be explained by the mixing of the parabolic contribution of the "conventional" bands at E_F with the linear contribution expected from a slightly populated band featuring a linear crossing, as first theoretically considered in [289] and as observed later in many materials (see, e.g., [290]). In contrast, in the case of Cr_2AlC, which is devoid of such topological features at E_F , the MR was found to be almost perfectly parabolic [159].

6.4 Summary

The applicability of the rigid band model to 211 MAX phases has been successfully assessed by means of ARPES analysis and DFT calculations. Changing the M atom leads to rigid shifts of the Fermi level that leave the bands almost unchanged. It also allows for a complete classification of 211 phases based on simple criteria: all those that can be modeled by the same rigid band model would belong to a given subfamily of 211 MAX phase, which leads to the typology of five subfamilies from the five A element columns from which one can obtain every known MAX phases. Such classification is compatible with others that were built upon a different criterion, i.e., bond stiffness [291]. It is also expected that a similar classification would describe the 312 and 413 phases. One of the implications of a unified description of MAX phases by rigid band models is the possibility to navigate through their electronic structure by playing with a single parameter (e.g., a tunable atomic fraction of (M,N) elements in a given $(M_xN_{1-x})_2AX$ solid solution or, still better, using totally ordered phases combining M,N elements [7]). The presence of band inversions (see figure 6.9) that lead to

the existence of many crossings and topological nodes in the rigid band structure of M_2AC (A = Al, Ga, In, Tl) shows even greater promise. Tuning the atomic ratio of M elements in solid solutions could thus open the possibility for MAX phases to be established as a promising arena for metal physicists exploring topological properties of matter. To achieve this, one still has to experimentally prove that E_F can be tuned close to the existing topological nodes. As for other compound or elemental materials, those topological features coexist in the same energy window with the contributions of more conventional bands (see, e.g., [279]) and thus differ from the few unique systems such as, e.g., Cd_3As_2 [288], which simply displays a Dirac-like point at E_F . But this does not preclude the observation of some specific effects usually associated with such nodes, e.g., the spin Hall effect or a linear MR component.

Here, our focus was set specifically on 211 MAX phases. One may still ask if similar features are observed within 312 MAX phases electronic structures, especially regarding topological nodes and "Dirac-like" nodes. We will adress these questions in the last chapter of this thesis, devoted to the study of 312 Ti_3SiC_2 single crystals.

Also, as electronic correlation are found to be relatively weak for most 211 MAX phases, one can wonder how their properties will change if one artificially "insert" source of correlation within these compounds. This was our leitmotiv for the synthesis and exploration of rare earth based quaternary iMAX and 4473 phases, and we will outline a few of our results within the section at the end of this manuscript.

Chapter 7

From Ti_3SiC_2 Fermi surface determination to Ti_3SiC_2 thermopower anisotropy

Drawn from an article first signed by the author of this thesis and published recently [292], this chapter is focused on the exploration of the electronic structure of the compound that is likely the most widely studied among MAX phases, 312 Ti_3SiC_2 [1].

Among the $M_{n+1}AX_n$ family, Ti_3SiC_2 has indeed occupied a central place as it was the first pure phase to be thoroughly investigated by *Barsoum and El Raghy* [11], about 25 years after the early work of *Nowotny* [10]. A method was only very recently developed in order to exfoliate Ti_3SiC_2 and obtain the bidimensional Ti_3C_2 MXene [293], Ti_3C_2 also being the first MXene to be synthetized by chemical exfoliation of Ti_3AlC_2 in 2011 [47]. As detailed throughout chapter 1, many of MAX phases' basic properties (e.g., electrical conductivity, thermoelectric coefficients, and mechanical properties) have already been extensively studied by both experimental and computational means.

In the case of polycrystalline Ti_3SiC_2, thermopower was found negligible over a wide temperature range [294], a fact later explained by a compensation of electron and hole-like contributions (although those contributions take place out-of or in-plane, respectively, and are thus not compensated in single crystals, polycrystals average them over all random directions, thus leading to a net zero thermopower). For single crystals, a substantial thermopower anisotropy was predicted [145, 295, 296], and later confirmed by in-plane measurements performed on single-crystalline thin films [297]. A prominent role is played by highly anisotropic intertwined pockets centered on the H point of the hexagonal BZ. For a many-band metallic system like Ti_3SiC_2, and as discussed for Cr_2AlC in chapter 3, the determination of FS and near Fermi level band structure is necessary to be able to rigorously derive the conductivity and other Onsager coefficients [**pinek_unified_2019** , 40, 154]. The FS and band structure of Ti_3SiC_2 are featured in several ab initio studies [145, 295, 296] [152, 156, 298] but little work has been done to experimentally measure them, mainly due to

the lack of availability of bulk single crystals required for measuring either de Haas–van Alphen oscillations or ARPES.

As presented within this chapter, Ti_3SiC_2 bulk single crystals were probed by ARPES. As for the electronic structure of 211 MAX bulk single crystals detailed in the previous chapters, ARPES BS and FS mapping are compared to the output of DFT calculations. This chapter reports on the first experimental study of the FS and BS of a 312 MAX phase [292], aiming at bringing deeper insight into the complex morphology of Ti_3SiC_2 electronic states. In particular, we verify the existence and examine the shape and nature of the pockets presumably responsible for the zero thermopower in polycrystalline Ti_3SiC_2. BS and FS ARPES maps show remarkable agreement with theory. Complex three-dimensional (3D) features in reciprocal space seem to link one H point centered platelike pocket to a tubular surface also centered on the KH axis, while the FSs centered in Γ are found to be hole-like. k_z-projected band structure analysis reveals that the electron FS platelets centered in H are connected together through tiny open tubes exhibiting linear dispersion features. The effect of spin-orbit coupling at those band crossings is studied in detail.

7.1 Experimental and computational details, basic outputs of DFT

7.1.1 ARPES and DFT setups for Ti3SiC2 analysis

Self-nucleated Ti_3SiC_2 single crystals were synthesized by high-temperature solution growth within an induction-heated growth reactor, following a procedure detailed in chapter 2 and in [35]. The platelet dimensions reach up to 1 cm^2. Platelets are up to 200 μm thick, and are oriented toward (0001). Due to the growth process, unwanted $TiSi_2$ solid droplets are found on top of the freshly grown crystals. They result from incomplete dewetting of the flux when the crystals are pulled out. However, this was not detrimental to ARPES, since we studied surfaces after cleaving the crystals in UHV conditions.

Similarly to V_2AlC and Cr_2AlC, single crystals were cut in $3mm \times 3mm$ squares before being cleaved, within the UHV chamber of either the BL5U (BL7U) line at UVSOR-III (AichiSR) or the Cassiopée line at SOLEIL, respectively equipped with a MBS A-1 and a SCIENTA R4000 analyzer. Base pressure reached about 10^9 Pa for each line. Temperature was set at 20 K (10 K) for the measurements at BL5U (BL7U) (figures 7.3, 7.6 and 7.5a) and 13.4 K at Cassiopée (figures 7.4, 7.5b, 7.7, and 7.8). Energy resolution was of the order of 10 meV. In order to obtain FS and BS mappings centered on M or K points, samples were tilted so that the detector angular range was centered elsewhere than on Γ. Photon energy was set to 66.5 eV (figures 7.3 and 7.6) and 70 eV (figures 7.4 and 7.7). For ΓKHA ARPES mapping, $h\nu$ was swept from 50 to 120 eV (figure 7.5a) and from 60 to 75 eV (figure 7.5b). Linear horizontal (referred to here as S-pol for a vertically aligned analyzer slit) and vertical (P-pol) polarized light [228, 299] were used in order to take advantage of the orbital dependence of the photoionization cross section. The angle between the light beam and the detector was always set to 45°. All calculations were performed with the full potential APW+lo (augmented

plane wave+localized orbitals) method implemented within WIEN2k . As for all the calculations within this manuscript, the standard spinless PBE GGA functional was chosen. Spin-orbit coupling was treated within the full relativistic calculation frame of WIEN2k. Wave functions were expanded up to a more stringent value of the RKM cutoff parameter of 9 to guarantee that convergence was reached . Similarly to the DFT calculations presented in past chapters, a very dense $79 \times 79 \times 11$ Monkhorst-Pack cell was used. The overall level of convergence in energy was set to 0.01 mRy. The basic FS plots were computed using X-CRYSDEN.

7.1.2 DFT Fermi surfaces and thermopower

DFT calculations of Ti_3SiC_2 electronic structure are already quite well documented in the litterature [145, 295, 296] [152, 156, 298], but we still had to perform these calculations again because, (i) the best fit to the experimentally determined FS requires slightly shifting the Fermi energy value, (ii) comparing theory and experiment requires computations along uncommon directions or points (that were not present in the literature for Ti_3SiC_2), and (iii) precise FS fitting also requires the use of large grids.

Assessing the electronic structure of a given solid through numerical calculations has become handful when interpreting the results of photoemission experiments. The methodology described here is very close to the one previously applied to Cr_2AlC and V_2AlC. As for all MAX phases, Ti_3SiC_2 crystallizes in the $P6_3/mmc$ space group, though its unit cell is different from the 211 phases (See figure 2.1) . Its FS is pictured in figure 7.1, as computed by DFT calculations. Its crystal structure is given in figure 7.2a. Here we note that in order to obtain better agreement with experiment (discussed below), a rigid energy shift of about 2 mRy (27 meV) is applied to all the isoenergy surfaces and band structures (see figure 7.1a). This value is close to the one applied by *Chaput et.al.* [295] to obtain a thermopower consistent with experimental results. It is worth noticing that due to the intricate topology of the intersecting bands around the K point, and although such a shift does not drastically change the overall shape of the surfaces, it modifies the connectivity of the various surfaces and, in particular, it changes the band indexation of some regions (see figure 7.1a; left FS is unshifted whereas right FS is the closest to ARPES; left FS looks closer to results published by *Chaput et.al.* [295]). This required shift could originate from numerical instabilities. It could also be partly attributed to the final state effects which, as aforementioned in section 3.2.3 revealed in the next section, can intrinsically limit the accuracy of ARPES analysis for three-dimensional systems.

Six bands cross the Fermi level, with bands 45–48 being hole bands. To get a clearer picture of the morphology of all pockets, the all-band Fermi surface is plotted over a cell centered on the L point of the hexagonal BZ. The FSs of bands 45 and 46 are Γ centered, quasi-two-dimensional (2D) free-electron tubes, while the FSs of bands 47 and 48 show a warping in k_z and have an in-plane component in the shape of a six-pointed star. The pockets of bands 49 and 50 are centered on H and are nested into one another. Band 50 shows a very strong delocalized character along c, with an associated pocket looking like a thin triangular plate in k-space. This implies that, as we saw for V_2AlC in chapter 5, Ti_3SiC_2 is definitely more three dimensional

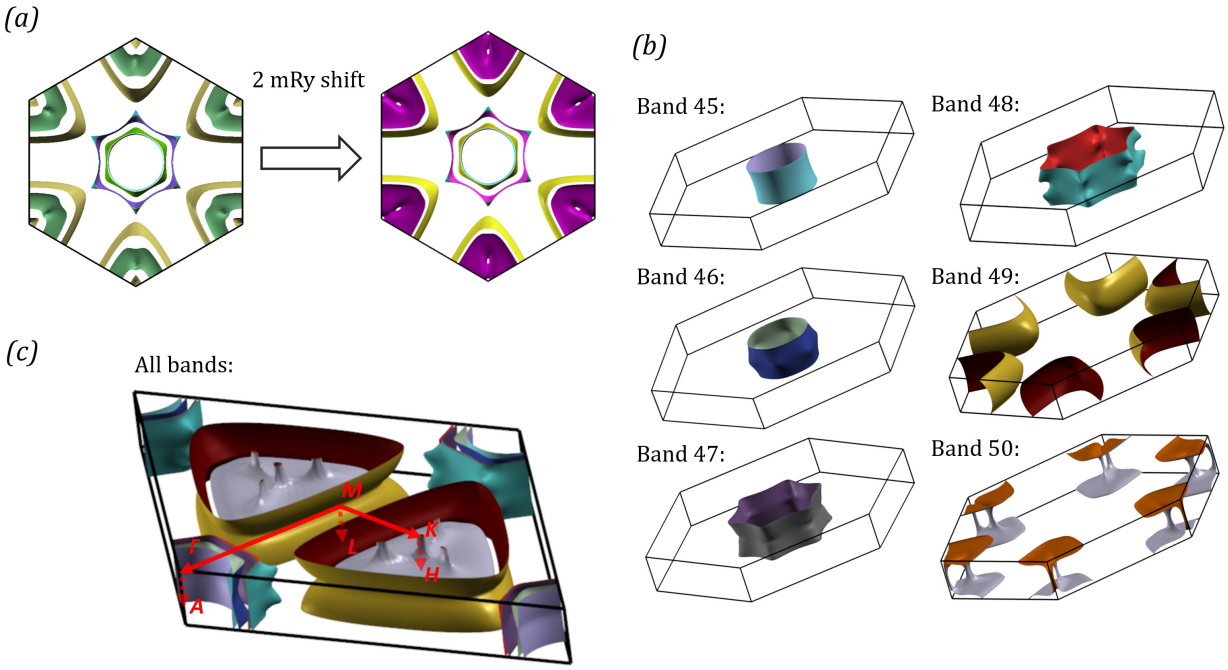

FIGURE 7.1: (a) Isoenergy surface of Ti_3SiC_2 2 mRy (27 meV) above E_F , computed by DFT calculations. The latter shows a better agreement with experimental data than the actual DFT Fermi surface. In (b), Ti_3SiC_2 all-band Fermi surface which is plotted over a cell that is centered in the L point of the first BZ. (c) Individual bands are plotted within the first Brillouin zone. Bands 45–48 are found to be hole bands while bands 49 and 50 are not as easily defined (see section 7.2.2 and 7.2.3), but can be considered mainly as electron bands.

than many other MAX phases such as, e.g., Cr2AlC (see chapter 4). This will be discussed in further detail in section 7.2.2. In contrast, all other bands are mainly delocalized in the (k_x, k_y) plane.

As explained in [296, 297], the peculiar thermopower properties of polycrystalline Ti_3SiC_2 were previously assigned to the prevailing influence of bands 49 and 50 [295]. From the point of view of thermoelectric power, the carriers in band 50 were found to behave as electrons along c [295], and those of band 49 as holes. The case of bands 49 and 50 is indeed quite involved, and one of our purpose here is to explain in more detail the behavior of complex bands using simple arguments. This is where we shall rely once again on both our ARPES data and DFT calculations. Although a complicated FS shape makes the "hole" concept one of limited content, let us first list two common ways to define a band as "holelike" or "electronlike."

Firstly, one can define a hole (electron) band as one for which a small increase in Fermi energy E_F leads to a decrease (increase) of the FS area, respectively. This definition rules magnetotransport, for the electron velocities point inside (out of) the FS, leading to a positive (negative) Hall coefficient.

Alternatively, one can define a hole (electron) band as one for which the $E(\mathbf{k})$ relation exhibits a negative (positive) curvature in the vicinity of the Fermi level. The second definition rules the sign of the thermoelectric power S, positive for holes and negative for electrons (with a negative curvature, electrons thermally spreading in energy see their velocity decrease with increasing energy, so that electron diffusion takes place

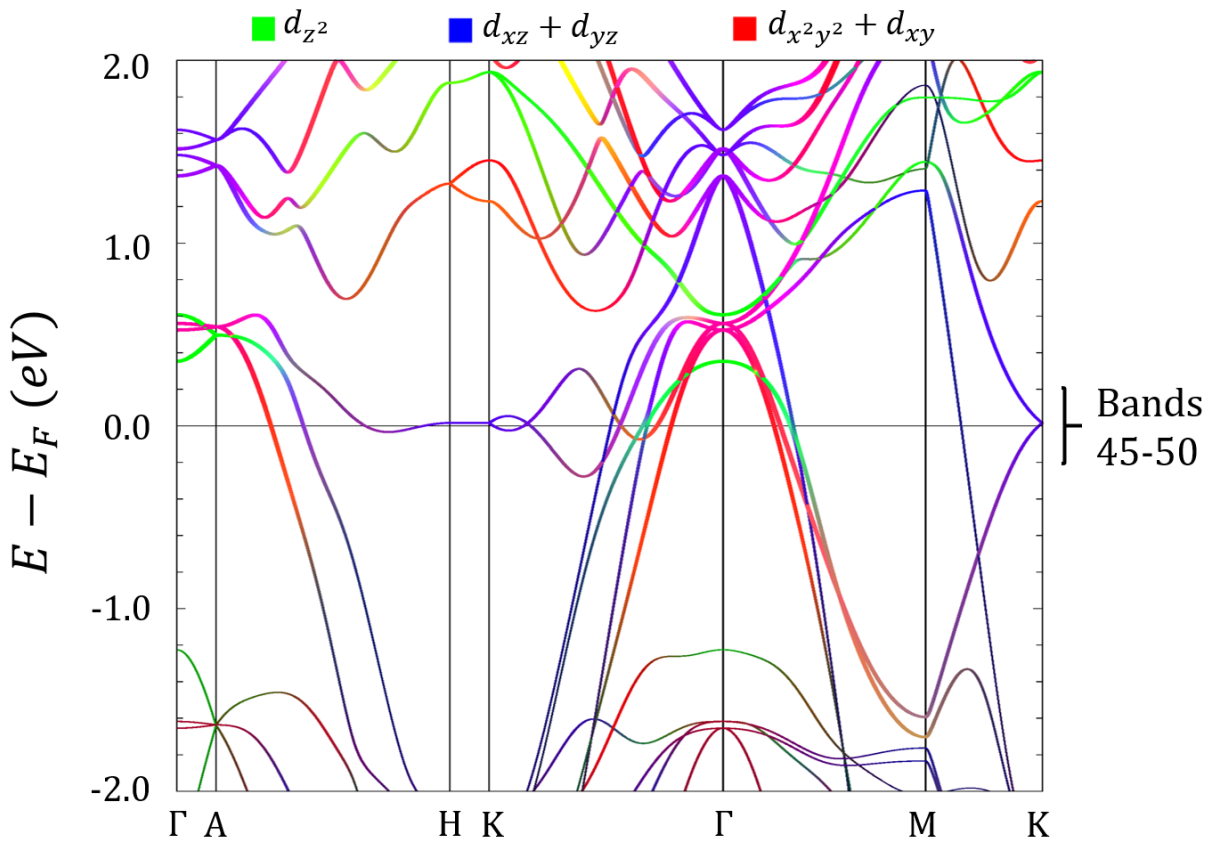

FIGURE 7.2: Ti_3SiC_2 BS projected onto Ti *d* orbitals, dominant at the Fermi level. The projection is taken over the two Ti sites simultaneously.

from the colder to the hotter region, giving a positive value for S, which is the expected sign in the conventional "hole" picture).

Both definitions often coincide, for if the Fermi level lies reasonably close to the top or the bottom of a band, and in the absence of band crossing, the existence of an energy extremum fixes the sign of the band curvature in agreement with the FS expansion criterion. In our case, the latter is easily verified by increasing E_F slightly, which leads to an increase of the FS area for both bands 49 and 50. However, taking into account the dispersion relations along particular directions shows that the picture is actually much more complex if one wants to apply the second criterion. It may even turn out that depending on the k-point considered in a given band, the electrons exhibit either a positive or a negative mass inside the same band. Applying the second rule thus does not lead to so clear a classification, and requires investigation of the dispersion relation along k_x, k_y, ork_z directly at particular and suitably chosen points; this is achieved and explained at the end of section 7.2.3.

7.1.3 Orbital character of near Fermi level bands

Figure 7.2 shows the band structure of Ti_3SiC_2, where the orbital population of each band is highlighted through a color contrast. Ti d orbitals are the only ones considered since they dominate the electronic structure of Ti_3SiC_2 near the Fermi level [1, 2, 3]. The orbital population of each band appears to be more mixed than the V_2AlC and Cr_2AlC 211 phases. This can be accounted for by the presence of two different transition-metal sites on 312 MAX phases, thus leading to a larger variety of possible hybridization of the different $3d$ states. Owing to selection rules, the angular dependence of the photoionization cross sections of Ti $3d$ orbitals should be similar to that of Cr in Cr_2AlC, as given in figure 4.5 for both S-pol and P-pol configurations. One needs only to invert the θ_x and θ_y variables indicated in chapters 4 and 5 to fit the experimental conditions of the Cassiopée line, and to match the (kx, k_y) denomination for most of the figures within this chapter. The band showing a d_{z^2} component would show the highest signal in the ARPES spectra at a low angle while bands with other orbital character would be visible at a higher angle, closer to the BZ boundaries. Although Si orbitals participate to a lesser extent in the states at E_F , they are not discussed further here. Still they are key for ensuring delocalization along c for Ti_3SiC_2 , and were, for instance, experimentally evidenced and discussed in [297].

7.2 Results and discussion

7.2.1 ARPES in-plane and out-of-plane Fermi surface mapping

The above analysis is consistent with the integrated ARPES mappings in figure 7.3. Here we integrate the isoenergy surfaces from E_F to 100 meV below; the more intense signal we obtain by this averaging allows us to analyze in detail the effect of polarization. One finds again the K-centered platelike pocket in figures 7.3a and 7.3b. Also, the fact that the relative intensity associated to the electron pocket of band 50 (mainly populated by d_{xz} and d_{yz} near E_F) is relatively lower than the central star-shaped bands in S-pol mode (figure 7.3a) and at a similar intensity level in P-pol. mode can be explained from the discussions in chapter 4 [228]: The d_{xz} contribution to the photoionization cross section is substantially higher than the one of other orbitals for high angle (near the BZ boundaries) in P-pol, while the contribution of d_{xy}, d_{xz}, and d_{yz} orbitals in S-pol at high angle are all non-negligible. At low angles, the d_{z^2} star-shaped tube should be more intense than the other part of the FS in the ARPES spectra, which correspond to what is observed in figure 7.3c, with an asymmetry in intensity with respect to k_x that is predicted by cross section calculation (See figure 4.5 and [228]). There is a good correspondence between experiment and theory, as highlighted in figure 7.4: An extended FS mapping in the S-pol configuration, centered on the K (H) point, is compared with the projected isoenergy surface of figure 7.1, plotted over several Brillouin zones. With such a high level of correspondence

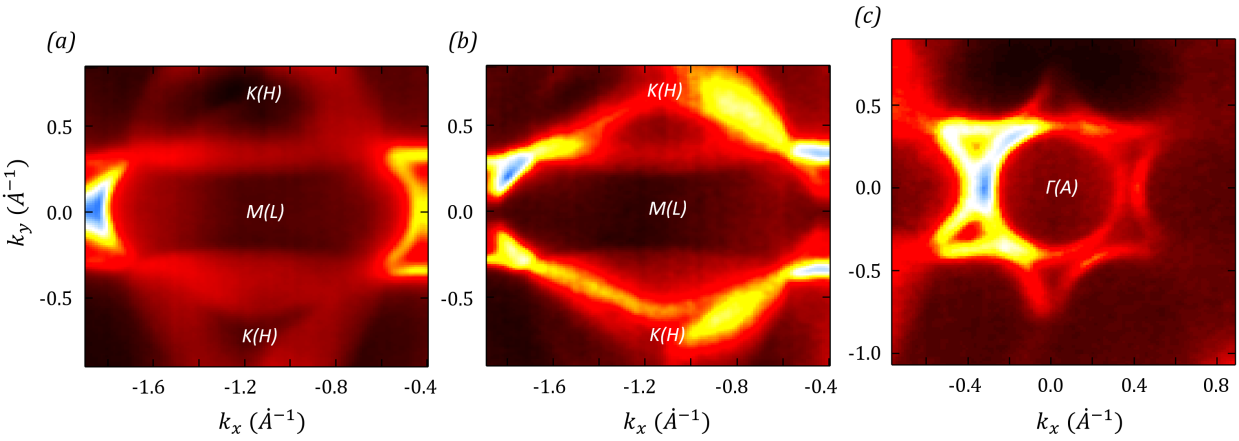

FIGURE 7.3: Integrated isoenergy surface mapping (with the energy window from E_F to 100 meV) of highly tilted Ti_3SiC_2 single crystals (a), (b) and in S-pol. (a) and S pol. (b) configuration. Tilting allows one to center the mapping on the edge of the BZ (on the M (L) point) and changing the polarization configuration reveals bands of different orbital character, due to the polarization and orbital dependence of the photoionization cross section. (c) Normal incidence mapping in S pol. configuration, centered in Γ.

between the output DFT and ARPES mappings, it becomes possible to access detailed information regarding the near Fermi level electronic structure of Ti_3SiC_2.

From DFT calculations, the FS of band 50 has the shape of very thin plates perpendicular to k_z and centered in H. These plates are connected through thin tubes parallel to c^*, one crossing the BZ through KH and the three others located somewhat close to the KH axis. When considering k_z broadening (discussed in detail later on), the three-pointed star area that encompasses the tubes should be completely averaged and give a slightly more important contribution to the ARPES spectra than the plate which is averaged over only a single k_z value. It thus explains why there is a contrast over the three-pointed star area on the ARPES spectra of figure 7.4 (highlighted in brown in the projected DFT isoenergy surface), even if it shows the same orbital character as the rest of the platelike hole pocket of band 50. It also demonstrates the three-dimensional character of band 49 and 50 FSs, while the other bands' FSs are mainly quasi-two-dimensional tubes.

Figure 7.5 shows the Γ$KMLHA$ ARPES mapping, obtained by varying the incident photon energy $h\nu$. Following the free electron-like approximation of the final state [179, 180, 184], the inner potential V_0 was set to 19.0 eV. In order to obtain the DFT isoenergy surface lines, many band structures over ΓK were computed, for 88 k_z values ranging from 0 to π/c. Then, for each of them, the wave vectors were selected for which each band reaches the shifted Fermi level. All the FSs appear at thek_x value predicted by theory even though, for the higher $h\nu$ values, the intensity of the overall spectra seems to be appreciably smaller. The ARPES signal in figure 7.5a clearly shows the inner FS tubes with a quasi-2D character, their FS cross section roughly appearing here as two vertical patterns almost symmetrically located around the ΓA axis, and extending over all BZs. ARPES in figure 7.5b shows the bands 49 and 50, centered around K (H). Explaining the detailed dependence of cross section effects on energy and angle is beyond the scope of this work, but the observed asymmetry in the ARPES signal intensity in figure 7.5a mainly results from the S-pol configuration

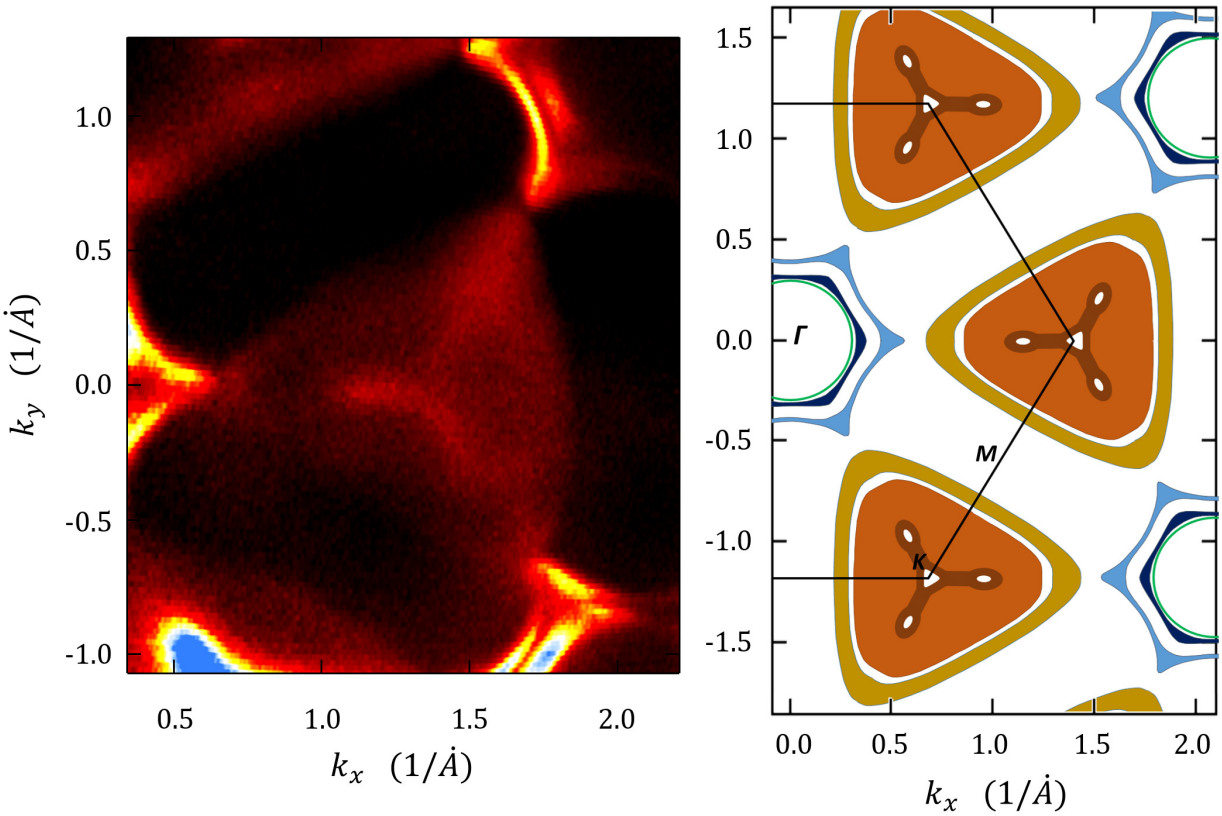

FIGURE 7.4: (a) Extended Fermi surface mapping centered in K (H) and in S pol configuration. The central plate-like pocket exhibits a brighter three-pointed starlike pattern at its center. This can explain the almost tubular features of this FS, connecting one plate to another. (b) *kz*-projected FS over the same area of reciprocal space. The area where the FSs plates are connected is highlighted in brown, and the three-pointed starlike pattern is recovered.

and d_{z^2} orbital contribution (see, e.g., the photoionization cross sections computed and given by figure 4.5). One should note that DFT makes bands 49 and 50 appear degenerate in the AHL plane. The fact that this degeneracy does not appear in figures 7.1 and 7.4b (DFT) can be explained by the two different wave-vector meshes used.

A total of 6000×88 k-points in the $\Gamma KMLHA$ plane was needed to get the FS in figure 7.5 while only $79 \times 79 \times 11$ were used in the IBZ for figures 7.1 and 7.4b. Also, a first order XCRYSDEN interpolation scheme [35] was applied, while no interpolation was needed for the very dense k-mesh used in figure 7.5.

7.2.2 Polarization dependence and kz-broadening

As further analyzed below, ARPES band structure analysis is also fully supported by DFT calculations and finer details such as orbital character (figure 7.6), k_z broadening (figure 7.7), or the effect of SOC (figure 6.8). When switching the polarization from S-pol (figure 7.6a) to P-pol mode (figure 7.6b) over ΓM, different bands will appear on the ARPES spectra depending on their respective orbital character. The electronic structure should be dominated by transition-metal d orbitals near E_F [298, 152, 156] and then be overcome by carbon $2p$ and silicon $3p$ orbitals near 1.5 to 2 eV below E_F as going below a minimum of the DOS [298,

152, 156]. Such a drop of 3*d* orbitals population is observed in figure 7.2, where the thinning of the color bands corresponds to a fall of the weight of the *d* orbital in the orbital mix.

In S-pol configuration, the bands located in between E_F and 2 eV are all visible and show nearly parabolic dispersions. ARPES features corresponding to other bands are present at lower energy, but the spectra appear to be significantly more blurred. In P-pol configuration, the parabolic bands disappear and significantly flatter dispersions are well defined at higher binding energies, one centered at 2 and the other at 3 eV. Thus, the bands that appear in P-pol would match the expected 3*p* and 2*p* bands expected from Ti_3SiC_2 partial density of states [298, 152, 156], while the S-pol configuration would reveal the bands with a predominant Ti 3*d* character. Taking the difference between the two P-pol and S-pol spectra allows one to recover all the bands predicted by DFT (figure 7.6c) while highlighting the differences of orbital weights. We applied this scheme to obtain the band structure over other reciprocal space directions (figures 7.6d and 7.6e). One should take note that the same 2mRy shift mentioned earlier on was applied to the DFT band structure. Another detail to take note of is the presence of clear linear band crossings apparent over KM (figure 7.6e), about 0.6 eV below E_F .

Ti_3SiC_2 band structure over Γ*K* happens to be more complex and intricate than the free parabolic and flatter bands seen over Γ*M* near the Fermi level. In an ARPES plot such as that reported in figure 7.7, the

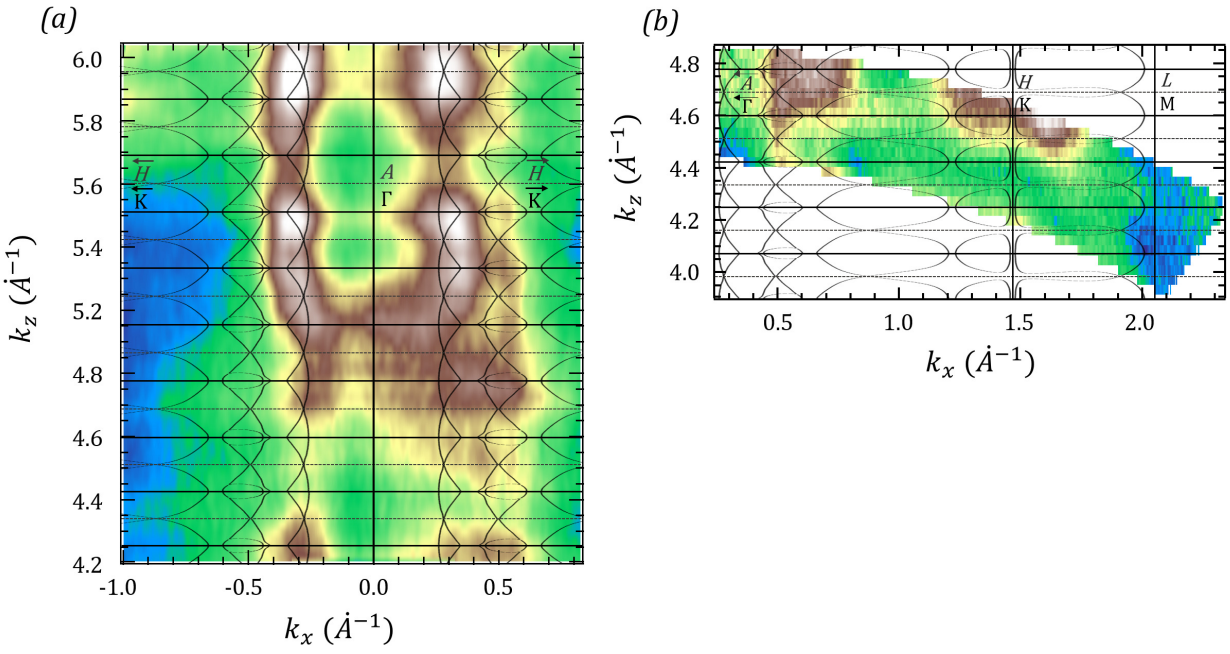

FIGURE 7.5: (a) ARPES out-of-plane Fermi surface over Γ*AHK*, close to the Γ*A* axis. The mapping is obtained from successive band structure plots, recorded with an incident beam energy $h\nu$ ranging from 50 to 120 eV, in S-pol. configuration. The dotted black lines represent isoenergy lines computed by DFT. In (b), the out-of-plane Fermi surface was measured beyond the Γ*A* axis, encompassing the KH and ML axes, with $h\nu$ going from 60 to 75 eV and with the polarization always set to S-pol mode. In order to convert both maps from $h\nu$ to k_z units, the inner potential V_0 was set to 19.0 eV following the free-electron approximation of the final state as in equation (4.2). This value allowed us to obtain the correct k_z periodicity of lower-energy bands on the ARPES band structure (as achieved in [249]).

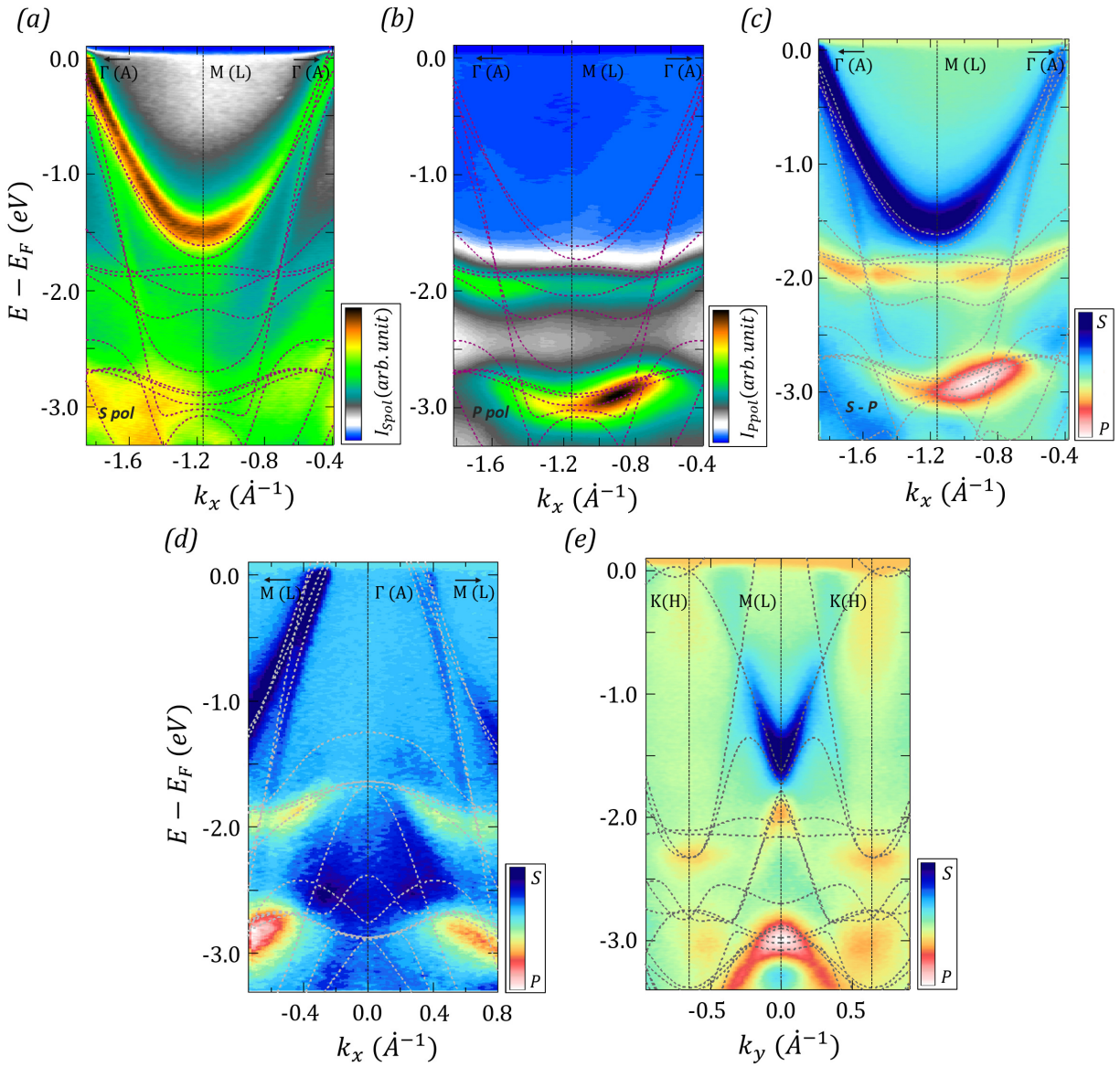

FIGURE 7.6: (a)–(c) Ti3SiC2 band structure mapping centered in M (L), plotted together with DFT band structure along M (dotted lines). (a), (b), respectively depict ARPES spectra obtained in S-pol and P-pol while (c) is the difference of the spectra obtained for these two polarizations. (d), (e) are, respectively, the difference between S-pol and P-pol ARPES spectra over ΓM (centered in Γ) (d) and KM (centered in M) (e).

ARPES signal of a given energy band, plotted as a function of kx (here directed along ΓK), is not restricted to a single value of k_z. This is the "kz broadening" effect we described in chapter 5, resulting in the formation of full regions of the ARPES spectra with enhanced ARPES signal, not restricted to well-defined dispersion lines as usually plotted in theoretical $E(\mathbf{k})$ dispersion curves. As for other V_2AlC materials, the case of Ti_3SiC_2 actually exemplifies the importance of k_z broadening for the interpretation of the ARPES spectra of bulk materials. k_z broadening is due either to the fact that energy bands are dispersive along k_z, or to a fundamental process in the photoelectron emission in three-dimensional systems that we did not describe until now, and which arises from the damping of the electron in the photoemission final state toward the interior of the solid [300, 186]. If the photoelectron escape length is of the order of magnitude or smaller

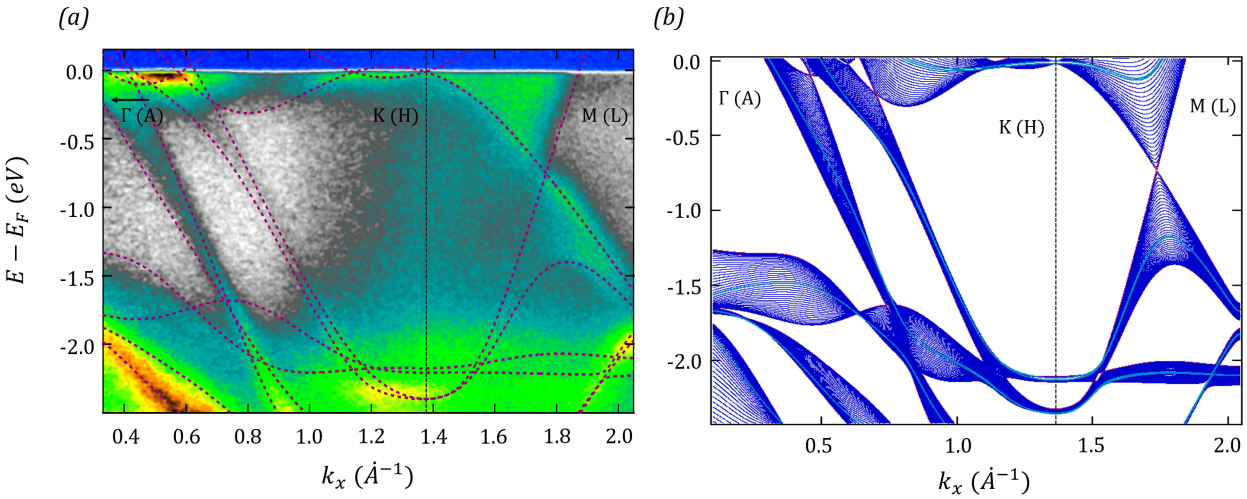

FIGURE 7.7: (a) S-pol ARPES spectra over ΓKM (AHL) and spinless GGA band structure along ΓKM (purple dotted lines). (b) k_z-projected SOC relativistic GGA band structure over ΓKM (purple lines) to AHL (light blue lines).

than the out-of-plane lattice parameter, the electrons probed will be confined in a relatively well-defined volume of real space. The momentum component perpendicular to the surface will then be broadened, as a consequence of the Heisenberg uncertainty principle [300].

First we summarize the strict impact of energy dispersion along k_z: Let us fix k_x and k_y to a given value so that we consider only the effect of k_z. On the one hand, and as highlighed in chapter 3, for a given value of k_x, and in a given band, equation (3.7) for k_z (it was labelled as $k_\perp$ in that section):

$$k_z \approx \frac{1}{\hbar}\sqrt{(2mE_{kin}cos^2(\theta_k) + V_0)} \tag{7.1}$$

Independently of cross section effects, this implies that for a given kx, the whole band contributes to the ARPES signal, spanned over a full BZ along k_z. The associated broadening can thus be predicted by plotting a set of dispersion curves with k_z as a parameter and varying over one BZ, as shown in figure 7.7b. This analysis similar to the one performed for figure 6.12 in chapter 6.

On the other hand, considering the energy distribution curve of a single band and neglecting the contribution of the finite excitation hole lifetime to the ARPES spectra [300], the k_z-averaged intensity of the ARPES signal I can be simplistically portrayed by:

$$I(E) \propto \int_{-\infty}^{+\infty} |T_f|^2 |M_{fi}(k_z, E)|^2 \times \frac{2Im[k_z^f]}{(k_z - RE[k_z^f])^2 + (Im[k_z^f])^2} A(E) dk_z \tag{7.2}$$

where T_f denotes the final state surface transmission coefficient, M_{fi} the photoexcitation matrix element, A the energy-dependent part of the spectral function, and k_z^f the k_z component of the final state wave vector. The real part of k_z^f stands for the kz wave vector of the final state being probed while the imaginary part gives the final state intrinsic broadening, which can be expressed as $Im[k_z^f] \propto \frac{1}{\lambda}$ where λ is the photoelectron escape

length or attenuation in the material [300]. Due to the usually short attenuation length λ, the measured final state photoexcited electrons cannot travel within little more than a few unit cells of Ti_3SiC_2 before seeing their wave function be completely damped or before they are transmitted to vacuum through the surface. This intrinsic k_z-broadening would be maintained when attempting to extract the $E(k_z)$ dispersion by further data analysis. It should be noted that k_z resolution can be greatly enhanced when working with higher photon energy(soft x-ray ARPES).

As can be seen by comparing figures 7.7a and 7.7b, there is indeed a good match between the DFT predicted and ARPES domains. Said otherwise, in figure 7.7a, the DFT ΓK bands mostly encompass the experimental band signature, so that what is seen is the whole k_z-projected band structure of figure 7.7b, with an electronic structure averaged over a BZ along c. This makes obvious that in figure 7.7a, the main effect is the first described above (not the intrinsic one), and indicates that the quality of our ARPES data is sufficient to allow us to obtain a satisfying insight into the electronic structure of bulk Ti_3SiC_2.

7.2.3 Fine structure and effect of spin orbit coupling

In figure 7.8a, we set side by side the $\Gamma K(AH)$ ARPES spectra to the SOC GGA band structure over a very narrow range of energies and wave vectors. DFT bands encompass a lobe before K. At K, the lobe closes into a cusp point (gapped by SOC), also evidenced on the ARPES spectra. Above the K point, bands 49 and 48 form a sandclock-like shape and linearly cross about 0.75 eV below E_F (figure 7.8a). SOC would then open another 12meV gap, at the coordinates where the ARPES spectrum shows an intensity extinction.

From this observation, we suggest that spin-orbit coupling does have an effect on the electronic structure of Ti_3SiC_2. As exposed in figure 7.8b, the shape of the bands responsible for the FSs three-pointed star patterns centered in H is characteristic of a band inversion [301]. One of the linear crossings from the band inversion is located in K [figures 7.8a–7.8c]. Its position does not change with k_z. The other set of linear crossings from the band inversion follows the h_1 line, as k_z varies from 0 to π/c(figures 7.8a–7.8c). At all the other (k_x, k_y) coordinates within the three-pointed stars in figure 7.4 (and also along the lateral sides of the band 50 FS platelet; see figure 7.1), bands 49 and 50 become degenerate when k_z reaches the border of the BZ (figure 7.8d). Ultimately, this degeneracy is slightly lifted by SOC, as discussed later on. Despite the evidence of band inversion, the shape of the associate isoenergy surface (figure 7.1) does not seem to match with the existence of a nodal line near the Fermi level, contrary to the case of V_2AlC and M_2AlC phases where a nodal line was clearly evidenced.

Figure 7.4 already gives a direct observation of the fine structure of the energy band pockets around K and H, and figure 7.8 gives additional information about the role played by bands 49 and 50. The E_F position required to get the best possible fit to figure 7.4 is superimposed to the dispersions along k_z presented in figures 7.8d–7.8f (respectively, with and without SOC) for three different points (h_3 is located in the plateau region of band 50 FS, and thus representative of its largest contribution to the thermopower; see figure 7.4).

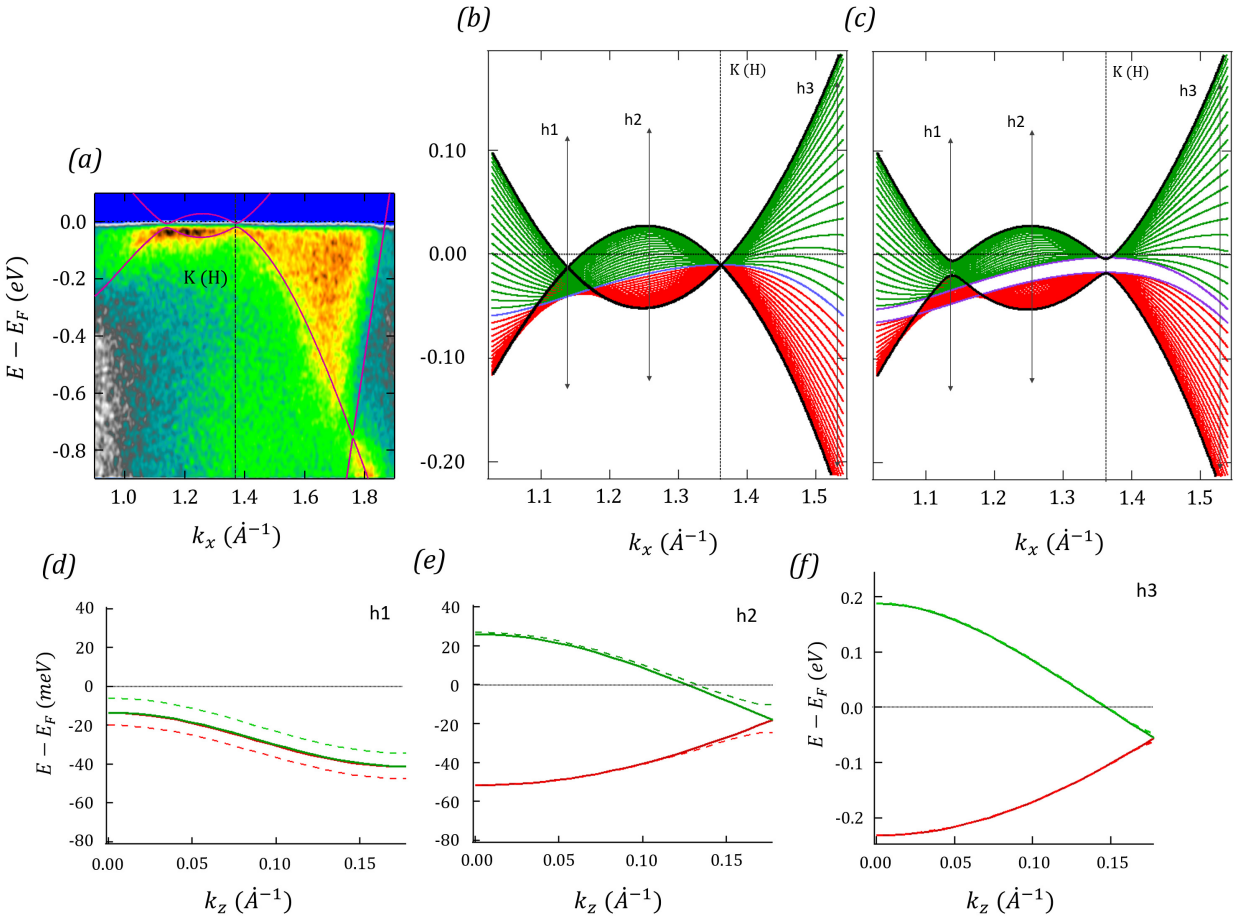

FIGURE 7.8: (a) ARPES spectra compared to SOC calculations over a restricted range of energies and wave vectors. A 12-meV gap opens in the SOC band structure, at a band crossing between K and M about 0.75 eV below E_F , at coordinates where an extinction is observed in the ARPES spectra. The cusp point of the lobe-shaped feature of bands 49 and 50 at the K point is consistent with the ARPES signal. (b) kz projection of spinless GGA bands 49 (red) and 50 (green). Both bands meet for $k_z = \pi/c$ (purple curve), and the band shape for $k_z = 0$ is a clear signature of band inversion (black curve). Band crossings in h_1 and K (H) are found to be linear for the whole range $[0, \pi/c]$. In (c), a 13.5 meV gaps opens in the whole wave-vector range of the figure. The effect of spin-orbit coupling in particular k_z directions is highlighted in (d)–(f).

To analyze the expected contribution to the thermopower, we may use the second criterion developped in section 6.1.2. Fully supporting the thermopower theoretical calculations in [295], one sees that in the FS triangular platelet region of band 50 (line h_3), the intersection between E_F and band 50 occurs at the bottom of the band, where curvature is electronlike, explaining the negative contribution to the thermopower along c [295] (figure 7.8f). Point h_2 also shows an electronlike curvature (figure 7.8e). Interestingly, at point h_1, the full band remains below E_F (figure 7.8d), which means that the top of the band starts to cross E_F at some point when going from h_1 to h_2 (see figures 7.8b and 7.8c), and is therefore hole-like, before turning electron-like as one moves toward h_2. However, the restricted area corresponding to a hole-like behavior is quite small in front of the full plateau area, limited to the surrounding of one of the tiny tubes (somehow close to HK axis) visible in the FS shown in figure 7.1, so that the net contribution of band 50 to the S_{zz} thermopower component must clearly be electronlike. It is interesting to note that without operating the small shift in E_F

required to fit the ARPES data, one could reach different conclusions. This is an indication that the small shift in E_F needed to fit the ARPES data is not due to intrinsic k_z broadening, but is a real feature of the band structure.

In the case of band 50, most of the FS area is formed of points like h_3, forming the plateau-like shape of the corresponding FS. Although bands 49 and 50 are degenerate along a closed line located in the AHL plane (the lateral border of the FS platelet), in the plateau region of band 50, band 49 is located appreciably below E_F , and interactions between bands 49 and 50 due, e.g., to phonon-induced modifications of the electronic dispersion as mentioned in [297], or to thermal spreading of the electrons of band 49 into band 50, are not relevant here. The situation changes when examining the case of band 49. The contribution of band 49 to S_{zz} can first be analyzed with the help of figure 7.9, and using the same reasoning as above. Figure 7.9a (respectively, figure 7.9b) shows the dispersion along k_z for the lines h_4 and h_5 indicated on the energy dispersion curves plotted versus k_x in figure 7.9.c (see also figure 7.4), with k_z as a parameter. As k_x varies, the top of band 49 starts to cross E_F at point M_1 (corresponding to k_z in the AHL plane) and is continuously shifted through E_F until the bottom of the band crosses E_F at point M_2. As shown in figure 7.9b, for a point h_4 close to M_1, the band is hole-like along k_z but for the points closer to M_2, it is electron-like. Therefore there is also a competition between electron and hole-like behaviors, which, as computed by *Chaput et.al.* [295], results in an overall holelike behavior. From figures 7.9a and 6.9b, the hole mass appears much smaller than the electron mass (and its very existence is due to SOC).

Here, it is indeed not straightforward why, in spite of opposite contributions, the holelike behavior, limited to a very narrow part of the band, prevails and gives a positive contribution to S_{zz}, as computed in [295]. But there is more than this for, as obvious from figure 7.9, SOC does not lift the degeneracy between bands 49 and 50 occurring in the AHL plane to an extent which would make thermal processes in the two bands independent from one another. Close to M_1 (and along an entire closed line), bands almost touch one another and dispersion along k_z is Dirac-like. Estimated band splitting (around 11 meV at M_1) is smaller than thermal fluctuations k_BT in the whole 300–800 K range. It is therefore not accurate to compute thermopower by just making use of the electronic structure in each band independently. The influence of T and the phonons has to be explicitly taken into account through two different processes:

a direct modification of the electronic structure as discussed in [297], or thermal fluctuations coupling band 49 to band 50. The contribution of band 50 to in-plane S_{xx} thermopower component is small, since just a very small part of the FS is perpendicular to the (k_x, k_y) plane, and is electron-like. This is in full agreement with the findings of *Chaput et al.* [295]. However, in contrast to their prediction of a positive contribution of band 49 to S_{xx}, in figure 7.9 all dispersion curves along k_x seem to exhibit either a positive curvature, or to be quasi-linear, thus seemingly electron-like.

This might be putted it in line with the calculations in [295], where the hole-like contribution of band 49 seems to be curiously restricted to a very narrow range around E_F , whereas any other energy region in the

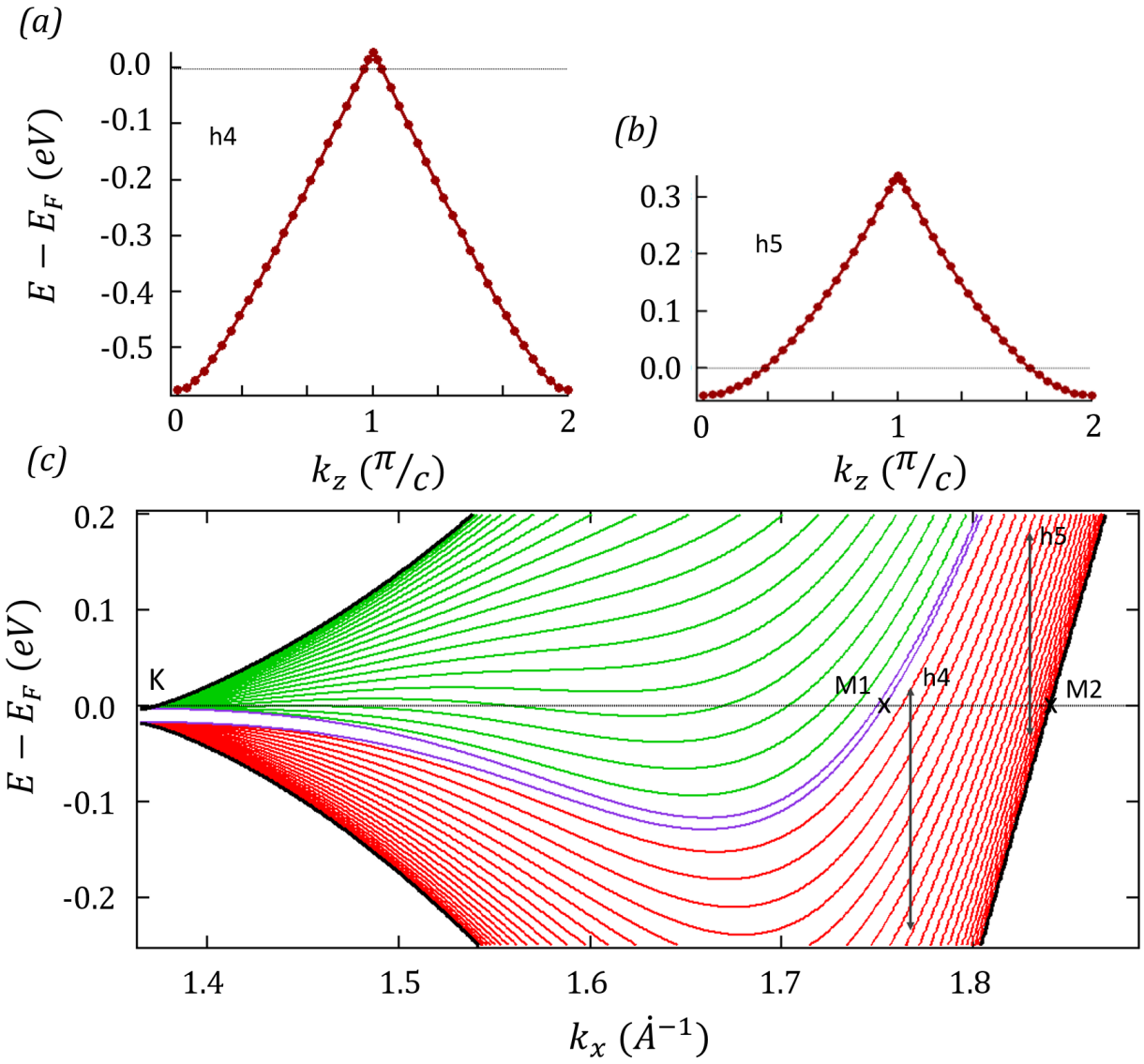

FIGURE 7.9: (a), (b) SOC Out-of-plane profile of band 49 for two specific (k_x, k_y) fixed coordinates, h_4 and h_5. Both are close to the borders of the FS of band 49 over ΓK, respectively at M_1 and M_2. The local hole- or electronlike character at these k points is explored. The respective positions of M_1, M_2, h_4, and h_5 in the ΓK k_z-projected profile of band 49 (red) are given in (c) (band 50 is in green).

band exhibit an electron-like signature. In light of our own results, maybe this finding could be revisited. We note that a computationally accurate estimation of S_{xx} requires to sum up not only velocities over the FS, which are derivatives of FS points, but also their derivatives, a thing not so easy to assess accurately over a complicated FS shape.

The FS of band 50 encompasses a very thin volume of k-space (with a very small k_z width), and a significant part of this FS exhibits quasi-linear dispersion relationships and thus small effective masses. We are in the conditions where the "high-field unitarity scattering limit" described by *Abrikosov* can be met [289]. Thus, magnetoresistance should show a non-negligible linear component at high magnetic field. This is typically observed in bismuth single crystals [302, 303], but it can also be observed in other compounds, such as

transition-metal dichalcogenide WTe_2 [304, 305, 306], where a significant part of the FS would not fulfill the high-field unitary limit conditions while only a small pocket would. This suggests that peculiar transport properties should be observed on Ti_3SiC_2 single crystals at high magnetic fields which, to our knowledge, have not yet been reported (preliminary in-plane MR data obtained in 2017 during the Ph.D. studies of *Lu Shi* from Ti_3SiC_2 single crystals displayed a substantial linear component, added to a parabolic one [307]). When SOC is activated, gaps of about 13–14 meV open for the crossings over the whole area corresponding to the three-pointed star, from 39 meV below to 24 meV above EF and from 1.0 to 1.5 A^1 (figure 7.8c). It implies that a non-negligible part of the BZ near the Fermi level shows a SOC degeneracy lift, especially the crossings of band 49 and 50 due to band inversion. We are in the typical case where the intrinsic deflection mechanism of the anomalous Hall effect [308], also at the origin of the spin Hall effect (SHE) [308], can be significant. While the intrinsic spin Hall effect was shown to arise in gapped nodal line systems such as β-tungsten [279] and some rutile oxides [278], Ti_3SiC_2 could as well be a worthy candidate for SHE, even if no gapped nodes are observed at E_F but large portions of the BZ corresponding to the FSs of band 49 and 50 exhibit band anticrossings. As for the linear magnetoresistance mentioned above, the possible generation of pure spin current in MAX phases through intrinsic SHE has, to our knowledge, not been addressed yet.

7.3 Summary

Within this chapter, we presented a detailed analysis of Ti_3SiC_2 near Fermi level electronic structure. The experimental spectra are found to be in good agreement with the computed FS and BS. A mixture of electron and hole bands contribute to the FS. From orbital character and polarization dependence analysis, Ti d orbitals seem to dominate the electronic structure at the Fermi level, but Si and C p orbitals show a stronger contribution at intermediate energy, starting from 1 eV below E_F . k_z-broadening is found to make a significant contribution to the ARPES spectra, mainly due to the 3D character of several energy bands. The interpretation of Ti_3SiC_2 near zero thermopower taking place in polycrystalline phases was revisited in light of our results, which allowed us to rely upon a simple analysis of the calculated or measured dispersion curves. Although it does not contradict the results of other studies, the contribution of one band is probably more complex than initially thought [145, 295, 296, 297], and would certainly require taking into account phonons, as already discussed in [297]. Band inversions near K points (from band 49 and band 50) lead to the appearance of a complex three-pointed star feature within the first BZ, at the Fermi level, and SOC opens gaps in a significant part of the intricate FSs of bands 49 and 50. A direct measurement of the FS's around H,K allowed us to verify experimentally an old but important finding, previously described in [145]: H-centered pockets are fully delocalized along c, and confer to Ti_3SiC_2 a definitive 3D character, not always observed for other quasi-2D MAX phases. Along with the conclusions of chapter 6, these results suggest the usefulness of future investigations of MAX phase high-field magnetotransport and spintronic related properties.

Chapter 8

Conclusion and prospects

8.1 Conclusion: Unity in diversity

As we have seen throughout this manuscript, $M_{n+1}AX_n$ phases form a very large class of materials that show great promises for applications in extreme conditions and as precursors for the 2D MXENES. Henceforth, most of MAX phase basic properties have been studied in great detail over the past twenty years [1]. Nevertheless, the microscopic origin of several features of MAX phases -including transport and thermopower coefficients and their respective anisotropies, magnetic order as well as the relationships between macroscopic properties and electronic structure- were still under debate before the beginning of my PhD [159, 154]. The applicability of two bands models to describe MAX phase electronic transport was notably questioned.

In 2017, we combined ARPES and DFT calculations to bring the first experimental determination of the Fermi surface and Band structure of a MAX phase: Cr_2AlC. V_2AlC and Ti_3SiC_2 followed, and an overall good agreement between experiments and theory was found for all of them. To some extent, one could humbly say it shed light on some of the open questions mentioned above:

- Cr_2AlC Fermi surface was found to be a complex combination of quasi-bidimensional electron and hole FSs, and its anisotropy is consistent with the output of past magneto-transport measurements on single crystals. Near E_F band renormalization arises near the Fermi level and it appears to be in line with electron-phonon coupling predictions. Despite claims that Cr_2AlC ground state would be AFM, non magnetic DFT calculations allowed to recover most of the features of the bands and no clear signature of AFM ordering nor AFM transition were hinted by neutron powder diffraction. DFT Fermi lines were used to compute in-plane transport coefficients through Boltzmann's equation and an approximation of the relaxation time. The experimental temperature dependence of the in-plane resistivity and Hall coefficient were recovered by calculation for this many bands system, as well as the electron density. It allowed to demonstrate the inadequacy of the two bands Drude model to describe MAX phase electronic transport.

- In contrast to Cr_2AlC, ARPES and DFT analysis revealed that V_2AlC near Fermi level electronic structure

was more three-dimensional. k_z-broadening was successfully assessed and came in support to the assessment of the three dimensional character of the electronic structure of this material. A rough analysis of the Fermi surface and Fermi velocities anisotropies indicated that our results did not match past resistivity anisotropy measurement on single crystals, for which ρ_c/ρ_{ab} was found to be one order of magnitude higher than Cr_2AlC. A MAX phase volatile surface states were observed for the first time, centered at the M points of the V_2AlC BZ. A gapped nodal line within V_2AlC band structure was also evidenced around 0.27-0.29 eV below the Fermi level.

-Ti_3SiC_2 DFT FS and BS successfully reproduced the output of our ARPES mappings. After taking into account a few meV shift of the Fermi level, our FS appeared to be slightly different from past studies [296, 295]. It still exhibits a mixture of hole and electron bands at the Fermi level, with the FS of band 50 accounting for the electron delocalization over c axis. The level of agreement between ARPES and DFT allowed us to investigate finer detail in the electronic structure of this compound, notably SOC. Band inversion and linear band crossings were spotted at the Fermi level. Our DFT calculation showed that these crossings are gapped by SOC. That makes Ti_3SiC_2 a potential candidate for some exotic transport features such as charge current to spin current conversion through intrinsic SHE.

Looking at the respective conclusions of each chapter of this thesis, one could state that MAX phases show a panel of diverse electronic structures and Fermi surfaces. But despite the obvious differences between the near Fermi level electronic structure Cr_2AlC, V_2AlC, Ti_3SiC_2 and other MAX phases, we also uncovered some remarkable features shared by all these compounds:

- As stated in many past studies, we verified that the d orbitals of M atoms dominated the electronic structure of Cr_2AlC, V_2AlC and Ti_3SiC_2 near their respective Fermi levels.

- 5 different rigid band models are needed to describe the electronic structure of most 211 MAX phase, corresponding to the classification 211 which comprises five subfamilies. Varying the M element allows one to tune E_F and navigate through a single "rigid band structure".

- The applicability of rigid band models as well as the success of "standard" DFT calculation for modelling the electronic states of MAX phase suggest that electronic correlations shall not play a major role for the properties of these compounds.

From these consideration, it appears that despite their apparent diversity, the electronic structures of various MAX phases do share some fundamental features. In the case of 211 MAX phases, one could even refer to the applicability of rigid band models as a certain degree of unity within subfamilies of MAX phases.

Regarding all the work presented within this thesis, I was privileged to be involved at each step of the process of scientific production: Single crystal growth, ARPES measurement, ARPES data analysis, DFT calculations and of course the final process of scientific production: publication.

In total, I contributed to 3 scientific articles as a first author [249, 256, 292] , 2 as a second author [228, 229] and I was involved in projects that lead the publication of 4 other articles [123, 138, 176, 140].

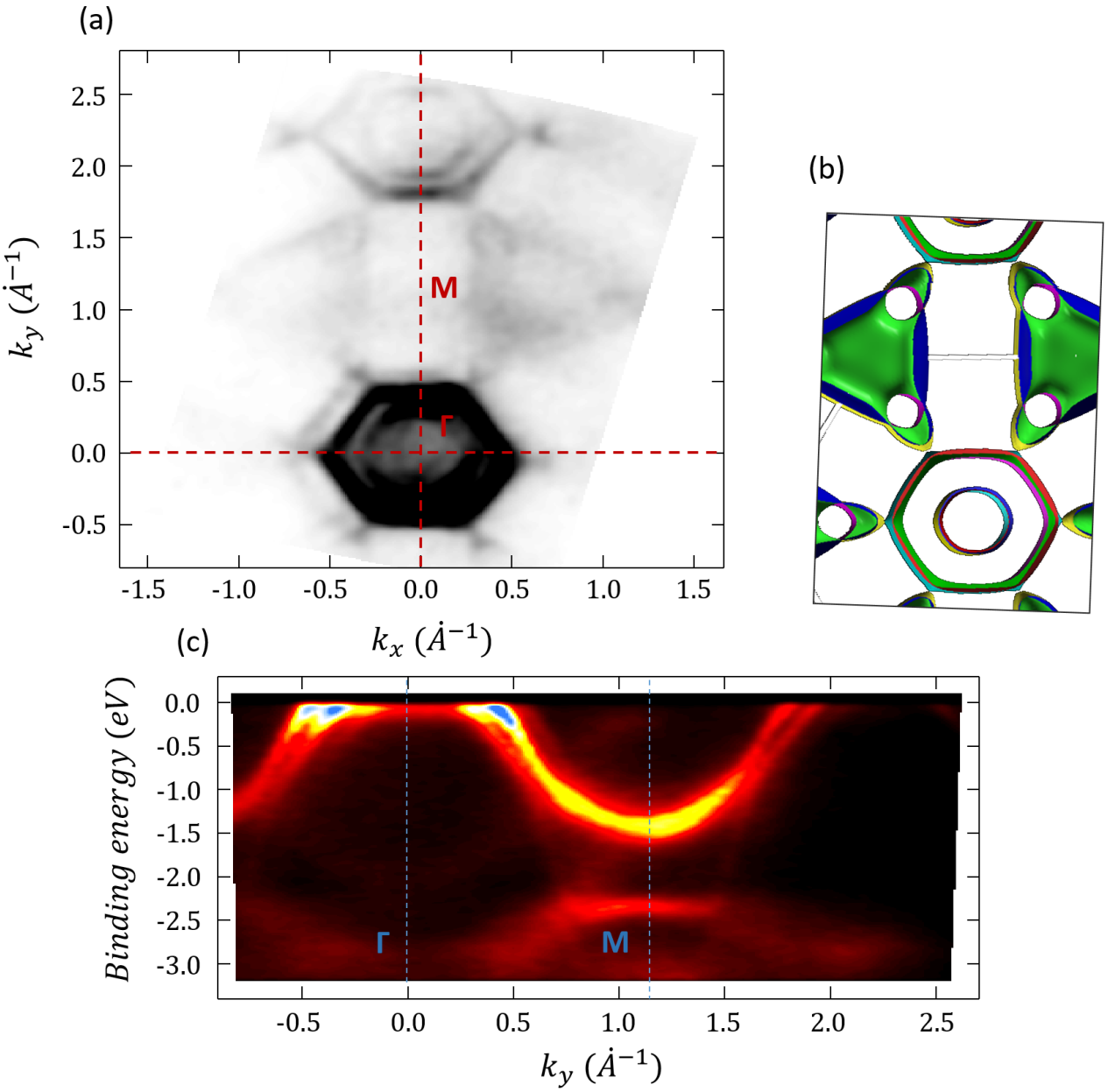

FIGURE 8.1: Ti_2SnC ARPES(a) and DFT (b) Fermi surface. Vertical and horizontal axis respectively stand for ΓM and ΓK direction. (c) Band structure mapping over ΓM

Most of my first two years of PhD were focused on single crystal growth and I now realize how crucial the availability of bulk single crystals was for our work. We could not have performed any experiment mentioned in this manuscript with polycristalline samples synthetized by pressureless sintering. It probably would not have been possible with available MAX phases thin films either. I also want to extend here the importance of our collaboration with Assoc. Prof. *Takahiro Ito*, who and with whom we performed all the ARPES experiment presented in this manuscript and who kindly taught me everything I know about this technique. In addition to ARPES, DFT was an invaluable tool I used for understanding and interpreting experimental spectra. I must admit I am still impressed at how DFT efficiently models many properties of solid state systems and how remarkable was the agreement we obtained between as computed Fermi

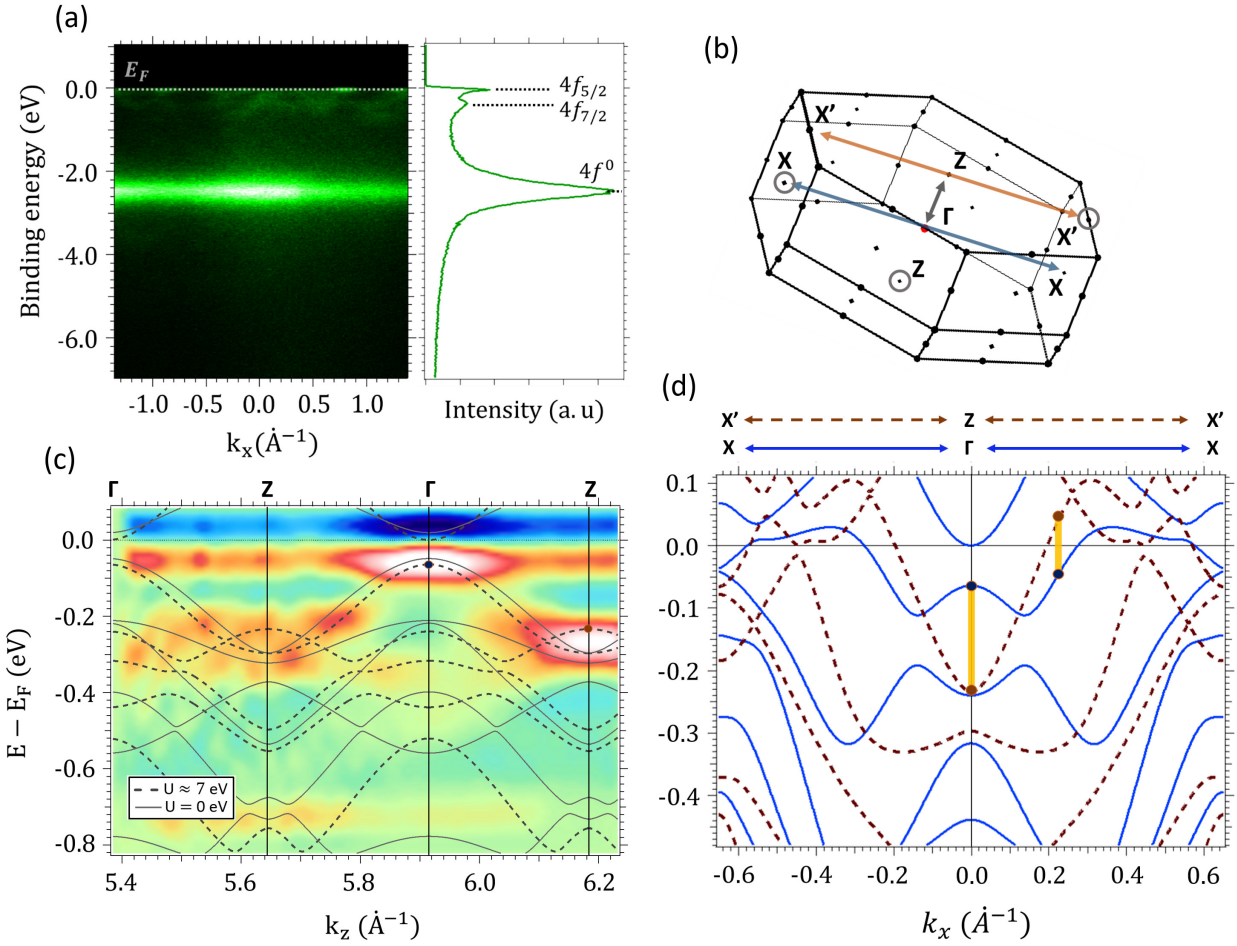

FIGURE 8.2: (a) Integrated spectra of a $Mo_4Ce_4Al_7C_3$ single crystal over a specific direction, with $h\nu$ = 122 eV. The intense flat band at 2.2 eV below E_F corresponds to the $4f_0$ final states, while clear dispersive features close to EF are visible and coexist with the peak corresponding to the $4f_1^{5/2}$ together with nondispersive $4f_1^{5/2}$ final states. (b) BZ of $Mo_4Ce_4Al_7C_3$. (c) Out-of-plane ARPES mapping over ΓZ, obtained by varying $h\nu$ from 100 to 137 eV, and compared with DFT and DFT + U bands. The two dots refer to specific points of band 90 (located in Γ and Z, respectively). (d) DFT + U band structure over ΓX and ZX. The effect of kz-broadening on band 90 is highlighted by the yellow lines, thus indicating a significant kz delocalization of the conduction band

surfaces and experimental ARPES mappings.

8.2 Prospects: New MAX phases, Solid solutions, Rare earth based iMAX and derivatives

I will now briefly outline a few of our latest work and objectives which stand as a direct continuation of this thesis.

-We mapped the Fermi surface and band structure of Ti_2SnC during our last experimental run at SOLEIL Cassiopée line. We obtained an apparent agreement between DFT FS and ARPES, as highlighted in figure 8.1. What might be a surface state similar to the one described in chapter 5 for V_2AlC is observed in figure

8.1c, within an energy interval of -0.7 eV to -1.5 eV and around M points, between 0.7 and 1.6 A^{-1}. The very straight parralel lines observed in the FSs surrounding the M point appear nested one into another. Similar kind of nesting is often at the root of peculiar transport behavior at low temperature, involving for example phonon-electron coupling if a phonon wavevector coincide with the distance between the nested sections of the FSs (A famous example here is the phonon-mediated supraconductivity of $YBa_2Cu_3O_7$ systems [309], which features nesting patterns somewhat similar to Ti_2SnC). Despite the fact that no supraconductive transition were observed at low T for polycristalline samples, measuring magneto-transport of Ti_2SnC single crystals at low temperature may nevertheless lead to interesting results.

-As outlined in chapter 6, synthetizing single crystalline MAX phase solid solutions $(M_xN_{1-x})_2AX$ would allow us to continuously navigate throughout 211 MAX phase rigid band structure. One could reach the nodal line located about 0.27 eV below V_2AlC Fermi level. If one could succeed to do so, SHE and other anomalous transport features may be observed for a MAX phase solid solution (See chapter 6). It is similar to what was described for Ti_3SiC_2 in chapter 7. We have to mention that very recent spin-resolved ARPES experiments performed at *Pr. S.Shin* laboratory at ISSP by *Takahiro Ito* revealed the existence of additional spin polarized surface states bands in the vicinity of the V_2AlC nodal line (these results are not published yet).

- One strategy to induce magnetic ordering and strongly correlated behaviour within a MAX phase would be to incorporate heavy lanthanides atoms featuring partially filled f shell within MAX phase crystal structure. Such materials are the rare earth based iMAX and 4473 phases described in section 2.2.3. As we stated in chapter 3, we successfuly grew bulk single crystals of $(Mo_{2/3}Ho_{1/3})_2AlC$, $(Mo_{2/3}Dy_{1/3})_2AlC$ and $(Mo_{2/3}Gd_{1/3})_2AlC$ iMAXs as well as 4473 $Mo_4Ce_4Al_7C_3$. Rare earth based iMAXs present AFM-like transition at temperatures below 10K while $Mo_4Ce_4Al_7C_3$ becomes ferromagnetic at 10.5K.

The case of $Mo_4Ce_4Al_7C_3$ is special, as it also shows a mixed valence behaviour between the two Ce site it possesses [138]. This has to be put in line with our recent work that indicated that this compound featured an interplay between Kondo lattice behavior and ferromagnetism [140]: Ferromagnetic behavior originates from the Ce atoms with $4f_1$ electronic configuration lying within the Al plane while we first believed that the Ce in the Mo-C conductive plane were solely responsible for the Kondo lattice behaviour of this material. In a recent study [140], we performed a ARPES and DFT+U analysis to demonstrate that the conduction electrons are delocalized over c axis, thus showing that the Ce atoms in the Al planes also participate in the Kondo regime. These results are summarized in figure 8.2. We basically hinted that at least one of the conduction bands must exhibit a k_z dependence. It illustrates well the competition between ferromagnetic and Kondo interactions within $Mo_4Ce_4Al_7C_3$.

ARPES experiments on $(Mo_{2/3}Ho_{1/3})_2AlC$ single crystals were recently performed, but further analysis is needed in order to decipher the morphology of the FSs and the band structure of this material (see figure 8.3).

As a final note, I believe that probing single crystals of MAX phase have allowed us to build a bridge

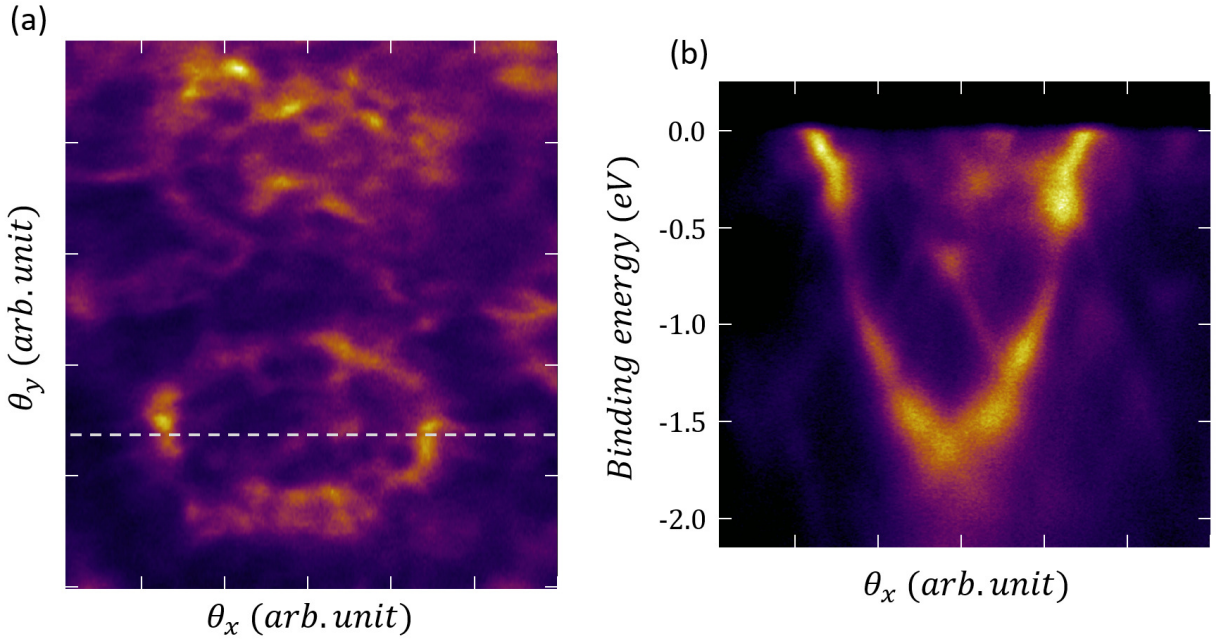

FIGURE 8.3: $(Mo2/3Ho_{1/3})_2AlC$ Fermi surface mapping (a) recorded at 13.4K, above the AFM transition of this compound. Here we kept the natural angular units and ploted a band structure map (b) over the direction corresponding to the white dashed line in (a)

between the Fermi surface (and band structure) of these compounds and some of their basic properties. It is amusing to think that what I used to label as purely conceptual when I was a younger student now appears to me as observables as concrete as the electrical conductivity or the specific heat of a material. In some sense, I now see the vizualisation of ARPES or photoemission spectra as an aperture through which one can watch the "real eigenstates" of the system, and DFT calculations as a binocular that allows one to get a clear image of what is going on further away, to interpret the spectra in greater details. Photoemission spectroscopy and DFT are both invaluable tools for condensed matter physics and material science, and I believe they still have much to tell us about MAX phases and their derivatives.

Bibliography

[1] M. W. Barsoum. "MAX Phases: Properties of Machinable Ternary Carbides and Nitrides". In: *Wiley* 1 (2013). DOI: 10.1002/9783527654581. URL: https://onlinelibrary.wiley.com/doi/book/10.1002/9783527654581.

[2] Michel W. Barsoum. "The MN+1AXN phases: A new class of solids". In: *Progress in Solid State Chemistry* 28.1 (Jan. 2000), pp. 201–281. ISSN: 00796786. DOI: 10.1016/S0079-6786(00)00006-6. URL: https://linkinghub.elsevier.com/retrieve/pii/S0079678600000066.

[3] Martin Magnuson and Maurizio Mattesini. "Chemical bonding and electronic-structure in MAX phases as viewed by X-ray spectroscopy and density functional theory". In: *Thin Solid Films* 621 (Jan. 2017), pp. 108–130. ISSN: 00406090. DOI: 10.1016/j.tsf.2016.11.005. URL: https://linkinghub.elsevier.com/retrieve/pii/S0040609016306903.

[4] Per Eklund, Johanna Rosen, and Per O Å Persson. "Layered ternary $M_{n+1}AX_n$ phases and their 2D derivative MXene: an overview from a thin-film perspective". In: *Journal of Physics D: Applied Physics* 50.11 (Mar. 22, 2017), p. 113001. ISSN: 0022-3727, 1361-6463. DOI: 10.1088/1361-6463/aa57bc. URL: http://stacks.iop.org/0022-3727/50/i=11/a=113001?key=crossref.81ad859564e595ca67c8cc4c3b9b0b12.

[5] Johannes Etzkorn, Martin Ade, and Harald Hillebrecht. "V_2AlC, V_4AlC_{3-x} ($x \approx 0.31$), and $V_{12}Al_3C_8$: Synthesis, Crystal Growth, Structure, and Superstructure". In: *Inorganic Chemistry* 46.18 (Sept. 2007), pp. 7646–7653. ISSN: 0020-1669, 1520-510X. DOI: 10.1021/ic700382y. URL: https://pubs.acs.org/doi/10.1021/ic700382y.

[6] Chenliang Li et al. "A new layer compound Nb_4SiC_3 predicted from first-principles theory". In: *Journal of Physics D: Applied Physics* 42.7 (Apr. 7, 2009), p. 075404. ISSN: 0022-3727, 1361-6463. DOI: 10.1088/0022-3727/42/7/075404. URL: https://iopscience.iop.org/article/10.1088/0022-3727/42/7/075404.

[7] Maxim Sokol et al. "On the Chemical Diversity of the MAX Phases". In: *Trends in Chemistry* 1.2 (May 2019), pp. 210–223. ISSN: 25895974. DOI: 10.1016/j.trechm.2019.02.016. URL: https://linkinghub.elsevier.com/retrieve/pii/S2589597419300292.

[8] Y. Gogotsi B. Anasori. "2D Metal Carbides and Nitrides (MXenes)". In: *Springer* 1 (2019). DOI: 10.1002/9783527654581. URL: https://link.springer.com/book/10.1007/978-3-030-19026-2.

[9] V Nowotny. "Strukturchemie einiger Verbindungen der Übergangsmetalle mit den elementen C, Si, Ge, Sn". In: *Progress in Solid State Chemistry* 5 (1971), pp. 27–70. ISSN: 00796786. DOI: 10.1016/0079-6786(71)90016-1. URL: https://linkinghub.elsevier.com/retrieve/pii/0079678671900161.

[10] H. Nowotny, H. Boller, and O. Beckmann. "Alloy phases crystallizing with structures which occur with non-metallic compounds". In: *Journal of Solid State Chemistry* 2.3 (Nov. 1970), pp. 462–471. ISSN: 00224596. DOI: 10.1016/0022-4596(70)90105-2. URL: https://linkinghub.elsevier.com/retrieve/pii/0022459670901052.

[11] Michel W. Barsoum and Tamer El-Raghy. "Synthesis and Characterization of a Remarkable Ceramic: Ti3SiC2". In: *Journal of the American Ceramic Society* 79.7 (July 1996), pp. 1953–1956. ISSN: 0002-7820, 1551-2916. DOI: 10.1111/j.1151-2916.1996.tb08018.x. URL: http://doi.wiley.com/10.1111/j.1151-2916.1996.tb08018.x.

[12] Michel W. Barsoum and Boen Houng. "Transient Plastic Phase Processing of Titanium-Boron-Carbon Composites". In: *Journal of the American Ceramic Society* 76.6 (June 1993), pp. 1445–1451. ISSN: 0002-7820, 1551-2916. DOI: 10.1111/j.1151-2916.1993.tb03924.x. URL: http://doi.wiley.com/10.1111/j.1151-2916.1993.tb03924.x.

[13] Michel W. Barsoum, Dmitri Brodkin, and Tamer El-Raghy. "Layered machinable ceramics for high temperature applications". In: *Scripta Materialia* 36.5 (Mar. 1997), pp. 535–541. ISSN: 13596462. DOI: 10.1016/S1359-6462(96)00418-6. URL: https://linkinghub.elsevier.com/retrieve/pii/S1359646296004186.

[14] M.W. Barsoum et al. "Thermal properties of Ti3SiC2". In: *Journal of Physics and Chemistry of Solids* 60.4 (Apr. 1999), pp. 429–439. ISSN: 00223697. DOI: 10.1016/S0022-3697(98)00313-8. URL: https://linkinghub.elsevier.com/retrieve/pii/S0022369798003138.

[15] M.W. Barsoum, G. Yaroschuk, and S. Tyagi. "Fabrication and characterization of M2SnC (M = Ti, Zr, Hf and Nb)". In: *Scripta Materialia* 37.10 (Nov. 1997), pp. 1583–1591. ISSN: 13596462. DOI: 10.1016/S1359-6462(97)00288-1. URL: https://linkinghub.elsevier.com/retrieve/pii/S1359646297002881.

[16] Michel W. Barsoum et al. "High-Resolution Transmission Electron Microscopy of Ti_4AlN_3, or $Ti_3Al_2N_2$ Revisited". In: *Journal of the American Ceramic Society* 82.9 (Sept. 1999), pp. 2545–2547. ISSN: 00027820. DOI: 10.1111/j.1151-2916.1999.tb02117.x. URL: http://doi.wiley.com/10.1111/j.1151-2916.1999.tb02117.x.

[17] Bouchaib Manoun et al. "High-pressure x-ray diffraction study of Ta4AlC3". In: *Applied Physics Letters* 88.20 (May 15, 2006), p. 201902. ISSN: 0003-6951, 1077-3118. DOI: 10.1063/1.2202387. URL: http://aip.scitation.org/doi/10.1063/1.2202387.

[18] Chunfeng Hu et al. "Crystal Structure of V_4AlC_3 : A New Layered Ternary Carbide". In: *Journal of the American Ceramic Society* 91.2 (Feb. 2008), pp. 636–639. ISSN: 0002-7820, 1551-2916. DOI: 10.1111/j.1551-2916.2007.02136.x. URL: http://doi.wiley.com/10.1111/j.1551-2916.2007.02136.x.

[19] Johannes Etzkorn et al. "Ti2GaC, Ti4GaC3 and Cr2GaC—Synthesis, crystal growth and structure analysis of Ga-containing MAX phases Mn+1GaCn with M=Ti, Cr and n=1, 3". In: *Journal of Solid State Chemistry* 182.5 (May 2009), pp. 995–1002. ISSN: 00224596. DOI: 10.1016/j.jssc.2009.01.003. URL: https://linkinghub.elsevier.com/retrieve/pii/S0022459609000061.

[20] Zhijun Lin et al. "Microstructures and Theoretical Bulk Modulus of Layered Ternary Tantalum Aluminum Carbides". In: *Journal of the American Ceramic Society* 89.12 (Dec. 2006), pp. 3765–3769. ISSN: 0002-7820, 1551-2916. DOI: 10.1111/j.1551-2916.2006.01303.x. URL: http://doi.wiley.com/10.1111/j.1551-2916.2006.01303.x.

[21] Liya Zheng et al. "(Ti0.5Nb0.5)5AlC4: A New-Layered Compound Belonging to MAX Phases: Rapid Communications of the American Ceramic Society". In: *Journal of the American Ceramic Society* 93.10 (Oct. 2010), pp. 3068–3071. ISSN: 00027820. DOI: 10.1111/j.1551-2916.2010.04056.x. URL: http://doi.wiley.com/10.1111/j.1551-2916.2010.04056.x.

[22] J.-P. Palmquist et al. "M n + 1 A X n phases in the Ti Si C system studied by thin-film synthesis and *ab initio* calculations". In: *Physical Review B* 70.16 (Oct. 1, 2004), p. 165401. ISSN: 1098-0121, 1550-235X. DOI: 10.1103/PhysRevB.70.165401. URL: https://link.aps.org/doi/10.1103/PhysRevB.70.165401.

[23] Y.C. Zhou. .B. Zhang Y.W. Bao. "H Current Status in Layered Ternary Carbide Ti3SiC2, a Review." In: *J Mater Sci Technol* 25(01) (2009), pp. 1–38.

[24] Daniel P. Riley et al. "Self-Propagating High-Temperature Synthesis of Ti3SiC2: I, Ultra-High-Speed Neutron Diffraction Study of the Reaction Mechanism". In: *Journal of the American Ceramic Society* 85.10 (Oct. 2002), pp. 2417–2424. ISSN: 0002-7820, 1551-2916. DOI: 10.1111/j.1151-2916.2002.tb00474.x. URL: http://doi.wiley.com/10.1111/j.1151-2916.2002.tb00474.x.

[25] C.L. Yeh and Y.G. Shen. "Effects of TiC addition on formation of Ti3SiC2 by self-propagating high-temperature synthesis". In: *Journal of Alloys and Compounds* 458.1 (June 2008), pp. 286–291. ISSN: 09258388. DOI: 10.1016/j.jallcom.2007.04.225. URL: https://linkinghub.elsevier.com/retrieve/pii/S0925838807010651.

[26] Lianjun Wang et al. “Rapid Reactive Synthesis and Sintering of Submicron TiC/SiC Composites through Spark Plasma Sintering”. In: *Journal of the American Ceramic Society* 87.6 (June 2004), pp. 1157–1160. ISSN: 00027820, 15512916. DOI: 10.1111/j.1551-2916.2004.01157.x. URL: http://doi.wiley.com/10.1111/j.1551-2916.2004.01157.x.

[27] Wubian Tian et al. “Synthesis and characterization of Cr2AlC ceramics prepared by spark plasma sintering”. In: *Materials Letters* 61.22 (Sept. 2007), pp. 4442–4445. ISSN: 0167577X. DOI: 10.1016/j.matlet.2007.02.023. URL: https://linkinghub.elsevier.com/retrieve/pii/S0167577X07001577.

[28] Xiaohui Wang and Yanchun Zhou. “Solid–liquid reaction synthesis of layered machinable Ti3AlC2 ceramic”. In: *Journal of Materials Chemistry* 12.3 (Feb. 22, 2002), pp. 455–460. ISSN: 09599428, 13645501. DOI: 10.1039/b108685e. URL: http://xlink.rsc.org/?DOI=b108685e.

[29] Yongming Luo et al. “Growth mechanism of Ti3SiC2 single crystals by in-situ reaction of polycarbosilane and metal titanium with CaF2 additive”. In: *Journal of Crystal Growth* 310.14 (July 2008), pp. 3372–3375. ISSN: 00220248. DOI: 10.1016/j.jcrysgro.2008.04.036. URL: https://linkinghub.elsevier.com/retrieve/pii/S0022024808003060.

[30] J.-P. Palmquist et al. “Magnetron sputtered epitaxial single-phase Ti3SiC2 thin films”. In: *Applied Physics Letters* 81.5 (July 29, 2002), pp. 835–837. ISSN: 0003-6951, 1077-3118. DOI: 10.1063/1.1494865. URL: http://aip.scitation.org/doi/10.1063/1.1494865.

[31] H. Högberg et al. “Growth and Property Characterization of Epitaxial MAX-Phase Thin Films from the Ti_{n+1}(Si, Ge, Sn)C_n Systems”. In: *Advances in Science and Technology* 45 (Oct. 2006), pp. 2648–2655. ISSN: 1662-0356. DOI: 10.4028/www.scientific.net/AST.45.2648. URL: https://www.scientific.net/AST.45.2648.

[32] Yan Jiang, Stanislav Mráz, and Jochen M. Schneider. “Growth of V–Al–C thin films by direct current and high power impulse magnetron sputtering from a powder metallurgical composite target”. In: *Thin Solid Films* 538 (July 2013), pp. 1–6. ISSN: 00406090. DOI: 10.1016/j.tsf.2012.09.021. URL: https://linkinghub.elsevier.com/retrieve/pii/S0040609012011352.

[33] T.H. Scabarozi et al. “Synthesis and characterization of Nb2AlC thin films”. In: *Thin Solid Films* 517.9 (Mar. 2009), pp. 2920–2923. ISSN: 00406090. DOI: 10.1016/j.tsf.2008.12.047. URL: https://linkinghub.elsevier.com/retrieve/pii/S0040609008016222.

[34] Per Eklund et al. “The Mn+1AXn phases: Materials science and thin-film processing”. In: *Thin Solid Films* 518.8 (Feb. 2010), pp. 1851–1878. ISSN: 00406090. DOI: 10.1016/j.tsf.2009.07.184. URL: https://linkinghub.elsevier.com/retrieve/pii/S0040609009013352.

[35] Frédéric Mercier et al. “Raman scattering from Ti3SiC2 single crystals”. In: *Applied Physics Letters* 98.8 (Feb. 21, 2011), p. 081912. ISSN: 0003-6951, 1077-3118. DOI: 10.1063/1.3558919. URL: http://aip.scitation.org/doi/10.1063/1.3558919.

[36] William Hume-Rothery. "CXXII. Metallic carbides and nitrides of the type MX". In: *The London, Edinburgh, and Dublin Philosophical Magazine and Journal of Science* 44.357 (Oct. 1953), pp. 1154–1160. ISSN: 1941-5982, 1941-5990. DOI: 10.1080/14786441008520375. URL: http://www.tandfonline.com/doi/abs/10.1080/14786441008520375.

[37] J. Häglund et al. "Theory of bonding in transition-metal carbides and nitrides". In: *Physical Review B* 48.16 (Oct. 15, 1993), pp. 11685–11691. ISSN: 0163-1829, 1095-3795. DOI: 10.1103/PhysRevB.48.11685. URL: https://link.aps.org/doi/10.1103/PhysRevB.48.11685.

[38] J. D. Hettinger et al. "Electrical transport, thermal transport, and elastic properties of M 2 Al C (M = Ti , Cr, Nb, and V)". In: *Physical Review B* 72.11 (Sept. 27, 2005), p. 115120. ISSN: 1098-0121, 1550-235X. DOI: 10.1103/PhysRevB.72.115120. URL: https://link.aps.org/doi/10.1103/PhysRevB.72.115120.

[39] S. Ted Oyama. "Crystal structure and chemical reactivity of transition metal carbides and nitrides". In: *Journal of Solid State Chemistry* 96.2 (Feb. 1992), pp. 442–445. ISSN: 00224596. DOI: 10.1016/S0022-4596(05)80279-8. URL: https://linkinghub.elsevier.com/retrieve/pii/S0022459605802798.

[40] N. Mermin N. Ashcroft. "Solid State Physics". In: *Wiley* (1976).

[41] V. Keppens et al. "Localized vibrational modes in metallic solids". In: *Nature* 395.6705 (Oct. 1998), pp. 876–878. ISSN: 0028-0836, 1476-4687. DOI: 10.1038/27625. URL: http://www.nature.com/articles/27625.

[42] B.C. Sales et al. "Atomic Displacement Parameters and the Lattice Thermal Conductivity of Clathrate-like Thermoelectric Compounds". In: *Journal of Solid State Chemistry* 146.2 (Sept. 1999), pp. 528–532. ISSN: 00224596. DOI: 10.1006/jssc.1999.8354. URL: https://linkinghub.elsevier.com/retrieve/pii/S0022459699983548.

[43] M. W. Barsoum. "Room-Temperature Deintercalation and Self-Extrusion of Ga from Cr2GaN". In: *Science* 284.5416 (May 7, 1999), pp. 937–939. ISSN: 00368075, 10959203. DOI: 10.1126/science.284.5416.937. URL: https://www.sciencemag.org/lookup/doi/10.1126/science.284.5416.937.

[44] J. Travaglini et al. "The corrosion behavior of Ti3SiC2 in common acids and dilute NaOH". In: *Corrosion Science* 45.6 (June 2003), pp. 1313–1327. ISSN: 0010938X. DOI: 10.1016/S0010-938X(02)00227-5. URL: https://linkinghub.elsevier.com/retrieve/pii/S0010938X02002275.

[45] V. D. Jovic and M. W. Barsoum. "Corrosion Behavior and Passive Film Characteristics Formed on Ti, Ti[sub 3]SiC[sub 2], and Ti[sub 4]AlN[sub 3] in H[sub 2]SO[sub 4] and HCl". In: *Journal of The Electrochemical Society* 151.2 (2004), B71. ISSN: 00134651. DOI: 10.1149/1.1637897. URL: https://iopscience.iop.org/article/10.1149/1.1637897.

[46] V. D. Jovic et al. "Corrosion Behavior of Ti[sub 3]GeC[sub 2] and Ti[sub 2]AlN in 1 M NaOH". In: *Journal of The Electrochemical Society* 153.7 (2006), B238. ISSN: 00134651. DOI: 10.1149/1.2199247. URL: https://iopscience.iop.org/article/10.1149/1.2199247.

[47] Michael Naguib et al. "Two-Dimensional Nanocrystals Produced by Exfoliation of Ti3AlC2". In: *Advanced Materials* 23.37 (Oct. 4, 2011), pp. 4248–4253. ISSN: 09359648. DOI: 10.1002/adma.201102306. URL: http://doi.wiley.com/10.1002/adma.201102306.

[48] Michel W. Barsoum and Miladin Radovic. "Elastic and Mechanical Properties of the MAX Phases". In: *Annual Review of Materials Research* 41.1 (Aug. 4, 2011), pp. 195–227. ISSN: 1531-7331, 1545-4118. DOI: 10.1146/annurev-matsci-062910-100448. URL: http://www.annualreviews.org/doi/10.1146/annurev-matsci-062910-100448.

[49] Shibo Li et al. "Mechanism for abnormal thermal shock behavior of Cr2AlC". In: *Journal of the European Ceramic Society* 34.5 (May 2014), pp. 1083–1088. ISSN: 09552219. DOI: 10.1016/j.jeurceramsoc.2013.12.003. URL: https://linkinghub.elsevier.com/retrieve/pii/S0955221913005633.

[50] Darin J. Tallman, Babak Anasori, and Michel W. Barsoum. "A Critical Review of the Oxidation of Ti $_2$ AlC, Ti $_3$ AlC $_2$ and Cr $_2$ AlC in Air". In: *Materials Research Letters* 1.3 (Sept. 2013), pp. 115–125. ISSN: 2166-3831. DOI: 10.1080/21663831.2013.806364. URL: http://www.tandfonline.com/doi/abs/10.1080/21663831.2013.806364.

[51] Mohammad Haftani et al. "Studying the oxidation of Ti 2 AlC MAX phase in atmosphere: A review". In: *International Journal of Refractory Metals and Hard Materials* 61 (Dec. 2016), pp. 51–60. ISSN: 02634368. DOI: 10.1016/j.ijrmhm.2016.07.006. URL: https://linkinghub.elsevier.com/retrieve/pii/S0263436816300786.

[52] X.H. Wang and Y.C. Zhou. "High-Temperature Oxidation Behavior of Ti2AlC in Air". In: *Oxidation of Metals* 59.3 (2003), pp. 303–320. ISSN: 0030770X. DOI: 10.1023/A:1023092027697. URL: http://link.springer.com/10.1023/A:1023092027697.

[53] M. Sundberg et al. "Alumina forming high temperature silicides and carbides". In: *Ceramics International* 30.7 (Jan. 2004), pp. 1899–1904. ISSN: 02728842. DOI: 10.1016/j.ceramint.2003.12.046. URL: https://linkinghub.elsevier.com/retrieve/pii/S0272884204001245.

[54] Z.J. Lin et al. "Influence of water vapor on the oxidation behavior of Ti3AlC2 and Ti2AlC". In: *Scripta Materialia* 58.1 (Jan. 2008), pp. 29–32. ISSN: 13596462. DOI: 10.1016/j.scriptamat.2007.09.011. URL: https://linkinghub.elsevier.com/retrieve/pii/S135964620700646X.

[55] Michel Barsoum Miladin Radovic. "MAX Phases: Bridging the gap Between Metals and Ceramics". In: *American Ceramic Society Bulletin* 92 (Apr. 2013), pp. 20–27.

[56] A Farle et al. "Demonstrating the self-healing behaviour of some selected ceramics under combustion chamber conditions". In: *Smart Materials and Structures* 25.8 (Aug. 1, 2016), p. 084019. ISSN: 0964-1726, 1361-665X. DOI: 10.1088/0964-1726/25/8/084019. URL: https://iopscience.iop.org/article/10.1088/0964-1726/25/8/084019.

[57] E.N. Hoffman et al. "MAX phase carbides and nitrides: Properties for future nuclear power plant in-core applications and neutron transmutation analysis". In: *Nuclear Engineering and Design* 244 (Mar. 2012), pp. 17–24. ISSN: 00295493. DOI: 10.1016/j.nucengdes.2011.12.009. URL: https://linkinghub.elsevier.com/retrieve/pii/S0029549311010417.

[58] "Impact Coatings Company". In: *https://impactcoatings.com/* ().

[59] Jenny Frodelius et al. "Ti2AlC coatings deposited by High Velocity Oxy-Fuel spraying". In: *Surface and Coatings Technology* 202.24 (Aug. 2008), pp. 5976–5981. ISSN: 02578972. DOI: 10.1016/j.surfcoat.2008.06.184. URL: https://linkinghub.elsevier.com/retrieve/pii/S0257897208006178.

[60] S. W. Koch L. Bánya. "Semiconductor Quantum Dots". In: *World Scientific* (1993).

[61] Debasis Bera et al. "Quantum Dots and Their Multimodal Applications: A Review". In: *Materials* 3.4 (Mar. 24, 2010), pp. 2260–2345. ISSN: 1996-1944. DOI: 10.3390/ma3042260. URL: http://www.mdpi.com/1996-1944/3/4/2260.

[62] T. W. Ebbesen and P. M. Ajayan. "Large-scale synthesis of carbon nanotubes". In: *Nature* 358.6383 (July 1992), pp. 220–222. ISSN: 0028-0836, 1476-4687. DOI: 10.1038/358220a0. URL: http://www.nature.com/articles/358220a0.

[63] M.S. Dresselhaus, G. Dresselhaus, and R. Saito. "Physics of carbon nanotubes". In: *Carbon* 33.7 (1995), pp. 883–891. ISSN: 00086223. DOI: 10.1016/0008-6223(95)00017-8. URL: https://linkinghub.elsevier.com/retrieve/pii/0008622395000178.

[64] N. G. Chopra et al. "Boron Nitride Nanotubes". In: *Science* 269.5226 (Aug. 18, 1995), pp. 966–967. ISSN: 0036-8075, 1095-9203. DOI: 10.1126/science.269.5226.966. URL: https://www.sciencemag.org/lookup/doi/10.1126/science.269.5226.966.

[65] R. Dingle, W. Wiegmann, and C. H. Henry. "Quantum States of Confined Carriers in Very Thin Al x Ga 1 x As -GaAs- Al x Ga 1 x As Heterostructures". In: *Physical Review Letters* 33.14 (Sept. 30, 1974), pp. 827–830. ISSN: 0031-9007. DOI: 10.1103/PhysRevLett.33.827. URL: https://link.aps.org/doi/10.1103/PhysRevLett.33.827.

[66] K. S. Novoselov. "Electric Field Effect in Atomically Thin Carbon Films". In: *Science* 306.5696 (Oct. 22, 2004), pp. 666–669. ISSN: 0036-8075, 1095-9203. DOI: 10.1126/science.1102896. URL: https://www.sciencemag.org/lookup/doi/10.1126/science.1102896.

[67] K. S. Novoselov et al. "Two-dimensional gas of massless Dirac fermions in graphene". In: *Nature* 438.7065 (Nov. 2005), pp. 197–200. ISSN: 0028-0836, 1476-4687. DOI: 10.1038/nature04233. URL: http://www.nature.com/articles/nature04233.

[68] S. Das Sarma et al. "Electronic transport in two-dimensional graphene". In: *Reviews of Modern Physics* 83.2 (May 16, 2011), pp. 407–470. ISSN: 0034-6861, 1539-0756. DOI: 10.1103/RevModPhys.83.407. URL: https://link.aps.org/doi/10.1103/RevModPhys.83.407.

[69] J. W. McClure. "Band Structure of Graphite and de Haas-van Alphen Effect". In: *Physical Review* 108.3 (Nov. 1, 1957), pp. 612–618. ISSN: 0031-899X. DOI: 10.1103/PhysRev.108.612. URL: https://link.aps.org/doi/10.1103/PhysRev.108.612.

[70] M. Sprinkle et al. "First Direct Observation of a Nearly Ideal Graphene Band Structure". In: *Physical Review Letters* 103.22 (Nov. 24, 2009), p. 226803. ISSN: 0031-9007, 1079-7114. DOI: 10.1103/PhysRevLett.103.226803. URL: https://link.aps.org/doi/10.1103/PhysRevLett.103.226803.

[71] Sheneve Z. Butler et al. "Progress, Challenges, and Opportunities in Two-Dimensional Materials Beyond Graphene". In: *ACS Nano* 7.4 (Apr. 23, 2013), pp. 2898–2926. ISSN: 1936-0851, 1936-086X. DOI: 10.1021/nn400280c. URL: https://pubs.acs.org/doi/10.1021/nn400280c.

[72] Chaoliang Tan et al. "Recent Advances in Ultrathin Two-Dimensional Nanomaterials". In: *Chemical Reviews* 117.9 (May 10, 2017), pp. 6225–6331. ISSN: 0009-2665, 1520-6890. DOI: 10.1021/acs.chemrev.6b00558. URL: https://pubs.acs.org/doi/10.1021/acs.chemrev.6b00558.

[73] Kin Fai Mak et al. "Atomically Thin MoS 2 : A New Direct-Gap Semiconductor". In: *Physical Review Letters* 105.13 (Sept. 24, 2010), p. 136805. ISSN: 0031-9007, 1079-7114. DOI: 10.1103/PhysRevLett.105.136805. URL: https://link.aps.org/doi/10.1103/PhysRevLett.105.136805.

[74] Manish Chhowalla et al. "The chemistry of two-dimensional layered transition metal dichalcogenide nanosheets". In: *Nature Chemistry* 5.4 (Apr. 2013), pp. 263–275. ISSN: 1755-4330, 1755-4349. DOI: 10.1038/nchem.1589. URL: http://www.nature.com/articles/nchem.1589.

[75] K. S. Novoselov et al. "2D materials and van der Waals heterostructures". In: *Science* 353.6298 (July 29, 2016), aac9439. ISSN: 0036-8075, 1095-9203. DOI: 10.1126/science.aac9439. URL: https://www.sciencemag.org/lookup/doi/10.1126/science.aac9439.

[76] V. Nicolosi et al. "Liquid Exfoliation of Layered Materials". In: *Science* 340.6139 (June 21, 2013), pp. 1226419–1226419. ISSN: 0036-8075, 1095-9203. DOI: 10.1126/science.1226419. URL: https://www.sciencemag.org/lookup/doi/10.1126/science.1226419.

[77] Michael Naguib et al. "Two-Dimensional Transition Metal Carbides". In: *ACS Nano* 6.2 (Feb. 28, 2012), pp. 1322–1331. ISSN: 1936-0851, 1936-086X. DOI: 10.1021/nn204153h. URL: https://pubs.acs.org/doi/10.1021/nn204153h.

[78] Michael Naguib et al. "25th Anniversary Article: MXenes: A New Family of Two-Dimensional Materials". In: *Advanced Materials* 26.7 (Feb. 2014), pp. 992–1005. ISSN: 09359648. DOI: 10.1002/adma.201304138. URL: http://doi.wiley.com/10.1002/adma.201304138.

[79] Babak Anasori and Yury Gogotsi. *2D Metal Carbides and Nitrides (MXenes) Structure, Properties and Applications*. OCLC: 1162760781. Cham: Springer International Publishing : Imprint: Springer, 2019. URL: https://link.springer.com/10.1007/978-3-030-19026-2.

[80] Mohammad Khazaei et al. "Novel Electronic and Magnetic Properties of Two-Dimensional Transition Metal Carbides and Nitrides". In: *Advanced Functional Materials* 23.17 (May 6, 2013), pp. 2185–2192. ISSN: 1616301X. DOI: 10.1002/adfm.201202502. URL: http://doi.wiley.com/10.1002/adfm.201202502.

[81] Aurélie Champagne and Jean-Christophe Charlier. "Physical properties of 2D MXenes: from a theoretical perspective". In: *Journal of Physics: Materials* 3.3 (July 27, 2020), p. 032006. ISSN: 2515-7639. DOI: 10.1088/2515-7639/ab97ee. URL: https://iopscience.iop.org/article/10.1088/2515-7639/ab97ee.

[82] Joseph Halim et al. "X-ray photoelectron spectroscopy of select multi-layered transition metal carbides (MXenes)". In: *Applied Surface Science* 362 (Jan. 2016), pp. 406–417. ISSN: 01694332. DOI: 10.1016/j.apsusc.2015.11.089. URL: https://linkinghub.elsevier.com/retrieve/pii/S0169433215027841.

[83] Paula Mori-Sánchez, Aron J. Cohen, and Weitao Yang. "Localization and Delocalization Errors in Density Functional Theory and Implications for Band-Gap Prediction". In: *Physical Review Letters* 100.14 (Apr. 7, 2008), p. 146401. ISSN: 0031-9007, 1079-7114. DOI: 10.1103/PhysRevLett.100.146401. URL: https://link.aps.org/doi/10.1103/PhysRevLett.100.146401.

[84] A. Miranda et al. "Electronic properties of freestanding $Ti_3C_2T_x$ MXene monolayers". In: *Applied Physics Letters* 108.3 (Jan. 18, 2016), p. 033102. ISSN: 0003-6951, 1077-3118. DOI: 10.1063/1.4939971. URL: http://aip.scitation.org/doi/10.1063/1.4939971.

[85] Athanasios Gkountaras et al. "Mechanical Exfoliation of Select MAX Phases and $Mo_4Ce_4Al_7C_3$ Single Crystals to Produce MAXenes". In: *Small* 16.4 (Jan. 2020), p. 1905784. ISSN: 1613-6810, 1613-6829. DOI: 10.1002/smll.201905784. URL: https://onlinelibrary.wiley.com/doi/abs/10.1002/smll.201905784.

[86] Babak Anasori, Maria R. Lukatskaya, and Yury Gogotsi. "2D metal carbides and nitrides (MXenes) for energy storage". In: *Nature Reviews Materials* 2.2 (Feb. 2017), p. 16098. ISSN: 2058-8437. DOI: 10.1038/natrevmats.2016.98. URL: http://www.nature.com/articles/natrevmats201698.

[87] Kai Huang et al. “Two-dimensional transition metal carbides and nitrides (MXenes) for biomedical applications”. In: *Chemical Society Reviews* 47.14 (2018), pp. 5109–5124. ISSN: 0306-0012, 1460-4744. DOI: 10.1039/C7CS00838D. URL: http://xlink.rsc.org/?DOI=C7CS00838D.

[88] Aleksandra Szuplewska et al. “Future Applications of MXenes in Biotechnology, Nanomedicine, and Sensors”. In: *Trends in Biotechnology* 38.3 (Mar. 2020), pp. 264–279. ISSN: 01677799. DOI: 10.1016/j.tibtech.2019.09.001. URL: https://linkinghub.elsevier.com/retrieve/pii/S0167779919302136.

[89] Chuanfang (John) Zhang and Valeria Nicolosi. “Graphene and MXene-based transparent conductive electrodes and supercapacitors”. In: *Energy Storage Materials* 16 (Jan. 2019), pp. 102–125. ISSN: 24058297. DOI: 10.1016/j.ensm.2018.05.003. URL: https://linkinghub.elsevier.com/retrieve/pii/S2405829718304823.

[90] F. Shahzad et al. “Electromagnetic interference shielding with 2D transition metal carbides (MXenes)”. In: *Science* 353.6304 (Sept. 9, 2016), pp. 1137–1140. ISSN: 0036-8075, 1095-9203. DOI: 10.1126/science.aag2421. URL: https://www.sciencemag.org/lookup/doi/10.1126/science.aag2421.

[91] Chen Si et al. “Large-Gap Quantum Spin Hall State in MXenes: d -Band Topological Order in a Triangular Lattice”. In: *Nano Letters* 16.10 (Oct. 12, 2016), pp. 6584–6591. ISSN: 1530-6984, 1530-6992. DOI: 10.1021/acs.nanolett.6b03118. URL: https://pubs.acs.org/doi/10.1021/acs.nanolett.6b03118.

[92] Nathan C. Frey et al. “Tuning Noncollinear Spin Structure and Anisotropy in Ferromagnetic Nitride MXenes”. In: *ACS Nano* 12.6 (June 26, 2018), pp. 6319–6325. ISSN: 1936-0851, 1936-086X. DOI: 10.1021/acsnano.8b03472. URL: https://pubs.acs.org/doi/10.1021/acsnano.8b03472.

[93] J.C. Schuster, H. Nowotny, and C. Vaccaro. “The ternary systems: CrAlC, VAlC, and TiAlC and the behavior of H-phases (M2AlC)”. In: *Journal of Solid State Chemistry* 32.2 (Apr. 1980), pp. 213–219. ISSN: 00224596. DOI: 10.1016/0022-4596(80)90569-1. URL: https://linkinghub.elsevier.com/retrieve/pii/0022459680905691.

[94] S Sridharan and H Nowotny. “Studies in the ternary system Ti-Ta-Al and in the quaternary system Ti-Ta-Al-C”. In: *Z. Metallkd.; (Germany, Federal Republic of)* 74:7 (1983).

[95] El’ad N. Caspi et al. “Ordering of (Cr,V) Layers in Nanolamellar $(Cr_{0.5}V_{0.5})_{n+1}AlC_n$ Compounds”. In: *Materials Research Letters* 3.2 (Apr. 3, 2015), pp. 100–106. ISSN: 2166-3831. DOI: 10.1080/21663831.2014.975294. URL: https://www.tandfonline.com/doi/full/10.1080/21663831.2014.975294.

[96] Chung-Chuan Lai et al. "Phase formation of nanolaminated Mo $_2$ AuC and Mo $_2$ (Au $_{1x}$ Ga $_x$) $_2$ C by a substitutional reaction within Au-capped Mo $_2$ GaC and Mo $_2$ Ga $_2$ C thin films". In: *Nanoscale* 9.45 (2017), pp. 17681–17687. ISSN: 2040-3364, 2040-3372. DOI: 10.1039/C7NR03663A. URL: http://xlink.rsc.org/?DOI=C7NR03663A.

[97] Chung-Chuan Lai et al. "Magnetic properties and structural characterization of layered (Cr $_{0.5}$ Mn $_{0.5}$) $_2$ AuC synthesized by thermally induced substitutional reaction in (Cr $_{0.5}$ Mn $_{0.5}$) $_2$ GaC". In: *APL Materials* 6.2 (Feb. 2018), p. 026104. ISSN: 2166-532X. DOI: 10.1063/1.5006304. URL: http://aip.scitation.org/doi/10.1063/1.5006304.

[98] M. Naguib et al. "New Solid Solution MAX Phases: (Ti $_{0.5}$, V $_{0.5}$) $_3$ AlC $_2$, (Nb $_{0.5}$, V $_{0.5}$) $_2$ AlC, (Nb $_{0.5}$, V $_{0.5}$) $_4$ AlC $_3$ and (Nb $_{0.8}$, Zr $_{0.2}$) $_2$ AlC". In: *Materials Research Letters* 2.4 (Oct. 2, 2014), pp. 233–240. ISSN: 2166-3831. DOI: 10.1080/21663831.2014.932858. URL: http://www.tandfonline.com/doi/abs/10.1080/21663831.2014.932858.

[99] Zhimou Liu et al. "(Cr $_{2/3}$ Ti $_{1/3}$) $_3$ AlC $_2$ and (Cr $_{5/8}$ Ti $_{3/8}$) $_4$ AlC $_3$: New MAX-phase Compounds in Ti-Cr-Al-C System". In: *Journal of the American Ceramic Society* 97.1 (Jan. 2014). Ed. by G. P. Bei, pp. 67–69. ISSN: 00027820. DOI: 10.1111/jace.12731. URL: http://doi.wiley.com/10.1111/jace.12731.

[100] Nishad A. Phatak et al. "Synthesis of a new MAX compound (Cr0.5V0.5)2GeC and its compressive behavior up to 49GPa". In: *Journal of Alloys and Compounds* 475.1 (May 2009), pp. 629–634. ISSN: 09258388. DOI: 10.1016/j.jallcom.2008.07.102. URL: https://linkinghub.elsevier.com/retrieve/pii/S092583880801270X.

[101] Bouchaib Manoun et al. "On the compression behavior of Ti2InC, (Ti0.5, Zr0.5)2InC, and M2SnC (, Nb, Hf) to quasi-hydrostatic pressures up to 50 GPa". In: *Solid State Communications* 149.43 (Nov. 2009), pp. 1978–1983. ISSN: 00381098. DOI: 10.1016/j.ssc.2009.05.043. URL: https://linkinghub.elsevier.com/retrieve/pii/S0038109809003135.

[102] R. Salikhov et al. "Magnetic properties of nanolaminated (Mo $_{0.5}$ Mn $_{0.5}$) $_2$ GaC MAX phase". In: *Journal of Applied Physics* 121.16 (Apr. 28, 2017), p. 163904. ISSN: 0021-8979, 1089-7550. DOI: 10.1063/1.4982197. URL: http://aip.scitation.org/doi/10.1063/1.4982197.

[103] Andrejs Petruhins et al. "Synthesis and characterization of magnetic (Cr0.5Mn0.5)2GaC thin films". In: *Journal of Materials Science* 50.13 (July 2015), pp. 4495–4502. ISSN: 0022-2461, 1573-4803. DOI: 10.1007/s10853-015-8999-8. URL: http://link.springer.com/10.1007/s10853-015-8999-8.

[104] Christin M. Hamm et al. "Non-conventional synthesis and magnetic properties of MAX phases (Cr/Mn) $_2$ AlC and (Cr/Fe) $_2$ AlC". In: *Journal of Materials Chemistry C* 5.23 (2017), pp. 5700–5708. ISSN: 2050-7526, 2050-7534. DOI: 10.1039/C7TC00112F. URL: http://xlink.rsc.org/?DOI=C7TC00112F.

[105] Christin M. Hamm et al. “Structural, magnetic and electrical transport properties of non-conventionally prepared MAX phases V_2AlC and $(V/Mn)_2AlC$”. In: *Materials Chemistry Frontiers* 2.3 (2018), pp. 483–490. ISSN: 2052-1537. DOI: 10.1039/C7QM00488E. URL: http://xlink.rsc.org/?DOI=C7QM00488E.

[106] Y.C. Zhou, J.X. Chen, and J.Y. Wang. “Strengthening of Ti3AlC2 by incorporation of Si to form Ti3Al1xSixC2 solid solutions”. In: *Acta Materialia* 54.5 (Mar. 2006), pp. 1317–1322. ISSN: 13596454. DOI: 10.1016/j.actamat.2005.10.057. URL: https://linkinghub.elsevier.com/retrieve/pii/S1359645405006749.

[107] Denis Horlait et al. “Synthesis and DFT investigation of new bismuth-containing MAX phases”. In: *Scientific Reports* 6.1 (May 2016), p. 18829. ISSN: 2045-2322. DOI: 10.1038/srep18829. URL: http://www.nature.com/articles/srep18829.

[108] Eugenio Zapata-Solvas et al. “Synthesis and physical properties of $(Zr_{1-x},Ti_x)_3AlC_2$ MAX phases”. In: *Journal of the American Ceramic Society* 100.8 (Aug. 2017), pp. 3393–3401. ISSN: 00027820. DOI: 10.1111/jace.14870. URL: http://doi.wiley.com/10.1111/jace.14870.

[109] Markus A. Pietzka and Julius C. Schuster. “Phase Equilibria in the Quaternary System Ti-Al-C-N”. In: *Journal of the American Ceramic Society* 79.9 (Sept. 1996), pp. 2321–2330. ISSN: 0002-7820, 1551-2916. DOI: 10.1111/j.1151-2916.1996.tb08979.x. URL: http://doi.wiley.com/10.1111/j.1151-2916.1996.tb08979.x.

[110] Thierry Cabioc’h et al. “Structural investigation of substoichiometry and solid solution effects in Ti2Al(Cx,N1x)y compounds”. In: *Journal of the European Ceramic Society* 32.8 (July 2012), pp. 1803–1811. ISSN: 09552219. DOI: 10.1016/j.jeurceramsoc.2011.12.011. URL: https://linkinghub.elsevier.com/retrieve/pii/S0955221911006601.

[111] Bouchaib Manoun et al. “Synthesis and compressibility of Ti3(Al,Sn0.2)C2 and Ti3Al(C0.5,N0.5)2”. In: *Journal of Applied Physics* 101.11 (June 2007), p. 113523. ISSN: 0021-8979, 1089-7550. DOI: 10.1063/1.2733644. URL: http://aip.scitation.org/doi/10.1063/1.2733644.

[112] Mustapha Nechiche et al. “Evidence for Symmetry Reduction in $Ti_3(Al_{1-\delta}Cu_\delta)C_2$ MAX Phase Solid Solutions”. In: *Inorganic Chemistry* 56.23 (Dec. 4, 2017), pp. 14388–14395. ISSN: 0020-1669, 1520-510X. DOI: 10.1021/acs.inorgchem.7b01003. URL: https://pubs.acs.org/doi/10.1021/acs.inorgchem.7b01003.

[113] Zhimou Liu et al. “Crystal structure and formation mechanism of (Cr2/3Ti1/3)3AlC2 MAX phase”. In: *Acta Materialia* 73 (July 2014), pp. 186–193. ISSN: 13596454. DOI: 10.1016/j.actamat.2014.04.006. URL: https://linkinghub.elsevier.com/retrieve/pii/S1359645414002456.

[114] Hui Zhang et al. “Partial dislocation in carbon-vacancy-ordered Nb12Al3C8”. In: *Scripta Materialia* 145 (Mar. 2018), pp. 85–89. ISSN: 13596462. DOI: 10.1016/j.scriptamat.2017.10.020. URL: https://linkinghub.elsevier.com/retrieve/pii/S1359646217306164.

[115] Babak Anasori et al. "Experimental and theoretical characterization of ordered MAX phases Mo $_2$ TiAlC $_2$ and Mo $_2$ Ti $_2$ AlC $_3$". In: *Journal of Applied Physics* 118.9 (Sept. 7, 2015), p. 094304. ISSN: 0021-8979, 1089-7550. DOI: 10.1063/1.4929640. URL: http://aip.scitation.org/doi/10.1063/1.4929640.

[116] Martin Dahlqvist and Johanna Rosen. "Order and disorder in quaternary atomic laminates from first-principles calculations". In: *Physical Chemistry Chemical Physics* 17.47 (2015), pp. 31810–31821. ISSN: 1463-9076, 1463-9084. DOI: 10.1039/C5CP06021D. URL: http://xlink.rsc.org/?DOI=C5CP06021D.

[117] Babak Anasori et al. "Two-Dimensional, Ordered, Double Transition Metals Carbides (MXenes)". In: *ACS Nano* 9.10 (Oct. 27, 2015), pp. 9507–9516. ISSN: 1936-0851, 1936-086X. DOI: 10.1021/acsnano.5b03591. URL: https://pubs.acs.org/doi/10.1021/acsnano.5b03591.

[118] Quanzheng Tao et al. "Two-dimensional Mo1.33C MXene with divacancy ordering prepared from parent 3D laminate with in-plane chemical ordering". In: *Nature Communications* 8.1 (Apr. 2017), p. 14949. ISSN: 2041-1723. DOI: 10.1038/ncomms14949. URL: http://www.nature.com/articles/ncomms14949.

[119] Martin Dahlqvist et al. "Prediction and synthesis of a family of atomic laminate phases with Kagomé-like and in-plane chemical ordering". In: *Science Advances* 3.7 (July 2017), e1700642. ISSN: 2375-2548. DOI: 10.1126/sciadv.1700642. URL: https://advances.sciencemag.org/lookup/doi/10.1126/sciadv.1700642.

[120] J. Lu et al. "Theoretical and Experimental Exploration of a Novel In-Plane Chemically Ordered (Cr $_{2/3}$ M $_{1/3}$) $_2$ AlC *i* -MAX Phase with M = Sc and Y". In: *Crystal Growth & Design* 17.11 (Nov. 2017), pp. 5704–5711. ISSN: 1528-7483, 1528-7505. DOI: 10.1021/acs.cgd.7b00642. URL: https://pubs.acs.org/doi/10.1021/acs.cgd.7b00642.

[121] Liugang Chen et al. "Theoretical Prediction and Synthesis of (Cr $_{2/3}$ Zr $_{1/3}$) $_2$ AlC *i* -MAX Phase". In: *Inorganic Chemistry* 57.11 (June 4, 2018), pp. 6237–6244. ISSN: 0020-1669, 1520-510X. DOI: 10.1021/acs.inorgchem.8b00021. URL: https://pubs.acs.org/doi/10.1021/acs.inorgchem.8b00021.

[122] Quanzheng Tao et al. "Atomically Layered and Ordered Rare-Earth *i* -MAX Phases: A New Class of Magnetic Quaternary Compounds". In: *Chemistry of Materials* 31.7 (Apr. 9, 2019), pp. 2476–2485. ISSN: 0897-4756, 1520-5002. DOI: 10.1021/acs.chemmater.8b05298. URL: https://pubs.acs.org/doi/10.1021/acs.chemmater.8b05298.

[123] A. Champagne et al. "First-order Raman scattering of rare-earth containing i -MAX single crystals (Mo 2 / 3 RE 1 / 3) 2 AlC (RE = Nd , Gd , Dy , Ho , Er)". In: *Physical Review Materials* 3.5 (May 31, 2019), p. 053609. ISSN: 2475-9953. DOI: 10.1103/PhysRevMaterials.3.053609. URL: https://link.aps.org/doi/10.1103/PhysRevMaterials.3.053609.

[124] P Gegenwart et al. "High-field phase diagram of the heavy-fermion metal YbRh $_2$ Si $_2$". In: *New Journal of Physics* 8.9 (Sept. 1, 2006), pp. 171–171. ISSN: 1367-2630. DOI: 10.1088/1367-2630/8/9/171. URL: https://iopscience.iop.org/article/10.1088/1367-2630/8/9/171.

[125] J. Flouquet et al. "The heavy fermion compound CeRu2Si2: Magnetic instability, lattice quasicollapse and metamagnetism". In: *Physica B: Condensed Matter* 215.1 (Oct. 1995), pp. 77–87. ISSN: 09214526. DOI: 10.1016/0921-4526(95)00028-8. URL: https://linkinghub.elsevier.com/retrieve/pii/0921452695000288.

[126] T. T. M. Palstra et al. "Superconducting and Magnetic Transitions in the Heavy-Fermion System U Ru 2 Si 2". In: *Physical Review Letters* 55.24 (Dec. 9, 1985), pp. 2727–2730. ISSN: 0031-9007. DOI: 10.1103/PhysRevLett.55.2727. URL: https://link.aps.org/doi/10.1103/PhysRevLett.55.2727.

[127] E. Bucher et al. "Electronic properties of beryllides of the rare earth and some actinides". In: *Physical Review B* 11.1 (Jan. 1, 1975), pp. 440–449. ISSN: 0556-2805. DOI: 10.1103/PhysRevB.11.440. URL: https://link.aps.org/doi/10.1103/PhysRevB.11.440.

[128] J. Flouquet et al. "Low-temperature properties of CeAl $_3$". In: *Journal of Applied Physics* 53.3 (Mar. 1982), pp. 2127–2130. ISSN: 0021-8979, 1089-7550. DOI: 10.1063/1.330755. URL: http://aip.scitation.org/doi/10.1063/1.330755.

[129] G. R. Stewart, Z. Fisk, and M. S. Wire. "New Ce Heavy-Fermion System: CeCu 6". In: *Physical Review B* 30.1 (July 1, 1984), pp. 482–484. ISSN: 0163-1829. DOI: 10.1103/PhysRevB.30.482. URL: https://link.aps.org/doi/10.1103/PhysRevB.30.482.

[130] Piers Coleman. "Heavy Fermions: Electrons at the Edge of Magnetism". In: *Handbook of Magnetism and Advanced Magnetic Materials*. Ed. by Helmut Kronmüller and Stuart Parkin. Chichester, UK: John Wiley & Sons, Ltd, Dec. 15, 2007, hmm105. URL: http://doi.wiley.com/10.1002/9780470022184.hmm105.

[131] C. M. Varma. "Phenomenological Aspects of Heavy Fermions". In: *Physical Review Letters* 55.24 (Dec. 9, 1985), pp. 2723–2726. DOI: 10.1103/PhysRevLett.55.2723. URL: https://link.aps.org/doi/10.1103/PhysRevLett.55.2723.

[132] W. Lieke et al. "Superconductivity in CeCu $_2$ Si $_2$ (invited)". In: *Journal of Applied Physics* 53.3 (Mar. 1982), pp. 2111–2116. ISSN: 0021-8979, 1089-7550. DOI: 10.1063/1.330714. URL: http://aip.scitation.org/doi/10.1063/1.330714.

[133] E. Schuberth et al. "Emergence of superconductivity in the canonical heavy-electron metal YbRh2Si2". In: *Science* 351.6272 (Jan. 29, 2016), pp. 485–488. ISSN: 0036-8075, 1095-9203. DOI: 10.1126/science.aaa9733. URL: https://www.sciencemag.org/lookup/doi/10.1126/science.aaa9733.

[134] M. F. Hundley et al. "Hybridization gap in Ce 3 Bi 4 Pt 3". In: *Physical Review B* 42.10 (Oct. 1, 1990), pp. 6842–6845. ISSN: 0163-1829, 1095-3795. DOI: 10.1103/PhysRevB.42.6842. URL: https://link.aps.org/doi/10.1103/PhysRevB.42.6842.

[135] Qimiao Si et al. "Locally critical quantum phase transitions in strongly correlated metals". In: *Nature* 413.6858 (Oct. 2001), pp. 804–808. ISSN: 0028-0836, 1476-4687. DOI: 10.1038/35101507. URL: http://www.nature.com/articles/35101507.

[136] Q. Si and F. Steglich. "Heavy Fermions and Quantum Phase Transitions". In: *Science* 329.5996 (Sept. 3, 2010), pp. 1161–1166. ISSN: 0036-8075, 1095-9203. DOI: 10.1126/science.1191195. URL: https://www.sciencemag.org/lookup/doi/10.1126/science.1191195.

[137] M Barbier and et.Al. "Unpublished". In: (2020).

[138] Q. Tao et al. "Rare-earth (RE) nanolaminates Mo 4 RE 4 Al 7 C 3 featuring ferromagnetism and mixed-valence states". In: *Physical Review Materials* 2.11 (Nov. 5, 2018), p. 114401. ISSN: 2475-9953. DOI: 10.1103/PhysRevMaterials.2.114401. URL: https://link.aps.org/doi/10.1103/PhysRevMaterials.2.114401.

[139] Peter Day, Noel S Hush, and Robin J.H Clark. "Mixed valence: origins and developments". In: *Philosophical Transactions of the Royal Society A: Mathematical, Physical and Engineering Sciences* 366.1862 (Jan. 13, 2008), pp. 5–14. ISSN: 1364-503X, 1471-2962. DOI: 10.1098/rsta.2007.2135. URL: https://royalsocietypublishing.org/doi/10.1098/rsta.2007.2135.

[140] Maxime Barbier et al. "Mo 4 Ce 4 Al 7 C 3 : A nanolamellar ferromagnetic Kondo lattice". In: *Physical Review B* 102.15 (Oct. 16, 2020), p. 155121. ISSN: 2469-9950, 2469-9969. DOI: 10.1103/PhysRevB.102.155121. URL: https://link.aps.org/doi/10.1103/PhysRevB.102.155121.

[141] C. Kittel. "Introduction to Solid States Physics". In: *Wiley* (2004).

[142] F. Laloe C.C. Tanudji B. Diu. "Mecanique Quantique". In: *Hermann* (1997).

[143] Glenn A. Burdick. "Energy Band Structure of Copper". In: *Physical Review* 129.1 (Jan. 1, 1963), pp. 138–150. DOI: 10.1103/PhysRev.129.138. URL: https://link.aps.org/doi/10.1103/PhysRev.129.138.

[144] G. Hug, M. Jaouen, and M. W. Barsoum. "X-ray absorption spectroscopy, EELS, and full-potential augmented plane wave study of the electronic structure of Ti 2 Al C , Ti 2 Al N , Nb 2 Al C , and (Ti 0.5 Nb 0.5) 2 Al C". In: *Physical Review B* 71.2 (Jan. 18, 2005), p. 024105. ISSN: 1098-0121, 1550-235X. DOI: 10.1103/PhysRevB.71.024105. URL: https://link.aps.org/doi/10.1103/PhysRevB.71.024105.

[145] M. Magnuson et al. "Electronic structure investigation of Ti 3 AlC 2 , Ti 3 SiC 2 , and Ti 3 GeC 2 by soft x-ray emission spectroscopy". In: *Physical Review B* 72.24 (Dec. 1, 2005), p. 245101. ISSN: 1098-0121, 1550-235X. DOI: 10.1103/PhysRevB.72.245101. URL: https://link.aps.org/doi/10.1103/PhysRevB.72.245101.

[146] M. Magnuson et al. "Electronic structure and chemical bonding in Ti 2 Al C investigated by soft x-ray emission spectroscopy". In: *Physical Review B* 74.19 (Nov. 14, 2006), p. 195108. ISSN: 1098-0121, 1550-235X. DOI: 10.1103/PhysRevB.74.195108. URL: https://link.aps.org/doi/10.1103/PhysRevB.74.195108.

[147] M. Magnuson et al. "Electronic structure and chemical bonding in Ti 4 Si C 3 investigated by soft x-ray emission spectroscopy and first-principles theory". In: *Physical Review B* 74.20 (Nov. 3, 2006), p. 205102. ISSN: 1098-0121, 1550-235X. DOI: 10.1103/PhysRevB.74.205102. URL: https://link.aps.org/doi/10.1103/PhysRevB.74.205102.

[148] N. I. Medvedeva et al. "Electronic properties of Ti 3 SiC 2 -based solid solutions". In: *Physical Review B* 58.24 (Dec. 15, 1998), pp. 16042–16050. ISSN: 0163-1829, 1095-3795. DOI: 10.1103/PhysRevB.58.16042. URL: https://link.aps.org/doi/10.1103/PhysRevB.58.16042.

[149] S.E. Stoltz, H.I. Starnberg, and M.W. Barsoum. "Core level and valence band studies of layered Ti3SiC2 by high resolution photoelectron spectroscopy". In: *Journal of Physics and Chemistry of Solids* 64.12 (Dec. 2003), pp. 2321–2328. ISSN: 00223697. DOI: 10.1016/S0022-3697(03)00267-1. URL: https://linkinghub.elsevier.com/retrieve/pii/S0022369703002671.

[150] Yanchun Zhou et al. "*Ab initio* geometry optimization and ground state properties of layered ternary carbides Ti $_3$ MC $_2$ (M = Al, Si and Ge)". In: *Journal of Physics: Condensed Matter* 13.44 (Nov. 5, 2001), pp. 10001–10010. ISSN: 0953-8984, 1361-648X. DOI: 10.1088/0953-8984/13/44/313. URL: https://iopscience.iop.org/article/10.1088/0953-8984/13/44/313.

[151] Jingyang Wang and Yanchun Zhou. "Dependence of elastic stiffness on electronic band structure of nanolaminate M 2 AlC (M = Ti , V , Nb , and Cr) ceramics". In: *Physical Review B* 69.21 (June 30, 2004), p. 214111. ISSN: 1098-0121, 1550-235X. DOI: 10.1103/PhysRevB.69.214111. URL: https://link.aps.org/doi/10.1103/PhysRevB.69.214111.

[152] R. Ahuja et al. "Electronic structure of Ti3SiC2". In: *Applied Physics Letters* 76.16 (Apr. 17, 2000), pp. 2226–2228. ISSN: 0003-6951, 1077-3118. DOI: 10.1063/1.126304. URL: http://aip.scitation.org/doi/10.1063/1.126304.

[153] I.R. Shein and A.L. Ivanovskii. "Structural, elastic, and electronic properties of new 211 MAX phase Nb2GeC from first-principles calculations". In: *Physica B: Condensed Matter* 410 (Feb. 2013), pp. 42–48. ISSN: 09214526. DOI: 10.1016/j.physb.2012.10.036. URL: https://linkinghub.elsevier.com/retrieve/pii/S0921452612009714.

[154] Thierry Ouisse and Michel W. Barsoum. "Magnetotransport in the MAX phases and their 2D derivatives: MXenes". In: *Materials Research Letters* 5.6 (Nov. 2, 2017), pp. 365–378. ISSN: 2166-3831. DOI: 10.1080/21663831.2017.1333537. URL: https://www.tandfonline.com/doi/full/10.1080/21663831.2017.1333537.

[155] T.H. Scabarozi et al. "Weak electronic anisotropy in the layered nanolaminate Ti 2 GeC". In: *Solid State Communications* 146.11 (June 2008), pp. 498–501. ISSN: 00381098. DOI: 10.1016/j.ssc.2008.03.026. URL: https://linkinghub.elsevier.com/retrieve/pii/S0038109808001658.

[156] Y C Zhou et al. "Electronic structure of the layered ternary carbides Ti $_2$ SnC and Ti $_2$ GeC". In: *Journal of Physics: Condensed Matter* 12.46 (Nov. 20, 2000), pp. 9617–9627. ISSN: 0953-8984, 1361-648X. DOI: 10.1088/0953-8984/12/46/309. URL: https://iopscience.iop.org/article/10.1088/0953-8984/12/46/309.

[157] T. Ouisse et al. "High temperature solution growth and characterization of Cr2AlC single crystals". In: *Journal of Crystal Growth* 384 (Dec. 2013), pp. 88–95. ISSN: 00220248. DOI: 10.1016/j.jcrysgro.2013.09.021. URL: https://linkinghub.elsevier.com/retrieve/pii/S0022024813006222.

[158] L. Shi et al. "Synthesis of single crystals of V2AlC phase by high-temperature solution growth and slow cooling technique". In: *Acta Materialia* 83 (Jan. 2015), pp. 304–309. ISSN: 13596454. DOI: 10.1016/j.actamat.2014.10.018. URL: https://linkinghub.elsevier.com/retrieve/pii/S1359645414007708.

[159] T. Ouisse et al. "Magnetotransport properties of nearly-free electrons in two-dimensional hexagonal metals and application to the M n + 1 A X n phases". In: *Physical Review B* 92.4 (July 31, 2015), p. 045133. ISSN: 1098-0121, 1550-235X. DOI: 10.1103/PhysRevB.92.045133. URL: https://link.aps.org/doi/10.1103/PhysRevB.92.045133.

[160] J. Czochralski. "Ein neues Verfahren zur Messung der Kristallisationsgeschwindigkeit der Metalle". In: *Zeitschrift für Physikalische Chemie* 92U.1 (Jan. 1, 1918). ISSN: 2196-7156, 0942-9352. DOI: 10.1515/zpch-1918-9212. URL: http://www.degruyter.com/view/j/zpch.1918.92.issue-1/zpch-1918-9212/zpch-1918-9212.xml.

[161] Olli Anttila. "Czochralski Growth of Silicon Crystals". In: *Handbook of Silicon Based MEMS Materials and Technologies*. Elsevier, 2010, pp. 19–36. ISBN: 978-0-8155-1594-4. DOI: 10.1016/B978-0-8155-1594-4.00002-4. URL: https://linkinghub.elsevier.com/retrieve/pii/B9780815515944000024.

[162] Brian R Pamplin. *Crystal Growth: International Series on the Science of the Solid State*. Kent: Elsevier Science, 2014. ISBN: 978-1-4831-6146-4. URL: http://qut.eblib.com.au/patron/FullRecord.aspx?p=1834286.

[163] S. G. Singh et al. "Growth of germanium single crystals by Czochralski technique". In: SOLID STATE PHYSICS: Proceedings of the 56th DAE Solid State Physics Symposium 2011. SRM University, Kattankulathur, Tamilnadu, India, 2012, pp. 1091–1092. DOI: 10.1063/1.4710387. URL: http://aip.scitation.org/doi/abs/10.1063/1.4710387.

[164] K. Kliemt and C. Krellner. "Crystal growth by Bridgman and Czochralski method of the ferromagnetic quantum critical material YbNi 4 P 2". In: *Journal of Crystal Growth* 449 (Sept. 2016), pp. 129–133. ISSN: 00220248. DOI: 10.1016/j.jcrysgro.2016.05.042. URL: https://linkinghub.elsevier.com/retrieve/pii/S0022024816302731.

[165] C Krellner et al. "Ferromagnetic quantum criticality in the quasi-one-dimensional heavy fermion metal YbNi $_4$ P $_2$". In: *New Journal of Physics* 13.10 (Oct. 12, 2011), p. 103014. ISSN: 1367-2630. DOI: 10.1088/1367-2630/13/10/103014. URL: https://iopscience.iop.org/article/10.1088/1367-2630/13/10/103014.

[166] R. Nitsche, H.U. Bölsterli, and M. Lichtensteiger. "Crystal growth by chemical transport reactions—I". In: *Journal of Physics and Chemistry of Solids* 21.3 (Dec. 1961), pp. 199–205. ISSN: 00223697. DOI: 10.1016/0022-3697(61)90098-1. URL: https://linkinghub.elsevier.com/retrieve/pii/0022369761900981.

[167] Yu. A. Vodakov et al. "Epitaxial growth of silicon carbide layers by sublimation „sandwich method" (I) growth kinetics in vacuum". In: *Kristall und Technik* 14.6 (1979), pp. 729–740. ISSN: 00234753, 15214079. DOI: 10.1002/crat.19790140618. URL: http://doi.wiley.com/10.1002/crat.19790140618.

[168] G. Muller and J. Friedrich. "Crystal Growth, Bulk: Methods". In: *Elsevier* (2005).

[169] Jun Takahashi, Masatoshi Kanaya, and Yuichiro Fujiwara. "Sublimation growth of SiC single crystalline ingots on faces perpendicular to the (0001) basal plane". In: *Journal of Crystal Growth* 135.1 (Jan. 1994), pp. 61–70. ISSN: 00220248. DOI: 10.1016/0022-0248(94)90726-9. URL: https://linkinghub.elsevier.com/retrieve/pii/0022024894907269.

[170] M. B. Panish. "Molecular Beam Epitaxy". In: *Science* 208.4446 (May 23, 1980), pp. 916–922. ISSN: 0036-8075, 1095-9203. DOI: 10.1126/science.208.4446.916. URL: https://www.sciencemag.org/lookup/doi/10.1126/science.208.4446.916.

[171] Suk-Joong L. Kang et al. "Solid-State Conversion of Single Crystals: The Principle and the State-of-the-Art". In: *Journal of the American Ceramic Society* 98.2 (Feb. 2015). Ed. by D. J. Green, pp. 347–360. ISSN: 00027820. DOI: 10.1111/jace.13420. URL: http://doi.wiley.com/10.1111/jace.13420.

[172] Iva Milisavljevic and Yiquan Wu. "Current status of solid-state single crystal growth". In: *BMC Materials* 2.1 (Dec. 2020), p. 2. ISSN: 2524-8138. DOI: 10.1186/s42833-020-0008-0. URL: https://bmcmaterials.biomedcentral.com/articles/10.1186/s42833-020-0008-0.

[173] Robert Feigelson, ed. *50 years progress in crystal growth: a reprint collection*. Amsterdam: Elsevier, 2004. 240 pp. ISBN: 978-0-444-51650-3.

[174] J. Abrahamson. "Graphite sublimation temperatures, carbon arcs and crystallite erosion". In: *Carbon* 12.2 (Apr. 1974), pp. 111–141. ISSN: 00086223. DOI: 10.1016/0008-6223(74)90019-0. URL: https://linkinghub.elsevier.com/retrieve/pii/0008622374900190.

[175] F. Lévy. "Single-crystal growth of layered crystals". In: *Il Nuovo Cimento B Series 11* 38.2 (Apr. 1977), pp. 359–368. ISSN: 1826-9877. DOI: 10.1007/BF02723506. URL: http://link.springer.com/10.1007/BF02723506.

[176] A. Champagne et al. "Phonon dispersion curves in Cr $_2$ AlC single-crystals". In: *Materials Research Letters* 6.7 (July 3, 2018), pp. 378–383. ISSN: 2166-3831. DOI: 10.1080/21663831.2018.1463298. URL: https://www.tandfonline.com/doi/full/10.1080/21663831.2018.1463298.

[177] A. Einstein. "Über einem die Erzeugung und Verwandlung des Lichtes betreffenden heuristischen Gesichtspunkt". In: *Annalen der Physik* 17 (1905), p. 132.

[178] K. Siegbahn. "Electron spectroscopy - an outlook". In: *Journal of Electron Spectroscopy and Related Phenomena* 5.1 (Jan. 1974), pp. 3–97. ISSN: 03682048. DOI: 10.1016/0368-2048(74)85005-X. URL: https://linkinghub.elsevier.com/retrieve/pii/036820487485005X.

[179] Stefan Hüfner. *Photoelectron Spectroscopy*. Vol. 82. Berlin, Heidelberg, 1996.

[180] Andrea Damascelli, Zahid Hussain, and Zhi-Xun Shen. "Angle-resolved photoemission studies of the cuprate superconductors". In: *Reviews of Modern Physics* 75.2 (Apr. 17, 2003), pp. 473–541. ISSN: 0034-6861, 1539-0756. DOI: 10.1103/RevModPhys.75.473. URL: https://link.aps.org/doi/10.1103/RevModPhys.75.473.

[181] C.S. Fadley. "X-ray photoelectron spectroscopy: Progress and perspectives". In: *Journal of Electron Spectroscopy and Related Phenomena* 178-179 (May 2010), pp. 2–32. ISSN: 03682048. DOI: 10.1016/j.elspec.2010.01.006. URL: https://linkinghub.elsevier.com/retrieve/pii/S0368204810000095.

[182] Simon Moser. "An experimentalist's guide to the matrix element in angle resolved photoemission". In: *Journal of Electron Spectroscopy and Related Phenomena* 214 (Jan. 2017), pp. 29–52. ISSN: 03682048. DOI: 10.1016/j.elspec.2016.11.007. URL: https://linkinghub.elsevier.com/retrieve/pii/S0368204816301724.

[183] Stephen Douglas Kevan. *Angle-resolved photoemission: theory and current applications*. Amsterdam; New York: Elsevier, 1992. URL: http://site.ebrary.com/id/10258949.

[184] Andrea Damascelli. "Probing the Electronic Structure of Complex Systems by ARPES". In: *Physica Scripta* T109 (2004), p. 61. ISSN: 0031-8949. DOI: 10.1238/Physica.Topical.109a00061. URL: https://iopscience.iop.org/article/10.1238/Physica.Topical.109a00061.

[185] V. V. Nemoshkalenko and V. G. Aleshin. "Fundamentals of the Method of Photoelectron Spectroscopy". In: *Electron Spectroscopy of Crystals*. Boston, MA: Springer US, 1979, pp. 1–44.

[186] T. Mitsuhashi et al. “Influence of k broadening on ARPES spectra of the (110) and (001) surfaces of SrVO 3 films”. In: *Physical Review B* 94.12 (Sept. 28, 2016), p. 125148. ISSN: 2469-9950, 2469-9969. DOI: 10.1103/PhysRevB.94.125148. URL: https://link.aps.org/doi/10.1103/PhysRevB.94.125148.

[187] S Hüfner et al. “Photoemission spectroscopy in metals:” in: *Journal of Electron Spectroscopy and Related Phenomena* 100.1 (Oct. 1999), pp. 191–213.

[188] Jinghua Guo, ed. *X-Rays in Nanoscience: Spectroscopy, Spectromicroscopy, and Scattering Techniques*. Weinheim, Germany: Wiley-VCH Verlag GmbH & Co. KGaA, Oct. 27, 2010. URL: http://doi.wiley.com/10.1002/9783527632282.

[189] E. H. Hwang and S. Das Sarma. “Quasiparticle spectral function in doped graphene: Electron-electron interaction effects in ARPES”. In: *Physical Review B* 77.8 (Feb. 29, 2008), p. 081412. ISSN: 1098-0121, 1550-235X. DOI: 10.1103/PhysRevB.77.081412. URL: https://link.aps.org/doi/10.1103/PhysRevB.77.081412.

[190] M. R. Norman et al. “Condensation energy and spectral functions in high-temperature superconductors”. In: *Physical Review B* 61.21 (June 1, 2000), pp. 14742–14750. ISSN: 0163-1829, 1095-3795. DOI: 10.1103/PhysRevB.61.14742. URL: https://link.aps.org/doi/10.1103/PhysRevB.61.14742.

[191] M. P. Seah and W. A. Dench. “Quantitative electron spectroscopy of surfaces: A standard data base for electron inelastic mean free paths in solids”. In: *Surface and Interface Analysis* 1.1 (Feb. 1979), pp. 2–11. ISSN: 0142-2421, 1096-9918. DOI: 10.1002/sia.740010103. URL: http://doi.wiley.com/10.1002/sia.740010103.

[192] David S. Sholl and Janice A. Steckel. *Density Functional Theory*. Hoboken, NJ, USA: John Wiley & Sons, Inc., Mar. 30, 2009. ISBN: 978-0-470-44771-0 978-0-470-37317-0. DOI: 10.1002/9780470447710. URL: http://doi.wiley.com/10.1002/9780470447710.

[193] V. Fock. “Naherungsmethode zur Losung des quantenmechanischen Mehrkorperproblems”. In: *Zeitschrift fur Physik* 61.1 (Jan. 1930), pp. 126–148. ISSN: 1434-6001, 1434-601X. DOI: 10.1007/BF01340294. URL: http://link.springer.com/10.1007/BF01340294.

[194] L. Brillouin. “Le champ self-consistent de Fock pour les electrons des métaux”. In: *Journal de Physique et le Radium* 5.8 (1934), pp. 413–418. ISSN: 0368-3842. DOI: 10.1051/jphysrad:0193400508041300. URL: http://www.edpsciences.org/10.1051/jphysrad:0193400508041300.

[195] J. C. Slater. “A Simplification of the Hartree-Fock Method”. In: *Physical Review* 81.3 (Feb. 1, 1951), pp. 385–390. ISSN: 0031-899X. DOI: 10.1103/PhysRev.81.385. URL: https://link.aps.org/doi/10.1103/PhysRev.81.385.

[196] J. C. Slater. "The Theory of Complex Spectra". In: *Physical Review* 34.10 (Nov. 15, 1929), pp. 1293–1322. ISSN: 0031-899X. DOI: 10.1103/PhysRev.34.1293. URL: https://link.aps.org/doi/10.1103/PhysRev.34.1293.

[197] "The band structure of aluminium III. A self-consistent calculation". In: *Proceedings of the Royal Society of London. Series A. Mathematical and Physical Sciences* 240.1222 (June 11, 1957), pp. 361–374. ISSN: 0080-4630, 2053-9169. DOI: 10.1098/rspa.1957.0091. URL: https://royalsocietypublishing.org/doi/10.1098/rspa.1957.0091.

[198] F. Bassani and M. Yoshimine. "Electronic Band Structure of Group IV Elements and of III-V Compounds". In: *Physical Review* 130.1 (Apr. 1, 1963), pp. 20–33. ISSN: 0031-899X. DOI: 10.1103/PhysRev.130.20. URL: https://link.aps.org/doi/10.1103/PhysRev.130.20.

[199] L. Dagens and F. Perrot. "Hartree-Fock Band Structure and Optical Gap in Solid Neon and Argon". In: *Physical Review B* 5.2 (Jan. 15, 1972), pp. 641–648. ISSN: 0556-2805. DOI: 10.1103/PhysRevB.5.641. URL: https://link.aps.org/doi/10.1103/PhysRevB.5.641.

[200] R. Dovesi et al. "The electronic structure of α-quartz: A periodic Hartree–Fock calculation". In: *The Journal of Chemical Physics* 86.12 (June 15, 1987), pp. 6967–6971. ISSN: 0021-9606, 1089-7690. DOI: 10.1063/1.452344. URL: http://aip.scitation.org/doi/10.1063/1.452344.

[201] T. Mizokawa and A. Fujimori. "Electronic structure and orbital ordering in perovskite-type 3 *d* transition-metal oxides studied by Hartree-Fock band-structure calculations". In: *Physical Review B* 54.8 (Aug. 15, 1996), pp. 5368–5380. ISSN: 0163-1829, 1095-3795. DOI: 10.1103/PhysRevB.54.5368. URL: https://link.aps.org/doi/10.1103/PhysRevB.54.5368.

[202] Robin Haunschild, Andreas Barth, and Werner Marx. "Evolution of DFT studies in view of a scientometric perspective". In: *Journal of Cheminformatics* 8.1 (Dec. 2016), p. 52. ISSN: 1758-2946. DOI: 10.1186/s13321-016-0166-y. URL: https://jcheminf.biomedcentral.com/articles/10.1186/s13321-016-0166-y.

[203] P. Hohenberg and W. Kohn. "Inhomogeneous Electron Gas". In: *Physical Review* 136.3 (Nov. 9, 1964), B864–B871. ISSN: 0031-899X. DOI: 10.1103/PhysRev.136.B864. URL: https://link.aps.org/doi/10.1103/PhysRev.136.B864.

[204] W. Kohn. "Nobel Lecture: Electronic structure of matter—wave functions and density functionals". In: *Reviews of Modern Physics* 71.5 (Oct. 1, 1999), pp. 1253–1266. ISSN: 0034-6861, 1539-0756. DOI: 10.1103/RevModPhys.71.1253. URL: https://link.aps.org/doi/10.1103/RevModPhys.71.1253.

[205] Matthias Ernzerhof, John P. Perdew, and Kieron Burke. "Density functionals: Where do they come from, why do they work?" In: *Density Functional Theory I*. Vol. 180. Berlin, Heidelberg: Springer Berlin Heidelberg, 1996, pp. 1–30. URL: http://link.springer.com/10.1007/3-540-61091-X_1.

[206] John P. Perdew and Yue Wang. "Accurate and simple analytic representation of the electron-gas correlation energy". In: *Physical Review B* 45.23 (June 15, 1992), pp. 13244–13249. ISSN: 0163-1829, 1095-3795. DOI: 10.1103/PhysRevB.45.13244. URL: https://link.aps.org/doi/10.1103/PhysRevB.45.13244.

[207] John P. Perdew, Kieron Burke, and Matthias Ernzerhof. "Generalized Gradient Approximation Made Simple". In: *Physical Review Letters* 77.18 (Oct. 28, 1996), pp. 3865–3868. ISSN: 0031-9007, 1079-7114. DOI: 10.1103/PhysRevLett.77.3865. URL: https://link.aps.org/doi/10.1103/PhysRevLett.77.3865.

[208] Zhigang Wu and R. E. Cohen. "More accurate generalized gradient approximation for solids". In: *Physical Review B* 73.23 (June 20, 2006), p. 235116. ISSN: 1098-0121, 1550-235X. DOI: 10.1103/PhysRevB.73.235116. URL: https://link.aps.org/doi/10.1103/PhysRevB.73.235116.

[209] W. Kohn and L. J. Sham. "Self-Consistent Equations Including Exchange and Correlation Effects". In: *Physical Review* 140.4 (Nov. 15, 1965), A1133–A1138. ISSN: 0031-899X. DOI: 10.1103/PhysRev.140.A1133. URL: https://link.aps.org/doi/10.1103/PhysRev.140.A1133.

[210] D. J. Singh and L. Nordstrom. *Planewaves, Pseudopotentials and the LAPW Method*. Springer US, 2006. ISBN: 978-0-387-28780-5. DOI: 10.1007/978-0-387-29684-5. URL: http://link.springer.com/10.1007/978-0-387-29684-5.

[211] John P. Perdew. "Density functional theory and the band gap problem". In: *International Journal of Quantum Chemistry* 28 (S19 June 19, 2009), pp. 497–523. ISSN: 00207608, 1097461X. DOI: 10.1002/qua.560280846. URL: http://doi.wiley.com/10.1002/qua.560280846.

[212] Diola Bagayoko. "Understanding density functional theory (DFT) and completing it in practice". In: *AIP Advances* 4.12 (Dec. 2014), p. 127104. ISSN: 2158-3226. DOI: 10.1063/1.4903408. URL: http://aip.scitation.org/doi/10.1063/1.4903408.

[213] Adèle D. Laurent and Denis Jacquemin. "TD-DFT benchmarks: A review". In: *International Journal of Quantum Chemistry* 113.17 (Sept. 5, 2013), pp. 2019–2039. ISSN: 00207608. DOI: 10.1002/qua.24438. URL: http://doi.wiley.com/10.1002/qua.24438.

[214] Dorothea Golze, Marc Dvorak, and Patrick Rinke. "The GW Compendium: A Practical Guide to Theoretical Photoemission Spectroscopy". In: *Frontiers in Chemistry* 7 (July 9, 2019), p. 377. ISSN: 2296-2646. DOI: 10.3389/fchem.2019.00377. URL: https://www.frontiersin.org/article/10.3389/fchem.2019.00377/full.

[215] Stephan Lany and Alex Zunger. "Many-body G W calculation of the oxygen vacancy in ZnO". In: *Physical Review B* 81.11 (Mar. 12, 2010), p. 113201. ISSN: 1098-0121, 1550-235X. DOI: 10.1103/PhysRevB.81.113201. URL: https://link.aps.org/doi/10.1103/PhysRevB.81.113201.

[216] Gabriel Kotliar and Dieter Vollhardt. "Strongly Correlated Materials: Insights From Dynamical Mean-Field Theory". In: *Physics Today* 57.3 (Mar. 2004), pp. 53–59. ISSN: 0031-9228, 1945-0699. DOI: 10.1063/1.1712502. URL: http://physicstoday.scitation.org/doi/10.1063/1.1712502.

[217] Antoine Georges et al. "Dynamical mean-field theory of strongly correlated fermion systems and the limit of infinite dimensions". In: *Reviews of Modern Physics* 68.1 (Jan. 1, 1996), pp. 13–125. ISSN: 0034-6861, 1539-0756. DOI: 10.1103/RevModPhys.68.13. URL: https://link.aps.org/doi/10.1103/RevModPhys.68.13.

[218] Vladimir I. Anisimov, Jan Zaanen, and Ole K. Andersen. "Band theory and Mott insulators: Hubbard *U* instead of Stoner *I*". In: *Physical Review B* 44.3 (July 15, 1991), pp. 943–954. ISSN: 0163-1829, 1095-3795. DOI: 10.1103/PhysRevB.44.943. URL: https://link.aps.org/doi/10.1103/PhysRevB.44.943.

[219] Christoph Loschen et al. "First-principles LDA + U and GGA + U study of cerium oxides: Dependence on the effective U parameter". In: *Physical Review B* 75.3 (Jan. 11, 2007), p. 035115. ISSN: 1098-0121, 1550-235X. DOI: 10.1103/PhysRevB.75.035115. URL: https://link.aps.org/doi/10.1103/PhysRevB.75.035115.

[220] Peter Blaha et al. "Wien2k, An Augmented Plane Wave and Local Orbitals Program for Calculating Crystal Properties". In: (2001).

[221] Karlheinz Schwarz, Peter Blaha, and S.B. Trickey. "Electronic structure of solids with WIEN2k". In: *Molecular Physics* 108.21 (Nov. 10, 2010), pp. 3147–3166. ISSN: 0026-8976, 1362-3028. DOI: 10.1080/00268976.2010.506451. URL: http://www.tandfonline.com/doi/abs/10.1080/00268976.2010.506451.

[222] Peter Blaha et al. "WIEN2k: An APW+lo program for calculating the properties of solids". In: *The Journal of Chemical Physics* 152.7 (Feb. 21, 2020), p. 074101. ISSN: 0021-9606, 1089-7690. DOI: 10.1063/1.5143061. URL: http://aip.scitation.org/doi/10.1063/1.5143061.

[223] A H MacDonald, W E Picket, and D D Koelling. "A linearised relativistic augmented-plane-wave method utilising approximate pure spin basis functions". In: *Journal of Physics C: Solid State Physics* 13.14 (May 20, 1980), pp. 2675–2683. ISSN: 0022-3719. DOI: 10.1088/0022-3719/13/14/009. URL: https://iopscience.iop.org/article/10.1088/0022-3719/13/14/009.

[224] G. Kresse and J. Furthmüller. "Efficiency of ab-initio total energy calculations for metals and semiconductors using a plane-wave basis set". In: *Computational Materials Science* 6.1 (July 1996), pp. 15–50. ISSN: 09270256. DOI: 10.1016/0927-0256(96)00008-0. URL: https://linkinghub.elsevier.com/retrieve/pii/0927025696000080.

[225] David Vanderbilt. "Soft self-consistent pseudopotentials in a generalized eigenvalue formalism". In: *Physical Review B* 41.11 (Apr. 15, 1990), pp. 7892–7895. ISSN: 0163-1829, 1095-3795. DOI: 10.1103/PhysRevB.41.7892. URL: https://link.aps.org/doi/10.1103/PhysRevB.41.7892.

[226] Paul Adrien Maurice Dirac. "The quantum theory of the electron". In: *Proceedings of the Royal Society of London. Series A, Containing Papers of a Mathematical and Physical Character* 117.778 (Feb. 1928), pp. 610–624. ISSN: 0950-1207, 2053-9150. DOI: 10.1098/rspa.1928.0023. URL: https://royalsocietypublishing.org/doi/10.1098/rspa.1928.0023.

[227] Paul Adrien Maurice Dirac. "Relativistic quantum mechanics". In: *Proceedings of the Royal Society of London. Series A, Containing Papers of a Mathematical and Physical Character* 136.829 (May 2, 1932), pp. 453–464. ISSN: 0950-1207, 2053-9150. DOI: 10.1098/rspa.1932.0094. URL: https://royalsocietypublishing.org/doi/10.1098/rspa.1932.0094.

[228] Takahiro Ito et al. "Electronic structure of C r 2 AlC as observed by angle-resolved photoemission spectroscopy". In: *Physical Review B* 96.19 (Nov. 30, 2017), p. 195168. ISSN: 2469-9950, 2469-9969. DOI: 10.1103/PhysRevB.96.195168. URL: https://link.aps.org/doi/10.1103/PhysRevB.96.195168.

[229] T. Ouisse, D. Pinek, and M.W. Barsoum. "Modelling in-plane magneto-transport in Cr2AlC". In: *Ceramics International* 45.17 (Dec. 2019), pp. 22956–22960. ISSN: 02728842. DOI: 10.1016/j.ceramint.2019.07.339. URL: https://linkinghub.elsevier.com/retrieve/pii/S0272884219321595.

[230] J. M. Harris et al. "Violation of Kohler's Rule in the Normal-State Magnetoresistance of YBa 2 Cu 3 O 7 δ and La 2 Sr x CuO 4". In: *Physical Review Letters* 75.7 (Aug. 14, 1995), pp. 1391–1394. ISSN: 0031-9007, 1079-7114. DOI: 10.1103/PhysRevLett.75.1391. URL: https://link.aps.org/doi/10.1103/PhysRevLett.75.1391.

[231] S. Kasahara et al. "Evolution from non-Fermi- to Fermi-liquid transport via isovalent doping in BaFe 2 (As 1 x P x) 2 superconductors". In: *Physical Review B* 81.18 (May 19, 2010), p. 184519. ISSN: 1098-0121, 1550-235X. DOI: 10.1103/PhysRevB.81.184519. URL: https://link.aps.org/doi/10.1103/PhysRevB.81.184519.

[232] Y. Nakajima et al. "Non-Fermi Liquid Behavior in the Magnetotransport of Ce M In $_5$ (M : Co and Rh): Striking Similarity between Quasi Two-Dimensional Heavy Fermion and High- T_c Cuprates". In: *Journal of the Physical Society of Japan* 76.2 (Feb. 15, 2007), p. 024703. ISSN: 0031-9015, 1347-4073. DOI: 10.1143/JPSJ.76.024703. URL: http://journals.jps.jp/doi/10.1143/JPSJ.76.024703.

[233] M. Dahlqvist, B. Alling, and J. Rosén. "Correlation between magnetic state and bulk modulus of Cr $_2$ AlC". In: *Journal of Applied Physics* 113.21 (June 7, 2013), p. 216103. ISSN: 0021-8979, 1089-7550. DOI: 10.1063/1.4808239. URL: http://aip.scitation.org/doi/10.1063/1.4808239.

[234] A S Ingason, M Dahlqvist, and J Rosen. "Magnetic MAX phases from theory and experiments; a review". In: *Journal of Physics: Condensed Matter* 28.43 (Nov. 2, 2016), p. 433003. ISSN: 0953-8984, 1361-648X. DOI: 10.1088/0953-8984/28/43/433003. URL: https://iopscience.iop.org/article/10.1088/0953-8984/28/43/433003.

[235] Jochen M. Schneider et al. "Ab initio calculations and experimental determination of the structure of Cr2AlC". In: *Solid State Communications* 130.7 (May 2004), pp. 445–449. ISSN: 00381098. DOI: 10.1016/j.ssc.2004.02.047. URL: https://linkinghub.elsevier.com/retrieve/pii/S0038109804001541.

[236] Michel Jaouen et al. "Invar Like Behavior of the Cr_2AlC MAX Phase at Low Temperature". In: *Journal of the American Ceramic Society* 96.12 (Dec. 2013). Ed. by Y. Zhou, pp. 3872–3876. ISSN: 00027820. DOI: 10.1111/jace.12635. URL: http://doi.wiley.com/10.1111/jace.12635.

[237] S.M. Goldberg, C.S. Fadley, and S. Kono. "Photoionization cross-sections for atomic orbitals with random and fixed spatial orientation". In: *Journal of Electron Spectroscopy and Related Phenomena* 21.4 (Jan. 1981), pp. 285–363. ISSN: 03682048. DOI: 10.1016/0368-2048(81)85067-0. URL: https://linkinghub.elsevier.com/retrieve/pii/0368204881850670.

[238] X.-P. Wang et al. "Orbital characters determined from Fermi surface intensity patterns using angle-resolved photoemission spectroscopy". In: *Physical Review B* 85.21 (June 19, 2012), p. 214518. ISSN: 1098-0121, 1550-235X. DOI: 10.1103/PhysRevB.85.214518. URL: https://link.aps.org/doi/10.1103/PhysRevB.85.214518.

[239] Yuelei Bai, Xiaodong He, and Rongguo Wang. "Lattice dynamics of Al-containing MAX-phase carbides: a first-principle study: Lattice dynamics of Al-containing MAX-phase carbides". In: *Journal of Raman Spectroscopy* 46.9 (Sept. 2015), pp. 784–794. ISSN: 03770486. DOI: 10.1002/jrs.4720. URL: http://doi.wiley.com/10.1002/jrs.4720.

[240] Anton Kokalj. "Computer graphics and graphical user interfaces as tools in simulations of matter at the atomic scale". In: *Computational Materials Science* 28.2 (Oct. 2003), pp. 155–168. ISSN: 09270256. DOI: 10.1016/S0927-0256(03)00104-6. URL: https://linkinghub.elsevier.com/retrieve/pii/S0927025603001046.

[241] GuoZhu Jia and LiJun Yang. "Ab initio calculations for properties of Ti2AlN and Cr2AlC". In: *Physica B: Condensed Matter* 405.21 (Nov. 2010), pp. 4561–4564. ISSN: 09214526. DOI: 10.1016/j.physb.2010.08.038. URL: https://linkinghub.elsevier.com/retrieve/pii/S0921452610008082.

[242] Eric Fawcett. "Spin-density-wave antiferromagnetism in chromium". In: *Reviews of Modern Physics* 60.1 (Jan. 1, 1988), pp. 209–283. ISSN: 0034-6861. DOI: 10.1103/RevModPhys.60.209. URL: https://link.aps.org/doi/10.1103/RevModPhys.60.209.

[243] M. Hengsberger et al. "Photoemission Study of a Strongly Coupled Electron-Phonon System". In: *Physical Review Letters* 83.3 (July 19, 1999), pp. 592–595. ISSN: 0031-9007, 1079-7114. DOI: 10.1103/PhysRevLett.83.592. URL: https://link.aps.org/doi/10.1103/PhysRevLett.83.592.

[244] Toru Hirahara et al. "The effective mass of a free-electron-like surface state of the Si(111)-Ag surface investigated by photoemission and scanning tunneling spectroscopies". In: *Surface Science* 563.1 (Aug. 2004), pp. 191–198. ISSN: 00396028. DOI: 10.1016/j.susc.2004.06.157. URL: https://linkinghub.elsevier.com/retrieve/pii/S0039602804008465.

[245] J.E. Gayone et al. "Determining the electron-phonon mass enhancement parameter λ on metal surfaces". In: *Applied Physics A* 80.5 (Feb. 2005), pp. 943–949. ISSN: 0947-8396, 1432-0630. DOI: 10.1007/s00339-004-3120-1. URL: http://link.springer.com/10.1007/s00339-004-3120-1.

[246] J. Gielis. "A generic geometric transformation that unifies a wide range of natural and abstract shapes". In: *American Journal of Botany* 90.3 (Mar. 1, 2003), pp. 333–338. ISSN: 0002-9122, 1537-2197. DOI: 10.3732/ajb.90.3.333. URL: http://doi.wiley.com/10.3732/ajb.90.3.333.

[247] J. M. Ziman. *Electrons and phonons: the theory of transport phenomena in solids*. Oxford classic texts in the physical sciences. Oxford : New York: Clarendon Press ; Oxford University Press, 2001. 554 pp. ISBN: 978-0-19-850779-6.

[248] N. P. Ong. "Geometric interpretation of the weak-field Hall conductivity in two-dimensional metals with arbitrary Fermi surface". In: *Physical Review B* 43.1 (Jan. 1, 1991), pp. 193–201. ISSN: 0163-1829, 1095-3795. DOI: 10.1103/PhysRevB.43.193. URL: https://link.aps.org/doi/10.1103/PhysRevB.43.193.

[249] Damir Pinek et al. "Electronic structure of V 2 AlC". In: *Physical Review B* 98.3 (July 16, 2018), p. 035120. ISSN: 2469-9950, 2469-9969. DOI: 10.1103/PhysRevB.98.035120. URL: https://link.aps.org/doi/10.1103/PhysRevB.98.035120.

[250] A. Bansil et al. "Influence of the third dimension of quasi-two-dimensional cuprate superconductors on angle-resolved photoemission spectra". In: *Physical Review B* 71.1 (Jan. 6, 2005), p. 012503. ISSN: 1098-0121, 1550-235X. DOI: 10.1103/PhysRevB.71.012503. URL: https://link.aps.org/doi/10.1103/PhysRevB.71.012503.

[251] M. Lindroos et al. "Role of kz-dispersion in photoemission from quasi-2D cuprates". In: *Journal of Physics and Chemistry of Solids* 67.1 (Jan. 2006), pp. 244–248. ISSN: 00223697. DOI: 10.1016/j.jpcs.2005.10.157. URL: https://linkinghub.elsevier.com/retrieve/pii/S0022369705005214.

[252] Thomas Grandke, Lothar Ley, and Manuel Cardona. "Angle-resolved uv photoemission and electronic band structures of the lead chalcogenides". In: *Physical Review B* 18.8 (Oct. 15, 1978), pp. 3847–3871. ISSN: 0163-1829. DOI: 10.1103/PhysRevB.18.3847. URL: https://link.aps.org/doi/10.1103/PhysRevB.18.3847.

[253] Zhimei Sun et al. "Electronic origin of shearing in M $_2$ AC (M = Ti,V,Cr,A = Al,Ga)". In: *Journal of Physics: Condensed Matter* 17.46 (Nov. 23, 2005), pp. 7169–7176. ISSN: 0953-8984, 1361-648X. DOI: 10.1088/0953-8984/17/46/001. URL: https://iopscience.iop.org/article/10.1088/0953-8984/17/46/001.

[254] Haizhou Wang, Yongzhong Zhan, and Mingjun Pang. "The structure, elastic, electronic properties and Debye temperature of M2AlC (MV, Nb and Ta) under pressure from first-principles". In: *Computational Materials Science* 54 (Mar. 2012), pp. 16–22. ISSN: 09270256. DOI: 10.1016/j.commatsci.2011.11.003. URL: https://linkinghub.elsevier.com/retrieve/pii/S0927025611006173.

[255] V. Brouet et al. "Angle-resolved photoemission study of the evolution of band structure and charge density wave properties in R Te 3 (R = Y , La, Ce, Sm, Gd, Tb, and Dy)". In: *Physical Review B* 77.23 (June 4, 2008), p. 235104. ISSN: 1098-0121, 1550-235X. DOI: 10.1103/PhysRevB.77.235104. URL: https://link.aps.org/doi/10.1103/PhysRevB.77.235104.

[256] Damir Pinek et al. "Unified description of the electronic structure of M 2 A C nanolamellar carbides". In: *Physical Review B* 100.7 (Aug. 23, 2019), p. 075144. ISSN: 2469-9950, 2469-9969. DOI: 10.1103/PhysRevB.100.075144. URL: https://link.aps.org/doi/10.1103/PhysRevB.100.075144.

[257] M.H. Cohen and V. Heine. "Electronic band structures of the alkali metals and of the noble metals and their α-phase alloys". In: *Advances in Physics* 7.28 (Oct. 1958), pp. 395–434. ISSN: 0001-8732, 1460-6976. DOI: 10.1080/00018735800101307. URL: http://www.tandfonline.com/doi/abs/10.1080/00018735800101307.

[258] S. Raimes. "The rigid-band model". In: *Journal de Physique et le Radium* 23.10 (1962), pp. 639–643. ISSN: 0368-3842. DOI: 10.1051/jphysrad:019620023010063901. URL: http://www.edpsciences.org/10.1051/jphysrad:019620023010063901.

[259] Edward A. Stern. "Rigid-Band Model of Alloys". In: *Physical Review* 157.3 (May 15, 1967), pp. 544–551. ISSN: 0031-899X. DOI: 10.1103/PhysRev.157.544. URL: https://link.aps.org/doi/10.1103/PhysRev.157.544.

[260] Uichirō Mizutani. *Introduction to the electron theory of metals*. Cambridge ; New York: Cambridge University Press, 2001. 590 pp. ISBN: 978-0-521-58334-3 978-0-521-58709-9.

[261] N. Hamdad, N. Benosman, and B. Bouhafs. "First principles calculation of electronic structure, bonding and chemical stability of TiB2, NbB2 and their ternary alloy Ti0.5Nb0.5B2". In: *Physica B: Condensed Matter* 405.2 (Jan. 2010), pp. 540–546. ISSN: 09214526. DOI: 10.1016/j.physb.2009.09.061. URL: https://linkinghub.elsevier.com/retrieve/pii/S0921452609011600.

[262] C.M. Julien. "Lithium intercalated compounds". In: *Materials Science and Engineering: R: Reports* 40.2 (Jan. 2003), pp. 47–102. ISSN: 0927796X. DOI: 10.1016/S0927-796X(02)00104-3. URL: https://linkinghub.elsevier.com/retrieve/pii/S0927796X02001043.

[263] G Y Guo and W Y Liang. "Electronic structures of intercalation complexes of the layered compound 2H-TaS $_2$". In: *Journal of Physics C: Solid State Physics* 20.27 (Sept. 30, 1987), pp. 4315–4334. ISSN: 0022-3719. DOI: 10.1088/0022-3719/20/27/011. URL: https://iopscience.iop.org/article/10.1088/0022-3719/20/27/011.

[264] W. Jaegermann et al. "Photoelectron spectroscopy of UHV in situ intercalated Li/TiSe2. Experimental proof of the rigid band model". In: *Chemical Physics Letters* 221.5 (Apr. 1994), pp. 441–446. ISSN: 00092614. DOI: 10.1016/0009-2614(94)00286-X. URL: https://linkinghub.elsevier.com/retrieve/pii/000926149400286X.

[265] L. F. Mattheiss. "Energy Bands for the Iron Transition Series". In: *Physical Review* 134.4 (May 18, 1964), A970–A973. ISSN: 0031-899X. DOI: 10.1103/PhysRev.134.A970. URL: https://link.aps.org/doi/10.1103/PhysRev.134.A970.

[266] Wandong Xing, Fanyan Meng, and Rong Yu. "Strengthening materials by changing the number of valence electrons". In: *Computational Materials Science* 129 (Mar. 2017), pp. 252–258. ISSN: 09270256. DOI: 10.1016/j.commatsci.2016.12.037. URL: https://linkinghub.elsevier.com/retrieve/pii/S0927025616306644.

[267] J. Park et al. "Angle-resolved photoemission study of the rare-earth intermetallic compounds: R Ni 2 Ge 2 (R = Eu , Gd)". In: *Physical Review B* 70.7 (Aug. 18, 2004), p. 075105. ISSN: 1098-0121, 1550-235X. DOI: 10.1103/PhysRevB.70.075105. URL: https://link.aps.org/doi/10.1103/PhysRevB.70.075105.

[268] Paolo Vilmercati et al. "Nonrigid band shift and nonmonotonic electronic structure changes upon doping in the normal state of the pnictide high-temperature superconductor Ba (F e 1 x C o x) 2 A s 2". In: *Physical Review B* 94.19 (Nov. 28, 2016), p. 195147. ISSN: 2469-9950, 2469-9969. DOI: 10.1103/PhysRevB.94.195147. URL: https://link.aps.org/doi/10.1103/PhysRevB.94.195147.

[269] H. C. Choi et al. "Electronic structures and magnetic properties of layered compound RCrSb3 (R=La,Yb)". In: *Journal of Applied Physics* 101.9 (May 2007), 09G513. ISSN: 0021-8979, 1089-7550. DOI: 10.1063/1.2710335. URL: http://aip.scitation.org/doi/10.1063/1.2710335.

[270] Jürgen Winterlik et al. "Superconductivity in palladium-based Heusler compounds". In: *Physical Review B* 79.6 (Feb. 4, 2009), p. 064508. ISSN: 1098-0121, 1550-235X. DOI: 10.1103/PhysRevB.79.064508. URL: https://link.aps.org/doi/10.1103/PhysRevB.79.064508.

[271] Conyers Herring. "Accidental Degeneracy in the Energy Bands of Crystals". In: *Physical Review* 52.4 (Aug. 15, 1937), pp. 365–373. ISSN: 0031-899X. DOI: 10.1103/PhysRev.52.365. URL: https://link.aps.org/doi/10.1103/PhysRev.52.365.

[272] N. P. Armitage, E. J. Mele, and Ashvin Vishwanath. "Weyl and Dirac semimetals in three-dimensional solids". In: *Reviews of Modern Physics* 90.1 (Jan. 22, 2018), p. 015001. ISSN: 0034-6861, 1539-0756. DOI: 10.1103/RevModPhys.90.015001. URL: https://link.aps.org/doi/10.1103/RevModPhys.90.015001.

[273] Motoaki Hirayama, Ryo Okugawa, and Shuichi Murakami. "Topological Semimetals Studied by Ab Initio Calculations". In: *Journal of the Physical Society of Japan* 87.4 (Apr. 15, 2018), p. 041002. ISSN: 0031-9015, 1347-4073. DOI: 10.7566/JPSJ.87.041002. URL: http://journals.jps.jp/doi/10.7566/JPSJ.87.041002.

[274] Shuo-Ying Yang et al. "Symmetry demanded topological nodal-line materials". In: *Advances in Physics: X* 3.1 (Jan. 2018), p. 1414631. ISSN: 2374-6149. DOI: 10.1080/23746149.2017.1414631. URL: https://www.tandfonline.com/doi/full/10.1080/23746149.2017.1414631.

[275] B Ya Shapiro et al. "Type I superconductivity in Dirac materials". In: *Journal of Physics: Condensed Matter* 30.33 (Aug. 22, 2018), p. 335403. ISSN: 0953-8984, 1361-648X. DOI: 10.1088/1361-648X/aad305. URL: https://iopscience.iop.org/article/10.1088/1361-648X/aad305.

[276] S. Banerjee et al. "Tight-Binding Modeling and Low-Energy Behavior of the Semi-Dirac Point". In: *Physical Review Letters* 103.1 (July 1, 2009), p. 016402. ISSN: 0031-9007, 1079-7114. DOI: 10.1103/PhysRevLett.103.016402. URL: https://link.aps.org/doi/10.1103/PhysRevLett.103.016402.

[277] D. Takane et al. "Dirac-node arc in the topological line-node semimetal HfSiS". In: *Physical Review B* 94.12 (Sept. 8, 2016), p. 121108. ISSN: 2469-9950, 2469-9969. DOI: 10.1103/PhysRevB.94.121108. URL: https://link.aps.org/doi/10.1103/PhysRevB.94.121108.

[278] Yan Sun et al. "Dirac nodal lines and induced spin Hall effect in metallic rutile oxides". In: *Physical Review B* 95.23 (June 2, 2017), p. 235104. ISSN: 2469-9950, 2469-9969. DOI: 10.1103/PhysRevB.95.235104. URL: http://link.aps.org/doi/10.1103/PhysRevB.95.235104.

[279] Jiangxu Li et al. "Topological massive Dirac fermions in β -tungsten". In: *Physical Review B* 99.16 (Apr. 8, 2019), p. 165110. ISSN: 2469-9950, 2469-9969. DOI: 10.1103/PhysRevB.99.165110. URL: https://link.aps.org/doi/10.1103/PhysRevB.99.165110.

[280] Koichiro Yaji et al. "High-resolution three-dimensional spin- and angle-resolved photoelectron spectrometer using vacuum ultraviolet laser light". In: *Review of Scientific Instruments* 87.5 (May 2016), p. 053111. ISSN: 0034-6748, 1089-7623. DOI: 10.1063/1.4948738. URL: http://aip.scitation.org/doi/10.1063/1.4948738.

[281] W. Jeitschko, H. Nowotny, and F. Benesovsky. "Kohlenstoffhaltige ternare Verbindungen (H-Phase)". In: *Monatshefte fur Chemie* 94.4 (1963), pp. 672–676. DOI: 10.1007/BF00913068. URL: http://link.springer.com/10.1007/BF00913068.

[282] L. F. Mattheiss. "Electronic Structure of Niobium and Tantalum". In: *Physical Review B* 1.2 (Jan. 15, 1970), pp. 373–380. ISSN: 0556-2805. DOI: 10.1103/PhysRevB.1.373. URL: https://link.aps.org/doi/10.1103/PhysRevB.1.373.

[283] R. F. W. Bader. "Atoms in molecules". In: *Accounts of Chemical Research* 18.1 (Jan. 1985), pp. 9–15. ISSN: 0001-4842, 1520-4898. DOI: 10.1021/ar00109a003. URL: https://pubs.acs.org/doi/abs/10.1021/ar00109a003.

[284] A.L. Allred. "Electronegativity values from thermochemical data". In: *Journal of Inorganic and Nuclear Chemistry* 17.3 (June 1961), pp. 215–221. ISSN: 00221902. DOI: 10.1016/0022-1902(61)80142-5. URL: https://linkinghub.elsevier.com/retrieve/pii/0022190261801425.

[285] J. Kim et al. "Observation of tunable band gap and anisotropic Dirac semimetal state in black phosphorus". In: *Science* 349.6249 (Aug. 14, 2015), pp. 723–726. ISSN: 0036-8075, 1095-9203. DOI: 10.1126/science.aaa6486. URL: https://www.sciencemag.org/lookup/doi/10.1126/science.aaa6486.

[286] M. R. Scholz et al. "Topological surface state of α Sn on InSb(001) as studied by photoemission". In: *Physical Review B* 97.7 (Feb. 1, 2018), p. 075101. ISSN: 2469-9950, 2469-9969. DOI: 10.1103/PhysRevB.97.075101. URL: https://link.aps.org/doi/10.1103/PhysRevB.97.075101.

[287] Daichi Takane et al. "Observation of a Dirac nodal line in AlB 2". In: *Physical Review B* 98.4 (July 17, 2018), p. 041105. ISSN: 2469-9950, 2469-9969. DOI: 10.1103/PhysRevB.98.041105. URL: https://link.aps.org/doi/10.1103/PhysRevB.98.041105.

[288] M. Hakl et al. "Energy scale of Dirac electrons in Cd 3 As 2". In: *Physical Review B* 97.11 (Mar. 26, 2018), p. 115206. ISSN: 2469-9950, 2469-9969. DOI: 10.1103/PhysRevB.97.115206. URL: https://link.aps.org/doi/10.1103/PhysRevB.97.115206.

[289] A. A Abrikosov. "Quantum linear magnetoresistance". In: *Europhysics Letters (EPL)* 49.6 (Mar. 15, 2000), pp. 789–793. ISSN: 0295-5075, 1286-4854. DOI: 10.1209/epl/i2000-00220-2. URL: https://iopscience.iop.org/article/10.1209/epl/i2000-00220-2.

[290] I. Pallecchi et al. "Role of Dirac cones in magnetotransport properties of REFeAsO (RE = rare earth) oxypnictides". In: *The European Physical Journal B* 86.8 (Aug. 2013), p. 338. ISSN: 1434-6028, 1434-6036. DOI: 10.1140/epjb/e2013-40148-6. URL: http://link.springer.com/10.1140/epjb/e2013-40148-6.

[291] G. Hug. "Electronic structures of and composition gaps among the ternary carbides Ti 2 M C". In: *Physical Review B* 74.18 (Nov. 13, 2006), p. 184113. ISSN: 1098-0121, 1550-235X. DOI: 10.1103/PhysRevB.74.184113. URL: https://link.aps.org/doi/10.1103/PhysRevB.74.184113.

[292] Damir Pinek et al. "Near Fermi level electronic structure of Ti 3 Si C 2 revealed by angle-resolved photoemission spectroscopy". In: *Physical Review B* 102.7 (Aug. 7, 2020), p. 075111. ISSN: 2469-9950, 2469-9969. DOI: 10.1103/PhysRevB.102.075111. URL: https://link.aps.org/doi/10.1103/PhysRevB.102.075111.

[293] Mohamed Alhabeb et al. "Selective Etching of Silicon from Ti $_3$ SiC $_2$ (MAX) To Obtain 2D Titanium Carbide (MXene)". In: *Angewandte Chemie International Edition* 57.19 (May 4, 2018), pp. 5444–5448. ISSN: 14337851. DOI: 10.1002/anie.201802232. URL: http://doi.wiley.com/10.1002/anie.201802232.

[294] H. -I. Yoo, M. W. Barsoum, and T. El-Raghy. "Ti3SiC2 has negligible thermopower". In: *Nature* 407.6804 (Oct. 2000), pp. 581–582. ISSN: 0028-0836, 1476-4687. DOI: 10.1038/35036686. URL: http://www.nature.com/articles/35036686.

[295] Laurent Chaput et al. "Anisotropy and thermopower in Ti 3 SiC 2". In: *Physical Review B* 71.12 (Mar. 22, 2005), p. 121104. ISSN: 1098-0121, 1550-235X. DOI: 10.1103/PhysRevB.71.121104. URL: https://link.aps.org/doi/10.1103/PhysRevB.71.121104.

[296] L. Chaput et al. "Thermopower of the 312 MAX phases Ti 3 Si C 2 , Ti 3 Ge C 2 , and Ti 3 Al C 2". In: *Physical Review B* 75.3 (Jan. 8, 2007), p. 035107. ISSN: 1098-0121, 1550-235X. DOI: 10.1103/PhysRevB.75.035107. URL: https://link.aps.org/doi/10.1103/PhysRevB.75.035107.

[297] Martin Magnuson et al. "Electronic-structure origin of the anisotropic thermopower of nanolaminated Ti 3 SiC 2 determined by polarized x-ray spectroscopy and Seebeck measurements". In: *Physical Review B* 85.19 (May 22, 2012), p. 195134. ISSN: 1098-0121, 1550-235X. DOI: 10.1103/PhysRevB.85.195134. URL: https://link.aps.org/doi/10.1103/PhysRevB.85.195134.

[298] Alexander L. Ivanovsky, Dmitry L. Novikov, and Gennady P. Shveikin. "Electronic Structure of Ti3SiC2". In: *Mendeleev Communications* 5.3 (Jan. 1995), pp. 90–91. ISSN: 09599436. DOI: 10.1070/MC1995v005n03ABEH000469. URL: https://linkinghub.elsevier.com/retrieve/pii/S0959943695714870.

[299] Veronika Sunko et al. "Maximal Rashba-like spin splitting via kinetic-energy-coupled inversion-symmetry breaking". In: *Nature* 549.7673 (Sept. 2017), pp. 492–496. ISSN: 0028-0836, 1476-4687. DOI: 10.1038/nature23898. URL: http://www.nature.com/articles/nature23898.

[300] V.N. Strocov. "Intrinsic accuracy in 3-dimensional photoemission band mapping". In: *Journal of Electron Spectroscopy and Related Phenomena* 130.1 (July 2003), pp. 65–78. ISSN: 03682048. DOI: 10.1016/S0368-2048(03)00054-9. URL: https://linkinghub.elsevier.com/retrieve/pii/S0368204803000549.

[301] Chen Fang et al. "Topological nodal line semimetals". In: *Chinese Physics B* 25.11 (Nov. 2016), p. 117106. ISSN: 1674-1056. DOI: 10.1088/1674-1056/25/11/117106. URL: https://iopscience.iop.org/article/10.1088/1674-1056/25/11/117106.

[302] P. Kapitza. "The study of the specific resistance of bismuth crystals and its change in strong magnetic fields and some allied problems". In: *Proceedings of the Royal Society of London. Series A, Containing Papers of a Mathematical and Physical Character* 119.782 (June 1928), pp. 358–443. ISSN: 0950-1207, 2053-9150. DOI: 10.1098/rspa.1928.0103. URL: https://royalsocietypublishing.org/doi/10.1098/rspa.1928.0103.

[303] F. Y. Yang. "Large Magnetoresistance of Electrodeposited Single-Crystal Bismuth Thin Films". In: *Science* 284.5418 (May 21, 1999), pp. 1335–1337. ISSN: 00368075, 10959203. DOI: 10.1126/science.284.5418.1335. URL: https://www.sciencemag.org/lookup/doi/10.1126/science.284.5418.1335.

[304] Kaifei Kang et al. "Nonlinear anomalous Hall effect in few-layer WTe2". In: *Nature Materials* 18.4 (Apr. 2019), pp. 324–328. ISSN: 1476-1122, 1476-4660. DOI: 10.1038/s41563-019-0294-7. URL: http://www.nature.com/articles/s41563-019-0294-7.

[305] Tetsuro Habe and Mikito Koshino. "Anomalous Hall effect in 2 H -phase M X 2 transition-metal dichalcogenide monolayers on ferromagnetic substrates (M = Mo, W, and X = S, Se, Te)". In: *Physical Review B* 96.8 (Aug. 7, 2017), p. 085411. ISSN: 2469-9950, 2469-9969. DOI: 10.1103/PhysRevB.96.085411. URL: http://link.aps.org/doi/10.1103/PhysRevB.96.085411.

[306] Z. Z. Du et al. "Band Signatures for Strong Nonlinear Hall Effect in Bilayer WTe 2". In: *Physical Review Letters* 121.26 (Dec. 26, 2018), p. 266601. ISSN: 0031-9007, 1079-7114. DOI: 10.1103/PhysRevLett.121.266601. URL: https://link.aps.org/doi/10.1103/PhysRevLett.121.266601.

[307] .L Shi. "Ph.D thesis". In: *UC Louvain university* (2017).

[308] Naoto Nagaosa et al. "Anomalous Hall effect". In: *Reviews of Modern Physics* 82.2 (May 13, 2010), pp. 1539–1592. ISSN: 0034-6861, 1539-0756. DOI: 10.1103/RevModPhys.82.1539. URL: https://link.aps.org/doi/10.1103/RevModPhys.82.1539.

[309] O.K. Andersen et al. "Electrons, phonons, and their interaction in YBa2Cu3O7". In: *Physica C: Superconductivity* 185-189 (Dec. 1991), pp. 147–155. ISSN: 09214534. DOI: 10.1016/0921-4534(91)91964-6. URL: https://linkinghub.elsevier.com/retrieve/pii/0921453491919646.